

# **Investigation of Charge Transport Mechanisms in Lead-Free Perovskites in Presence of Carbon Nanotubes for Optoelectronic Device Applications**

**Thesis submitted for the Degree of Doctor of Philosophy (Science)  
Of  
Jadavpur University  
2024**

*by*  
**Dipankar Sahoo**



**Condensed Matter Physics Research Centre  
Department of Physics  
Jadavpur University  
Kolkata 700 032  
INDIA**

*Dedicated*


*to*

*my family*

## **CERTIFICATE FROM THE SUPERVISOR**

*This is to certify that the thesis entitled “Investigation of Charge Transport Mechanisms in Lead-Free Perovskites in Presence of Carbon Nanotubes for Optoelectronic Device Applications”, submitted by Mr. Dipankar Sahoo who got his name registered on 20<sup>th</sup> September 2018 for the award of Ph. D. (Science) Degree of Jadavpur University, is absolutely based upon his own work under the supervision of Professor Nabin Baran Manik and that neither this thesis nor any part of it has been submitted for either any degree / diploma or any other academic award anywhere before.*

Date: 19.06.24

  
.....  
Dr. Nabin Baran Manik  
Supervisor  
Professor  
Condensed Matter Physics Research Centre  
Department of Physics  
Jadavpur University  
Kolkata 700 032  
India




Dr. NABIN BARAN MANIK  
Professor  
Department of Physics  
Jadavpur University  
Kolkata - 700 032

## **DECLARATION BY THE AUTHOR**

*"I do hereby declare that the work embodied in this thesis entitled **"Investigation of Charge Transport Mechanisms in Lead-Free Perovskites in Presence of Carbon Nanotubes for Optoelectronic Device Applications"** which is being submitted for the degree of Doctor of Philosophy (Science), is my own work and that, to the best of my knowledge and belief, neither the thesis nor any part thereof has been accepted for the award of any other degree or diploma of the university or other institute of higher learning, except where due acknowledgement has been made in the text.*

Date:

Place:

  
19.06.24  
.....  
(Dipankar Sahoo)"  
Signature of the Research Fellow

## **Acknowledgement**

In this thesis, I have presented a summary of my five-year research work. During this period, I had a rewarding experience pursuing my Ph.D. at Jadavpur University, Kolkata.

I am deeply grateful to my supervisor, Professor Nabin Baan Manik, for granting me significant independence, which I thoroughly enjoyed during my research. I would like to express my sincere gratitude for his invaluable guidance, patient encouragement, and direction over the years. His daily instructions were crucial in carrying out the experimental work, developing devices, and establishing new concepts. Without his active support, pursuing this work would have been challenging.

I would also like to thank Dr. Chittaranjan Sinha, Professor of the Department of Chemistry, Jadavpur University, for his support and insightful discussions during the initiation of my research. My heartfelt thanks go to Dr. Koustav Das, Associate Professor of the Department of Physics, Jadavpur University, for providing me with access to his laboratory and instruments during my work. I am also grateful to Dr. Bharati Tudu, Assistant Professor of the Department of Physics, Jadavpur University, for granting me the opportunity to use the instrument DC Sputtering and AFM during my research.

I owe a lot to my peers for their help in this endeavour. I extend my thanks to Sri A. K. Karan, Dr. S. Sen, Miss S. Rakshit, Dr. S. Bhunia, and Dr. P. Das for their assistance with measurements and engaging in various discussions. I am equally thankful to research scholars B. Jana, P. Sengupta M. Pramanik and Z. Mallick for their help with formal data analysis and discussions.

I would like to take this opportunity to express my gratitude to all the members of Jadavpur Central Library and the Physics Departmental Library, from where I collected many scientific references required for my dissertation. Additionally, I appreciate the support provided by the Central Instrumental Facility of the Department of Physics, Jadavpur University. The Department of Physics also allowed me to access various measurements, including FESEM, XRD, TEM, UV-Visible spectroscopy, and FTIR.

I am thankful to the Department of Science and Technology (DST), Government of India, for awarding me an INSPIRE Fellowship (IF180342). The electrical and optical measurements were conducted in our laboratory, with most instruments and chemicals procured from the

research project funded by RUSA 2.0 and contingency provided by DST, Govt. of India. I acknowledge and thank both for the financial assistance.

I want to express my heartfelt appreciation to my family for their unwavering support and continuous encouragement. Without their inspiration, completing this work would have been almost impossible. They made significant sacrifices during my research, and I am profoundly grateful for their presence and support. Thank you for being with me throughout this journey.

Lastly, I would like to express my heartfelt gratitude to my closest friend, whose unwavering presence has been an incredible pillar of support throughout the years. Your constant encouragement and boundless inspiration serve as an enduring source of motivation, propelling me forward on my journey. Your steadfast belief in me never wavers, and for that, I am truly thankful.

Jadavpur University  
Kolkata  
2024

Dipankar Sahoo

## **List of Abbreviations**

Al	Aluminium
$\phi_b$	Barrier height
C-V	Capacitance - Voltage
CNT	Carbon nanotube
COOH	Carboxylic acid functionalized
CsSnCl <sub>3</sub>	Cesium tin chloride
Cs <sub>2</sub> SnCl <sub>6</sub>	Cesium tin chloride double perovskite
T <sub>C</sub>	Characteristic temperature
N <sub>D</sub>	Concentration of donor atoms
$\sigma$	Electrical conductivity
Cu	Copper
I-V	Current-Voltage characteristic
DMSO	Dimethyl sulfoxide
DMF	Dimethylformamide
DWCNT	Double walled carbon nanotube
N <sub>C</sub>	Effective density of states
ETL	Electron transport layer
E <sub>F</sub>	Fermi energy
HOMO	Highest occupied molecular orbital
HTL	Hole transport layer
$\eta$	Ideality factor
ITO	Indium tin oxides
Pb	Lead
LED	Light emitting diode
LUMO	Lowest unoccupied molecular orbital
M/S	Metal semiconductor contact
CH <sub>3</sub> NH <sub>3</sub> SnI <sub>3</sub>	Methylammonium tin iodide
MWCNT	Multi walled carbon nanotube
Pe-LED	Perovskite light emitting diode
Pe-PD	Perovskite photodiode
PSC	Perovskite solar cell

PD	Photodiode
$R_s$	Series resistance
SWCNT	Single walled carbon nanotube
SCLC	Space charge limited current
$V_{th}$	Threshold voltage
Sn	Tin
$SnF_2$	Tin fluoride
$TiO_2$	Titanium dioxide
$E_t$	Trap energy

## **List of Figures**

**Figure 1.1:** Lattice of perovskite (one unit cell structure). Green denotes larger cation atoms, red denotes smaller cation atoms, blue denotes oxygen atoms of cells of cubic, tetragonal and orthorhombic structures

**Figure 2.1:** Schematic device structure of FTO)/ETM/perovskite/HTM/Au

**Figure 2.2:** Schematic diagram of several transport mechanism in metal- sample (semiconductor)-metal structure

**Figure 2.3:** Different types of trap distributions in the bandgap of a sample

**Figure 2.4:** Types of carbon nanotubes (CNTs)

**Figure 3.1:** Spin coating setup for development of thin film.

**Figure 3.2:** (a) Components of a diffractometer (b) schematic diagram of working of X-ray diffraction (XRD) (c) displays the X-ray powder diffractometer (Bruker D 8 Advance)

**Figure 3.3:** Shows the digital image of UV-Vis spectrophotometer

**Figure 3.4:** (a) Components of a FESEM (b) digital image of FESEM FEI INSPECT F50

**Figure 3.5:** Shows laboratory AFM setup to measure film roughness

**Figure 3.6:** Keithley 2400 SMU with computer interface for the electrical measurements

**Figure 3.7:** Shows self-designed laboratory glove box setup for Sn-based perovskite synthesis

**Figure 3.8:** Shows depicts a schematic diagram of XPS with different parts

**Figure 3.9:** (a) Schematic diagram of  $\text{CH}_3\text{NH}_3\text{SnI}_3$  perovskite preparation, Solution A:  $\text{CH}_3\text{NH}_3\text{I}$ , Solution B:  $\text{SnI}_2$ , Solution C: Oleic phase (b) perovskite Schottky device

**Figure 3.10:** (a) PXRD refinement of  $\text{CH}_3\text{NH}_3\text{SnI}_3$  perovskite sample in the range of  $2\theta$  from  $10^\circ$  to  $70^\circ$  (b) refined ball and stick structure obtained using vesta software

**Figure 3.11:** Solid-state absorption spectra of  $\text{CH}_3\text{NH}_3\text{SnI}_3$  perovskite thin film in the range of 500-1100 nm. The inset represents Tauc's plot

**Figure 3.12:** X-ray photoelectron spectrum of perovskite films **(a)** as prepared **(b)** after exposure in the air till experiments were taking place

**Figure 3.13:** **(a)** TGA curve **(b)** FTIR of the  $\text{CH}_3\text{NH}_3\text{SnI}_3$  perovskite sample

**Figure 3.14:** **(a)** FESEM images of  $\text{CH}_3\text{NH}_3\text{SnI}_3$  films processed using spin coating technique **(b)** Cube size distribution shows the maximum particle size lies between 60 to 70 nm. **(c)** EDX spectrum for methylammonium tin iodide ( $\text{CH}_3\text{NH}_3\text{SnI}_3$ ) perovskite

**Figure 3.15:** Atomic force microscopy of the thin film prepared on a silicon substrate **(a)** Z-axis -scan forward line fit **(b)** Z-axis-scan backwards derived data

**Figure 3.16:** **(a)** Frequency-dependent of  $Z'(\omega)$  &  $Z''(\omega)$  plot **(b)** Cole-Cole or Nyquist plot of  $\text{CH}_3\text{NH}_3\text{SnI}_3$  perovskite at room temperature, inset of **(b)** represents the equivalent circuit model of the corresponding plot

**Figure 3.17:** **(a)** Dielectric constant (blue) and dielectric loss (red) variation with frequency. The inset of **(a)** Represents the model used to explain the dielectric variation. **(b)** variation of  $\tan \delta$  with frequency

**Figure 3.18:** **(a)** Frequency dependence real (blue) and an imaginary (red) component of electric modulus **(b)** ac conductivity

**Figure 3.19:** **(a)** Keithley 2400 SMU for I-V measurements **(b)** a typical I-V characteristic of a Schottky device

**Figure 3.20:** **(a)** Energy level diagram **(b)** band alignment of the device in the forward biased condition **(c)** I-V characteristic curves for  $\text{CH}_3\text{NH}_3\text{SnI}_3$  perovskite-based device under light and dark conditions

**Figure 3.21:** **(a)**  $dV/d\ln I$  vs.  $I$  (A) **(b)**  $H(I)$  vs.  $I$  (A) curves of the MS device under dark and photo illumination conditions

**Figure 3.22:** **(a)**  $\ln I$  vs.  $\ln V$  plots and **(b)**  $I$  vs.  $V^2$  curves for  $\text{CH}_3\text{NH}_3\text{SnI}_3$ -based perovskite device in dark and light conditions

**Figure 4.1:** Structure **(a)** visualization of cubic  $\text{CH}_3\text{NH}_3\text{SnI}_3$  perovskite by VESTA **(b)** COOH functionalized SWCNT

**Figure 4.2:** (a) Schematic representation of components of TEM (b) laboratory setup of TEM

**Figure 4.3:** (a) PXRD of experimentally observed  $\text{CH}_3\text{NH}_3\text{SnI}_3$  perovskite (Red), its composite with SWCNT (Blue), and referenced COD ID #7015448 sample (Green) in the two-theta range of  $10^\circ$ - $60^\circ$  (b) Solid state absorption spectra of  $\text{CH}_3\text{NH}_3\text{SnI}_3$  perovskite thin film in the range of 500-1100 nm

**Figure 4.4:** Details XPS measurements of various elements present in the  $\text{CH}_3\text{NH}_3\text{SnI}_3$ -SWCNT composite sample

**Figure 4.5:** (a) XPS in the valence band region of composite perovskite (b) Tauc's plot to determine the optical bandgap of the perovskite (c) concluded band diagram of the sample from (a) and (b), shows  $\text{CH}_3\text{NH}_3\text{SnI}_3$  is a p-type semiconductor

**Figure 4.6:** (a) FESEM images of  $\text{CH}_3\text{NH}_3\text{SnI}_3$  (b) and (c) represent FESEM and TEM image of SWCNT-perovskite composite shows SWCNT acts as a channel to carrier (d) TEM micrograph of a perovskite: SWCNTs composite with perovskite and SWCNTs nearby, producing intimate interfaces

**Figure 4.7:** (a) EDX spectra of the composite sample (inset shows the EDX compositional values of perovskite-SWCNT composite) (b)-(f) demonstrates its corresponding elemental (C, N, Sn, I) mapping

**Figure 4.8:** (a) IR spectra in the range of  $500$ - $3500\text{ cm}^{-1}$  (b) TGA in the range of  $27$ - $500\text{ C}$  of  $\text{CH}_3\text{NH}_3\text{SnI}_3$  perovskite and its composite with SWCNT. The inset of the figure (b) represents the corresponding first derivative of TGA showing the major change in the curve

**Figure 4.9:** (a) Energy level diagram of the different layers (b) device band alignment in a forward biased situation. Dark and light I-V characteristics of the device (c) ITO/ $\text{CH}_3\text{NH}_3\text{SnI}_3$ /Al and (d) ITO/ $\text{CH}_3\text{NH}_3\text{SnI}_3$ -SWCNT/Al measured at room temperature. The corresponding  $\ln I$  vs.  $V$  plot has been presented in the inset of both graphs

**Figure 4.10:** Photocurrent growth in (a) perovskite device only (b) SWCNT and perovskite composite device. The figures show the first switching in presence of SWCNT in the perovskite active layer

**Figure 4.11:** Temperature dependent Richardson plot to estimate Richardson constant and voltage dependent barrier height

**Figure 4.12:** (a) and (b) depict  $dV/d\ln I$  vs.  $I$  and  $H(I)$  vs.  $I$  plot of ITO/  $\text{CH}_3\text{NH}_3\text{SnI}_3$ /Al device whereas (c), (d) represent the same plots of ITO/ $\text{CH}_3\text{NH}_3\text{SnI}_3$ + SWCNT/Al device in presence of light and dark conditions, respectively to estimate  $\phi_b$ ,  $\eta$ , and  $R_s$  of the devices

**Figure 4.13:**  $1/C^2$  vs. voltage measurements of devices to estimate acceptor density and barrier height

**Figure 4.14:**  $\ln I$  vs.  $\ln V$  curves of both (a) perovskite and (b) perovskite and SWCNT composite devices under dark and illumination conditions (c) shows Al/ $\text{CH}_3\text{NH}_3\text{SnI}_3$ +SWCNT/ITO device configuration to explain the charge transport mechanism. The right-side image shows the transport mechanism of the middle layer (active) of the device made up of perovskite and SWCNT composite. Whenever an electron-hole pair generates within perovskite, the electron gets recombined with  $\text{Sn}^{2+}$  and the hole gets transported through SWCNT as it works as a channel

**Figure 5.1:** Structure of (a) MWCNT and (b) visualization of cubic  $\text{CH}_3\text{NH}_3\text{SnI}_3$  perovskite by VESTA

**Figure 5.2:** (a) Preferred (b) and (c) not acceptable (d) acceptable geometrical structures of the film used for Van der Pauw resistivity measurement (e) laboratory film formation set up on a glass plate (f) resistivity measurement of the thin films

**Figure 5.3:** (a) I-V measurement setup of the sandwich structured device (b) I-V characteristics of the device Al/ $\text{CH}_3\text{NH}_3\text{SnI}_3$ /ITO (blue) and Al/ $\text{CH}_3\text{NH}_3\text{SnI}_3$ +MWCNT nanocomposite/ITO (red)

**Figure 5.4:** (a) Powder XRD of the as-synthesized sample and its MWCNT composite; (b) FESEM image of  $\text{CH}_3\text{NH}_3\text{SnI}_3$  perovskite film; (c) FESEM image of  $\text{CH}_3\text{NH}_3\text{SnI}_3$  perovskite and MWCNT nanocomposite film

**Figure 5.5:** (a) EDX spectroscopy of  $\text{CH}_3\text{NH}_3\text{SnI}_3$ -MWCNT nanocomposite. (b) to (e) elemental mapping of C, Sn, and I of  $\text{CH}_3\text{NH}_3\text{SnI}_3$ -MWCNT nanocomposite. The mapping of N is omitted in this case because it is forbidden by the instrument

**Figure 5.6:**  $\ln I$  vs  $\ln V$  plot of the I-V behaviours of the devices (a) ITO/perovskite/Al and (b) ITO/perovskite-MWCNTs composite/Al show distinct linear regions

**Figure 5.7:** (a) Comparative I-V characteristics of the devices ITO /perovskite/ Al (blue) and ITO /perovskite+MWCNT/ Al (red) (b) schematic diagram of a cross-sectional view of the device to understand the charge transport mechanism in a combined manner. It shows that some of the perovskite crystals are interconnected via MWCNTs and some of the perovskite crystals are connected to electrodes

**Figure 6.1:** CsSnCl<sub>3</sub> perovskite microrod (a) during synthesis (b) after solvent evaporation (c) laboratory electrical measurement setup (d-f) FESEM images of CsSnCl<sub>3</sub> perovskite microrods of thickness 136, 356, and 334  $\mu\text{m}$

**Figure 6.2:** (a) Experimentally and calculated PXRD of CsSnCl<sub>3</sub> perovskite sample (b) EDS graph to show the elemental composition of the perovskite, inset of this figure represents atomic ratio present in the sample and (c) to (d) demonstrates the FESEM image, Cs, Sn, and Cl elements mapping, respectively

**Figure 6.3:** (a) The I-V characteristics of cesium tin tri-chloride perovskite microrods (b)-(d)  $\ln I$  vs  $\ln V$  plots of corresponding I-V characteristics showing different zones of the charge transport mechanism

**Figure 7.1:** Block diagram of smartphone-based photo detector using ESP 32 MCU

**Figure 7.2:** (a) X-Ray crystallography measurements of perovskite and nanocomposite perovskite (b) Lattice structure of Cs<sub>2</sub>SnCl<sub>6</sub> double perovskite (c) XPS survey curves (d) characteristic XPS peak spectra of the Sn element of samples (e) Fermi energy spectra (f) UPS spectra for work function measurements

**Figure 7.3:** (a) and (b) demonstrate FESEM images for morphology of Cs<sub>2</sub>SnCl<sub>6</sub> and CNT-perovskite composite, while below their SEM images show elemental mappings of Cs<sub>2</sub>SnCl<sub>6</sub> and CNT-perovskite composite

**Figure 7.4:** (a) and (b) EDX spectra of Cs<sub>2</sub>SnCl<sub>6</sub> and nanocomposite-Cs<sub>2</sub>SnCl<sub>6</sub> perovskite, respectively (c) absorption spectra and Tauc plots to determine the optical bandgaps of the samples (d) energy band diagrams of both the samples drawn using information obtained from UPS (work function) and Tauc plots (bandgap). Dark and UV light I-V characteristics of the

device (e) ITO/ Cs<sub>2</sub>SnCl<sub>6</sub>/Al and (f) ITO/ Cs<sub>2</sub>SnCl<sub>6</sub>-MWCNT/Al measured at room temperature

**Figure 7.5:** (a) Energy level diagram of the different layers (b) device band alignment in forward biased situation. I-V characteristics recorded in the temperature range of 308-393K by applying bias within  $\pm 2$  V across two thin film-based (c) ITO/Cs<sub>2</sub>SnCl<sub>6</sub>/Al and (d) ITO/nanocomposite-Cs<sub>2</sub>SnCl<sub>6</sub>/Al devices

**Figure 7.6:** Shows Richardson plot to estimate the Richardson constant value for (a) Cs<sub>2</sub>SnCl<sub>6</sub> perovskite (b) Cs<sub>2</sub>SnCl<sub>6</sub>-MWCNT composite

**Figure 7.7:** (a) and (b) depict  $dV/d(\ln I)$  vs.  $I$  plot for the determination of series resistances whereas (c) and (d) represents  $\ln I$  vs  $\ln V$  plots to explain charge transport mechanism of the devices based on perovskite and CNT based perovskites, respectively

**Figure 7.8:** Shows Al/Cs<sub>2</sub>SnCl<sub>6</sub>+MWCNT/ITO device configuration to explain the charge transport mechanism. The right-side image shows the transport mechanism of the middle layer (active) of the device made up of perovskite and MWCNT composite. Whenever an electron-hole pair generates within perovskite, the electron gets recombined with Sn<sup>2+</sup> and the hole gets transported through MWCNT as it works as a channel

**Figure 7.9:** (a) and (b) show the I-V characteristics of UV photodetectors without and with MWCNTs, respectively. (c) illustrates the spectral responses of both devices. (d) depicts the temporal response under 360 nm illumination at a bias of 1.5 V for the perovskite device (black) and the MWCNT-perovskite composite device (red). (e) and (f) display the photocurrent rise and decay for both devices

**Figure 7.10:** UV photodetector module with full setup wirelessly connected to smartphone showing digitized '0' and '1' output under UV light and absence of UV light, respectively

## **List of Tables**

**Table 3.1:** XRD analysis parameters of the perovskite sample

**Table 3.2:** The values of equivalent resistances and capacitances obtained from the fitted model

**Table 3.3:** Estimated values of the relaxation time ( $\tau$ ), exponent ( $n$ ), parameter ( $\beta$ ), conductivity owing to space ( $\sigma_{sc}$ ) and free charge ( $\sigma_{fc}$ ) derived by fitting a modified Cole-Cole model of frequency-dependent  $\varepsilon'$  and  $\varepsilon''$

**Table 3.4:** The Schottky Device Parameters for the Thin Film Devices

**Table 3.5:** Charge conduction parameters of the perovskite Based MS Thin Film Device

**Table 4.1:** Photosensing parameters of the  $\text{CH}_3\text{NH}_3\text{SnI}_3$  perovskite Schottky devices

**Table 4.2:** The values of Schottky device parameters like ideality factor ( $\eta$ ), barrier height ( $\phi_b$ ), and series resistance ( $R_s$ ) estimated using different methods

**Table 4.3:** Charge transport parameters of both devices in dark and light conditions

**Table 5.1:** Measurements of resistances using Van der Pauw method. These values were used to calculate conductivity of the perovskite and its MWCNTs nanocomposite films

**Table 5.2:** Comparative electrical parameters of the devices

**Table 6.1:** The values of electrical parameters of the samples

**Table 6.2:** Trap density, threshold voltages, and carrier transit time of perovskite microrods.

**Table 7.1:** The values of Schottky device parameters like ideality factor ( $\eta$ ), barrier height ( $\phi_b$ ) and series resistance ( $R_s$ ) estimated using different methods

**Table 7.2:** Charge transport parameters of both devices in dark and light conditions

**Table 7.3:** Photosensing parameters of the  $\text{Cs}_2\text{SnCl}_6$  perovskite Schottky junction device

## **Contents**

<b>Chapter 1: Motivation and Outline</b>	<b>1</b>
<b>1.1 Introduction</b>	<b>2</b>
1.1.1 Perovskite	2
1.1.2 Perovskite Structure	3
1.1.3 Classification of Perovskites	4
<b>1.2 Motivation of the Work</b>	<b>5</b>
1.2.1 Double Perovskite	5
1.2.2 Perovskite-Carbon Nanotube Composite	6
<b>1.3 Objective of the Work</b>	<b>6</b>
<b>1.4 Organization of the Thesis</b>	<b>7</b>
<b>1.5 References</b>	<b>9</b>
<b>Chapter 2: Charge Transport Mechanism in Perovskite Optoelectronic Devices in Presence of CNTs</b>	<b>11</b>
<b>2.1 Introduction</b>	<b>12</b>
<b>2.2 Background of the Perovskite-Based Optoelectronic Devices</b>	<b>12</b>
2.2.1 Working Principle of a Perovskite Optoelectronic Devices	12
2.2.2 Performance of Lead-Based Perovskite	13
2.2.3 Limitation of Lead-Based Perovskite	14
2.2.4 Turning Towards the Lead-Free Perovskite	15
2.2.5 Tin-Based Perovskites: Its Advantages and Challenges	16
<b>2.3 A Review on Charge Transport Mechanisms in Perovskite Devices</b>	<b>18</b>
2.3.1 Electrode Limited Charge Transport	18
2.3.1.1 Thermionic Emission Model	19
2.3.1.2 Direct Tunneling Model	20
2.3.2 Bulk-Limited Transport	20
2.3.2.1 Hopping Conduction	21
2.3.2.2 Ohmic Conduction	22
2.3.2.3 Space Charge- Limited Conduction	22
<b>2.4 Importance of CNT in Perovskite Optoelectronic Devices</b>	<b>26</b>
2.4.1 Properties of CNTs	26

2.4.2 Role of CNT in Perovskite Optoelectronic Devices	27
2.4.2.1 CNTs in PSCs	28
2.4.2.2 CNTs as Conducting Substrates	28
2.4.2.3 CNTs as Hole Extraction Material	29
2.4.2.4 CNTs in LEDs	29
2.4.2.5 CNTs in Photodiodes	29
<b>2.5 Optoelectronic Parameters of the Schottky Device</b>	<b>30</b>
<b>2.6 References</b>	<b>31</b>
<b>Chapter 3: Study on Lead-Free Methylammonium Tin Iodide (CH<sub>3</sub>NH<sub>3</sub>SnI<sub>3</sub>) Nano Cubic Perovskite Schottky Diode</b>	<b>36</b>
<b>3.1 Introduction</b>	<b>38</b>
<b>3.2 Experimental Section</b>	<b>38</b>
3.2.1 Materials	38
3.2.2 Instruments Used	39
3.2.2.1 Spin Coater	39
3.2.2.2 Bruker's X-ray Diffractometer (XRD)	39
3.2.2.3 UV-Vis. Spectrophotometer	40
3.2.2.4 Field Emission Scanning Electron Microscopy (FESEM) and Energy Dispersive X-ray Spectroscopy (EDX)	41
3.2.2.5 Thermogravimetric Analysis (TGA)	42
3.2.2.6 Fourier Transform Infrared Spectroscopy (FTIR)	43
3.2.2.7 Atomic Force Microscopy (AFM)	43
3.2.2.8 LCR Meter	44
3.2.2.9 Keithley 2400 SMU	44
3.2.2.10 Glove Box	45
3.2.2.11 X-ray Photoelectron Spectroscopy (XPS)	46
3.2.3 Perovskite Nanocubes Synthesis	47
3.2.4 Device Fabrication	48
<b>3.3 Characterization</b>	<b>48</b>
<b>3.4 Result and Discussions</b>	<b>49</b>
3.4.1 X-Ray Crystallography	49
3.4.2 Optical Spectroscopy	51

3.4.3 X-ray Photoelectron Spectroscopy (XPS)	52
3.4.4 Thermo-Gravimetric (TGA) and Fourier Transform Infrared Radiation (FTIR)	52
3.4.5 Field Emission Scanning Electron Microscopy (FESEM), Energy Dispersive Spectroscopy (EDS) and Atomic Force Microscopy (AFM)	54
3.4.6 Complex Impedance Spectroscopy (CIS) Analysis	56
3.4.7 Dielectric Properties Study	57
3.4.8 Study of Electric Modulus	60
3.4.9 Study of Electrical Conductivity	62
3.4.10 Analysis of Schottky Device Characterization	63
<b>3.5 Conclusions</b>	<b>68</b>
<b>3.6 References</b>	<b>69</b>
 <b>Chapter 4: Effect of SWCNT on the Electrical Behaviour of a Lead-Free Methylammonium Tin Iodide (CH<sub>3</sub>NH<sub>3</sub>SnI<sub>3</sub>) Perovskite Schottky device</b>	 <b>72</b>
<b>4.1 Introduction</b>	<b>73</b>
<b>4.2 Experimental Section</b>	<b>74</b>
4.2.1 Materials	74
4.2.2 Instruments Used	75
4.2.2.1 Transmission Electron Microscope (TEM)	75
4.2.3 Sample Preparation	76
4.2.4 Development of Perovskite Schottky Device (PSD)	76
<b>4.3 Characterization</b>	<b>76</b>
<b>4.4 Results and Discussions</b>	<b>77</b>
4.4.1 X-Ray Crystallography and Optical Characterization	77
4.4.2 X-ray Photoelectron Spectroscopy (XPS)	78
4.4.3 FESEM and TEM	80
4.4.4 Fourier Transform Infrared Spectroscopy (FTIR) and Thermal Gravimetric Analysis (TGA)	82
4.4.5 Optoelectronic Study	83
<b>4.5 Conclusions</b>	<b>95</b>
<b>4.6 References</b>	<b>95</b>

<b>Chapter 5: Effect of MWCNT on the Electrical Behaviour of a Lead-Free Methylammonium Tin Iodide (<math>\text{CH}_3\text{NH}_3\text{SnI}_3</math>) Perovskite Schottky device</b>	<b>98</b>
<b>5.1 Introduction</b>	<b>99</b>
<b>5.2 Experimental Section</b>	<b>99</b>
5.2.1 Materials	99
5.2.2 Instruments Used	99
5.2.3 Synthesis of Perovskite and Nanocomposite	100
<b>5.3 Material Characterization</b>	<b>100</b>
<b>5.4 Van der Pauw Measurement Setup</b>	<b>101</b>
<b>5.5 I-V Characterization</b>	<b>102</b>
<b>5.6 Results and Discussions</b>	<b>103</b>
<b>5.7 Conclusions</b>	<b>110</b>
<b>5.8 References</b>	<b>111</b>
<b>Chapter 6: Study on Charge Conduction Mechanisms of Lead-Free Cesium Tin Chloride Perovskite Microrods</b>	<b>113</b>
<b>6.1 Introduction</b>	<b>114</b>
<b>6.2 Experimental Section</b>	<b>115</b>
6.2.1 Materials	115
6.2.2 Perovskite Microstructure Synthesis	115
6.2.3 Measurement Methodology	116
6.2.4 Instruments Used	116
6.2.5 Characterizations	116
<b>6.3 Results and Discussions</b>	<b>116</b>
<b>6.4 Conclusions</b>	<b>121</b>
<b>6.5 References</b>	<b>121</b>
<b>Chapter 7: Study on Charge Transport Mechanisms in <math>\text{Cs}_2\text{SnCl}_6</math> Double Perovskite Schottky Device in Presence of MWCNTs</b>	<b>123</b>
<b>7.1 Introductions</b>	<b>124</b>
<b>7.2 Experimental Section</b>	<b>125</b>
7.2.1 Materials	125
7.2.2 Instruments Used	125

7.2.3 Synthesis of Cs <sub>2</sub> SnCl <sub>6</sub> Perovskite and Its MWCNT Composite	125
7.2.4 Fabrication of UV Detector	126
7.2.5 Smartphone Interfacing with Device	126
<b>7.3 Device Measurement and Characterization</b>	<b>127</b>
<b>7.4 Results and Discussions</b>	<b>127</b>
7.4.1 Optoelectronic Study	131
7.4.2 Smartphone Interfaced UV Detector	141
<b>7.5 Conclusions</b>	<b>142</b>
<b>7.6 References</b>	<b>143</b>
 <b>Chapter 8: Conclusions and Future Scope</b>	 <b>146</b>
<b>8.1 Summary</b>	<b>147</b>
<b>8.2 Findings of the Work</b>	<b>149</b>
<b>8.3 Overall Conclusion</b>	<b>153</b>
<b>8.4 Future Scopes of the Work</b>	<b>153</b>
 <b>List of Publications</b>	 <b>155</b>

## **Preface**

In recent years, significant progress has been made in the field of optoelectronic devices, which is driven by the rapid evolution of materials and technologies. In addition, green and renewable energy sources have become a global concern, not only to meet the rapidly growing electricity demand, but also to address various pressing concerns such as the energy crisis, the depletion of fossil fuel reserves, environmental pollution, etc. The growing demand for renewable energy sources has encouraged intensive research in the field of more efficient and cost-effective technologies. In this context, the emergence of materials such as perovskite stands out as a promising advance that can surpass existing conventional semiconductor technologies. Perovskite materials offer unique advantages that address the critical limitations of traditional semiconductors in the use of renewable energy. Their tuneable properties, low-cost production methods, and impressive energy conversion efficiency make them an attractive choice for optoelectronics applications such as photodetectors, solar cells, etc. Unlike conventional semiconductors, materials such as perovskite exhibit enhanced absorption capabilities across a broad spectrum of light, which increases their efficiency in converting sunlight into electricity. Although challenges remain in terms of long-term stability, the environmental impact due to the presence of lead and commercial viability, the impact of charge transport in the devices due to the presence of traps in the active layer.

Among the various classes of perovskites, lead-free perovskites have garnered significant attention as environmentally friendly alternatives to their lead-based counterparts, addressing concerns related to environmental toxicity. These materials have been explored for use in optoelectronic applications; however, their efficiencies have not met theoretical expectations. This discrepancy may be due to significant inhomogeneities in local chemistry, defect density, and lattice structure introduced through the facile synthesis methods typically used to grow perovskite films for these applications, which adversely affect charge transport in the devices. Since charge transport is crucial in optoelectronic devices, it is essential to study the intrinsic charge transport properties of perovskites and perovskite-based devices in detail. This understanding will help assess their potential in various applications. Additionally, carbon nanotubes (CNTs) have emerged as a game-changing element in the realm of material science. Their exceptional mechanical strength, electrical conductivity, thermal properties, and unique structure have paved the way for transformative advancements. CNTs find applications as reinforcements in composites, conductive materials in electronics, and components in energy

harvesting and storage devices. Their versatile role extends to sensors, actuators, and even medical applications. By harnessing the remarkable properties of CNTs, material scientists are revolutionizing industries and enabling innovative solutions that were once deemed impossible. The synergy between lead-free perovskites and CNTs presents an exciting avenue for the development of high-performance optoelectronic devices.

This thesis, entitled "Investigation of Charge Transport Mechanisms in Lead-Free Perovskites in Presence of Carbon Nanotubes for Optoelectronic Device Applications", delves into the multifaceted realm of charge transport in lead-free perovskite materials when combined with carbon nanotubes. The primary objective of this research is to unravel the underlying mechanisms governing charge transport in these composite materials and to explore the potential synergistic effects between lead-free perovskites and CNTs. The insights gained from this study have the potential to advance the design and optimization of optoelectronic devices with enhanced performance characteristics.

This thesis represents an extensive exploration into the development and charge transport analysis of lead-free perovskite materials for optoelectronic devices, both with and without CNTs. Chapters 1 and 2 laid the groundwork by introducing perovskite structures, emphasizing the importance of lead-free alternatives, and reviewing charge transport mechanisms, with a focus on incorporating CNTs into perovskite devices. In subsequent experimental chapters (Chapters 3 to 7), we synthesized and characterized various lead-free perovskites like  $\text{CH}_3\text{NH}_3\text{SnI}_3$ ,  $\text{CsSnCl}_3$ , and  $\text{Cs}_2\text{SnCl}_6$ , investigating their physical, optical, and electrical properties. The study included fabricating devices to explore charge transport mechanisms and assess the impact of CNT incorporation on device performance. Notably, in Chapter 7, a MWCNT-  $\text{Cs}_2\text{SnCl}_6$  composite was developed for a UV detector, showcasing improved charge transport and optoelectronic properties. Chapter 8 concludes with a comprehensive summary of our research findings, highlighting the significance of our work and proposing future directions in the field of perovskite semiconductor devices.

This thesis represents a contribution to the growing body of knowledge surrounding lead-free perovskite materials, carbon nanotubes, and their synergistic interactions for advanced optoelectronic devices. It is my hope that the insights presented herein will inspire further exploration and innovation in the pursuit of sustainable and high-performance optoelectronic technologies.

# **Chapter 1: Motivation and Outline**

## **1.1 Introduction**

1.1.1 Perovskite

1.1.2 Perovskite Structure

1.1.3 Classification of Perovskites

## **1.2 Motivation of the Work**

1.2.1 Double Perovskite

1.2.2 Perovskite-Carbon Nanotube Composite

## **1.3 Objective of the Work**

## **1.4 Organization of the Thesis**

## **1.5 References**

## **1.1 Introduction**

In this chapter, we first reviewed the origin and importance of perovskite materials in material science. Perovskite materials, distinguished by their unique  $ABX_3$  crystal structure, have sparked widespread interest due to their versatility and potential applications in optoelectronics [1,2]. This chapter begins by looking over the basic structures and classification of perovskites. It then delves into the motive for finding environmentally friendly alternatives to lead-based perovskites, which have substantial toxicity concerns [3]. The focus is on lead-free perovskites, such as double perovskites and perovskite-carbon nanocomposites, with the goal of addressing device performance limits caused by synthesis inhomogeneities and defects [4–6]. The next section of the chapter outlines the goals of the thesis before summarizing the general organization of the thesis.

### **1.1.1 Perovskite**

Perovskite refers to a unique class of materials that share a specific crystal structure, which was first discovered in the mineral calcium titanate ( $CaTiO_3$ ) in the Ural Mountains by Gustav Rose in 1839 [7]. The term "perovskite" has since been adopted to describe a wide range of compounds that exhibit this same crystal structure, named after Russian mineralogist Lev Perovski. The perovskite crystal structure is characterized by a cubic arrangement of organic or inorganic cations at its corners and centre, surrounded by oxygen anions. This basic structure can accommodate a variety of different cations, leading to a diverse family of perovskite compounds with various properties. Perovskite materials have gained significant attention and importance in various scientific and technological fields due to their unique combination of properties, such as electrical, magnetic, optical, and catalytic behaviours. One of the most exciting recent developments involving perovskites is in the field of photovoltaics. Perovskite solar cells have gained immense popularity due to their remarkable light-absorbing capabilities, relatively low production costs, and potential for high energy conversion efficiencies. Researchers have been able to achieve rapid improvements in the efficiency of perovskite solar cells, making them a promising contender for next-generation solar technology. Perovskites have also found applications in other areas such as light-emitting diodes (LEDs), lasers, sensors, and catalysts for chemical reactions [8,9]. Their tuneable properties, ease of synthesis, and versatility have made them an attractive subject of research and innovation.

However, despite their enormous promise, perovskite materials face obstacles like as instability in certain climatic conditions and toxicity concerns due to the usage of lead in some perovskite

formulations [10,11]. Researchers are actively attempting to overcome these obstacles and create more stable, efficient, and environmentally friendly perovskite materials for a variety of applications.

### 1.1.2 Perovskite Structure

Perovskite materials have gained widespread attention in the scientific community due to their cubic lattice-nested octahedral layered structures and distinct thermal, optical, and electromagnetic characteristics. The basic chemical formula of a halide cubic perovskite compound is  $AMX_3$ , where A is organic or inorganic cation; B denotes a transition metal ion ( $Pb^{2+}$ ,  $Ge^{2+}$ ,  $Bi^+$ ,  $Sn^{2+}$ , etc.). A is larger than B. The centre and apex of the octahedron are occupied by a metal cation, B, and a halide anion, X, which is commonly oxygen but might also be fluorine, chlorine, nitrogen, sulphur, or carbon.  $BX_6$  is a regular tetrahedral symmetric structure with B in the positive centre,  $A^+$  in the cubic centre, and regular octahedrons surrounding it. The metal-halogen octahedral are connected to produce a three-dimensional stable network structure.

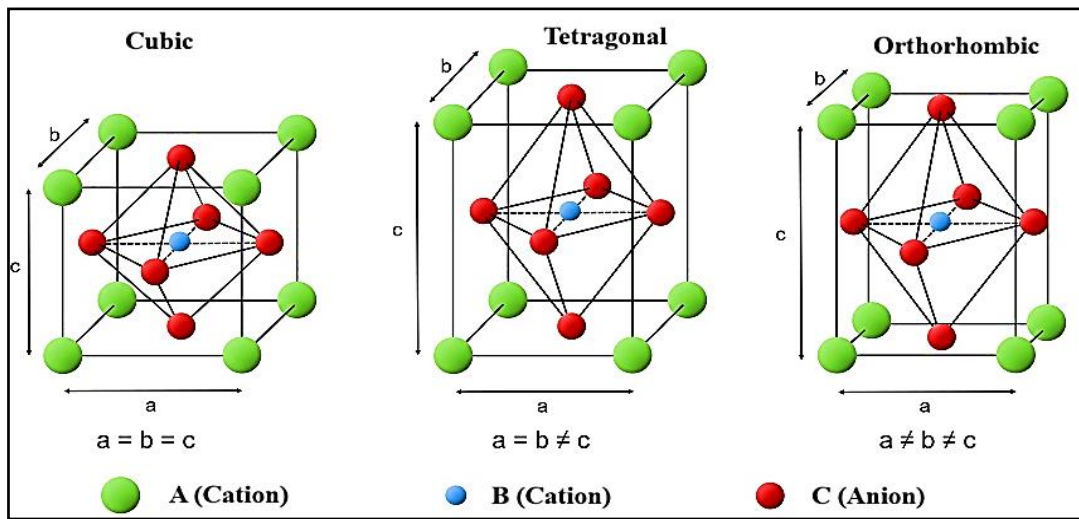


**Figure 1.1: Lattice of perovskite (one unit cell structure). Green denotes larger cation atoms, red denotes smaller cation atoms, blue denotes oxygen atoms of cells of cubic, tetragonal and orthorhombic structures**

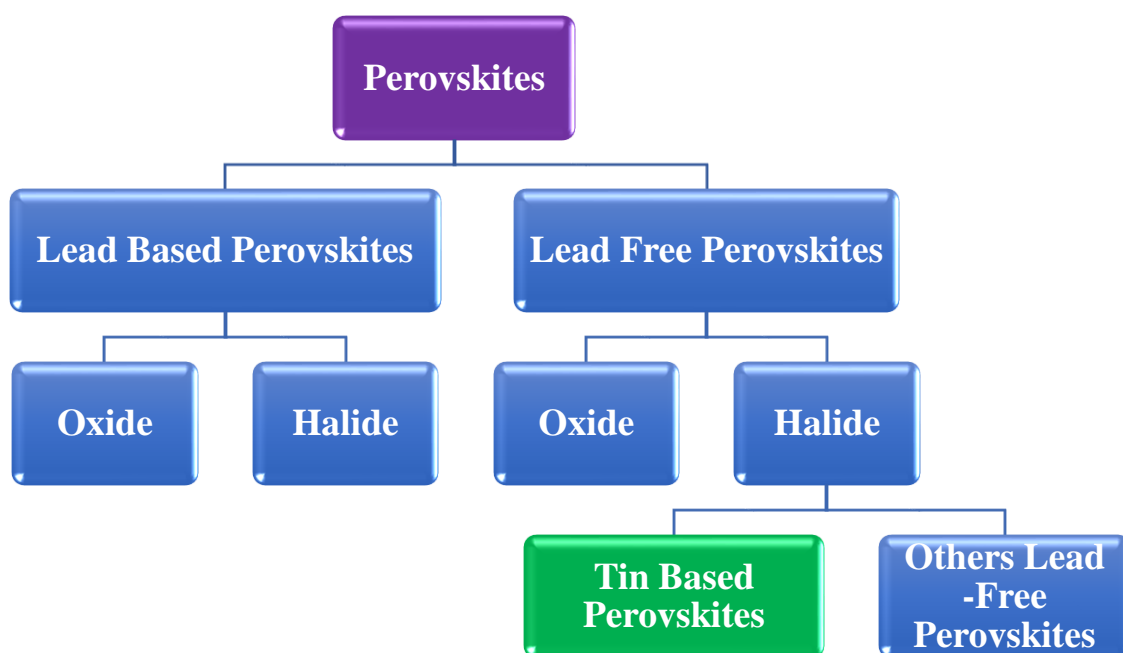
These structures impose strict ion size limitations [12]. Minor lattice distortion or expansion has a substantial impact on the symmetry and structural stability of the perovskite material. The tolerance factor is given by:  $t = \frac{R_A + R_X}{\sqrt{2(R_B + R_X)}}$ , where  $t$  is the ratio of the distance A-X to the distance B-X, and  $R_A$ ,  $R_B$ , and  $R_X$  are the effective radii of the A, B, and X ions, respectively.

The investigation revealed that some perovskite materials have four different crystal structures [13]. There are three types of black perovskite structures (**Figure 1.1**): cubic phase (B- $\alpha$  phase,  $Pm\bar{3}m$ ), tetragonal phase (B- $\beta$  phase,  $P4/mbm$ ), and orthorhombic phase (B- $\gamma$  phase,  $Pbnm$ ) with different phase-transition temperatures, such as  $CsSnI_3$  at 431 K and 352 K, respectively [14].

Materials with these structures exhibit four notable characteristics. First, they have high optical absorption coefficients (up to  $10^5 \text{ cm}^{-1}$ ), excellent photoelectric properties, and low exciton binding energies. Second, when used as light-absorbing layers, these perovskite materials efficiently capture solar energy. Third, their high dielectric constant allows for efficient electron and hole transport and collection. Lastly, these materials enable simultaneous electron and hole transmission over distances up to 100 nm or more.

### 1.1.3 Classification of Perovskites

Perovskite compounds can be broadly classified into several categories based on their compositions. Here are some key classifications of perovskites:



Compositional variations can affect various properties of perovskites. Due to the toxicity of lead-based perovskites, we focused on lead-free perovskites in this study. The second chapter discusses the adverse effects of lead perovskite and the development of lead-free perovskite, including a detail review.

## **1.2 Motivation of the Work**

Perovskite based optoelectronic devices gained much attention of researchers in very short period of time due to their high optical absorption coefficient and easy fabrication process. But the most efficient perovskite devices are lead based which has lots of bad implications. Therefore, as an alternative of lead-based perovskite, Sn based perovskite is the best avenue in the realm of perovskite materials to replace the toxic lead from perovskite based optoelectronic devices. The rapid improvement in the performance of the Sn based perovskite is the evident in this regard. The details progress of perovskite-based devices both lead based and lead-free devices have been discussed in chapter 2. However, the performance of Sn based perovskites are under consideration in comparison to lead based perovskites. As research and development in this area continue, lead-free Sn based halide perovskites could play a crucial role in shaping the future of sustainable and environmentally friendly optoelectronic technologies. Certainly, as a researcher, I am enthusiastic about the burgeoning field of tin-based halide perovskites, a captivating area of research within the realm of perovskite materials and devices.

From the literature review, it is concluded that the limitations in lead free perovskite field can be resolved in few ways. One approach focuses more on the development of stable Sn-based perovskites [15]. Explore more Sn-based compounds, such as double perovskite material, which is already an oxidized variant of basic perovskite material. Another essential technique is to increase the charge transport mechanism in the perovskites to compensate for the deterioration effect of the perovskite caused by oxidation, as well as the presence of traps in the film, which occur mostly during film development in these types of devices. We found that the best way to improve the charge transport of the perovskite-based devices is the incorporation of CNTs in the materials [16,17]. Therefore, the objective of this work is defined in following section.

### **1.2.1 Double Perovskite**

Lead-free double perovskites represent a significant advancement in material science, offering a safer and more sustainable alternative to traditional lead-containing compounds. Lead-free double perovskites exhibit a wide range of properties that can be tailored for diverse applications, including solar cells, sensors, and optoelectronic devices [18]. By focusing on environmentally friendly compositions, researchers are paving the way for a new era of functional materials that not only deliver remarkable performance but also prioritize the wellbeing of both ecosystems and human health.

### **1.2.2 Perovskite-Carbon Nanotube Composite**

Perovskite-carbon nanotube composites are hybrid materials that blend the unique properties of perovskite compounds with the versatile characteristics of carbon-based materials like carbon nanotubes (CNTs), graphene, and carbon nanofibers. These composites have generated significant interest across various scientific and technological fields due to their synergistic effects and potential applications in areas spanning energy storage, conversion, sensors, and catalysis [19,20]. These materials combine perovskite and carbon-based nanomaterials to enhance properties like electrical conductivity, mechanical strength, and stability, thereby improving the performance of perovskite-based devices. Additionally, carbon nanomaterials aid efficient charge transport within the perovskite-carbon composite, particularly benefiting applications such as optoelectronic devices and batteries [21]. As progress continues, perovskite-carbon nanocomposites are anticipated to advance energy storage, sensing, catalysis, and optoelectronic devices, exerting a substantial impact across diverse technological fields.

### **1.3 Objective of the Work**

The goal of this thesis is to investigate charge transport in lead-free perovskites in presence of CNTs in order to contribute to global research on improving the performance of lead-free perovskite devices as well as finding the best alternative to lead-based perovskites. In this work, whole study will be conducted on tin-based lead-free perovskites. Some tin-based perovskites will be synthesized, characterized, and applied for developing metal-semiconductor contact Schottky devices. I-V characteristics in the dark and, in some circumstances, in the light will be analysed to understand the charge transport mechanism of devices and bulk samples. Additionally, the research will be involving the synthesis and application of nanocomposites comprising CNTs and perovskites to further investigate the intricate interactions and charge transport mechanisms in lead-free perovskite systems. Key goals include examining charge injection and trapping processes at the metal/perovskite (M/S) junction, as well as understanding the underlying charge transport mechanisms in the composite system. This investigation will encompass aspects such as trap states, conductivity ( $\sigma$ ), barrier height ( $\phi_b$ ), and ideality factors ( $\eta$ ). Advanced experimental techniques such as I-V measurements, impedance spectroscopy, and photocurrent measurements will be employed to gain deeper insights into these complex pathways of charge transport. Ultimately, this

research seeks to advance our understanding of lead-free perovskite materials and their potential for enhancing optoelectronic devices.

## **1.4 Organization of the Thesis**

In this study, our focus is on exploring charge transport in lead-free perovskite and its nanocomposite-based semiconductor devices. Our research objectives include synthesizing lead-free perovskite materials, fabricating devices with these materials, and analysing the charge transport mechanisms within these devices. The organization of this dissertation is described in the next part, which includes eight chapters that outline our complete analysis.

In **Chapter 1**, we provided a concise overview of perovskite, covering its structure and classification. We then delved into the motivation behind this work, highlighting the significance of double perovskites and carbon-perovskite nanocomposites in the current context. Following that, we discussed the specific objectives of this research. Finally, we outlined the organizational structure of this thesis.

In **Chapter 2**, we presented an extensive review of the current state of perovskite-based devices and the various charge transport mechanisms, with a particular emphasis on the role of CNTs in perovskite optoelectronic devices. Lead-based perovskite materials have gained popularity in numerous types of efficient optoelectronic device structures, which we have discussed briefly. Considering environmental concerns, we investigated the trend toward lead-free perovskite materials and their significance in the recent scenario. We then discussed the major constraints of lead-free perovskites, emphasizing the challenge of low charge transport in tin (Sn)-based perovskite devices. Various charge transfer mechanisms were investigated in this context. Furthermore, we thoroughly examined the use of CNTs in various ways within optoelectronic devices. Finally, this chapter outlined our primary goal that already mentioned in preceding chapter 1 to improve the charge transport of lead-free tin-based perovskite devices incorporating CNTs, thus encouraging the development of environmentally sustainable perovskite optoelectronic devices using insights gained from our comprehensive review of the current landscape.

Experimental part of the work is described in next five chapters from Chapter 3 to Chapter 7.

In **Chapter 3**, we synthesized lead-free  $\text{CH}_3\text{NH}_3\text{SnI}_3$  nano cubic perovskite using a solution processing technique in an  $\text{N}_2$ -atmosphere glove box. The structure and surface features of this perovskite were characterized using various techniques. For the first time, we conducted a

comprehensive study of the device performance by investigating impedance analysis, frequency-dependent dielectric analysis, and AC and DC conductivity analysis on the nano cubic  $\text{CH}_3\text{NH}_3\text{SnI}_3$  perovskite material. Additionally, a Schottky device was fabricated in the ITO/Perovskite/Al sandwich structure. The electrical charge conduction behaviour of the device, including conductivity ( $\sigma$ ), ideality factor ( $\eta$ ), barrier height ( $\phi_b$ ), and series resistance ( $R_s$ ), was investigated using thermionic emission theory (TE) and the Cheung method. Furthermore, bulk transport parameters such as effective mobility, transient time, diffusion length, etc., were studied using  $\ln I$  vs  $\ln V$  plots.

In **Chapters 4 and 5**, we investigated the effects of SWCNTs and MWCNTs on  $\text{CH}_3\text{NH}_3\text{SnI}_3$  perovskite, which was previously discussed in Chapter 1. In both chapters, we synthesized nanocomposites of  $\text{CH}_3\text{NH}_3\text{SnI}_3$  perovskite and CNTs, and characterized them using various techniques to study their optical, compositional, and morphological properties. Subsequently, thin-film perovskite devices based on these synthesized samples were developed to study and compare their charge transport capabilities with pure  $\text{CH}_3\text{NH}_3\text{SnI}_3$  perovskite. Various optoelectronic parameters of the devices were estimated using charge transport and conduction models. The comparative study revealed that the performance of the devices improved due to the incorporation of CNTs. The reasons behind this improvement were also discussed in these chapters.

In **Chapter 6**, we have synthesised lead-free  $\text{CsSnCl}_3$  perovskite microrods using a solution processing approach in a glove box. The sample was characterized by different methods such as PXRD, SEM, EDX, and elemental mapping. Three microrod's current-voltage (I-V) characteristics were measured to study its electrical properties. The charge injection into the material from the electrode has been explained using thermionic emission theory. A few important charge injection parameters like barrier height ( $\phi_b$ ), ideality factor ( $\eta$ ), and series resistance ( $R_s$ ) of the device have been estimated. The charge transport investigation of these rods shows that the sample exhibits a different conduction process after a transition voltage. The complete conduction mechanism through microrods has been explored considering the trap in the sample. Considering this characterization technique, different charge transport zones such as ohmic, trap assist space charge limited conduction (TA-SCLC), and trap-free SCLC have been linearly fitted, and a few useful material's electrical properties such as transit time, threshold voltage, and trap density have been estimated.

In **Chapter 7**, we conducted a study on another lead-free perovskite,  $\text{Cs}_2\text{SnCl}_6$ , also known as a double perovskite.  $\text{Cs}_2\text{SnCl}_6$  double perovskite was synthesized in an open atmosphere using a solution processing technique. Additionally, a MWCNT-  $\text{Cs}_2\text{SnCl}_6$  nanocomposite was synthesized. Both samples were characterized using various techniques and then used to develop a Schottky UV detector. The I-V characteristics were measured and analysed to estimate different optoelectronic properties. The findings from the analysis demonstrate the exciting potential of the composite material in enhancing charge transport properties and optoelectronic performance of UV detectors. This enables the development of a smartphone-integrated UV photodetector module, leveraging modern smartphones' capabilities for real-time UV radiation monitoring through Wi-Fi or Bluetooth. The study provides a comprehensive evaluation of the properties of  $\text{Cs}_2\text{SnCl}_6$ -MWCNT composites and offers valuable insights into the combined charge transport mechanism to optimize their performance for UV detector applications.

Lastly, **Chapter 8**, presents a comprehensive overview of our research findings and summarizes the key outcomes of our work. This section encapsulates the overall conclusions drawn from our study and discusses the potential avenues for future research in the field of perovskite semiconductor devices.

## 1.5 References

- [1] S. Gupta, T. Bendikov, G. Hodes, D. Cahen,  $\text{CsSnBr}_3$ , A Lead-Free Halide Perovskite for Long-Term Solar Cell Application: Insights on  $\text{SnF}_2$  Addition, *ACS Energy Lett* 1 (2016) 1028–1033.
- [2] H. Zhang, G. Chen, D.W. Bahnemann, Photoelectrocatalytic materials for environmental applications, *J Mater Chem* 19 (2009) 5089–5121.
- [3] J. Li, H.L. Cao, W. Bin Jiao, Q. Wang, M. Wei, I. Cantone, J. Lü, A. Abate, Biological impact of lead from halide perovskites reveals the risk of introducing a safe threshold, *Nat Commun* 11 (2020) 310.
- [4] H.T. Nicolai, M.M. Mandoc, P.W.M. Blom, Electron traps in semiconducting polymers: Exponential versus Gaussian trap distribution, *Phys Rev B Condens Matter Mater Phys* 83 (2011) 195204.
- [5] R. Zeng, K. Bai, Q. Wei, T. Chang, J. Yan, B. Ke, J. Huang, L. Wang, W. Zhou, S. Cao, J. Zhao, B. Zou, Boosting triplet self-trapped exciton emission in Te(IV)-doped  $\text{Cs}_2\text{SnCl}_6$  perovskite variants, *Nano Res* 14 (2021) 1551–1558.
- [6] S. Heo, G. Seo, Y. Lee, D. Lee, M. Seol, J. Lee, J.B. Park, K. Kim, D.J. Yun, Y.S. Kim, J.K. Shin, T.K. Ahn, M.K. Nazeeruddin, Deep level trapped defect analysis in  $\text{CH}_3\text{NH}_3\text{PbI}_3$  perovskite solar cells by deep level transient spectroscopy, *Energy Environ Sci* 10 (2017) 1128–1133.

- [7] E.A. Katz, Perovskite: Name Puzzle and German-Russian Odyssey of Discovery, *Helv Chim Acta* 103 (2020) e2000061.
- [8] N. Gopinathan, S.S. Basha, I.B.S. Banu, M.H. Mamat, M.M.S. Sirajudeen, Solvents driven structural, morphological, optical and dielectric properties of lead-free perovskite  $\text{CH}_3\text{NH}_3\text{SnCl}_3$  for optoelectronic applications: Experimental and DFT study, *Mater Res Express* 6 (2019) 125921.
- [9] A. Reinders, P. Verlinden, W. van Sark, A. Freundlich, Photovoltaic solar energy: from fundamentals to applications, (2017) 978-1-118-92746-5.
- [10] G. Schileo, G. Grancini, Lead or no lead? Availability, toxicity, sustainability and environmental impact of lead-free perovskite solar cells, *J Mater Chem C Mater* 9 (2021) 67–76.
- [11] X. Zhao, N.G. Park, Stability issues on perovskite solar cells, *Photonics* 2 (2015) 1139–1151.
- [12] Z. Li, M. Yang, J.S. Park, S.H. Wei, J.J. Berry, K. Zhu, Stabilizing Perovskite Structures by Tuning Tolerance Factor: Formation of Formamidinium and Cesium Lead Iodide Solid-State Alloys, *Chemistry of Materials* 28 (2016) 284–292.
- [13] D. Yang, Y. Fu, Y. Sun, Y. Li, K. Wang, Z. Xiao, K. Biswas, L. Zhang, Phase transition pathway of hybrid halide perovskites under compression: Insights from first-principles calculations, *Phys Rev Mater* 5 (2021) 054603.
- [14] Kontos AG, Kaltzoglou A, Siranidi E, Palles D, Angeli GK, Arfanis MK, Psycharis V, Raptis YS, Kamitsos EI, Trikalitis PN, Stoumpos CC, Kanatzidis MG, Falaras P. Structural Stability, Vibrational Properties, and Photoluminescence in  $\text{CsSnI}_3$  Perovskite upon the Addition of  $\text{SnF}_2$ . *Inorg Chem.* 56 (2016) 84-91.
- [15] M.M. Byranvand, W. Zuo, R. Imani, M. Pazoki, M. Saliba, Tin-based halide perovskite materials: properties and applications, *Chem Sci* 13 (2022) 6766–6781.
- [16] S.N. Habisreutinger, J.L. Blackburn, Carbon nanotubes in high-performance perovskite photovoltaics and other emerging optoelectronic applications, *J Appl Phys* 129 (2021) 010903.
- [17] T.T. Oo, S. Debnath, Application of carbon nanotubes in perovskite solar cells: A review, in: *AIP Conf Proc*, American Institute of Physics Inc., 2017.
- [18] Anh Thi Le, Thanh Binh Dinh, T. Anh Thu Do, Truong Giang Ho, Duy Manh Le, Minh Tan Man, Lattice dynamics of double perovskite  $\text{Cs}_2\text{SnCl}_6$  from first principles and experimental studies, *Materials Letters* 309 (2022) 131386, 0167-577X.
- [19] S.N. Habisreutinger, T. Leijtens, G.E. Eperon, S.D. Stranks, R.J. Nicholas, H.J. Snaith, Carbon nanotube/polymer composites as a highly stable hole collection layer in perovskite solar cells, *Nano Lett* 14 (2014) 5561–5568.
- [20] R. Pinedo, I. Ruiz De Larramendi, D. Jimenez De Aberasturi, I. Gil De Muro, A.T. Aguayo, J.I. Ruiz De Larramendi, T. Rojo, A straightforward synthesis of carbon nanotube-perovskite composites for solid oxide fuel cells, *J Mater Chem* 21 (2011) 10273–10276.
- [21] J. Wang, J. Li, X. Xu, G. Xu, H. Shen, Enhanced Photovoltaic Performance with Carbon Nanotubes Incorporating into Hole Transport Materials for Perovskite Solar Cells, *J Electron Mater* 45 (2016) 5127–5132.

# **Chapter 2: Charge Transport Mechanism in Perovskite Optoelectronic Devices in Presence of CNTs**

## **2.1 Introduction**

## **2.2 Background of the Perovskite-Based Optoelectronic Devices**

2.2.1 Working Principle of a Perovskite Optoelectronic Devices

2.2.2 Performance of Lead-Based Perovskite

2.2.3 Limitation of Lead-Based Perovskite

2.2.4 Turning Towards the Lead-Free Perovskite

2.2.5 Tin-Based Perovskites: Its Advantages and Challenges

## **2.3 A Review on Charge Transport Mechanisms in Perovskite Devices**

2.3.1 Electrode Limited Charge Transport

2.3.1.1 Thermionic Emission Model

2.3.1.2 Direct Tunneling Model

2.3.2 Bulk-Limited Transport

2.3.2.1 Hopping Conduction

2.3.2.2 Ohmic Conduction

2.3.2.3 Space Charge- Limited Conduction

## **2.4 Importance of CNT in Perovskite Optoelectronic Devices**

2.4.1 Properties of CNTs

2.4.2 Role of CNT in Perovskite Optoelectronic Devices

2.4.2.1 CNTs in PSCs

2.4.2.2 CNTs as Conducting Substrates

2.4.2.3 CNTs as Hole Extraction Material

2.4.2.4 CNTs in LEDs

2.4.2.5 CNTs in Photodiodes

## **2.5 Optoelectronic Parameters of the Schottky Device**

## **2.6 References**

## **2.1 Introduction**

In recent years, perovskite-based optoelectronic devices have emerged as promising candidates for next-generation photovoltaics, light-emitting diodes (LEDs), and photodetectors due to their exceptional optical and electronic properties [1,2]. However, achieving efficient charge transport within lead-free perovskite-based devices remains a critical challenge for realizing their full potential [3–5]. Understanding the charge transport mechanisms within perovskite materials and identifying strategies to enhance them is crucial for advancing the performance and stability of perovskite-based devices. This work explores the charge transport mechanisms within perovskite-based optoelectronic devices, focusing on the role of carbon nanotubes (CNTs) as promising materials for improving charge transport properties [6,7].

In this chapter, we have reviewed first the background of the lead-free perovskite materials that have been chosen for developing lead-free optoelectronic devices in this work. Then several charge transport theories have been reviewed, which are analysed to understand the charge transport mechanism of the optoelectronic devices in this work. Regarding this charge transfer process, we have also examined the role of carbon nanotubes (CNTs) in perovskite-based optoelectronic devices, since our objective is to enhance it in their presence.

## **2.2 Background of the Perovskite-Based Optoelectronic Devices**

### **2.2.1 Working Principle of a Perovskite Optoelectronic Devices**

Perovskite optoelectronic devices such as PSCs, pe-PDs, and pe-LEDs have gained great success due to their outstanding optical and electrical properties. When perovskites are utilized as sensitizers, dye-sensitized solar cells give rise to PSCs. Several device structures have been developed for PSCs so far. A common structure; the fluorine-doped tin oxide (FTO)/ETM/perovskite/HTM/Au device structure is shown in **Figure 2.1** [8,9]. When the perovskite layer is illuminated, electron-hole pairs are generated, which are subsequently split apart and transferred to the proper electrodes. The perovskite layer of pe-PDs absorbs light. The photoelectric effect converts optical signals into electrical ones under external bias, resulting in a photo-generated current from the directional drift of photo-generated carriers. Photodiodes, phototransistors, and photoconductors are the three categories into which pe-PDs fall based on their operational principles and device structure. The simplest semiconductor structure is a photoconductor, which has two electrodes placed at either end. To cause charge

separation, a voltage must be supplied. Typically, p-n, p-i-n, or Schottky junctions make up photodiodes.

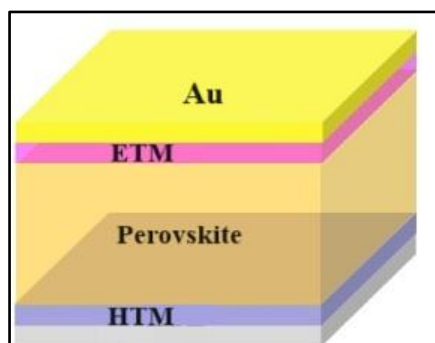


**Figure 2.1: Schematic device structure of FTO)/ETM/perovskite/HTM/Au**

Because of the junction barrier in the device, low dark current may be achieved with ease, and photogenerated carriers can be separated at extremely low bias, even at zero applied voltage. The source, drain, and gate electrodes are the three terminal electrodes of a phototransistor. Between the semiconductor and the gate electrode is a thin dielectric film, through which the gate bias can adjust the charge flow. In pe-LEDs, a double heterojunction structure is created by sandwiching a perovskite emitter between the HTM and ETM [10]. From the anode and cathode, holes and electrons move through the HTM and ETM to the perovskite layer under applied voltages. There, they combine to produce excitons, which subsequently release photons. The inherent characteristics of perovskite materials, including as defect density, crystallinity, absorption capacity, photoluminescence quantum yield, and charge transport rate, dictate the performance of pe-LEDs. However, as our objective in this work is to examine the impact of CNTs on charge transport in the device, we have opted for a straightforward Metal-Semiconductor-Metal (MSM) Schottky junction device configuration.

### 2.2.2 Performance of Lead-Based Perovskites

Perovskite material has emerged as a superior choice for thin-film optoelectronic devices in recent times. The optoelectronic applications of organic-inorganic metal halide perovskites  $\text{CH}_3\text{NH}_3\text{PbX}_3$  ( $\text{X} = \text{Cl}, \text{Br}, \text{or I}$ ) have shown great promise recently because of their exceptional optoelectronic properties, which include balanced carrier mobility, high absorption coefficient, long diffusion length, and so on, and their economical fabrication. Perovskite materials have thus far been employed in a variety of optoelectronic devices, including photodetectors, photovoltaic cells, phototransistors, lasers, and light-emitting diodes, because of their

remarkable optoelectronic properties. Perovskite solar cells (PSCs) made of lead iodide have attracted a lot of attention from researchers because they have the potential to outperform silicon solar cells. Even though they are incredibly efficient, their short lifespan makes them unfit for usage in commercial settings. In 2009, Miyasaka et al. successfully incorporated perovskite material ( $\text{CH}_3\text{NH}_3\text{PbBr}_3$ ) into solar cells, attaining a 3.8% efficiency [11]. However, because a liquid electrolyte was used to absorb the perovskite material, the devices turned out to be unstable. Later, Hou et al. used  $\text{In}_2\text{S}_3$  nanoflakes with  $\text{CH}_3\text{NH}_3\text{PbI}_3$  in a study, and they achieved a high efficiency of 18.22% with little hysteresis [12]. ZnSe was used as an Electron Transport Layer (ETL) by Li et al. in 2018, and they reported an efficiency of 17.78%, which rose to 18.57% when paired with  $\text{TiO}_2$  [13]. Teimouri et al. later reported an efficiency of 24.23% utilizing a  $\text{CH}_3\text{NH}_3\text{PbI}_3$  PSC with a Li-doped  $\text{TiO}_2$  ETL [14]. Most recently, the greatest recorded efficiency for lead-based PSCs sits at 29.15% with perovskite/silicon tandem solar cells [15].

The device performance of perovskite Schottky photodetectors (PDs) is significantly changing in parallel. The  $\text{ITO}/\text{CH}_3\text{NH}_3\text{PbI}_3$  Schottky device exhibits strong specific detectivity in the order of  $10^{12}$  Jones, as shown by Luo W. et al [16]. Perovskite photodetectors (pe-PDs) have achieved remarkable responsivity and detectivity of  $\sim 10^{14}$  J, including exceptional response speed ( $< 1 \mu\text{s}$ ) in comparison to other inorganic photo detectors [17]. Chen L. et al. fabricated an  $\text{Al}/\text{CH}_3\text{NH}_3\text{PbI}_3/\text{ITO}$  Schottky device in 2016 to estimate electrical parameters, and they found a high rectification ratio in the order of  $10^4$  at 6 V [18].

This succinct overview makes it evident that lead-based perovskite is rapidly expanding to rival conventional silicon material in the optoelectronic device market. Nevertheless, there are significant obstacles to the commercialization of optoelectronic devices based on perovskites. We have covered the limits of lead-based perovskites in the following section.

### **2.2.3 Limitation of Lead-Based Perovskites**

For thousands of years, humanity has been using lead (Pb), a hazardous metal on Earth. With very few exceptions, every common application of lead has been systematically outlawed because of its disastrous effects on the environment and human health. On the other hand, Pb-based optoelectronic devices and perovskites are relatively new technologies. Incredible advancements have been realized by perovskite devices. Lead salt perovskites, such as  $\text{PbI}_2$  and  $\text{PbBr}_2$ , are used to fabricate the most efficient optoelectronic devices. However, these Pb-

based efficient optoelectronic devices have inherent drawbacks, such as the element lead, which is hazardous to living things and the environment and is difficult for the body to expel. Several calculations indicate that a typical 550-nm-thick lead (Pb)-based PSC has approximately  $0.75 \text{ g/m}^2$  of Pb, which is 100 times more than the value of  $0.007 \text{ g/m}^2$  found in popular Pb-containing paints and seriously damaging to the human reproductive, central nervous system, kidney, and hematopoietic systems [19]. According to multiple studies, the outdoor operating phase of the life cycle of perovskite optoelectronic devices poses the greatest environmental risk due to the possibility of lead leakage from a cracked panel caused by water seeping in. Rain test simulations indicate that a PSC panel that is damaged can leak as much as 100% of its lead content. Furthermore, the survival of people, plants, and animals is significantly harmed by the ongoing lead ion poisoning of soil and water supplies. Lead poisoning eventually manifests as functional problems in the neurological, digestive, and blood systems because lead may enter the human body, attach itself to enzymes, and then be deposited in soft tissues and bones, the spleen, kidney, liver, and brain through blood circulation [20]. Two main approaches have been put forth by researchers to reduce the toxicity of lead: reducing lead leakage and replacing some or all of the lead in the system. The latter approach, which is also a focus of the research community, is more common to commercial development in the future by developing lead-free halide perovskite that is environmentally friendly and intrinsically stable. Therefore, in order to protect human safety and a clean environment, it is necessary to promote fewer or harmless metal ions to replace lead as the absorber layer of perovskite optoelectronic devices.

#### **2.2.4 Turning Towards the Lead-Free Perovskite**

The contemporary photovoltaic community requires the development of a less hazardous lead-free perovskite material that can provide high PCE and stability. The ideal lead-free perovskite material should have longer carrier diffusion lengths, high exciton binding energy, high charge carrier mobility, a high absorption coefficient, and a narrow bandgap. Fortunately, researchers are also looking for substitute elements of lead, such as Sn, Ge, Bi, and Sb, to form perovskite structures [21,22]. However, none of the investigated lead-free options exceeded the leading lead-based optoelectronic devices in terms of performance. Although some of the options have demonstrated outstanding permanence, the PCE obtained from them is considerably lower. Sn-based optoelectronic devices have received the greatest attention of all choices due to their electronic properties that are similar to those of lead perovskites. Furthermore, they are the

most preferred lead-free option due to their promising performance. In the following part, we go over the progress of lead-free tin-based perovskite devices in detail.

### 2.2.5 Tin-Based Perovskites: Its Advantages and Challenges

As previously discussed, Pb halide-based optoelectronic devices are now mature. The commercialization of Pb-based electronics has also begun. Despite their low cost and ease of manufacture, they are not being encouraged as quickly in the market due to poor device stability and probable toxicity (from lead). It has been claimed that replacing Pb with two material classes is a viable alternative. Double perovskite  $[AM(II)M(IV)X_6]$  is the first-class material; however, its indirect bandgap and large effective mass limit the maximum performance that may be attained [23]. This class of materials contains deep traps related with anti-site faults. Even though research into double perovskites is still in its early stages, the highest PCE achieved by this class of materials is roughly 6.37% [24]. The second type of material is tin halide perovskite ( $ASnX_3$ ). Tin halide perovskite is gaining popularity among researchers because to its remarkable performance. The  $ns^2$  electronic structures of  $Pb^{2+}$  and  $Sn^{2+}$  are similar. The energy content of the tin 5S orbital is higher than the lead 6S orbital [25,26]. This increases the material's valence band energy by enhancing the metal contribution to the valence band. The bandgap value, exciton binding energy, and carrier effective mass are all lowered as a result. Because of these characteristics, these materials are ideal for a wide range of optoelectronic devices, including PSCs and PDs. The biggest concern with Sn-based PSCs is their instability in ambient air. Sn (II) ions oxidise to generate Sn (IV) ions, resulting in high-density p-type doping. Compared to lead-based perovskites, this behaviour introduces an additional pathway for degradation. Second, the Sn vacancies become exceedingly stable because of the high valence band level. This causes additional p-type doping, culminating in a high hole concentration of around  $10^{20}/cm^3$ . Researchers have lately developed various strategies to overcome the obstacles that arise in Sn-deficient environments, achieving validated optoelectronic performance of 15.14% using this type of material [27]. Nevertheless, this result is significantly lower than the predicted efficiency of Sn-based perovskite devices. The literature claims that Sn-based optoelectronic devices have a theoretical efficiency of approximately 30% [28–30].

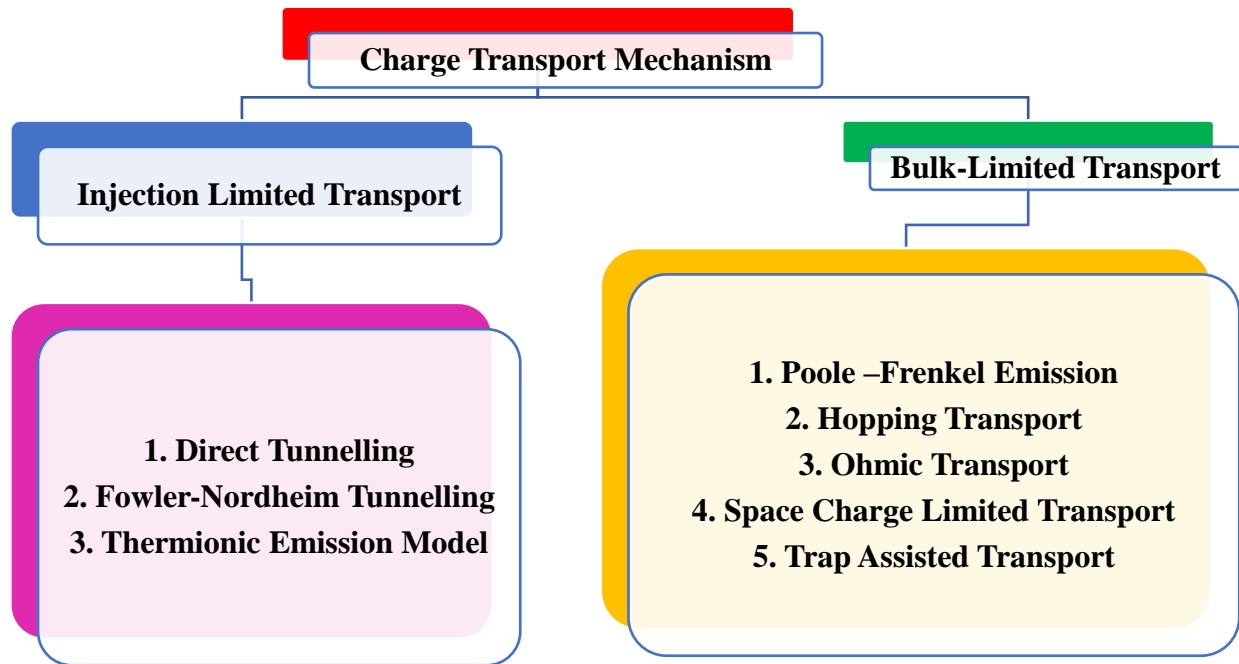
During film fabrication, various reducing agents, such as  $SnX_2$ ,  $SnX_2$ -pyrazine complex, gallic acid, hydrazine compounds, and Sn powders, are frequently added to maintain inert atmospheric conditions (where X is I, Br, Cl, F, and SCN) in order to improve the stability and

performance of optoelectronic devices [31]. In addition to these reducing agents, Sn compensation can help reduce the probability of Sn vacancy formation. The film's morphology improves, and the surface hole density decreases. In 2012, Chung et al. doped CsSnI<sub>3</sub> with SnF<sub>2</sub> and used the resulting material as an HTM in dye-sensitized solar cells (DSSC) [32]. Kumar et al. used this technique for the first time in the PSC area in 2014 [33]. CsSnI<sub>3</sub> was made less conductive by adding SnF<sub>2</sub>, which had a high current density of 22 mA/cm<sup>2</sup>. There were less Sn (IV) ions in the XPS data, indicating the presence of Sn (II) ions. Min et al. reported that SnF<sub>2</sub> was added to aid in the crystal formation of Sn perovskite. SnF<sub>2</sub> precipitates first during spin coating due to its low solubility. SnF<sub>2</sub> creates more nucleation sites, allowing for the development of compact and homogeneous perovskite. Researchers claim that by adding reducing agents, the content of Sn (IV) ions is lowered, resulting in superior thin films with more uniformity and stability. Chen et al. described the best performance for a tin-based, lead-free optoelectronic device in 2024, achieving a maximum efficiency of 15.14% to date. Two pyridyl-substituted fulleropyrrolidines (PPF) were synthesised and used as precursor additives, with cis (CPPF) and trans configurations. After 3,000 hours of storage and 500 hours of continuous illumination, the spatial configurations of the CPPF and TPPF had a significant impact on electron density distributions and interactions with perovskite components, increasing the device's efficiency to 15.14% and ensuring excellent stability. These results remained at 99% and 93% of their original efficiency. As a result, lead-free halide perovskites represent a promising new avenue for optoelectronic devices based on perovskite materials.

In this study, we will look at the most recent breakthroughs in the study of Sn-based optoelectronic devices. The intrinsic properties of Sn-based perovskite materials are discussed, as well as the specifics of current research into improving the performances of optoelectronic devices made with these materials. However, the optoelectronic performance of Sn-based perovskites is significantly lower than that of Pb-based devices. In order to improve performance, people in this fast-developing sector are continually considering and adopting new ideas. The material science community has recently become interested in the introduction of carbon nanotubes into semiconducting materials, which has resulted in increased device performance and charge transfer. In this study, we investigated how CNTs added to Sn-based perovskite devices contributed to their electrical and optical performance.

## 2.3 A Review on Charge Transport Mechanisms in Perovskite Devices

In a Metal-Semiconductor-Metal (MSM) structure, there are several mechanisms that facilitate the transport of electrons. Certain conduction mechanisms depend on the electrical characteristics of the electrode-sample interface, such as the energy barrier height of the interface and the conduction carriers in the sample films; other mechanisms rely on the characteristics of the sample itself, such as the density of states in conduction, trap level, trap spacing, and trap density, carrier drift mobility, and dielectric relaxation time. The following are examples of injection-limited transports or electrode-limited conduction mechanisms: Direct tunneling, Fowler-Nordheim (F-N) tunneling, and Schottky emission. Poole-Frenkel (P-F) emission, Ohmic conduction, Space Charge Limited Transport (SCLC), Hopping conduction, Trap-assisted tunneling (TAT), and Ohmic conduction are examples of bulk-limited conduction mechanisms [34–38]. In the following section, we will discuss a few of these transport models in brief, especially those have been utilized in this work.



### 2.3.1 Electrode Limited Charge Transport

Electrode-limited transport is a phenomenon that happens in systems where the characteristics of the electrode interfaces largely control the rate of transport or diffusion of charge carriers.

The electrical characteristics of the electrode-semiconductor contact determine the electrode-limited conduction mechanisms. The barrier height at the electrode-semiconductor contact is the most crucial factor in this kind of conduction mechanism. Few modes of electrode-limited conduction are: (1) Direct tunneling, (2) Fowler-Nordheim tunneling, and (3) Schottky or thermionic emission. Where the tunneling current is almost temperature independent, the thermionic emission current is temperature sensitive.

### 2.3.1.1 Thermionic Emission Model

The phenomenon when electrons transcend a potential energy barrier to escape from a material's surface into vacuum or another medium is referred to as thermionic emission theory. When a material's electrons gain enough thermal energy to cross the energy barrier at the surface, this process takes place. Consequently, the substance releases electrons, which enhance electrical conductivity or current flow. A large part of many electrical devices is thermionic emission. This hypothesis states that the formulation for the thermionic current can be expressed as [39]

$$J_0 = A^*T^2 \exp\{-e\phi/kT\} \quad (2.1)$$

Where  $A^* = \frac{4\pi me k^2}{h^3}$  and in which the numerical value of  $A$  is roughly  $120 \text{ [A/ (cm}^2 \text{ K}^2)]$ . If electrons encounter an external retarding potential of height  $V_s$  above  $\phi$ , fewer electrons will escape, resulting in a current  $J$  escaping from the cathode that is less than  $J_0$ . The derivation of **Equation 2.1** applies with the utilization of  $\phi + V_s$  instead of  $\phi$ . Thus, the above equation transforms into:

$$J = \frac{4\pi me k^2 T^2}{h^3} \exp\{-e(\phi + V_s)/kT\} \quad (2.2)$$

where the zero-field subscript is omitted. This equation now can also be written as

$$J = J_0 \exp\{-eV_s/kT\} \quad (2.3)$$

where  $J_0$  is given by **Equation 2.1**. Upon application of bias across the junction these **Equation 2.1** become [40,41]

$$J_0 = AT^2 \exp\{e(V_{app} - \phi_a)/kT\} \quad (2.4)$$

Where  $V_{app}$  is the applied bias and  $\phi_a$  is the anode potential. Therefore, when an electric field is applied, the potential energy barrier at the interface is lowered, increasing the flow of current

through the M-S junction. This increase in current flow and its reliance on the surrounding electric field are referred to as the Schottky effect. This model states that a metal can be infused with an electron if it has acquired enough thermal energy to overcome the maximum potential created by the superposition of the image charge potential and the external electric field [42]. The current flow at the interface generated by the junction of metal and perovskite material can be described and analysed using this model. We have utilized this model to examine current flow in the developed perovskite optoelectronic devices in the current thesis.

### 2.3.1.2 Direct Tunneling Model

DT is based on a quantum mechanical phenomenon in which, even at very small applied biases (i.e.,  $V < \phi_B$ ), electrons tunnel through an MSM junction barrier width. A suitably thin (usually  $< 4$  nm) and defect-free barrier or semiconductor allows the electrons to tunnel through the entire barrier thickness. In that instance, DT would control the MSM structure's current flow. When thermionic emission is sufficiently suppressed at low temperatures (e.g.,  $< 30$  K), the J-V characteristic of the structure can be measured to determine the degree of DT in that structure. The  $\ln(J/V^2)$  characteristic can then be plotted as a function of  $1/V$ . When the applied voltage is very low, a few millivolts, the resulting plot should be linear at those locations. The DT current can be expressed as follows [43,44]:

$$J_{DT} = J_0 [\{\phi_B \exp(-A_s \sqrt{\phi_B})\} - \{(\phi_B + V) \exp(-A_s \sqrt{\phi_B + V})\}] \quad (2.5)$$

Where  $J_0 = \frac{q^2}{2\pi\hbar d_i^2}$  and  $A_s = \frac{4\pi d_i \sqrt{2qm^*}}{\hbar}$ ,  $d_i$  is the thickness of the sample film. **Equation 2.5** can be understood as a current density, just as the Schottky Emission current density;  $J_0[\phi_B \exp(-A_s \sqrt{\phi_B})]$  flowing from metal-1 to metal-2, and another;  $J_0[(\phi_B + V) \exp(-A_s \sqrt{\phi_B + V})]$  flowing from metal-2 to metal-1.

### 2.3.2 Bulk-Limited Transport

Bulk-limited transport is a phenomenon in semiconductors where the intrinsic features of the semiconductor material itself play a major role in determining the pace of charge carrier movement. Bulk-limited transport concentrates on the bulk, or interior, of the semiconductor as opposed to interface-limited transport, which is dependent on the characteristics of material interfaces. For semiconductor device design and operation, bulk-limited transport is a basic factor. Understanding and managing the movement of charge carriers within the majority of

semiconductors is crucial, regardless of whether one is working with integrated circuits, diodes, transistors, or solar cells.

The electrical characteristics of the semiconductor itself determine the bulk-limited conduction mechanisms. The trap energy level in the semiconductor layer is the most crucial characteristic in this kind of conduction process. Poole-Frenkel emission, hopping conduction, ohmic conduction, space charge-limited conduction, and trap-assisted tunneling are the common types of bulk-limited conduction mechanisms [45,46]. Some significant electrical characteristics of the semiconducting films, such as the trap energy level, trap spacing, trap density, electronic drift mobility, and dielectric relaxation time, as well as the density of states in the conduction band, can be extracted based on the bulk limited conduction mechanisms.

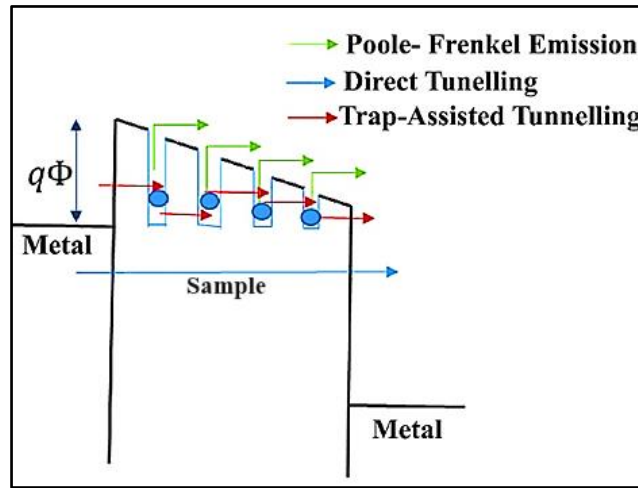


**Figure 2.2: Schematic diagram of several transport mechanism in metal- sample (semiconductor)-metal structure.**

### 2.3.2.1 Hopping Conduction

The tunneling effect of trapped electrons "hopping" from one trap site to another in semiconductor films is the cause of hopping conduction. The schematic energy band map for hopping conduction is displayed in **Figure 2.2**. Hopping conduction can be expressed as [37]

$$J = qanf \exp \left[ \frac{qaE - E_a}{kT} \right] \quad (2.6)$$

where  $f$  is the frequency of thermal vibration of electrons at trap sites,  $n$  is the electron concentration in the semiconductor's conduction band,  $a$  is the mean hopping distance (i.e., the mean spacing between trap sites), and  $E_a$  is the activation energy-that is, the energy level from the trap states to the bottom of the conduction band ( $E_C$ ).

### 2.3.2.2 Ohmic Conduction

In this conduction mechanism, a linear relationship exists between the current density and the electric field. Although the energy band gap of some perovskite semiconductors is relatively large than silicon, there will still be a small number of carriers that may be generated due to the thermal excitation. For instance, electrons can be excited from the valence band to the conduction band or from impurity levels. Although the number of carriers is very small, it is not zero. Ohmic conduction's current density can be expressed as a linear function of the electric field [47].

$$J = \sigma E = ne\mu E \quad (2.7)$$

Where  $n = N_C \exp\left[\frac{E_F - E_C}{kT}\right]$  and  $\sigma$  is electrical conductivity,  $n$  is the number of electrons in the conduction band,  $\mu$  is electron mobility, and  $N_C$  is the effective density of states of the conduction band. This current has a relatively small magnitude. This type of current mechanism can be observed when there are no substantial contributions from other modes of current transport in materials. Ohmic conduction current, resulting from mobile electrons in the conduction band or holes in the valence band, exhibits a linear dependence on the electric field. This behaviour is typically observed at very low voltages in the current-voltage ( $I$ - $V$ ) characteristics of semiconductors films.

### 2.3.2.3 Space Charge- Limited Conduction

Accurately characterizing a semiconductor's fundamental properties is essential for the advancement of electrical and optoelectronic devices. Among the different approaches available for charge transport characterization, space-charge limited current (SCLC) measurement is one of the most widely used steady-state methods. Current density-voltage ( $J$ - $V$ ) characteristics can be used to analyse electron and hole transport and injection characteristics. The theory initially proposed by C. D. Child and I. Langmuir between 1911 and 1913 focused on vacuum diodes. They observed that the current density ( $J$ ) between the diode plates followed a relationship of  $J \propto V^{3/2}$ , where  $V$  is the applied voltage [48]. However, this relationship did not hold true for devices containing materials like semiconductors, organics, or polymers sandwiched between electrodes.

Subsequently, Mott-Gurney developed a relation applicable to these materials under certain assumptions and in trap-free regions. The starting point of a space charge limited conduction

problem is the one-dimensional single carrier drift current **Equation 2.8** and Poisson **Equation 2.9**.

$$J = n(x)q\mu E \quad (2.8)$$

$$\frac{dE}{dx} = \frac{q}{\epsilon} n(x) \quad (2.9)$$

Here,  $q$  represents the electronic charge,  $\mu$  is the electronic mobility, and  $n$  denotes the density of thermally generated background free charges,  $\epsilon$  is the permittivity of the medium. When the density of thermally generated charge carriers ( $n$ ) is significantly lower than the injected charge density ( $n_{inj}$ ) and the system is free of traps, Mott-Gurney proposed an estimation for the relationship between current density ( $J$ ) and applied voltage ( $V$ ). They derived that in such conditions, space charge limited conduction (SCLC) follows a relationship described as follows [49]:

$$J = \frac{9}{8} \mu \epsilon \frac{V^2}{L^3} \quad (2.10)$$

Where  $L$  is the thickness of the sample. However, this relationship holds good when there is no trap in the system. But practically, perovskite, organic, even in some inorganic samples-based devices are also not trap free. Therefore, injected charge carriers at an ohmic contact of the device cannot reach the other electrode immediately causes space-charge-limited current. An electronic trap is defined as any defect that generates localized electronic states that are energetically and spatially distributed inside the semiconductor's bandgap. Trap states in perovskite semiconductor materials can be caused by impurities, structural flaws, geminate pairs, or self-trapping. Because of the weak molecular interactions in perovskite materials, a molecule's HOMO or LUMO generates a trap state when positioned between host molecules [50]. Fluctuations in conjugation length produced by structural flaws can result in tail states below the transport energy level, which contribute to trap states. Structural defects are not restricted to tail states; every structural imperfection has the potential to produce traps. Traps are categorized as shallow or deep according to their energy levels relative to the semiconductor's band edges at a certain temperature. Deep traps are located more distant from the band edges (several  $kT$ ), whereas shallow traps are closer to the band edges (a few  $kT$ ) [51,52]. Shallow traps are specific locations within the semiconductor's band gap that temporarily capture charge carriers, holding them until they are released back into the energy band due to the influence of an electric field, thermal energy, or photons. For instance, in the multiple-trap and release (MTR) model, localized shallow traps can capture charges moving

within delocalized states, subsequently releasing them back into the energy band with the assistance of thermal energy. Charge carriers trapped in densely populated traps can engage in transport via thermally activated hopping or tunneling between localized states. Compared to deep traps, charge carriers trapped in shallow traps are more likely to return to the energy band through thermal energy, as de-trapping is less probable in deep traps. Deep traps often function as recombination sites for charge carriers, which can diminish their lifetime. Traps may possess discrete energy levels or energy distributions, which can be represented using exponential or Gaussian functions. The **Figure 2.3** shows these traps distribution in the bandgap [53,54].

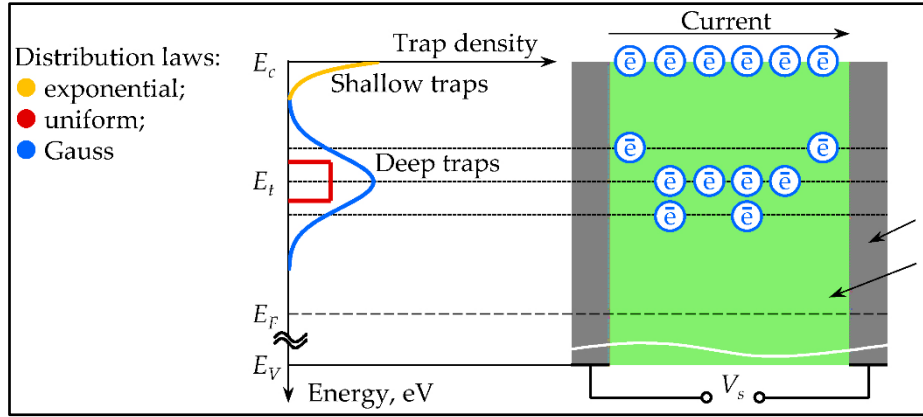


**Figure 2.3: Different types of trap distributions in the bandgap of a sample [55]**

For our analysis, we have only considered discrete and the exponential distribution of traps. In this case drift current equation as mentioned in **Equation 2.8** is remain same but Poisson equation is represented by **Equations 2.11**.

$$\frac{dE}{dx} = \frac{q}{\epsilon}(n + n_t) \quad (2.11)$$

Where  $n$  and  $n_t$  are the concentrations of free and trapped charges, respectively. The following scenarios can be obtained using the preceding equations.

At low voltages, it is often observed that ohmic conduction with low mobility dominates via thermally generated free charges over injected charge contributions. In this scenario, the current density  $J$  is described by:

$$J_d = nq\mu E \quad (2.12)$$

As the applied voltage increases, space charge limited current can be observed in a system with traps. Considering a system with discrete traps in the bandgap described by **Equation 2.13**, the

relationship between current and voltage follows **Equation 2.14** [56].

$$n_t = \frac{N_t}{1 + \exp\left[\frac{E_t - E_F}{kT}\right]} \quad (2.13)$$

$$J = \frac{9}{8} \mu \varepsilon \theta \frac{V^2}{L^3} \quad (2.14)$$

Where,  $N_t$ ,  $E_t$ ,  $k$  and  $T$  are trap density, single trap energy, Boltzmann constant and absolute temperature, respectively.  $\theta$  is defined as trap factor and can be related to free and trapped carrier density as

$$\theta = \frac{n_f}{n_f + n_t} \quad (2.15)$$

Typically, the presence of a single or discrete trap result in a sudden increase in current observed after the ohmic region in the  $\log(I)$  versus  $\log(V)$  curve.

Suppose the system contains an exponential trap distribution within the bandgap region, characterized by a trap density distribution as given by **Equation 2.16**. In that case, the behaviour of the current-voltage characteristics can be distinctly influenced [57].

$$n_t = H_t \exp\left(\frac{F_n}{kT_c}\right) \quad (2.16)$$

Where  $T_c$  is the characteristic temperature, where  $T_c = E_t/k$ , where,  $E_t$  is trap energy,  $H_t$  is trap density,  $F_n$  is the electron Fermi energy.  $n_t$  and  $n$  are interrelated as follows:

$$n_t = H_t \exp\left(\frac{F_n}{kT_c}\right) \quad (2.17)$$

$$n = N_c \exp\left(\frac{F_n}{kT}\right) \quad (2.18)$$

$$n_t = H_t \exp\left(\frac{F_n}{kT} * \frac{T}{T_c}\right) \quad (2.19)$$

$$n_c = H_t \left(\frac{n}{N_c}\right)^{1/m} \quad (2.20)$$

$$n_t = C n^{1/m} \quad (2.21)$$

The expression for current density can be derived from the solution of the Poisson **Equation 2.11** and **Equation 2.16** as follows [58]:

$$J = N_c \mu \left(\frac{2m+1}{m+1}\right)^{m+1} \left(\frac{\varepsilon m}{(m+1)H_t}\right)^m q^{m-1} \frac{V^{m+1}}{L^{2m+1}} \quad (2.22)$$

This process is known as Trap Charge Limited Conduction. The power law dependency, where  $J \sim V^{m+1}$ , is the most notable aspect of the **Equation 2.22** mentioned earlier. Using the value of slope ( $m$ ) and  $E_t = mkT$ , where  $E_t$  is the trap energy,  $k$  is Boltzmann constant and  $T$  is characteristics temperature, we can able to estimate the trap energy of the sample [59]. This specific current-voltage (I-V) relationship emerges due to exponential traps distribution in the bandgap.

In this section, we have discussed the different transport mechanisms utilized in our study to analyse the current-voltage characteristics. Our goal was to gain insights into the charge transport mechanisms in perovskite-based optoelectronic devices, including scenarios involving the presence of CNTs. Additionally, we have estimated several electrical parameters of the devices, directly illustrating the enhancements in charge transport within the system. In the next section, we shall delve into the significance of CNTs in optoelectronic devices and their role in improving the charge transport mechanism.

## 2.4 Important of CNT in Perovskite Optoelectronic Devices

### 2.4.1 Properties of CNTs

CNTs are one-dimensional nanomaterials that have been rolled into a cylindrical shape from one or more layers of a graphene sheet. Single-walled CNTs (SWCNTs;  $n_{\text{shell}} = 1$ ), double-walled CNTs (DWCNTs;  $n_{\text{shell}} = 2$ ), and multi-walled CNTs (MWCNTs;  $n_{\text{shell}} = 3$ ) are the three varieties of CNTs that may be distinguished based on the number of shells ( $n_{\text{shell}}$ ) (**Figure 2.4**) [60]. As graphene sheets can be rolled at different angles, SWCNTs have a very diverse structure in terms of length, diameter, and chirality. It is well known that roughly two thirds of the generated SWCNTs behave semiconducting (called s-SWCNTs), while the remainder SWCNTs have metallic characteristics (called m-SWCNTs). The various chirality and diameters of the nanotubes determine this electrical heterogeneity.

The s-SWCNTs are more advantageous for charge transport due to their appropriate energy band structure and high hole mobility, which tend to significantly boost charge transfer and transport in optoelectronic devices [61].

Whereas, structure of DWCNTs and MWCNTs is looks like combination of concentric, cylindrical scroll-shaped graphene sheets. The potential barrier of the band structure in DWCNTs is dependent on the chirality pairings and is unaffected by the interlayer interaction. DWCNTs have characteristics in between those of SWCNTs and MWCNTs. In terms of light

optical density, they are similar to SWCNTs, although they are more soluble and mechanically stable. Small diameter ( $<10$  nm) MWCNTs behave like SWCNTs with little to no shell-to-shell interaction, while large diameter MWCNTs exhibit metallic behaviour for each individual nanotube. All of a MWCNT's shells experience electron transport, which results in quasi-ballistic conduction.

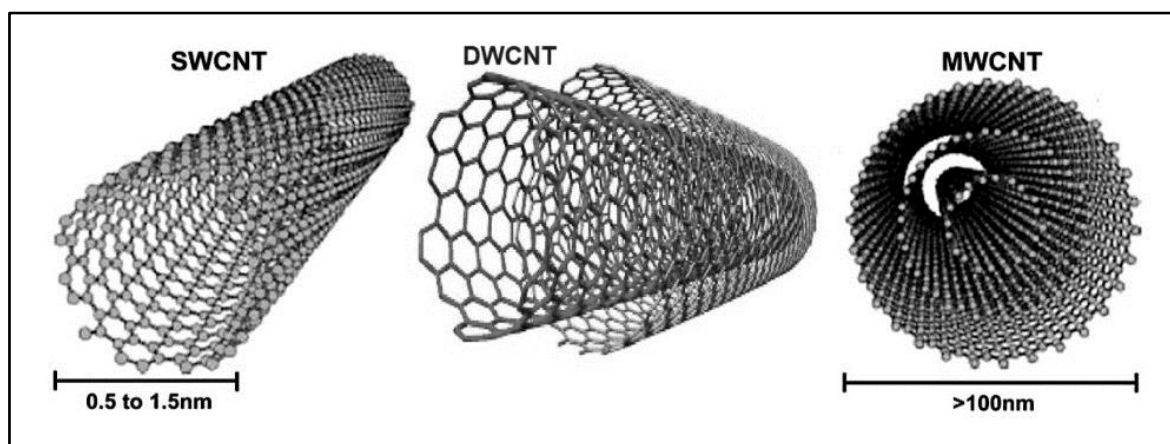


**Figure 2.4: Types of carbon nanotubes (CNTs)**

Furthermore, at room temperature, the MWCNT layers rotate and slip with ease. Because of this, MWCNTs often have a less flawless structure than SWCNTs, which results in a reduced degree of inherent ballistic mechanism of conductivity. On the other hand, MWCNTs have a large number of conducting channels, which increases their conductivity. Excellent charge transport characteristics and strong chemical stability are displayed by all three varieties of CNTs. The electrical conductivity and high charge mobility of these characteristics are the most crucial for use in optoelectronic devices. The exceptional mechanical and thermal characteristics greatly aid in the creation of stable and flexible devices.

### 2.4.2 Role of CNT in Perovskite Optoelectronic Devices

CNTs are viable for use as conducting substrates or back electrodes in PSCs due to their affordability, flexibility, high electrical conductivity, and partial transparency [62–65]. They can also serve as additives in the hole transport material (HTM) to enhance hole selection or as hole extraction electrodes due to their superior charge extraction and transport capabilities, as well as appropriate energy levels. Additionally, CNTs can act as interlayers to passivate perovskite grains, reinforce interface connections, and adjust energy level alignment [66].

Furthermore, when added to perovskite, CNTs can improve charge separation and collection by serving as efficient pathways.

#### **2.4.2.1 CNTs in PSCs**

Because of the excellent ability of perovskite materials to convert sunlight into electricity, perovskite solar cells (PSCs) have become a very promising technology in recent years [67]. Single-junction PSCs have achieved a high certified power conversion efficiency (PCE) of 25.5%. Currently, record PCEs of 29.8%, 24.2%, and 25.6% have been reached by perovskite-silicon, perovskite/CIG-Se (copper indium-gallium-selenide), and perovskite-perovskite tandem devices, respectively [68]. Not only has efficiency improved, but stability of these devices has also increased significantly. These advancements are thanks to improvements in choosing additives, designing the devices, applying materials, and building techniques. Incorporating CNTs into PSCs has been particularly important due to their strong conductivity. CNTs are used in various ways in perovskite solar cells, such as flexible conducting surfaces, layers between different parts of the cell, electrodes to extract electricity, layers that help charges move through the cell, back electrodes, and as additives [69].

#### **2.4.2.2 CNTs as Conducting Substrates**

Transparent electrodes like indium tin oxide (ITO) or fluorine-doped tin oxide (FTO) are commonly used in various optoelectronic devices. However, there are challenges with these materials, such as brittleness and high cost, which hinder their widespread industrial use. The cost of materials and deposition processes for ITO and FTO is significant. Researchers are exploring alternative conducting substrates, with CNT films emerging as a promising option [70]. CNT films offer transparency, conductivity, low cost, ease of fabrication, and mechanical robustness. Initially, SWCNTs were used but faced limitations due to low conductivity, which was improved by doping with materials like  $\text{MoO}_3$  [70]. Adjusting the energy levels of  $\text{MoO}_3$  through film thickness control led to better compatibility with perovskite layers, resulting in improved device performance. Further advancements involved doping SWCNTs with trifluoromethanesulfonic acid (TFMS) to enhance conductivity and device efficiency. CNT-based, ITO-free perovskite solar cells (PSCs) achieved high power conversion efficiency (PCE) of 17% with optimized  $\text{MoO}_3$  film thickness.

#### **2.4.2.3 CNTs as Hole Extraction Material**

HTMs are plays important role in the extraction of holes from perovskite and the inhibition of electron transport in PSCs. Typically, unstable organic compounds (such as spiro-OMeTAD) are used as HTMs in conventional PSCs. Carbon materials have been utilized to extract holes, which are inexpensive and stable, in order to eliminate these drawbacks. CNTs are a common choice for carbon electrodes in PSCs among various carbon materials because they have a work function of 4.7-5.1 eV, which is ideal for hole extraction [71,72]. CNTs have outstanding thermostability, which guarantees that devices can withstand high temperatures.

#### **2.4.2.4 CNTs in LEDs**

CNTs, whether introduced into the perovskite layer or employed as electrodes, improve charge carrier mobility, electrical conductivity, and allow for more efficient charge injection and transfer. This integration addresses common concerns including charge recombination and energy losses, improving the overall performance and efficiency of perovskite LEDs [73]. Furthermore, CNTs' flexibility and mechanical resilience contribute to the longevity and stability of these LEDs, opening the door for their prospective use in flexible and wearable electronic systems. The combination of CNTs and perovskite materials is a promising step toward the development of next-generation optoelectronic devices.

#### **2.4.2.5 CNTs in Photodiodes**

CNTs are also used by perovskite-based photodiodes to improve device performance. High photodetection properties and quick photoreactions are typically seen in presence of CNTs [74]. Due to the ultrahigh charge carrier mobility and substantial absorption of CNTs in the NIR, perovskite-CNT composites can be used in photodiodes to further improve the responsivity and enable broadband photodetection in both the visible and NIR domains. Li et al. created a photodiode by embedding s-SWCNTs in a perovskite layer in order to demonstrate this possibility [75]. The s-SWCNT-mixed  $\text{PbI}_2/\text{PbBr}_2$  film was first coated onto a PEDOT:PSS layer for the perovskite-CNTs layer, and then an MAI layer was deposited by evaporation. A reaction between the  $\text{PbI}_2/\text{PbBr}_2$  and MAI layers would be induced by a post-annealing process, resulting in the formation of a perovskite layer with s-SWCNTs. While the bare device only displayed a responsivity of roughly 25 mA/W, the produced composite photodiode had a responsivity of approximately 65 mA/W. It was explained by the fact that the addition of s-SWCNTs greatly enhanced charge transport. The composite photodiode demonstrated a high response speed of roughly 10 ms under low bias voltages, as well as a detectivity ( $D^*$ ) of up to

$3.83 \times 10^{12}$  and  $1.23 \times 10^{12}$  Jones in the visible and NIR areas, respectively. Thus, the light sensitivity would be extended into the near-infrared range by employing s-SWNTs in a perovskite host.

We discussed the use of CNTs in a range of perovskite-based devices, with a primary emphasis on PSCs, pe-PDs, and pe-LEDs. By boosting charge transfer, speeding up charge transport, strengthening crystal quality, and expanding the optical response range, CNT applications in these devices may increase device performance. CNT electrodes could make it possible to fabricate flexible, affordable devices. Therefore, incorporation of CNTs in perovskite no doubt is a very recent and prosperous technique which may have the potential to advance the material-based devices.

## **2.5 Optoelectronic Parameters of the Schottky Device**

The preceding discussion shows that lead is a hazardous component in perovskites, prompting the transition from lead-based materials to lead-free perovskites, despite the excellent efficiency of lead-based perovskites in optoelectronic devices. Tin-based perovskites show potential among lead-free perovskites, but they face substantial problems such as tin oxidation, defect-induced charge trapping, and film non-uniformity, all of which limit charge transport efficiency. As a result, research efforts should focus on increasing the performance of lead-free perovskites in order to encourage their use in optoelectronic devices.

Nanomaterials such as  $\text{TiO}_2$ , ZnO nanoparticles, and several forms of CNTs (SWCNTs, DWCNTs, and MWCNTs) are promising materials in material science that have been extensively used to increase device performance. In this chapter, we also saw that these nanomaterials are utilized in perovskites and have demonstrated performance increases; however, most investigations have focused on lead-based perovskites, and the underlying mechanisms of these enhancements have not been thoroughly examined. As our goal is to transition to lead-free perovskites, we incorporated CNTs into lead-free perovskites to investigate their influence on the performance of lead-free perovskite-based devices. This method helps us understand the transport processes that explain these effects.

In our studies, we synthesized lead-free organic-inorganic halide perovskite and inorganic perovskite samples. Using these materials, we developed basic Schottky devices and studied their properties to better understand charge conduction and transport mechanisms using established theories. We evaluated device performance based on electrical parameters such as

conductivity ( $\sigma$ ), rectification ratio, ideality factor ( $\eta$ ), barrier height ( $\phi_b$ ), series resistance ( $R_s$ ) from TE theories, threshold voltage ( $V_{th}$ ), and trap energy ( $E_t$ ) from charge transport theories. In addition, we evaluated optical factors such as photosensitivity, responsivity, detectivity, and bulk transport qualities including transit time ( $\tau$ ) and mobility ( $\mu$ ). Some of these theories have already been explored in this chapter, providing techniques for obtaining these characteristics, while others will be discussed in subsequent chapters during the device performance study.

However, we found that the charge transfer in these devices was slower than in traditional lead-based perovskite devices. To address this issue, we added CNTs to the devices to improve charge transmission. Our results show that the presence of CNTs considerably improved the charge transfer and overall optoelectronic performance of Schottky devices.

## 2.6 References

- [1] D. Ma, K. Lin, Y. Dong, H. Choubisa, A.H. Proppe, D. Wu, Y.K. Wang, B. Chen, P. Li, J.Z. Fan, F. Yuan, A. Johnston, Y. Liu, Y. Kang, Z.H. Lu, Z. Wei, E.H. Sargent, Distribution control enables efficient reduced-dimensional perovskite LEDs, *Nature* 599 (2021) 594–598.
- [2] S. Pansri, R. Supruangnet, H. Nakajima, S. Rattanasuporn, S. Noothongkaew, Band offset determination of p-NiO/n-TiO<sub>2</sub> heterojunctions for applications in high-performance UV photodetectors, *J Mater Sci* 55 (2020) 4332–4344.
- [3] D. Han, C. Dai, S. Chen, Calculation studies on point defects in perovskite solar cells, *Journal of Semiconductors* 38 (2017) 011006.
- [4] M. Samiee, S. Konduri, B. Ganapathy, R. Kottokkaran, H.A. Abbas, A. Kitahara, P. Joshi, L. Zhang, M. Noack, V. Dalal, Defect density and dielectric constant in perovskite solar cells, *Appl Phys Lett* 105 (2014) 153502.
- [5] S. Huang, Z. Rui, D. Chi, D. Bao, Influence of defect states on the performances of planar tin halide perovskite solar cells, *Journal of Semiconductors* 40 (2019) 032201.
- [6] X. Wu, L. Xie, K. Lin, J. Lu, K. Wang, W. Feng, B. Fan, P. Yin, Z. Wei, Efficient and stable carbon-based perovskite solar cells enabled by the inorganic interface of CuSCN and carbon nanotubes, *J Mater Chem A Mater* 7 (2019) 12236–12243.
- [7] Y. Yang, H. Chen, X. Zheng, X. Meng, T. Zhang, C. Hu, Y. Bai, S. Xiao, S. Yang, Ultrasound-spray deposition of multi-walled carbon nanotubes on NiO nanoparticles-embedded perovskite layers for high-performance carbon-based perovskite solar cells, *Nano Energy* 42 (2017) 322–333.
- [8] H. Li, Y. Xue, B. Zheng, J. Tian, H. Wang, C. Gao, X. Liu, Interface modification with PCBM intermediate layers for planar formamidinium perovskite solar cells, *RSC Adv* 7 (2017) 30422–30427.
- [9] Y.F. Chen, Y.T. Tsai, D.M. Bassani, R. Clerc, D. Forgács, H.J. Bolink, M. Wussler, W. Jaegermann, G. Wantz, L. Hirsch, Evidence of band bending induced by hole trapping at MAPbI<sub>3</sub> perovskite/metal interface, *J Mater Chem A Mater* 4 (2016) 17529–17536.

- [10] N. Suresh Kumar, K. Chandra Babu Naidu, A review on perovskite solar cells (PSCs), materials and applications, *Journal of Materiomics* 7 (2021) 940–956.
- [11] A. Kojima, K. Teshima, Y. Shirai, T. Miyasaka, Organometal halide perovskites as visible-light sensitizers for photovoltaic cells, *J Am Chem Soc* 131 (2009) 6050–6051.
- [12] Y. Hou, X. Chen, S. Yang, Y.L. Zhong, C. Li, H. Zhao, H.G. Yang, Low-temperature processed  $\text{In}_2\text{S}_3$  electron transport layer for efficient hybrid perovskite solar cells, *Nano Energy* 36 (2017) 102–109.
- [13] X. Li, J. Yang, Q. Jiang, H. Lai, S. Li, J. Xin, W. Chu, J. Hou, Low-Temperature Solution-Processed  $\text{ZnSe}$  Electron Transport Layer for Efficient Planar Perovskite Solar Cells with Negligible Hysteresis and Improved Photostability, *ACS Nano* 12 (2018) 5605–5614.
- [14] R. Teimouri, Z. Heydari, M.P. Ghaziani, M. Madani, H. Abdy, M. Kolahdouz, E. Asl-Soleimani, Synthesizing Li doped  $\text{TiO}_2$  electron transport layers for highly efficient planar perovskite solar cell, *Superlattices Microstruct* 145 (2020) 106627.
- [15] A. Al-Ashouri, E. Köhnen, B. Li, A. Magomedov, H. Hempel, P. Caprioglio, J.A. Márquez, Monolithic perovskite/silicon tandem solar cell with >29% efficiency by enhanced hole extraction, *Science* 370 (2020) 1300–1309.
- [16] W. Luo, L. Yan, R. Liu, T. Zou, S. Zhang, C. Liu, Q. Dai, J. Chen, H. Zhou, High detectivity ITO/organolead halide perovskite Schottky photodiodes, *Semicond Sci Technol* 34 (2019) 074004.
- [17] H. Wang, D.H. Kim, Perovskite-based photodetectors: Materials and devices, *Chem Soc Rev* 46 (2017) 5204–5236.
- [18] G. Li, Y. Wang, L. Huang, W. Sun, Research Progress of High-Sensitivity Perovskite Photodetectors: A Review of Photodetectors: Noise, Structure, and Materials, *ACS Appl Electron Mater* 4 (2022) 1485–1505.
- [19] T. Wu, Z. Qin, Y. Wang, Y. Wu, W. Chen, S. Zhang, M. Cai, S. Dai, J. Zhang, J. Liu, Z. Zhou, X. Liu, H. Segawa, H. Tan, Q. Tang, J. Fang, Y. Li, L. Ding, Z. Ning, Y. Qi, Y. Zhang, L. Han, The Main Progress of Perovskite Solar Cells in 2020–2021, *Nanomicro Lett* 13 (2021) 152.
- [20] G. Schileo, G. Grancini, Lead or no lead? Availability, toxicity, sustainability and environmental impact of lead-free perovskite solar cells, *J Mater Chem C Mater* 9 (2021) 67–76.
- [21] M. Wang, W. Wang, B. Ma, W. Shen, L. Liu, K. Cao, S. Chen, W. Huang, Lead-Free Perovskite Materials for Solar Cells, *Nanomicro Lett* 13 (2021) 62.
- [22] M. Konstantakou, T. Stergiopoulos, A critical review on tin halide perovskite solar cells, *J Mater Chem A Mater* 5 (2017) 11518–11549.
- [23] F.H. Gourji, D. Velauthapillai, A review on Cs-based Pb-free double halide perovskites: From theoretical and experimental studies to doping and applications, *Molecules* 26 (2021) 7.
- [24] Z. Zhang, Q. Sun, Y. Lu, F. Lu, X. Mu, S.H. Wei, M. Sui, Hydrogenated  $\text{Cs}_2\text{AgBiBr}_6$  for significantly improved efficiency of lead-free inorganic double perovskite solar cell, *Nat Commun* 13 (2022) 3397.
- [25] D. Meggiolaro, D. Ricciarelli, A.A. Alasmari, F.A.S. Alasmari, F. De Angelis, Tin versus Lead Redox Chemistry Modulates Charge Trapping and Self-Doping in Tin/Lead Iodide Perovskites, *Journal of Physical Chemistry Letters* 11 (2020) 3546–3556.

- [26] X.L. Li, L.L. Gao, Q.Q. Chu, Y. Li, B. Ding, G.J. Yang, Green Solution-Processed Tin-Based Perovskite Films for Lead-Free Planar Photovoltaic Devices, *ACS Appl Mater Interfaces* 11 (2019) 3053–3060.
- [27] J. Chen, J. Luo, E. Hou, P. Song, Y. Li, C. Sun, W. Feng, S. Cheng, H. Zhang, L. Xie, C. Tian, Z. Wei, Efficient tin-based perovskite solar cells with trans-isomeric fulleropyrrolidine additives, *Nat Photonics* 18 (2024) 464–470.
- [28] M.M. Byranvand, W. Zuo, R. Imani, M. Pazoki, M. Saliba, Tin-based halide perovskite materials: properties and applications, *Chem Sci* 13 (2022) 6766–6781.
- [29] S.A.A. Shah, M.H. Sayyad, K. Khan, K. Guo, F. Shen, J. Sun, A.K. Tareen, Y. Gong, Z. Guo, Progress towards high-efficiency and stable tin-based perovskite solar cells, *Energies (Basel)* 13 (2020) 5092.
- [30] D. Sahoo, N.B. Manik, Study on the effect of temperature on electrical and photovoltaic parameters of lead-free tin-based Perovskite solar cell, *Indian Journal of Physics* 97 (2023) 447–455.
- [31] S.J. Lee, S.S. Shin, Y.C. Kim, D. Kim, T.K. Ahn, J.H. Noh, J. Seo, S. Il Seok, Fabrication of Efficient Formamidinium Tin Iodide Perovskite Solar Cells through SnF<sub>2</sub>-Pyrazine Complex, *J Am Chem Soc* 138 (2016) 3974–3977.
- [32] S.A.A. Shah, M.H. Sayyad, K. Khan, K. Guo, F. Shen, J. Sun, A.K. Tareen, Y. Gong, Z. Guo, Progress towards high-efficiency and stable tin-based perovskite solar cells, *Energies (Basel)* 13 (2020) 5092.
- [33] C. Hartmann, S. Gupta, T. Bendikov, X. Kozina, T. Kunze, R. Félix, G. Hodes, R.G. Wilks, D. Cahen, M. Bär, Impact of SnF<sub>2</sub> Addition on the Chemical and Electronic Surface Structure of CsSnBr<sub>3</sub>, *ACS Appl Mater Interfaces* 12 (2020) 12353–12361.
- [34] S. Sen, N.B. Manik, Correlation between barrier potential and charge trapping under the influence of Titanium Di oxide nanomaterials in organic devices, *Results in Materials* 8 (2020) 100145.
- [35] M. Soyulu, B. Abay, Analysing space charge-limited conduction in Au/n-InP Schottky diodes, *Physica E: Low-dimensional Systems and Nanostructures* 43 (2010) 534–538.
- [36] J. Wilson, J. Zhang, A. Song, Analytical Theory of Thin-Film Schottky Diodes, *ACS Appl Electron Mater* 1 (2019) 1570–1580.
- [37] E.W. Lim, R. Ismail, Conduction mechanism of valence change resistive switching memory: A survey, *Electronics (Switzerland)* 4 (2015) 586–613.
- [38] P.N. Murgatroyd, H.H. Wills, Theory of space-charge-limited current enhanced by Frenkel effect, *Phys. D: Appl. Phys.* 3 (1969) 151–156.
- [39] C.R. Crowbll, The Richardson constant for thermionic emission in Schottky barrier diodes, *Solid-State Electronics* 8 (1965) 395–399.
- [40] C. Pei, Y. Wong, C. Troadec, A.T.S. Wee, K. Eng, J. Goh, A Gaussian Thermionic Emission Model for Analysis of Au/MoS<sub>2</sub> Schottky Barrier Devices, *Phys. Rev. Applied*, 14 (2020) 054027.
- [41] C.Y. Wu, Interfacial layer-thermionic-diffusion theory for the Schottky barrier diode, *J Appl Phys* 53 (1982) 5947–5950.
- [42] O.C. Olawole, D.K. De, Theoretical studies of thermionic conversion of solar energy with graphene as emitter and collector, *J Photonics Energy* 8 (2018) 1.

- [43] M. Mehbou~, Y. Bruvnseraeue, Electron Tunneling through Barriers 203 pbys, 1975 203-211.
- [44] F.C. Chiu, A review on conduction mechanisms in dielectric films, *Advances in Materials Science and Engineering*, 2014 (2014) 578168.
- [45] J. Pospisil, O. Zmeskal, S. Nespurek, J. Krajcovic, M. Weiter, A. Kovalenko, Density of bulk trap states of hybrid lead halide perovskite single crystals: temperature modulated space-charge-limited-currents, *Sci Rep* 9 (2019) 3332.
- [46] C.P. Kwan, M. Street, A. Mahmood, Space-charge limited conduction in epitaxial chromia films grown on elemental and oxide-based metallic substrates, *AIP Adv* 055018 (2019) 1–7.
- [47] F. Maddalena, P.P. Boix, C. Xin Yu, N. Mathews, C. Soci, S. Mhaisalkar, Charge transport in organometal halide perovskites, in: *Organic-Inorganic Halide Perovskite Photovoltaics: From Fundamentals to Device Architectures*, Springer International Publishing, (2016) 201–222.
- [48] J.H. Werner, H.H. Güttler, Temperature dependence of Schottky barrier heights on silicon, *J Appl Phys* 73 (1993) 1315–1319.
- [49] A. Rose, Space-Charge-Limited Currents in Solids, *Phys. Rev.* 97 (1955) 1538.
- [50] S. Ne~porek, P. Smejtek, Space-charge limited currents in insulators with the Gaussian distribution of traps, *Czech J Phys* 22 (1972) 160–175.
- [51] M. Campos, J.A. Giacometti, M. Silver, Deep exponential distribution of traps in naphthalene, *Appl Phys Lett* 34 (1979) 226–228.
- [52] S. Heo, G. Seo, Y. Lee, D. Lee, M. Seol, J. Lee, J.B. Park, K. Kim, D.J. Yun, Y.S. Kim, J.K. Shin, T.K. Ahn, M.K. Nazeeruddin, Deep level trapped defect analysis in CH<sub>3</sub>NH<sub>3</sub>PbI<sub>3</sub> perovskite solar cells by deep level transient spectroscopy, *Energy Environ Sci* 10 (2017) 1128–1133.
- [53] T. Sakurai, K. Shoji, K. Itoh, R.K. Gartia, Origin of the exponential distribution of traps in glass, *J Appl Phys* 89 (2001) 2208–2212.
- [54] H.T. Nicolai, M.M. Mandoc, P.W.M. Blom, Electron traps in semiconducting polymers: Exponential versus Gaussian trap distribution, *Phys Rev B Condens Matter Mater Phys* 83 (2011) 195204.
- [55] D. Mizginov, O. Telminov, S. Yanovich, D. Zhevnenko, F. Meshchaninov, E. Gornev, Investigation of the Temperature Dependence of Volt-Ampere Characteristics of a Thin-Film Si<sub>3</sub>N<sub>4</sub> Memristor, *Crystals (Basel)* 13 (2023).
- [56] M.A. Lampert, Theory of Space-Charge-Limited Currents in an Insulator with Traps, *Phys. Rev.* 103 (1956) 1648.
- [57] R.H. Bube, Trap Density Determination by Space-Charge-Limited Currents, *J Appl Phys* 33 (1962) 1733–1737.
- [58] P. Mark, W. Helfrich, Space-charge-limited currents in organic crystals, *J Appl Phys* 33 (1962) 205–215.
- [59] D. Joung, A. Chunder, L. Zhai, S.I. Khondaker, Space charge limited conduction with exponential trap distribution in reduced graphene oxide sheets, *Appl. Phys. Lett.* 97 (2010) 093105.

- [60] C.L. Brito, J. V. Silva, R. V. Gonzaga, M.A. La-Scalea, J. Giarolla, E.I. Ferreira, A Review on Carbon Nanotubes Family of Nanomaterials and Their Health Field, *ACS Omega* 9 (2024) 8687–8708.
- [61] S. Sen, N.B. Manik, Effect of Different Sized Multi Walled Carbon Nanotubes on the Barrier Potential and Trap Concentration of Malachite Green Dye Based Organic Device, *Advances in Materials Science* 20 (2020) 16–26.
- [62] S.N. Habisreutinger, R.J. Nicholas, H.J. Snaith, Carbon Nanotubes in Perovskite Solar Cells, *Adv Energy Mater* 7 (2017) 1601839.
- [63] F. Li, Z. Qiu, S. Liu, H. Zhang, Carbon Nanotube-Perovskite Composites for Ultrasensitive Broadband Photodiodes, *ACS Appl Nano Mater* 2 (2019) 4974–4982.
- [64] X. Wu, L. Xie, K. Lin, J. Lu, K. Wang, W. Feng, B. Fan, P. Yin, Z. Wei, Efficient and stable carbon-based perovskite solar cells enabled by the inorganic interface of CuSCN and carbon nanotubes, *J Mater Chem A Mater* 7 (2019) 12236–12243.
- [65] A.S.R. Bati, L.P. Yu, S.A. Tawfik, M.J.S. Spencer, P.E. Shaw, M. Batmunkh, J.G. Shapter, Electrically Sorted Single-Walled Carbon Nanotubes-Based Electron Transporting Layers for Perovskite Solar Cells, *IScience* 14 (2019) 100–112.
- [66] S.N. Habisreutinger, J.L. Blackburn, Carbon nanotubes in high-performance perovskite photovoltaics and other emerging optoelectronic applications, *J Appl Phys* 129 (2021) 010903.
- [67] V.T. Tiong, N.D. Pham, T. Wang, T. Zhu, X. Zhao, Y. Zhang, Q. Shen, J. Bell, L. Hu, S. Dai, H. Wang, Octadecylamine-Functionalized Single-Walled Carbon Nanotubes for Facilitating the Formation of a Monolithic Perovskite Layer and Stable Solar Cells, *Adv Funct Mater* 28 (2018) 1705545.
- [68] T.T. Oo, S. Debnath, Application of carbon nanotubes in perovskite solar cells: A review, in: *AIP Conf Proc*, American Institute of Physics Inc., 1902 (2017) 020015.
- [69] Q. Lou, H. Li, Q. Huang, Z. Shen, F. Li, Q. Du, M. Jin, C. Chen, Multifunctional CNT: TiO<sub>2</sub> additives in spiro-OMeTAD layer for highly efficient and stable perovskite solar cells, *Eco Mat* 3 (2021) e12099.
- [70] Z. Dong, W. Li, H. Wang, X. Jiang, H. Liu, L. Zhu, H. Chen, Carbon nanotubes in perovskite-based optoelectronic devices, *Matter* 5 (2022) 448–481.
- [71] M. Cai, V.T. Tiong, T. Hreid, J. Bell, H. Wang, An efficient hole transport material composite based on poly(3-hexylthiophene) and bamboo-structured carbon nanotubes for high performance perovskite solar cells, *J Mater Chem A Mater* 3 (2015) 2784–2793.
- [72] J. Wang, J. Li, X. Xu, G. Xu, H. Shen, Enhanced Photovoltaic Performance with Carbon Nanotubes Incorporating into Hole Transport Materials for Perovskite Solar Cells, *J Electron Mater* 45 (2016) 5127–5132.
- [73] V. Jamali, F. Niroui, L.W. Taylor, O.S. Dewey, B.A. Koscher, M. Pasquali, A.P. Alivisatos, Perovskite-Carbon Nanotube Light-Emitting Fibers, *Nano Lett* 20 (2020) 3178–3184.
- [74] P. Bansal, X. Zhang, H. Wang, P. Kar, W.W. Yu, Charge transfer between lead halide perovskite nanocrystals and single-walled carbon nanotubes, *Nanoscale Adv* 2 (2020) 808–813.
- [75] F. Li, Z. Qiu, S. Liu, H. Zhang, Carbon Nanotube-Perovskite Composites for Ultrasensitive Broadband Photodiodes, *ACS Appl Nano Mater* 2 (2019) 4974–4982.

# **Chapter 3: Study on Lead-Free Methylammonium Tin Iodide ( $\text{CH}_3\text{NH}_3\text{SnI}_3$ ) Nano Cubic Perovskite Schottky Diode**

## **3.1 Introduction**

## **3.2 Experimental Section**

### 3.2.1 Materials

### 3.2.2 Instruments Used

#### 3.2.2.1 Spin Coater

#### 3.2.2.2 Bruker's X-ray Diffractometer (XRD)

#### 3.2.2.3 UV-Vis. Spectrophotometer

#### 3.2.2.4 Field Emission Scanning Electron Microscopy (FESEM) and Energy Dispersive X-ray Spectroscopy (EDX)

#### 3.2.2.5 Thermogravimetric Analysis (TGA)

#### 3.2.2.6 Fourier Transform Infrared Spectroscopy (FTIR)

#### 3.2.2.7 Atomic Force Microscopy (AFM)

#### 3.2.2.8 LCR Meter

#### 3.2.2.9 Keithley 2400 SMU

#### 3.2.2.10 Glove Box

#### 3.2.2.11 X-ray Photoelectron Spectroscopy (XPS)

### 3.2.3 Perovskite Nanocubes Synthesis

### 3.2.4 Device Fabrication

## **3.3 Characterization**

## **3.4 Result and Discussions**

### 3.4.1 X-Ray Crystallography

### 3.4.2 Optical Spectroscopy

### 3.4.3 X-ray Photoelectron Spectroscopy (XPS)

### 3.4.4 Thermo-Gravimetric (TGA) and Fourier Transform Infrared Radiation (FTIR)

### 3.4.5 Field Emission Scanning Electron Microscopy (FESEM), Energy Dispersive Spectroscopy (EDS) and Atomic Force Microscopy (AFM)

### 3.4.6 Complex Impedance Spectroscopy (CIS) Analysis

### 3.4.7 Dielectric Properties Study

### 3.4.8 Study of Electric Modulus

3.4.9 Study of Electrical Conductivity

3.4.10 Analysis of Schottky Device Characterization

### **3.5 Conclusions**

### **3.6 References**

### 3.1 Introduction

In the earlier chapter, we discussed the basic operating principles of perovskite devices, including various charge injection and transport models, as well as factors like trap concentration and types of traps that influence the charge conduction process in these devices. We also emphasized the importance of lead-free perovskites. In this chapter, we will focus on lead-free  $\text{CH}_3\text{NH}_3\text{SnI}_3$ , covering its synthesis, characterization, and application in forming a Schottky device. Additionally, we will analyse the charge transport to evaluate the device's performance.

In this work, we synthesized lead-free, tin-based  $\text{CH}_3\text{NH}_3\text{SnI}_3$  perovskite using a modified method in an  $\text{N}_2$ -atmospheric glove box via a solution processing technique, which is commonly used for synthesizing perovskite nanoparticles [1,2]. During the reactions, some  $\text{Sn}^{4+}$  ions formed due to the oxidation of tin. To convert these  $\text{Sn}^{4+}$  ions to  $\text{Sn}^{2+}$ , we added 5 mol% of Sn nanopowder as a compensator. The synproportionation reaction is  $\text{Sn} + \text{Sn}^{4+} \rightarrow 2\text{Sn}^{2+}$ . Literature also reports that using pyrazine complexes during synthesis can reduce the oxidation of the sample. Therefore, we added 5 mol% of pyrazine complexes during synthesis to obtain a high-quality sample.

The structure and surface features of this perovskite were characterized using physicochemical techniques. A comprehensive investigation, including impedance analysis, frequency-dependent dielectric analysis, and AC and DC conductivity analysis, was carried out for the first time on nano-cubic  $\text{CH}_3\text{NH}_3\text{SnI}_3$  perovskite material. A Schottky device was fabricated using an ITO/Perovskite/Al sandwich structure. The electrical charge conduction behaviour of the device in terms of conductivity ( $\sigma$ ), ideality factor ( $\eta$ ), barrier height ( $\phi_b$ ), and series resistance ( $R_s$ ) were investigated using thermionic emission theory (TE) and the Cheung method. Bulk transport parameters were also studied using the  $\ln I$  vs.  $\ln V$  plot.

### 3.2 Experimental Section

#### 3.2.1 Materials

$\text{SnI}_2$  (anhydrous, 99.99% purity),  $\text{CH}_3\text{NH}_3\text{I}$  (98% purity), Sn nanopowder and pyrazine were purchased from Sigma Aldrich, and a few solvents like Dimethylformamide (DMF), n-Hexane, Oleic Acid and ethanol were purchased from Merck (India), tert-butanol, n-Octylamine (>98.0%), were purchased from TCI. All the chemicals were used without further purification.

The deionised water used in the experiment was collected from the departmental Milli(Q) water plant.

### 3.2.2 Instruments Used

#### 3.2.2.1 Spin Coater

A spin coating unit is a device used to apply uniform thin films to flat substrates shown in **Figure 3.1**. In this research work, I used the EZspin-A1 from Apex Instruments for spin coating. The EZspin-A1 is a highly reliable and precise spin coating unit designed for uniform thin-film deposition. It operates by placing a small amount of coating solution on the substrate, which is then rapidly spun to spread the solution evenly across the surface due to centrifugal force. The speed and duration of the spin can be finely controlled to achieve the desired film thickness and uniformity. This unit is particularly suited for fabricating perovskite films, ensuring consistent and high-quality coatings essential for device performance.



**Figure 3.1: Spin coating setup for development of thin film.**

#### 3.2.2.2 Bruker's X-ray Diffractometer (XRD)

XRD systems are advanced instruments used in material science to analyse the crystallographic structure of materials. The working principle involves directing X-rays at a material sample and measuring the intensity and angle of the X-rays that are diffracted by the crystal lattice within the sample. In Bruker's instruments it operates by directing X-rays, with a wavelength of  $1.5406 \text{ \AA}$ , at a powdered/film sample (**Figure 3.2(a)**). As the X-rays interact with the crystal lattice, they are diffracted at specific angles, creating a diffraction pattern unique to the material's atomic structure. The resulting data is used to identify phases, determine crystallite size, and assess structural properties. In my research, all XRD measurements were performed

using the Bruker D-8 Advance, complemented by high-resolution data from the PETRA III beamline P 2.2 at DESY, Germany, with a shorter wavelength of 0.2074 Å. This combination of instruments provides comprehensive and precise crystallographic information, essential for the development and characterization of advanced materials. **Figure 3.2(b)** shows the digital photograph of the Bruker D-8 Advance diffractometer used in our study.

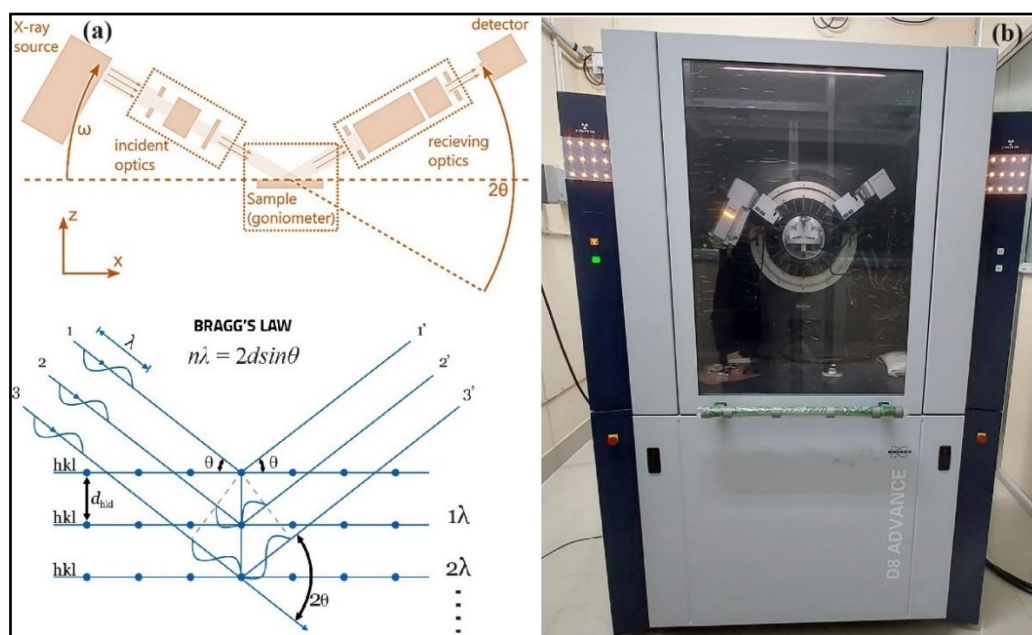


**Figure 3.2: (a) Components of a diffractometer (b) schematic diagram of working of X-ray diffraction (XRD) (c) displays the X-ray powder diffractometer (Bruker D 8 Advance)**

### 3.2.2.3 UV-Vis. Spectrophotometer

UV-Vis. spectrophotometer is a widely used analytical technique in material science for investigating the optical properties of materials, particularly thin films. This method involves measuring the absorption and transmission of ultraviolet and visible light by a sample. In the case of the SHIMADZU Ultraviolet-Visible spectrophotometer (UV-1900, **Figure 3.3**) used in this work, the instrument directs a beam of light across the UV-Vis spectrum (typically 190-1100 nm) through the sample. The spectrophotometer then detects the amount of light absorbed or transmitted at each wavelength.

The working mechanism involves a light source that emits a broad spectrum of UV and visible light. This light passes through a monochromator, which isolates individual wavelengths. The selected wavelength light then passes through the sample, and the detector measures the

intensity of light that passes through. The difference in intensity between the incident light and the transmitted light is used to calculate the absorbance.



**Figure 3.3: Shows the digital image of UV-Vis spectrophotometer**

In material science, UV-Vis. spectroscopy is essential for determining the optical band gap of semiconductors, analyzing the composition and quality of thin films, and studying the electronic transitions within materials. It helps in understanding the interaction of light with the material, which is critical for applications in photovoltaics, sensors, and optoelectronic devices. Using the SHIMADZU UV-1900, precise measurements of thin films can be conducted to evaluate their optical properties, aiding in the development and optimization of new materials.

#### **3.2.2.4 Field Emission Scanning Electron Microscopy (FESEM) and Energy Dispersive X-ray Spectroscopy (EDX)**

FESEM and EDX are essential tools in material science for detailed surface and compositional analysis of samples. FESEM, specifically the FEI INSPECT F50 model, operates by emitting a focused beam of high-energy electrons from a field emission source onto the surface of a sample. This interaction produces secondary and backscattered electrons as shown in **Figure 3.4(a)**, which are collected to form highly detailed images with superior resolution and depth of field, allowing for the examination of surface morphology and microstructure. In my research, the sample was prepared on a glass slide and coated with a thin layer of gold using the Quorum Q150R ES coating system to enhance conductivity and imaging quality. The digital image of laboratory FESEM instruments is shown in **Figure 3.4(b)**.

EDX, using the Bruker Quantax 200 detector, complements FESEM by providing elemental analysis of the sample. As the electron beam from the FESEM interacts with the sample, it excites atoms within the material, causing them to emit characteristic X-rays. The EDX detector captures these X-rays and generates a spectrum that identifies and quantifies the elemental composition of the sample.

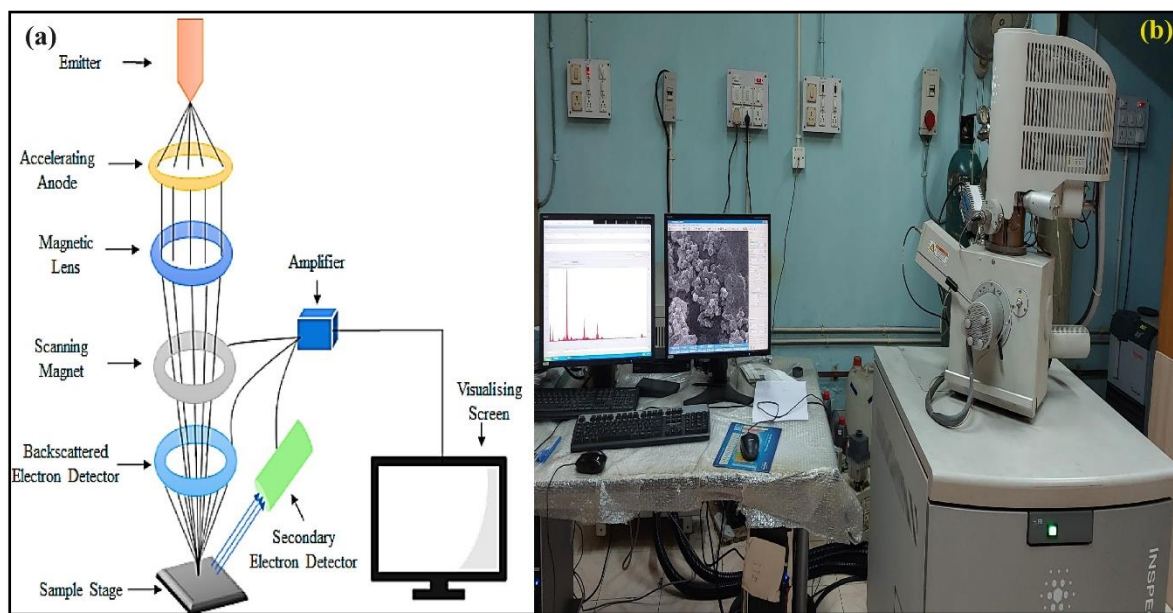


**Figure 3.4: (a) Components of a FESEM (b) digital image of FESEM FEI INSPECT F50**

Together, FESEM and EDX offer comprehensive insights into both the structural and compositional aspects of materials, making them invaluable for research in material science, including the development and analysis of new materials, quality control, and failure analysis.

### 3.2.2.5 Thermogravimetric Analysis (TGA)

TGA is a technique used to measure the change in mass of a material as it is heated over time. The NETZSCH TGA instrument employed in our laboratory conducts this analysis by precisely heating a sample in a controlled atmosphere while continuously recording its weight. The sample is placed on a high-precision balance inside a furnace, and the temperature is increased at a predetermined rate. As the temperature rises, the material undergoes physical and chemical changes, such as decomposition, oxidation, or loss of volatile components, which result in weight changes.

The working mechanism of TGA involves heating the sample in either an inert (e.g., nitrogen or argon) or reactive (e.g., oxygen) atmosphere to induce these changes. The weight loss or gain is plotted against temperature or time, producing a thermogram. This thermogram helps identify the temperatures at which specific reactions occur, the stability of the material, the composition of multi-component systems, and the kinetics of thermal decomposition.

### 3.2.2.6 Fourier Transform Infrared Spectroscopy (FTIR)

FTIR is an analytical technique used to identify and study chemical bonding and molecular structures by measuring the absorption of infrared radiation by a sample. The PerkinElmer FTIR spectrometer used in our research measured the FTIR spectrum of the sample in the range of  $780\text{--}3500\text{ cm}^{-1}$ . The working mechanism of FTIR involves directing a beam of infrared light at the sample. The sample absorbs specific wavelengths of this light, causing molecular vibrations that correspond to the chemical bonds within the material. The spectrometer detects the transmitted or reflected light and uses a mathematical Fourier transform to convert the raw data into an infrared spectrum. This spectrum displays the intensity of absorbed light as a function of wavelength, revealing characteristic absorption peaks that correspond to different functional groups and bonding environments within the sample.

### 3.2.2.7 Atomic Force Microscopy (AFM)

AFM is a high-resolution imaging technique used to measure surface topography at the nanometer scale.



**Figure 3.5: Shows laboratory AFM setup to measure film roughness**

**Figure 3.5** shows a laboratory setup for AFM. In our research, we utilized the Nanosurf AFM equipped with a Dyn190AI cantilever to analyse and measure the roughness of the sample. The working mechanism of AFM involves scanning a sharp tip attached to a flexible cantilever over the sample surface. As the tip interacts with the surface, forces between the tip and the sample cause deflections in the cantilever. These deflections are detected by a laser beam reflected off the back of the cantilever onto a position-sensitive photodetector. By maintaining a constant interaction force (in contact mode) or by measuring oscillation changes (in tapping or non-contact mode), the AFM can generate a detailed topographical map of the surface.

### 3.2.2.8 LCR Meter

An LCR meter is an electronic instrument used to measure the inductance (L), capacitance (C), and resistance (R) of electronic components and materials. In our work, we used the Hioki LCR Q meter (IM3536) to measure the impedance spectra of samples.

The working mechanism of an LCR meter involves applying an alternating current (AC) signal to the sample and measuring the resulting voltage and current. The LCR meter then calculates the impedance (Z) and phase angle ( $\theta$ ) from these measurements. The impedance is a complex quantity that encompasses resistance (real part) and reactance (imaginary part), which is determined by the inductance and capacitance of the sample. By varying the frequency of the AC signal, the LCR meter can produce an impedance spectrum, showing how impedance changes with frequency.

### 3.2.2.9 Keithley 2400 SMU

The Keithley 2400 Source Measure Unit (SMU) is a versatile instrument used for precision electrical measurements, providing both sourcing and measuring capabilities in a single device. In our research, we utilized the Keithley 2400 SMU to perform accurate electrical characterization of our samples. **Figure 3.6** shows the laboratory Keithley 2400 SMU setup used to measure electrical characterization.

The working mechanism of the Keithley 2400 SMU involves its ability to function as both a voltage source and a current source, as well as a voltmeter and an ammeter. It can source and measure current and voltage simultaneously, allowing for comprehensive analysis of electrical properties.



**Figure 3.6: Keithley 2400 SMU with computer interface for the electrical measurements**

The SMU can be programmed to sweep through a range of voltages or currents, while continuously measuring the corresponding current or voltage, respectively. This dual functionality enables detailed characterization of current-voltage (I-V) relationships, resistance, and other electrical parameters.

### 3.2.2.10 Glove Box

A glove box is a sealed enclosure with built-in gloves, allowing researchers to handle materials in a controlled atmosphere, typically inert gases like nitrogen or argon, to prevent contamination or oxidation.



**Figure 3.7: Shows self-designed laboratory glove box setup for Sn-based perovskite synthesis**

In our research, a self-designed glove box equipped with a nitrogen ( $N_2$ ) cylinder was used to synthesize lead-free tin-based perovskites. This setup is critical to ensure the integrity of the samples and prevent oxidation of tin during synthesis.

The glove box setup of our laboratory is shown in **Figure 3.7**. The importance of using a glove box in material science, particularly for synthesizing lead-free tin-based perovskites, lies in its ability to provide a controlled environment free from oxygen and moisture. This ensures the purity and stability of the synthesized materials, allowing for accurate characterization and reliable results. By conducting the synthesis process in a glove box, researchers can achieve precise control over experimental conditions, leading to the development of high-quality materials with desired properties.

### 3.2.2.11 X-ray Photoelectron Spectroscopy (XPS)

XPS is an analytical technique used to investigate the surface chemistry of materials. It provides quantitative analysis of the elemental composition, empirical formula, chemical state, and electronic state of the elements within a material. In this work, we employed the Thermo Scientific K-Alpha XPS with a monochromatic Al- $K\alpha$  X-ray source (1486.6 eV) to analyse the sample. The working mechanism of XPS involves several key components, as illustrated in the **Figure 3.8**. The X-ray source, an aluminum anode, is bombarded with high-energy electrons (20 kV), producing Al- $K\alpha$  X-rays.

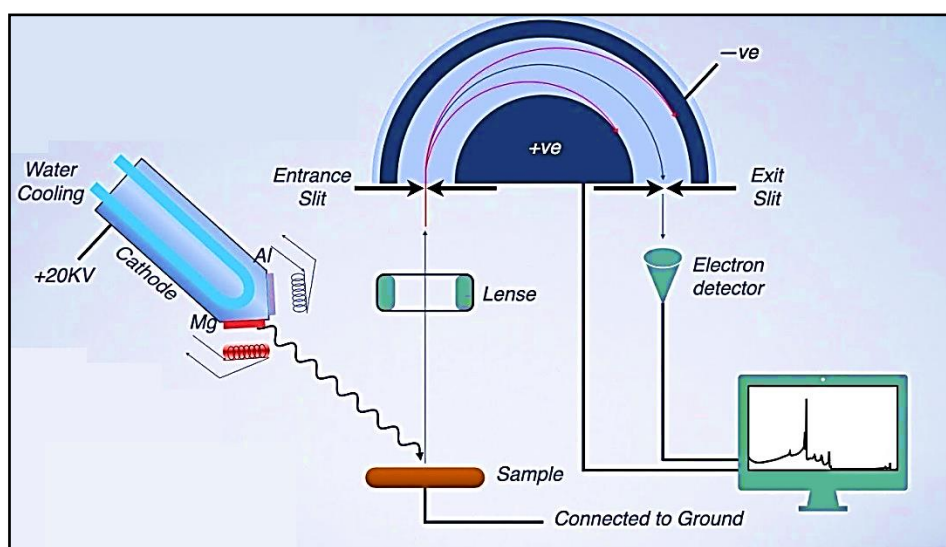


**Figure 3.8:** Shows depicts a schematic diagram of XPS with different parts

These X-rays are directed at the sample, causing the emission of photoelectrons from the surface atoms due to the photoelectric effect. The sample is mounted on a grounded stage to ensure electrical stability during the measurement. The emitted photoelectrons are then collected by an electron lens system, which focuses them into an energy analyser. The energy analyser, typically a hemispherical sector analyser, measures the kinetic energy of the photoelectrons. This kinetic energy is related to the binding energy of the electrons in the atoms, which is characteristic of specific elements and their chemical states. The analyser's entrance and exit slits help to select and filter the electrons based on their energies.

Once the photoelectrons pass through the energy analyser, they are detected by an electron detector, which counts the number of electrons at each energy level. This information is processed to produce an XPS spectrum, displaying the intensity of detected electrons as a function of their binding energy. Peaks in the spectrum correspond to specific elements and their chemical states within the sample.

XPS is critically important in material science for several reasons. It provides precise elemental and chemical state analysis of the top few nanometres of a material's surface, which is crucial for understanding surface reactions, thin film properties, and material interfaces. This makes XPS invaluable in the development and characterization of advanced materials, including lead-free tin-based perovskites, where controlling surface chemistry is essential for optimizing material performance and stability. The data obtained from XPS analysis help in tailoring material properties for specific applications, ensuring the development of high-quality, reliable materials.

### 3.2.3 Perovskite Nanocubes Synthesis

Methylammonium iodide ( $\text{CH}_3\text{NH}_3\text{I}$ , 158.6 mg, 1 mM) and tin (II) iodide ( $\text{SnI}_2$ , 372.5 mg, 1 mM) were dissolved separately and labelled as solutions A and B, respectively. A magnetic stirrer was used in an  $\text{N}_2$  atmosphere glove box for stirring the individual solutions for 30 min. An oleic phase was prepared by combining 10 ml hexane with 1 ml oleic acid and 0.5 ml n-octylamine in another beaker labelled as C. After an hour, 5 mol% Sn nanoparticle and 5 mol% pyrazines were added to this solution C. Then,  $\text{SnI}_2$  solution was added to solution C. **Figure 3.9(a)** depicts the sequential procedures in schematic form. After a few minutes, solution A was added to the final solution dropwise under rapid stirring. The reaction was continued for 1 hour in the glove box at 75 °C.

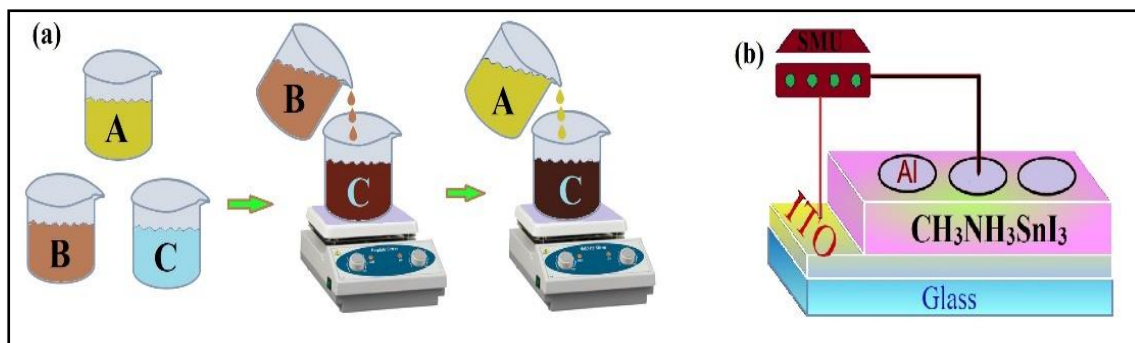


**Figure 3.9: (a) Schematic diagram of  $\text{CH}_3\text{NH}_3\text{SnI}_3$  perovskite preparation, Solution A:  $\text{CH}_3\text{NH}_3\text{I}$ , Solution B:  $\text{SnI}_2$ , Solution C: Oleic phase (b) perovskite Schottky device**

Finally, 5 ml tert-butanol was dropped into the solution to commence demulsification and formation of the nanocrystal. A dark brown precipitate was obtained, which was centrifuged and repeatedly rinsed with degassed ethanol. Finally, the precipitate was dried overnight in a vacuum oven at  $65^\circ\text{C}$ , and black powder was collected.

### 3.2.4 Device Fabrication

The schematic structure of the fabricated ITO/Perovskite/Al device is shown in **Figure 3.9(b)**. The fabrication process began with cleaning the ITO-coated glass substrate using an ultrasonic bath, sequentially with Extran MA 02 (Neutral) solution, deionized water, acetone, and finally 2-propanol, each for 10 minutes. After cleaning, the substrate was dried in a hot air oven at  $90^\circ\text{C}$  for 30 minutes. The contact area of the ITO was then masked with tape. A perovskite precursor solution was prepared by dissolving 15 mg of perovskite powder in  $200\ \mu\text{l}$  of DMF. Subsequently,  $60\ \mu\text{l}$  of this solution was spin-coated onto the ITO at 1500 rpm for 30 seconds to form a thin film. The film was immediately transferred to a hot plate set at  $75^\circ\text{C}$ , where a dark brown layer formed within seconds, indicating the formation of the perovskite film. Finally, pure aluminium was deposited using the plasma deposition method at a pressure of  $1 \times 10^{-6}$  mbar with a shadow mask. The effective area of the devices was approximately  $5 \times 7\ \text{mm}^2$ .

## 3.3 Characterization

The structural analysis of the synthesized perovskite powder was conducted using powder X-ray crystallography (PXRD) on a Bruker D8 SWAX diffractometer with  $\text{Cu-K}\alpha$  radiation (wavelength:  $1.5404\ \text{\AA}$ ), operated at 35 kV and 35 mA at room temperature. To obtain X-ray

diffraction peaks, measurements were taken in the 2-theta range of 20–70° at a scan rate of 0.75°/min, with the sample holder rotating at 10 rpm to ensure comprehensive peak information. The PXRD data were refined using Expo2014 software.

The optical properties of the  $\text{CH}_3\text{NH}_3\text{SnI}_3$  films were measured with a SHIMADZU UV-1900 Ultraviolet-Visible spectrophotometer. X-ray photoelectron spectroscopy (XPS) was performed using a Thermo Scientific K-Alpha spectrometer with a monochromatic Al- $K_\alpha$  source (1486.6 eV). Thermo-gravimetric analysis (TGA) was carried out using a NETZSCH analyser over a temperature range of 26 to 500°C. Chemical bonding was analysed using Fourier-transform infrared spectroscopy (FTIR) on a PerkinElmer spectrometer in the range of 780-3500  $\text{cm}^{-1}$ .

For morphological characterization and surface roughness determination, two films were prepared on a glass slide and a Si-substrate, respectively, following the same process outlined in the device fabrication section. The sample on the glass slide was coated with gold using a Quorum Q150R ES coating system. A field emission scanning electron microscope (FESEM) was used to capture images, and an energy dispersive spectroscopy (EDS) detector (Bruker Quantax, 200) was used for analysis. The roughness of the sample was measured with a Nanosurf atomic force microscope (AFM) using a Cantilever type Dyn190AI.

Impedance spectra were recorded using a Hioki LCR Q meter (IM3536) by placing a perovskite pellet (10 mm in diameter, 1.99 mm thick) between Au electrodes, covering a frequency range of 4 Hz to 8 MHz. The complex impedance spectra were analysed to study the dielectric response, impedance characteristics, relaxation time, electric modulus, AC conductivity, loss tangent, and other properties of the sample.

## 3.4 Result and Discussions

### 3.4.1 X-Ray Crystallography

The structure of perovskite shows crystallinity (**Figure 3.10(a)**) and belongs to the cubic space group Pm-3m symmetry. The Pearson VII function was used to model the profile shape,  $R_p=8.98$  and  $R_{wp}=10.59$ . The experimental, calculated, and the difference between experimental and calculated PXRD from refinement shows that the high-quality Sn-perovskite has been synthesised, and the corresponding ball and stick structure visualisation after refinement of the as-synthesised perovskite generated from the Vesta software has also been shown (**Figure 3.10(b)**). All of the peaks are well-matched with the COD ID #7015448 with the space group

(Pm-3m) symmetry. The calculated and experimental lattice parameters of the cubic perovskite were  $a=b=c= 6.23683$ ,  $\alpha=\beta=\gamma= 90^\circ$  and  $a=b=c= 6.23951$ ,  $\alpha=\beta=\gamma= 90^\circ$ . The PXRD refinement results demonstrate an excellent agreement in the crystalline phase formation of the sample.

The crystalline size (D) of the sample has been estimated from the following Scherrer's formula [3],

$$D = \frac{0.94\lambda}{\beta \cos \theta} \quad (3.1)$$

Where D is the particle size,  $\lambda$  is the wavelength of the used X-Ray,  $\beta$  is the Full width half maximum (FWHM), and  $\theta$  is the angle between the incident and the scattered X-Ray.

The dislocation density ( $\delta$ ) is the length of dislocation lines per unit volume of the crystal and has been calculated using the following relation,

$$\delta = \frac{1}{D^2} \quad (3.2)$$

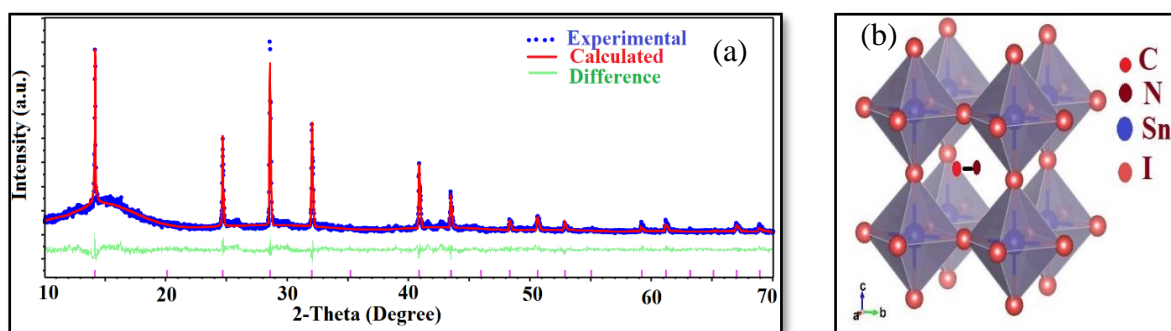


**Figure 3.10: (a) PXRD refinement of  $\text{CH}_3\text{NH}_3\text{SnI}_3$  perovskite sample in the range of  $2\theta$  from  $10^\circ$  to  $70^\circ$  (b) refined ball and stick structure obtained using vesta software**

The value of strain ( $\varepsilon$ ) has been evaluated by using the following relationship,

$$\varepsilon = \left[ \frac{\lambda}{D \cos \theta} - \beta \right] \times \frac{1}{\tan \theta} \quad (3.3)$$

The lattice spacing (d) of the crystal has been calculated from Bragg's formula

$$d = \frac{\lambda}{2 \sin \theta} \quad (3.4)$$

The lattice parameter has been calculated by the following expression

$$\frac{1}{d^2} = \frac{h^2 + k^2 + l^2}{a^2} \quad (3.5)$$

Where h, k, and l are representing the lattice plane. The estimated values of the above parameter have been tabulated in **Table 3.1**. The reproducibility of the sample has been checked three times.

**Table 3.1: XRD analysis parameters of the perovskite sample**

Average particle size (nm)	Dislocation density ( $\delta$ ) ( $\text{nm}^{-2}$ )	Strain ( $\epsilon$ ) ( $\text{lin}^{-2}/\text{m}^{-4}$ )	Lattice parameter ( $a=b=c$ ) ( $\text{\AA}$ )
62.90	$2.52 \times 10^{14}$	$6.12 \times 10^{-3}$	6.23951

### 3.4.2 Optical Spectroscopy

A thin film of  $\text{CH}_3\text{NH}_3\text{SnI}_3$  was prepared on a cleaned glass substrate to vide experimental section and an optical spectrum are collected (**Figure 3.11**) in the 500-1100 nm range.

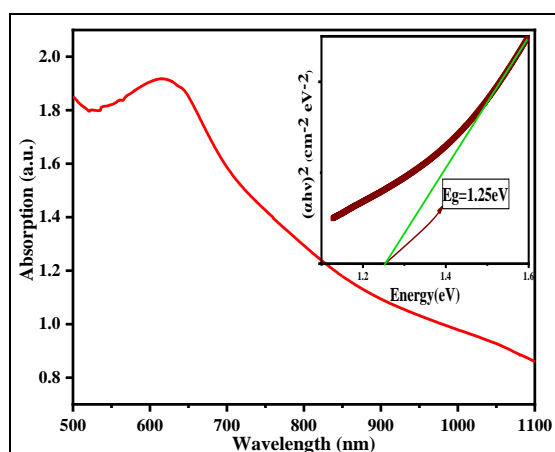


**Figure 3.11: Solid-state absorption spectra of  $\text{CH}_3\text{NH}_3\text{SnI}_3$  perovskite thin film in the range of 500-1100 nm. The inset represents Tauc's plot**

The optical band was calculated by using Tauc's equation (**Equation 3.6**).

$$(\alpha h\nu)^\gamma = K(h\nu - E_g) \quad (3.6)$$

Where the exponent  $\gamma$  is the electron transition process-dependent constant and  $\alpha$ ,  $E_g$ ,  $h$ , and  $\nu$  stand for absorption coefficient, bandgap energy, Planck's constant, and frequency of light, respectively.  $K$  is a proportionality constant, which was considered as 1 for the ideal case. To estimate the direct optical bandgap, the value of the exponent  $\gamma$  in the aforementioned equation was taken to be = 2. The direct optical band gap ( $E_g$ ) of the  $\text{CH}_3\text{NH}_3\text{SnI}_3$  perovskite film was

1.25 eV based on extrapolation of the linear region of the plot  $(\alpha h\nu)^2$  vs.  $h\nu$  displayed in the inset of **Figure 3.11**.

### 3.4.3 X-ray Photoelectron Spectroscopy (XPS)

XPS measurements were used to demonstrate that, the addition of Sn powder during synthesis, suppressed the oxidation state of Sn in the perovskite sample. **Figure 3.12** depicts XPS measurements of the as-synthesised perovskite sample and the sample exposed to air for 25 minutes until the experiment was completed. The HRXPS spectra of the as-prepared material (**Figure 3.12(a)**) shows two sharp peaks around 487 eV and 495.4 eV of binding energy, which corresponds to Sn 3d<sub>5/2</sub> and Sn 3d<sub>3/2</sub> orbitals, respectively [4]. The peaks are mainly composed of one type of tin, indicating the sole presence of the +2-oxidation state of Sn.

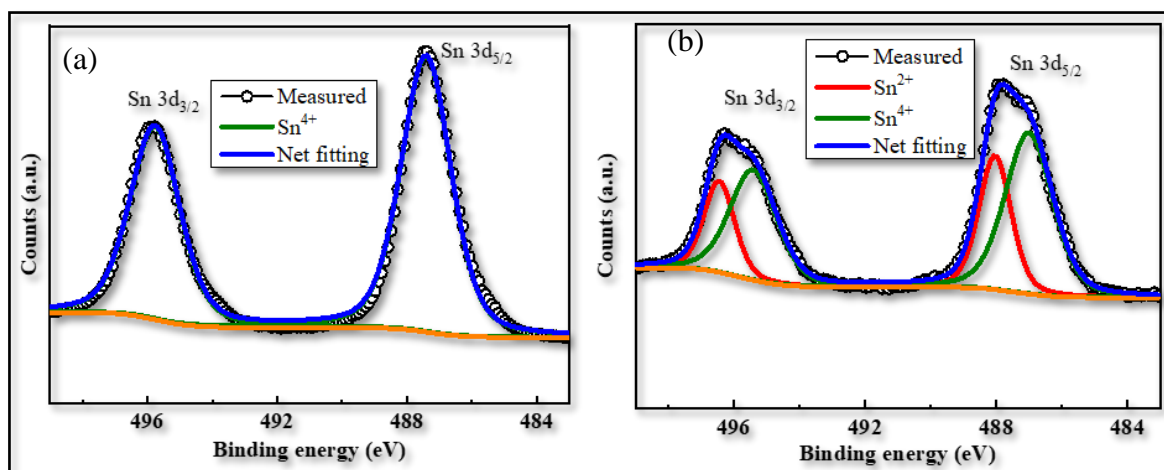


**Figure 3.12: X-ray photoelectron spectrum of perovskite films (a) as prepared (b) after exposure in the air till experiments were taking place**

The air-exposed sample (**Figure 3.12(b)**) seems to have a broader peak for Sn 3d<sub>5/2</sub> and 3d<sub>3/2</sub> orbitals, which could be deconvoluted further. The Sn 3d<sub>5/2</sub> peak can be deconvoluted into two peaks, 487 eV and 488 eV, suggesting the presence of both +2 and +4 oxidation states of Sn. The atomic percentage of these two states is determined to be 64% and 36%, respectively.

### 3.4.4 Thermo-Gravimetric (TGA) and Fourier Transform Infrared Radiation (FTIR)

The thermo-gravimetric analysis of CH<sub>3</sub>NH<sub>3</sub>SnI<sub>3</sub> perovskite was taken from 26 °C to 500 °C at a scan rate of 5 °C/min under N<sub>2</sub> flow. The thermogram (**Figure 3.13(a)**) shows different

regions of weight loss and a notable weight reduction was observed from 143 °C to 232.75 °C. Below 143 °C, there is a weight loss of about 7%, which can be attributed to the volatilization of the moisture absorbed by the sample. No thermal deterioration of the sample was noticed in this stage. In the subsequent stage, a weight loss of 85% was found between 143 and 232.75 °C. This can be interpreted in such a way that at about 143 °C, the perovskite began to disintegrate due to decomposition. The perovskite degrades into  $\text{CH}_3\text{NH}_3\text{I}$  and  $\text{SnI}_2$ . The produced  $\text{CH}_3\text{NH}_3\text{I}$  sublimates rapidly since the sublimation temperatures of  $\text{CH}_3\text{NH}_3\text{I}$  and  $\text{I}$  are roughly 150 °C and 184 °C, respectively. A final residue of 8% was produced when  $\text{SnI}_2$  was sublimated at high temperatures. The final residue is known as  $\text{SnO}_2$  [5,6]. The corresponding first derivative of the whole decomposition at 143 °C and 232.75 °C can be seen in the inset. The former can be related to the volatilization of water and the breakdown of the tiny quantities of remaining  $\text{CH}_3\text{NH}_3\text{I}$  from the synthesising process on the surface, while the latter continuous weight loss can be attributed to perovskite sample disintegration.

In comparison to lead-based perovskite [7], tin-based perovskite has low thermal stability. According to the literature,  $\text{CH}_3\text{NH}_3\text{PbI}_3$  begins to decay beyond a temperature of 250 °C, but in the case of the investigated tin-based sample, about 85% of it degraded between 143 and 232 °C. However, both materials' stability temperature ranges are enough for the development and operation of optoelectronic devices. The relative transmittance spectra of  $\text{CH}_3\text{NH}_3\text{SnI}_3$  perovskite in the range of 780 to 3500  $\text{cm}^{-1}$  are shown in **Figure 3.13(b)** to analyse the bond formation in the sample. Most of the vibrational peaks were observed due to the organic methyl ammonium function ( $\text{CH}_3\text{NH}_3$ ). The two peaks at 3101.62  $\text{cm}^{-1}$  and 2889.26  $\text{cm}^{-1}$  are caused by symmetric stretching of the N-H bond [8].

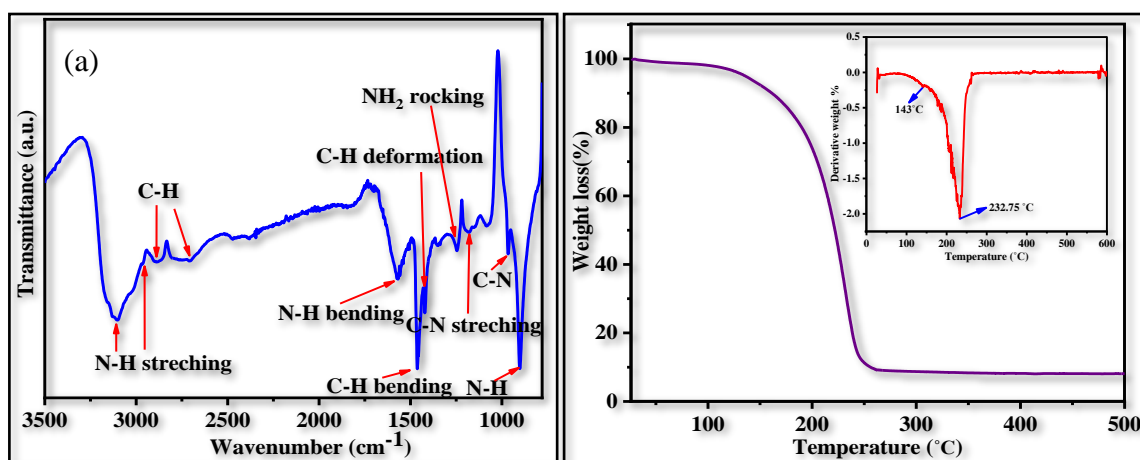


**Figure 3.13:** (a) TGA curve (b) FTIR of the  $\text{CH}_3\text{NH}_3\text{SnI}_3$  perovskite sample

The weak peaks at  $2711.05\text{ cm}^{-1}$  can be assigned to H-C-N stretching vibration, and the peak at  $1568.69\text{ cm}^{-1}$  corresponds to the in-plane bending vibration of N-H. The peaks at  $1462.08\text{ cm}^{-1}$  and  $1420.01\text{ cm}^{-1}$  correspond to the in-plane bending and deformation vibrations of C-H. The weak peaks at  $1246.11\text{ cm}^{-1}$ ,  $1179.52\text{ cm}^{-1}$  and  $965.01\text{ cm}^{-1}$  are mainly due to the weak  $\text{NH}_2$  rocking vibration, and amine stretching generated by the strong force between the C-N bonds and C-N bending, respectively [9]. Finally, the peak at  $906\text{ cm}^{-1}$  is caused by the N-H wagging vibration produced by the shift in H-bonding.

### 3.4.5 Field Emission Scanning Electron Microscopy (FESEM), Energy Dispersive Spectroscopy (EDS) and Atomic Force Microscopy (AFM)

The thin film of  $\text{CH}_3\text{NH}_3\text{SnI}_3$  was inserted in the vacuum chamber of the instruments immediately after preparation to perform FESEM imaging.

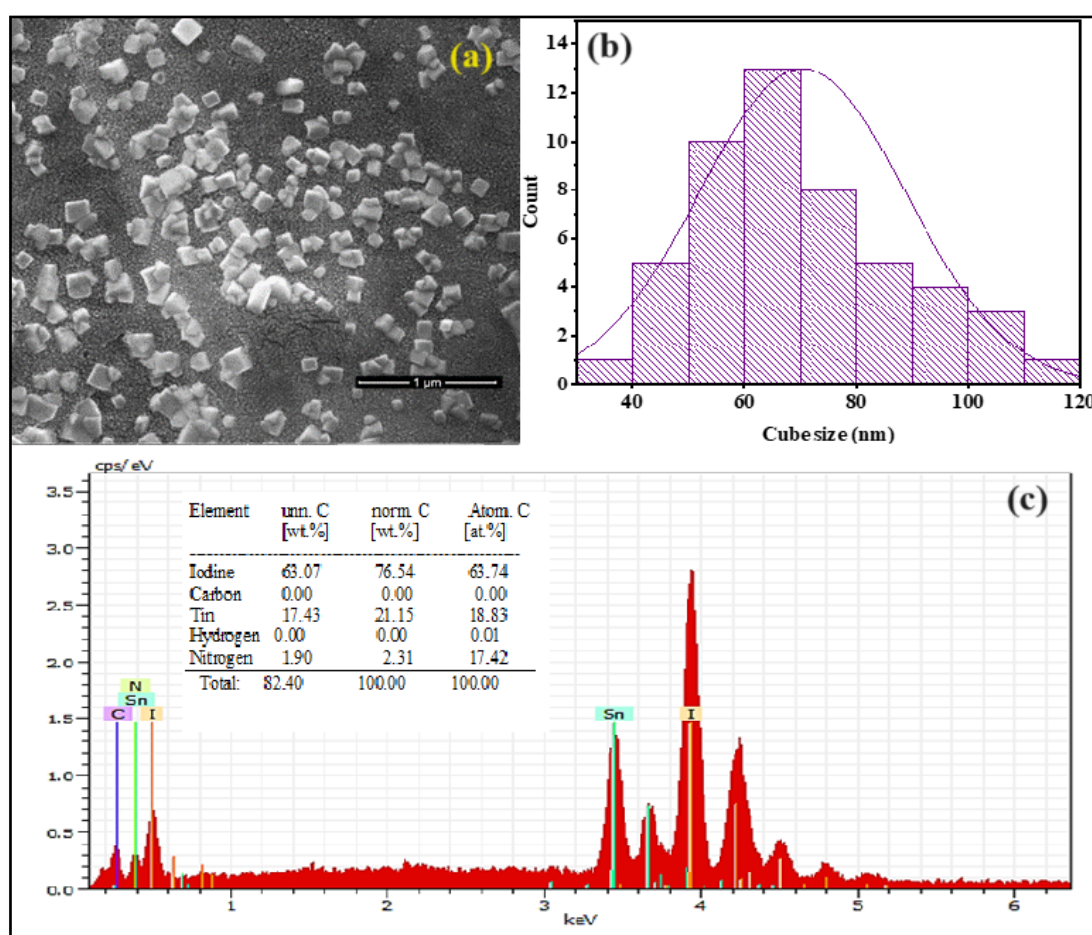


**Figure 3.14:** (a) FESEM images of  $\text{CH}_3\text{NH}_3\text{SnI}_3$  films processed using spin coating technique (b) cube size distribution shows the maximum particle size lies between 60 to 70 nm. (c) EDX spectrum for methylammonium tin iodide ( $\text{CH}_3\text{NH}_3\text{SnI}_3$ ) perovskite.

The experiment was carried out with an acceleration voltage of 20 kV and a spot size of 3.0. **(Figure 3.14(a))** shows a morphological image of the material. This image confirms the cube-like crystal structure as defined by the PXRD refinement result. The Gaussian distribution of the size of the cubic perovskite has been depicted in **Figure 3.14(b)**, with the x- and y-axes denoting particle size and number, respectively. The mean size of the particles of the sample is 68.95 nm. This result was quite nearest to the result obtained from the XRD analysis. Again, an EDX of the sample was performed to ensure the material's elemental composition (**Figure 3.14(c)**).

It can be seen from the inset of **Figure 3.14(c)** that, the elements N, Sn, and I of  $\text{CH}_3\text{NH}_3\text{SnI}_3$  exist in stoichiometric proportion (1:1.08:3.64). However, the dispersive energies for carbon and hydrogen elements were not obtained because these elements were forbidden in the instrument. However, according to the elemental composition, the organic-inorganic  $\text{CH}_3\text{NH}_3\text{SnI}_3$  perovskite was formed successfully.

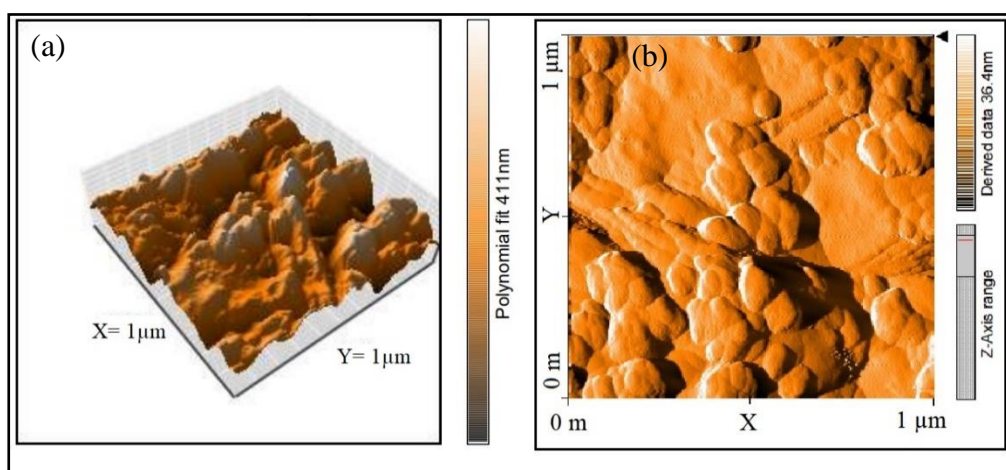


**Figure 3.15: Atomic force microscopy of the thin film prepared on a silicon substrate (a) Z-axis -scan forward line fit (b) Z-axis-scan backwards derived data.**

Atomic force microscopy (AFM) was performed on a thin film in addition to FESEM measurement to quantify the roughness of the film. **Figure 3.15** depicts a forward and backward z-axis scan of a  $1 \times 1 \mu\text{m}^2$  sample. The root-mean-square (RMS) and arithmetic roughness of the perovskite thin film determined by AFM is around 79.29 nm and 53.313 nm, respectively, indicating that the perovskite thin film is quite smooth. This shows that the contact layers of the fabricated device have developed properly.

### 3.4.6 Complex Impedance Spectroscopy (CIS) Analysis

The CIS spectra (**Figure 3.16(a)**) were utilised to explain the independent effects of grain and grain boundaries on net impedance as well as the electrical and ionic transport within the perovskite material. Semi-circles are typically used in Cole-Cole plots to show how the overall impedance is related to the grain, grain border, and electrode-sample interface.

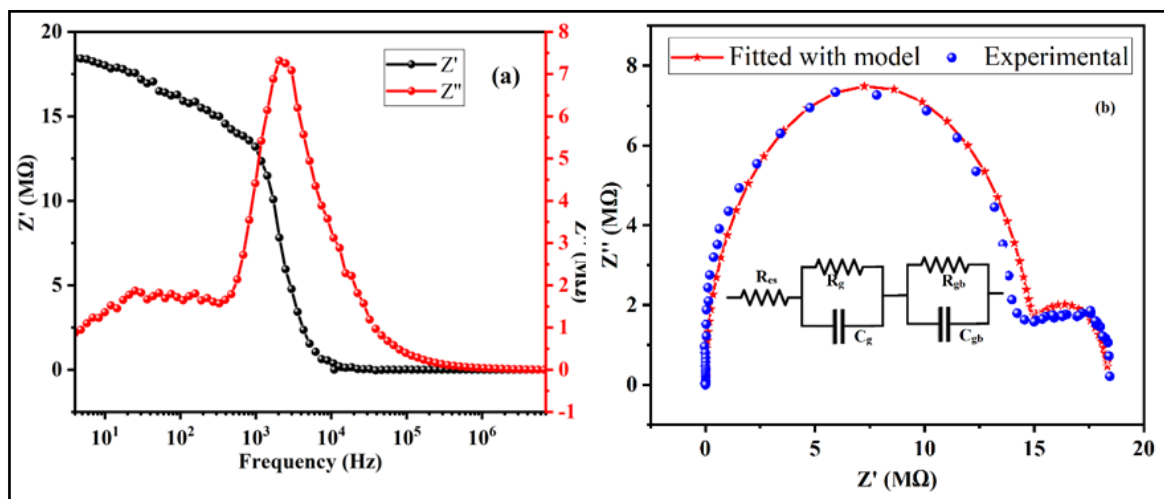


**Figure 3.16:** (a) Frequency-dependent of  $Z'(\omega)$  &  $Z''(\omega)$  plot (b) Cole-Cole or Nyquist plot of  $\text{CH}_3\text{NH}_3\text{SnI}_3$  perovskite at room temperature, inset of (b) represents the equivalent circuit model of the corresponding plot.

**Figure 3.16(b)** shows the  $\text{CH}_3\text{NH}_3\text{SnI}_3$  perovskite sample's Cole-Cole plot or Nyquist plot at room temperature. Since there are two consecutive suppressed semicircles obtained, the sample must have non-Debye-type dipolar relaxation [10].

The first semicircle (of larger radius) appeared in the Nyquist plot as a combinational contribution of the grain and grain boundary, while the second semicircle (of smaller radius) arose as a result of the influence of the electrode-material contact on total resistance. Therefore, the equivalent circuit for this lead-free  $\text{CH}_3\text{NH}_3\text{SnI}_3$  perovskite consists of series and parallel-arranged capacitance ( $C_b$ ,  $C_{gb}$ ) and resistance ( $R_{es}$ ,  $R_b$ ,  $R_{gb}$ ) (**Figure 3.16(b)**), where  $R_{es}$ ,  $R_b$ ,  $R_{gb}$ ,  $C_b$  and  $C_{gb}$  denote electrode-material interface resistance, grain resistance, grain boundary resistance, grain capacitance and grain boundary capacitance, respectively.

The EC lab software was used to fitting this CI spectrum. **Table 3.2** shows the obtained data for the individual factors' contribution to resultant impedance from the electrode material contact, grain, and grain boundary.

**Table 3.2: The values of equivalent resistances and capacitances obtained from the fitted model.**

$R_{es}$ ( $\Omega$ )	$R_g$ ( $M\Omega$ )	$R_{gb}$ ( $M\Omega$ )	$C_g$ (pF)	$C_{gb}$ (nF)	The goodness of the fitting factor
274	14.87	3.53	4.432	1.182	0.0952

It is possible to express the frequency-dependent complex impedance  $Z$  as

$$Z(\omega) = Z'(\omega) + jZ''(\omega) \quad (3.7)$$

Where  $Z'(\omega)$  and  $Z''(\omega)$  represent the real and imaginary part of the total impedance  $Z$  respectively and were given by the following **Equation 3.8** and **3.9**.

$$Z'(\omega) = R_{es} + \frac{R_g}{1+(\omega R_g C_g)^2} + \frac{R_{gb}}{1+(\omega R_{gb} C_{gb})^2} \quad (3.8)$$

$$Z''(\omega) = \frac{\omega C_g R_g^2}{1+(\omega R_g C_g)^2} + \frac{\omega C_{gb} R_{gb}^2}{1+(\omega R_{gb} C_{gb})^2} \quad (3.9)$$

Here,  $R_{es}$ ,  $R_g$  and  $R_{gb}$ ,  $C_g$  and  $C_{gb}$  carry the meaning as previously ascribed. From the  $Z'$ -axis intercept to the high-frequency side of the Cole-Cole plot ( $Z'$  vs.  $Z''$ ), the bulk resistance ( $R_b$ ) of the sample was calculated and is estimated to be  $14.87 M\Omega$ . Using this value, the DC conductivity was approximated as  $1.76 \times 10^{-6} S/m$  with the help of **Equation 3.10** [11].

$$\sigma_{dc} = \frac{l}{R_b \cdot A} \quad (3.10)$$

where the pallet's thickness and cross-sectional areas are  $l$  and  $A$ , respectively.

### 3.4.7 Dielectric Properties Study

The understanding of dielectric relaxation, polarisation reactions, and electrical conductivity was obtained from the investigation of complex dielectric behaviour. It is possible to express the sample's complicated dielectric nature by **Equation 3.11**.

$$\varepsilon^*(\omega) = \varepsilon'(\omega) - j\varepsilon''(\omega) \quad (3.11)$$

Where  $\varepsilon'(\omega)$  and  $\varepsilon''(\omega)$  represent the frequency-dependent dielectric constant and dielectric loss respectively. The value of the  $\varepsilon'(\omega)$  is related to the amount of energy stored in the sample whereas the  $\varepsilon''(\omega)$  stands for the amount of energy dissipated from the sample.

$$\varepsilon'(\omega) = \frac{Z''}{\omega C_0 (Z'^2 + Z''^2)} \quad (3.12)$$

$$\varepsilon''(\omega) = \frac{Z'}{\omega C_0 (Z'^2 + Z''^2)} \quad (3.13)$$

Where  $C_0$  is the free space capacitance. Using the formula,  $C_0 = \frac{\epsilon_0 A}{l}$ , where,  $\epsilon_0$  is the permittivity in vacuum ( $8.854 \times 10^{-12} \text{ F/m}^{-2}$ ), the estimated value of  $C_0$  is found to be  $4.79 \times 10^{-13} \text{ F}$ . Therefore, frequency-dependent  $\epsilon'(\omega)$  and  $\epsilon''(\omega)$  can be easily obtained using **Equation 3.12** and **3.13**, respectively, (**Figure 3.17(a)**). The figure shows that both  $\epsilon'(\omega)$  and  $\epsilon''(\omega)$  decrease with frequency. Interfacial or electrode polarisation, which plays a crucial role in ionic conduction, regulates the properties of the dielectric constant in the low-frequency domain. The interfacial polarisation and extensive bulk effects from grains both contribute to this whole dielectric behaviour of the sample [12,13]. The variation in the dielectric constant can be explained by Maxwell-Wagner's theory of interfacial polarization in connection with Koop's theory [14–16]. According to this theory, the sample is composed of a quite thick layer of conducting grains that are separated by high resistance grain of boundaries. The interfacial polarisation occurs due to the trapping of charge carriers at the grain boundary. Positive and negative space charges can jump from one point to another due to the presence of defects, traps, and irregularities in the material. As a result, when an electric field is applied, the nucleus of the methylammonium cation ( $\text{CH}_3\text{NH}_3^+$ ) moves toward the nucleus of the inorganic anion. As a consequence, a significant number of oscillating dipoles are developed, which can aggregate and line up at the interface along the direction of the external electric field, as seen in the inset of **Figure 3.17(a)**. Due to this effect of interfacial polarization in the low-frequency zone ( $\omega \ll 1/\tau$ ) the dielectric constant is high which confirms the non-Debye type.

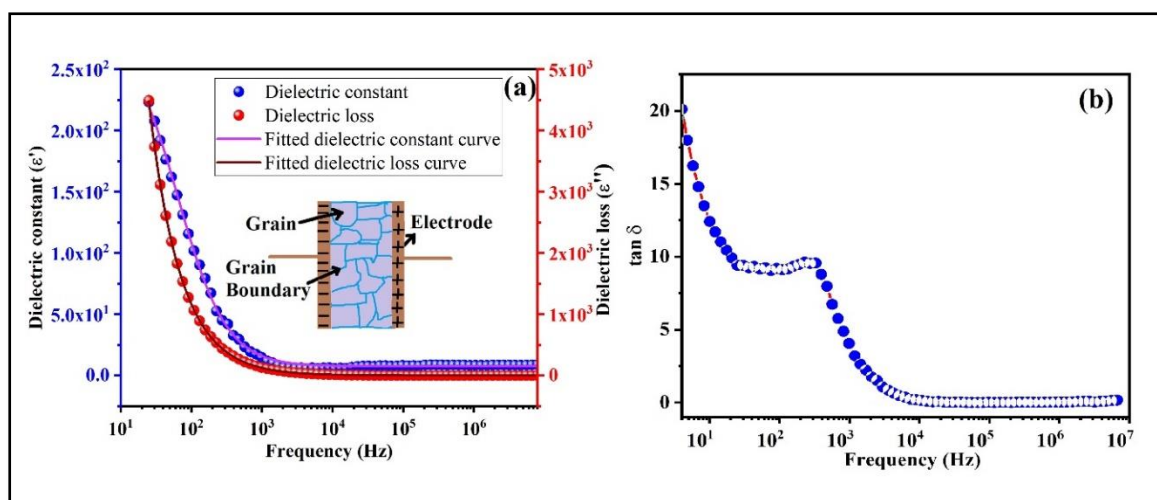


**Figure 3.17:** (a) Dielectric constant (blue) and dielectric loss (red) variation with frequency. The inset of (a) represents the model used to explain the dielectric variation. (b) variation of  $\tan \delta$  with frequency.

However, as frequency increases, dipoles lose their capacity to follow the direction of the applied electric field, causing the dielectric constant to gradually decrease [17]. In the high-frequency zone, the characteristics of the dielectric constant are controlled by electronic and ionic polarisation effects. The value of  $\epsilon'$  for  $\text{CH}_3\text{NH}_3\text{SnI}_3$  perovskite is 233.15 in the low-frequency zone and has decreased by 10.9 as the frequency increased.

As shown in **Figure 3.17(a)**, the value of  $\epsilon''$  also decreases as the frequency increases. According to Koop's theory, the presence of distortions, traps, and contaminants in the sample creates a potential barrier that impedes charge carrier conduction. The charges are thus constrained to the grain boundary in the low-frequency zone under the impact of space charge polarisation. Hence, the charge carriers must expend more energy to overcome the barrier, resulting in a substantial dielectric loss in the low-frequency regime. When operating in the high-frequency region, charge carriers don't require as much energy to jump due to the influence of highly-conducting grains. Therefore, the dielectric loss gradually decreases in the high-frequency zone. From this aspect, the free and space charge conductivity estimate. The measurement results were fitted with the modified Cole-Cole model of complex permittivity ( $\epsilon^*$ ), as described in **Equation 3.14**.

$$\epsilon^* = \epsilon_\infty + \frac{\epsilon_s - \epsilon_\infty}{1 + (j\omega\tau)^\beta} - \frac{j\sigma^*}{\omega^n \epsilon_0} \quad (3.14)$$

Here,  $\epsilon_\infty$  and  $\epsilon_s$  represents the dielectric constant at high and low frequencies,  $\omega$  angular frequency,  $\tau$  signifies the dielectric relaxation time,  $0 < \beta < 1$ ,  $\sigma^*$  is the resultant of space charge ( $\sigma_{sp}$ ) and free charge ( $\sigma_{fc}$ ) conductivity, and  $n$  is the exponent. The second term in the above equation arises due to dc conductivity correction. Therefore,  $\epsilon'$  and  $\epsilon''$  are given by **Equation 3.15** and **3.16**.

$$\epsilon' = \epsilon_\infty + \frac{(\epsilon_s - \epsilon_\infty) \left\{ 1 + (\omega\tau)^\beta \cos\left(\frac{\beta\pi}{2}\right) \right\}}{1 + 2(\omega\tau)^\beta \cos\left(\frac{\beta\pi}{2}\right) + (\omega\tau)^{2\beta}} + \frac{\sigma_{sc}}{\omega^n \epsilon_0} \quad (3.15)$$

$$\epsilon'' = \frac{(\epsilon_s - \epsilon_\infty)(\omega\tau)^\beta \sin\left(\frac{\beta\pi}{2}\right)}{1 + 2(\omega\tau)^\beta \cos\left(\frac{\beta\pi}{2}\right) + (\omega\tau)^{2\beta}} + \frac{\sigma_{fc}}{\omega^n \epsilon_0} \quad (3.16)$$

**Table III** lists the estimated values of these parameters  $n$ ,  $\tau$ ,  $\beta$ ,  $\sigma_{sc}$ , and  $\sigma_{fc}$  obtained using the modified Cole-Cole plot. These parameters provide little information to understand the above-discussed dielectric characteristics. The exponent “ $n$ ” is related to the carrier polarization mechanism which usually lies between  $0 < n < 1$ . For an ideal complex conductivity,  $n = 1$ . If  $n < 1$ , it implies that the polarization has a distribution of the carrier polarization mechanism [18].

The value (0.9520) obtained from fitting proves the presence of interfacial polarization in the previous section. For a given material, the value of  $\beta$  controls the width of the distribution and  $\beta = 1$  for Debye relaxation [16]. The smaller the value of  $\beta$ , the larger the distribution of relaxation times. In this case,  $\beta = 0.9913$ , which indicates relaxation is not Debye type. The larger value of  $\tau$  (0.0709 S) indicates that short-range motion at high frequency allows for displacement pathways of the carrier that are not allowed in the long-range excursions that give rise to dc conduction ( $\sigma_{sc}$  and  $\sigma_{fc}$ ). Therefore, the space charge decays with relaxation time which gives rise to net conduction in the system.

**Table 3.3: Estimated values of the relaxation time ( $\tau$ ), exponent ( $n$ ), parameter ( $\beta$ ), conductivity owing to space ( $\sigma_{sc}$ ) and free charge ( $\sigma_{fc}$ ) derived by fitting a modified Cole-Cole model of frequency-dependent  $\epsilon'$  and  $\epsilon''$ .**

Parameters	relaxation time ( $\tau$ )	exponent ( $n$ )	parameter ( $\beta$ )	Space charge conductivity ( $\sigma_{sc}$ ) S/m	Free charge conductivity ( $\sigma_{fc}$ ) S/m
Values	0.0709	0.9520	0.9913	$3.06 \times 10^{-8}$	$1.02 \times 10^{-6}$

Consequently, the movement of the molecular dipoles (dipole loss), space charge migration (interfacial polarisation contribution), and direct current (DC) conduction are the three primary independent elements that contribute to the dielectric loss of a dielectric material [12]. The dielectric loss tangent ( $\tan \delta$ ) or dissipation factor is defined as the ratio of dielectric loss to a dielectric constant given by the following relation and also shown in **Figure 3.17(b)**.

$$\tan \delta = \frac{\epsilon''(\omega)}{\epsilon'(\omega)} \quad (3.17)$$

It is observable that as the frequency rises, the loss tangent lowers. This can be explained by the high-frequency phenomenon of ions lagging behind the applied field and space charge direction. The dielectric relaxation process is connected to the peak of the loss tangent, which symbolises the dominance of dipolar polarisation.

### 3.4.8 Study of Electric Modulus

The complex electric modulus was employed to analyse the electrical response of this material in terms of the relaxation process of space charge distribution. The physical significance of the  $M^*$  is the relaxation mechanism of the sample in the electric field while the electric

displacement remains constant. The complex dielectric modulus using complex dielectric permittivity can be written as the following relation,

$$M^* = \frac{1}{\varepsilon^*} = M' + jM'' \quad (3.18)$$

Where  $M' = \frac{\varepsilon'}{\varepsilon' + \varepsilon''}$  and  $M'' = \frac{\varepsilon''}{\varepsilon' + \varepsilon''}$  represents the real and imaginary components of the electric modulus respectively [13,19]. **Figure 3.18(a)** depicts the frequency-dependent properties of  $M'$  (blue) and  $M''$  (red).

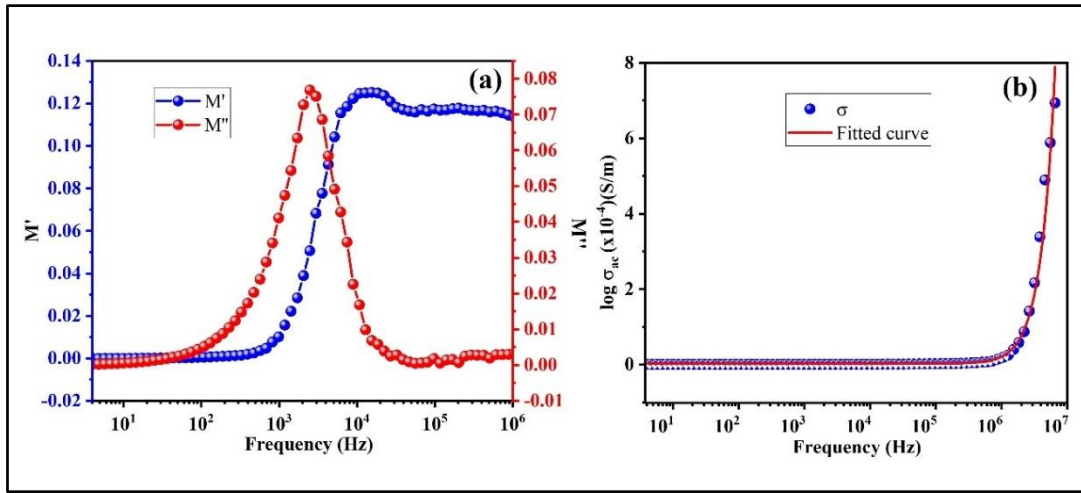


**Figure 3.18: (a) Frequency dependence real (blue) and an imaginary (red) component of electric modulus (b) ac conductivity**

The figure illustrates that  $M'$  was initially zero, but as the frequency was increased,  $M'$  increased. The saturation component in the high-frequency area indicates that the sample's electrical nature is frequency-independent. In the high-frequency region of  $M''$ , a single peak has been identified. It's due to a single relaxation in the dispersion area of the real part of the modulus ( $M'$ ), which is associated with the grain effect. Using the following relationship, the associated conductivity relaxation time (c) has been calculated from the peak point of the  $M''$  [20,21].

$$\tau_c = \frac{1}{2\pi f_{max}} \quad (3.19)$$

Where  $f_{max}$  represents relaxation frequency. The value of this conductivity relaxation time for the  $CH_3NH_3SnI_3$  sample was found to be  $6.45 \times 10^{-5}$  s.

### 3.4.9 Study of Electrical Conductivity

To better understand the charge transport process, this perovskite sample was subjected to a frequency-dependent AC conductivity investigation. **Figure 3.18(b)** shows that the curve is frequency independent in the low-frequency region, which is known as the DC conductivity of the sample [11]. However, the nature of the curve is found to be very frequency-dependent in the high-frequency area, which is related to AC conductivity. The relationship  $\sigma_{ac} = \sigma_{dc} \omega \epsilon' \epsilon_0 \tan \delta$  gives the AC conductivity. The jump relaxation model (JRM) introduced by Funk [13,18] can be used to analyse this AC and DC electrical conductivity. According to this model, ions are unable to remain in a state of equilibrium with their neighbouring ions after jumping from their original relaxed and stable state. As a result, nearby ions will likewise relocate appropriately to unwind in their new location. The ions can effectively leap to their open neighbouring places in the low-frequency zone in this fashion. The ions' successful hopping into low-frequency areas and subsequent contribution to DC conductivity are caused by their long-range mobility. A failed leap occurs when the ions return to their initial state following the jump to partially relax the new conformation (forward-backwards-forward state). In the high-frequency range, dispersive conductivity finally begins when the successful leap replaces the failed jumps.

The following Jonscher's power law, which is based on the universal dielectric model (UDR), can be applied to analyse the frequency-dependent AC conductivity [22].

$$\sigma_{ac} = \sigma_{dc} + \sigma_0 f^k \quad (3.20)$$

Where,  $\sigma_{ac}$  and  $\sigma_{dc}$  are AC and DC components of the sample's electrical conductivity,  $\sigma_0$  is a pre-factor and  $k$  is an exponent of frequency. **Equation 3.20** was used to fit the experimental results of the sample's electrical conductivity, as shown in **Figure 3.18(b)** (red curve). The values of  $\sigma_{dc}$ ,  $\sigma_0$  and  $k$  obtained from the best-fitted model is  $2.01 \times 10^{-6}$ ,  $4.63 \times 10^{-19}$  S/m and 1.99 respectively.

A survey of the literature was conducted to compare the conductivity, dielectric constant, bulk capacitance and bulk resistance of lead-free  $\text{CH}_3\text{NH}_3\text{SnI}_3$  with lead-based  $\text{CH}_3\text{NH}_3\text{PbI}_3$  perovskite. Almora et al. explored  $\text{CH}_3\text{NH}_3\text{PbI}_3$  perovskite impedance spectroscopy in 2020 and discovered DC and AC conductivity in the order of  $10^{-9}$  and  $10^{-7}$  S/cm, dielectric constant near about 23 in room temperature [23]. Md. Sheikh et al. published an excellent conductivity study of  $\text{CH}_3\text{NH}_3\text{PbI}_3$  perovskite in 2017 [24]. According to their hypothesis, they discovered conductivity on the order of  $10^{-4}$  S/m and the value of grain resistance and capacitance are 0.6

M $\Omega$  and 8.3pF, respectively. In 2020, Jayathissa discovered that the DC and AC conductivity of lead-based perovskite is in the order of  $10^{-7}$  and  $10^{-6}$  S/m, and the dielectric constant is approximately 30 [25]. According to Li and his colleagues, the conductivities were  $10^{-6}$  and  $10^{-4}$  S/m, respectively, and the dielectric constant is nearly 130 [26].

Based on the above explanation, the conductivity of this CH<sub>3</sub>NH<sub>3</sub>SnI<sub>3</sub> perovskite appears to be rather impressive. This perovskite can be used as a direct substitute for lead-based perovskites. Our synthesis method, as well as extensive dielectric, impedance, and conductivity analyses, will be extremely useful in the development of lead-free perovskite material-based electrical devices in this approach.

### 3.4.10 Analysis of Schottky Device Characterization

The current-voltage (I-V) data were collected at 300 K using a Keithley 2400 source metre (Figure 3.19(c)) with and without illumination (Intensity 100 mW.cm<sup>-2</sup>) by applying a bias voltage within a  $\pm 2$  V range with a step size of 0.025 V across the thin-film metal-semiconductors (MS) junction of the CH<sub>3</sub>NH<sub>3</sub>SnI<sub>3</sub> perovskite device.

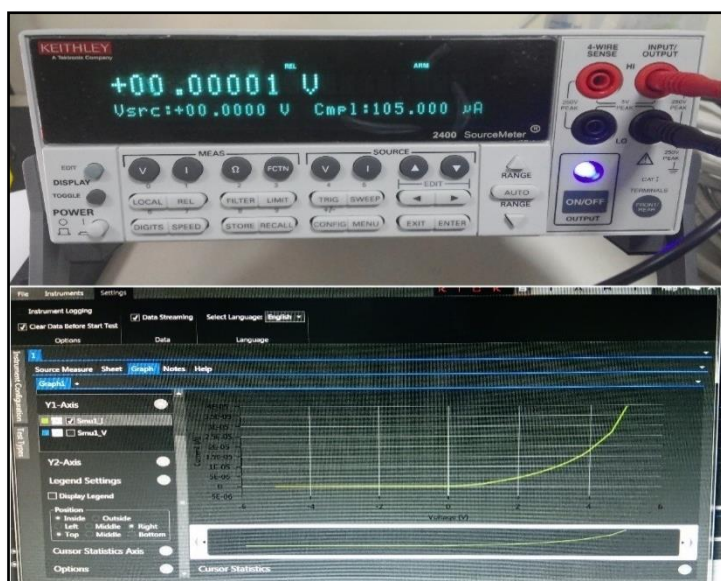


**Figure 3.19: (a) Keithley 2400 SMU for I-V measurements (b) a typical I-V characteristic of a Schottky device**

Electrical conductivities were  $1.04 \times 10^{-6}$  S m<sup>-1</sup> in the dark and improved to  $1.95 \times 10^{-6}$  S m<sup>-1</sup> after photo-illumination (Table 3.4). This increase in conductivity is attributable to the

sample's photosensitivity. The I-V properties display a highly nonlinear rectifying nature in both dark and light conditions which indicates the Schottky behaviour of the device.

Whenever the bias voltage is applied the build-in potential decreases depending on the value of bias and therefore electrons move from perovskite to the ITO electrode. But due to the presence of a high barrier height when reverse bias is applied the carriers are unable to move from ITO to perovskite. As a result, the device produces a high rectification ratio. The rectification ratio ( $I_{on}/I_{off}$ ) computed from the graphs is 11.84 in the dark phase and 12.03 in the light phase. The thermionic emission (TE) hypothesis was used to study the IV characteristics of the perovskite-based device. Using TE theory, the current of a fabricated device can be expressed as **Equation 3.21** [27]:

$$I = I_0 \left[ \exp\left(\frac{qV}{\eta kT}\right) - 1 \right] \quad (3.21)$$

Where V, q,  $\eta$ , k, and T denote the applied bias voltage, electronic charge, ideality factor, Boltzman constant, and operating temperature. **Equation 3.22** shows the reverse saturation current,  $I_0$ , of TE theory.

$$I_0 = AA^*T^2 \exp\left(-\frac{q\phi_b}{kT}\right) \quad (3.22)$$

Where A is the effective area of Schottky diodes, which is  $35 \times 10^{-6} \text{ m}^2$ ,  $A^*$  represents effective Richardson constant, which is assumed as  $1.20 \times 10^6 \text{ AK}^{-2} \text{ m}^{-2}$ ,  $\phi_b$  is the barrier height (BH) at the junction. The straight-line intercept of  $\ln I$  at  $V = 0$  was used to calculate the reverse saturation current. **Equation 3.23** expresses the temperature dependency of the ideality factor ( $\eta$ ). [27].

$$\eta = \frac{q}{kT} \left[ \frac{dV}{d(\ln I)} \right] \quad (3.23)$$

The temperature-dependent apparent BH ( $\phi_b$ ) at zero bias can be obtained from **Equation 3.22** and can be expressed as **Equation 3.24**.

$$\phi_b = \frac{kT}{q} \ln\left(\frac{AA^*T^2}{I_0}\right) \quad (3.24)$$

The values of  $\eta$  and  $\phi_b$  of the Schottky device can be estimated from the slope and intercept of  $\ln I$  vs. V plots respectively (**Table 3.4**). The important Schottky parameters like ideality factor ( $\eta$ ), series resistance ( $R_s$ ), and barrier height ( $\phi_b$ ) have been determined from the forward biased I-V characteristics employing Cheung's method (**Equation 3.25**) [28,29].

$$\frac{dV}{d(\ln I)} = IR_S + \frac{\eta kT}{q} \quad (3.25)$$

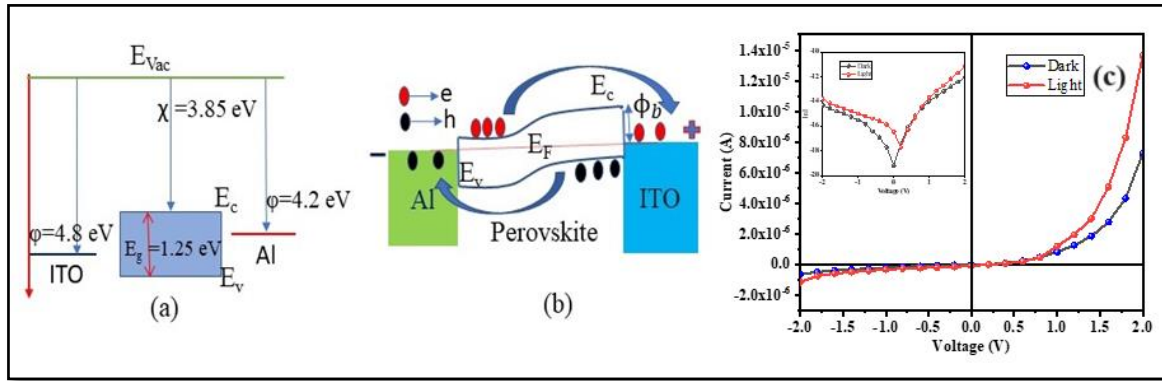


**Figure 3.20: (a) energy level diagram (b) band alignment of the device in the forward biased condition (c) I-V characteristic curves for  $\text{CH}_3\text{NH}_3\text{SnI}_3$  perovskite-based device under light and dark conditions**

From the intercept of  $dV/d\ln I$  vs.,  $I$  plot (**Figure 3.21(a)**) the ideality factor ( $\eta$ ) for the developed devices under both conditions has been estimated whereas the slope of this plot gives the value of series resistance ( $R_s$ ) of the MS device (**Equation 3.26**).

$$H(I) = V - \frac{\eta kT}{q} \ln\left(\frac{I}{AA^*T^2}\right) = \eta\phi_b + R_S I \quad (3.26)$$

The y-axis intercept of the  $H(I)$  vs.  $I$  curve (**Figure 3.21(b)**) provides the potential barrier height ( $\phi_b$ ).

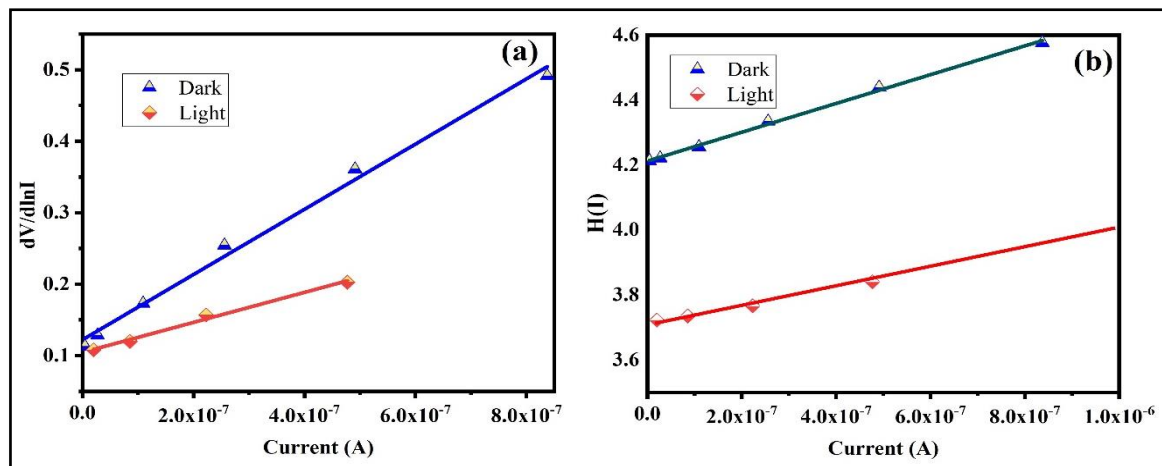


**Figure 3.21: (a)  $dV/d\ln I$  vs.  $I$  (A) (b)  $H(I)$  vs.  $I$  (A) curves of the MS device under dark and photo illumination conditions.**

In general, the ideality factor ( $\eta$ ) in the dark deviates from ideal behaviour due to Schottky barrier junction inhomogeneities, a high chance of electron and hole recombination in the depletion zone, and the presence of series resistance and interfacial states. Under dark and light conditions, the values of  $r$  of the device are 2.36 and 2.29 respectively. These values differ slightly from the desired value ( $\sim 1$ ). This may be due to Schottky barrier junction inhomogeneities and series resistance at the junction. In the presence of light, the drop in ideality factor shows that the device has less carrier recombination at the interface. As a result, under lighting conditions, the barrier potential height is likewise reduced. This reduction could be caused by a concentration of photo-induced charge carriers near the conduction band. Both approaches produce consistent series resistances. When exposed to light, the resulting series resistances were demonstrated to decrease (**Table 3.4**), showing their utility in the field of optoelectronic devices.

To get a clear image of the charge transfer kinetics, we evaluated the transit time and mobility. The different I-V curves of perovskite on the logarithmic scale demonstrated that it may be separated into two slope zones under dark and light conditions (**Figure 3.22(a)**). These I-V characteristics' varied regions represent diverse charge transfer techniques. Region-I has a slope  $\sim 1$ , indicating the Ohmic region, and it follows the  $I \propto V$  relation. The current is nearly proportional to  $V^2$  in Region II, indicating a space charge limited current (SCLC) regime.

**Table 3.4: The Schottky Device Parameters for the Thin Film Devices**

Condition	Conductivity ( $S \cdot m^{-1}$ )	Ideality factor ( $\eta$ )	Series Resistance from ( $R_s \times 10^5$ in $\Omega$ )		Barrier Height from ( $\phi_b$ in eV)	
			$dV/d\ln I$ vs $I$	$H(I)-I$	I-V plot	$H(I)-I$
Dark	$1.04 \times 10^{-6}$	2.36	4.91	4.39	0.682	0.652
Light	$1.95 \times 10^{-6}$	2.29	2.24	2.71	0.671	0.635

This means that as the voltage goes over a certain threshold, electrons are trapped by defect-induced traps of the sample that are distributed within the forbidden gap. As a result, the electrical current transport mechanism got changed. The injected charge carriers spread and produce a space-charge field if the number of injected charge carriers exceeds the number of background charge carriers. Following this method, the effective charge carrier mobility was

determined from the higher voltage section of the  $I$  vs.  $V^2$  curve (**Figure 3.22(b)**) using the Mott-Gurney equation (**Equation 3.27**) [29,30]:

$$I = \frac{9\mu_{eff}\epsilon_0\epsilon_r A}{8} \left( \frac{V^2}{d^3} \right) \quad (3.27)$$

where,  $I$ ,  $\mu_{eff}$ ,  $\epsilon_0$  and  $\epsilon_r$ , represent current through the material, effective mobility, the permittivity of free space and the relative dielectric constant of the perovskite materials, respectively. Using the value of  $\epsilon_r$  from **Figure 3.17(a)**, the diffusion length ( $L_D$ ), effective mobility ( $\mu_{eff}$ ) and transit time ( $\tau$ ) are three essential electrical parameters that have been determined (**Equation 3.28 -3.30**) to understand the charge transit through the interface.

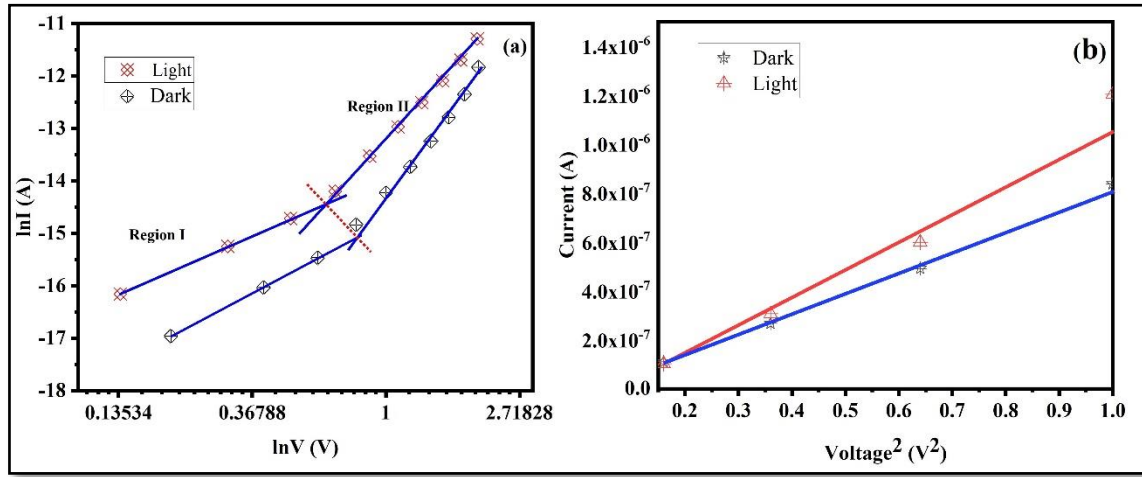


**Figure 3.22: (a)  $\ln I$  vs.  $\ln V$  plots and (b)  $I$  vs.  $V^2$  curves for  $\text{CH}_3\text{NH}_3\text{SnI}_3$ -based perovskite device in dark and light conditions.**

The slope of the logarithmic plot of forwarding biased  $I$ - $V$  characteristics in the SCLC region (**Region-II**), displayed in **Figure 3.22(a)**, was used to derive the value of  $\tau$  using **Equation 3.28**.

$$\tau = \frac{9\epsilon_0\epsilon_r A}{8d} \left( \frac{V}{I} \right) \quad (3.28)$$

$$\mu_{eff} = \frac{qD}{kT} \quad (3.29)$$

$$L_D = \sqrt{2D\tau} \quad (3.30)$$

where  $D$  denotes the diffusion coefficient determined by the Einstein-Smoluchowski equation (**Equation 3.29**). The charge carrier's diffusion length ( $L_D$ ), which describes the distance a carrier travels before recombination, is a crucial factor in the device's performance. This length has been calculated using **Equation 3.30**. The values of these charge conduction parameters

are listed in **Table 3.5**. The SCLC characteristics indicate that the device exhibits excellent charge transmission properties. Consequently, such materials hold significant promise for future device applications.

**Table 3.5: Charge conduction parameters of the perovskite Based MS Thin Film Device**

Condition	$\epsilon_r$	Effective mobility, $\mu_{eff}$ ( $\text{m}^2\text{V}^{-1}\text{s}^{-1}$ )	Transit time, $\tau$ (S)	$\mu_{eff}\tau$ ( $\text{m}^2\text{V}^{-1}$ )	Diffusion coefficient, $D$ ( $\times 10^{-13}$ ) ( $\text{m}^2\text{s}^{-1}$ )	Diffusion length, $L_D$ ( $\times 10^{-10}$ ) (nm)
Dark	233.1	$1.07 \times 10^{-11}$	$5.98 \times 10^{-8}$	$6.36 \times 10^{-19}$	2.75	1.81
Light	5	$1.61 \times 10^{-11}$	$4.99 \times 10^{-8}$	$7.98 \times 10^{-19}$	4.14	2.03

In this section, we reviewed several studies to compare the performance of Pb-based Schottky devices in terms of the aforementioned parameters. Cifci O. et al. (2018) demonstrated an Al/perovskite/p-type Si-based Schottky photodiode with an ideality factor of 2.12-2.13, a barrier height of 0.85-0.87 eV, and a series resistance of 311-342 k $\Omega$ . In 2019, Luo W. et al. constructed an ITO/CH<sub>3</sub>NH<sub>3</sub>PbI<sub>3</sub>/PCBM/BCP/Ag Schottky device with a barrier height of 0.97 eV. Shaikh P. et al. (2016) developed Pb-based Schottky devices with an ideality factor ranging from 1.7 to 3.3 and a series resistance of approximately 169.2 k $\Omega$ . Chen L. (2016) constructed an Al/ CH<sub>3</sub>NH<sub>3</sub>PbI<sub>3</sub>/ITO Schottky diode, reporting an ideality factor of 7.09 and a barrier height of 0.73 eV.

The parameter values found in our work are comparable to or better than those reported for Pb-based devices. The toxicity of Pb is the most critical concern in these studies. Our research indicates that CH<sub>3</sub>NH<sub>3</sub>SnI<sub>3</sub> perovskite is a viable candidate for replacing Pb in Schottky devices, offering a less toxic alternative while maintaining comparable performance.

### 3.5 Conclusions

In summary, lead-free cubic CH<sub>3</sub>NH<sub>3</sub>SnI<sub>3</sub> perovskite has been synthesized using a modified solution-processing method, which has proven effective for achieving high crystalline nano ranges (60-70 nm). By refining and analysing the XRD data, several structural parameters have been determined. This work includes a detailed investigation into the CIS of the perovskite sample. The fitted Nyquist plot of impedance spectroscopy provided a robust equivalent electrical

model for evaluating the effects of electrode polarization, grain, and grain boundary on net resistance and capacitance. The notable dielectric behaviour (233.15) of this perovskite suggests potential applications in batteries, capacitors, and storage devices. The contributions of space charge ( $3.06 \times 10^{-8}$  S/m) and free charge ( $1.02 \times 10^{-6}$  S/m) conductivity to overall conductivity were evaluated from the dielectric fitting of the modified Cole-Cole plot. The asymmetric imaginary component of the electric modulus provided the conductivity relaxation time ( $6.45 \times 10^{-6}$  s) of the sample. The frequency-dependent AC conductivity was studied and analysed using the JRM model. Additionally, a Schottky device in a sandwich structure was developed using this perovskite. Analysis of this device showed improvements in electrical conductivity and mobility from  $1.04 \times 10^{-6}$  S/m and  $1.07 \times 10^{-11}$  m<sup>2</sup>/V·s to  $1.95 \times 10^{-6}$  S/m and  $1.61 \times 10^{-11}$  m<sup>2</sup>/V·s, respectively, after illumination. Comparing this work with lead-based literature reveals that CH<sub>3</sub>NH<sub>3</sub>SnI<sub>3</sub> has the potential to replace ecologically toxic lead-based perovskites. This research encourages further investigation into impedance spectroscopy, dielectric behaviour, relaxation behaviour, and AC conductivity of lead-free CH<sub>3</sub>NH<sub>3</sub>SnI<sub>3</sub> -based perovskites for various electrical and energy harvesting systems.

### 3.6 References

- [1] N. Besra, T. Paul, P.K. Sarkar, S. Thakur, S. Sarkar, A. Das, K. Chanda, K. Sardar, K.K. Chattopadhyay, Room temperature solution processed low dimensional CH<sub>3</sub>NH<sub>3</sub>PbI<sub>3</sub> NIR detector, in: AIP Conf Proc, American Institute of Physics Inc., 1953 (2018) 030210.
- [2] T. Paul, B.K. Chatterjee, S. Maiti, S. Sarkar, N. Besra, B.K. Das, K.J. Panigrahi, S. Thakur, U.K. Ghorai, K.K. Chattopadhyay, Tunable cathodoluminescence over the entire visible window from all-inorganic perovskite CsPbX<sub>3</sub> 1D architecture, J Mater Chem C Mater 6 (2018) 3322–3333.
- [3] S. Venkatachalam, R.T.R. Kumar, D. Mangalaraj, S.K. Narayandass, K. Kim, J. Yi, Optoelectronic properties of Zn<sub>0.52</sub>Se<sub>0.48</sub>/Si Schottky diodes, Solid State Electron 48 (2004) 2219–2223.
- [4] M. Weiss, J. Horn, C. Richter, D. Schlettwein, Preparation and characterization of methylammonium tin iodide layers as photovoltaic absorbers, Physica Status Solidi (A) Applications and Materials Science 213 (2016) 975–981.
- [5] Y. Dang, Y. Zhou, X. Liu, D. Ju, S. Xia, H. Xia, X. Tao, Formation of Hybrid Perovskite Tin Iodide Single Crystals by Top-Seeded Solution Growth, Angewandte Chemie - International Edition 55 (2016) 3447–3450.
- [6] Y. Chen, X. Zhang, Z. Liu, Z. Zeng, H. Zhao, X. Wang, J. Xu, Light enhanced room temperature resistive NO<sub>2</sub> sensor based on a gold-loaded organic–inorganic hybrid perovskite incorporating tin dioxide, Microchimica Acta 186 (2019) 47.

- [7] E.J. Juarez-Perez, Z. Hawash, S.R. Raga, L.K. Ono, Y. Qi, Thermal degradation of  $\text{CH}_3\text{NH}_3\text{PbI}_3$  perovskite into  $\text{NH}_3$  and  $\text{CH}_3\text{I}$  gases observed by coupled thermogravimetry-mass spectrometry analysis, *Energy Environ Sci* 9 (2016) 3406–3410.
- [8] J. Idígoras, A. Todinova, J.R. Sánchez-Valencia, A. Barranco, A. Borrás, J.A. Anta, The interaction between hybrid organic-inorganic halide perovskite and selective contacts in perovskite solar cells: An infrared spectroscopy study, *Physical Chemistry Chemical Physics* 18 (2016) 13583–13590.
- [9] T. Glaser, C. Müller, M. Sendner, C. Krekeler, O.E. Semonin, T.D. Hull, O. Yaffe, J.S. Owen, W. Kowalsky, A. Pucci, R. Lovrinčić, Infrared Spectroscopic Study of Vibrational Modes in Methylammonium Lead Halide Perovskites, *Journal of Physical Chemistry Letters* 6 (2015) 2913–2918.
- [10] S.K. Patla, R. Ray, S. Karmakar, S. Das, S. Tarafdar, Nanofiller-Induced Ionic Conductivity Enhancement and Relaxation Property Analysis of the Blend Polymer Electrolyte Using Non-Debye Electric Field Relaxation Function, *Journal of Physical Chemistry C* 123 (2019) 5188–5197.
- [11] S.K. Patla, R. Ray, K. Asokan, S. Karmakar, Investigation of ionic conduction in PEO-PVDF based blend polymer electrolytes, *J Appl Phys* 123 (2018) 125102.
- [12] J.N. Wilson, J.M. Frost, S.K. Wallace, A. Walsh, Dielectric and ferroic properties of metal halide perovskites, *APL Mater* 7 (2019) 010901.
- [13] P. Sengupta, P. Sadhukhan, A. Ray, S. Mal, A. Singh, R. Ray, S. Bhattacharyya, S. Das, Influence of activation energy on charge conduction mechanism and giant dielectric relaxation of sol-gel derived  $\text{C}_3\text{H}_7\text{NH}_3\text{PbBr}_3$  perovskite; Act as high performing UV photodetector, *J Alloys Compd* 892 (2022) 162216.
- [14] S.O. Nelson, Dielectric properties measurement techniques and applications, *Transactions of the American Society of Agricultural Engineers* 42 (1999) 523–529.
- [15] A. Ray, P. Maji, A. Roy, S. Saha, P. Sadhukhan, S. Das, Temperature and frequency dependent dielectric relaxation of Ni-Fe-Oxide nanocomposites, *Mater Res Express* 6 (2019) 1250h4.
- [16] A. Dhahri, E. Dhahri, E.K. Hlil, Electrical conductivity and dielectric behaviour of nanocrystalline  $\text{La}_{0.6}\text{Gd}_{0.1}\text{Sr}_{0.3}\text{Mn}_{0.75}\text{Si}_{0.25}\text{O}_3$ , *RSC Adv* 8 (2018) 9103–9111.
- [17] M. Samiee, S. Konduri, B. Ganapathy, R. Kottokkaran, H.A. Abbas, A. Kitahara, P. Joshi, L. Zhang, M. Noack, V. Dalal, Defect density and dielectric constant in perovskite solar cells, *Appl Phys Lett* 105 (2014) 153502.
- [18] D.K. Pradhan, P. Misra, V.S. Puli, S. Sahoo, D.K. Pradhan, R.S. Katiyar, Studies on structural, dielectric, and transport properties of  $\text{Ni}_{0.65}\text{Zn}_{0.35}\text{Fe}_2\text{O}_4$ , *J Appl Phys* 115 (2014) 243904.
- [19] S.K. Patla, A. Roy Choudhury, R. Ray, S. Das, S. Karmakar, Plasticizer ethylene carbonate facilitates new ion coordination site in blend polymer electrolyte: Dielectric relaxation through two-parameter Mittag-Leffler function, *AIP Adv* 10 (2020) 115008.
- [20] C. Rayssi, S. el Kossi, J. Dhahri, K. Khirouni, Frequency and temperature-dependence of dielectric permittivity and electric modulus studies of the solid solution  $\text{Ca}_{0.85}\text{Er}_{0.1}\text{Ti}_{1-x}\text{XCo}_4\text{x}/3\text{O}_3$  ( $0 \leq x \leq 0.1$ ), *RSC Adv* 8 (2018) 17139–17150.

- [21] G. Raju, Dielectric Loss and Relaxation—I, in: Dielectrics in Electric Fields, Second Edition, CRC Press, (2016) 83–136.
- [22] P. Sengupta, P. Sadhukhan, A. Ray, R. Ray, S. Bhattacharyya, S. Das, Temperature and frequency dependent dielectric response of  $\text{C}_3\text{H}_7\text{NH}_3\text{PbI}_3$ : A new hybrid perovskite, *J Appl Phys* 127 (2020) 204103.
- [23] O. Almora, A. González-Lezcano, A. Guerrero, C.J. Brabec, G. Garcia-Belmonte, Ion-mediated hopping electrode polarization model for impedance spectra of  $\text{CH}_3\text{NH}_3\text{PbI}_3$ , *J Appl Phys* 128 (2020) 075104.
- [24] M.S. Sheikh, A.P. Sakhya, A. Dutta, T.P. Sinha, Dielectric relaxation of  $\text{CH}_3\text{NH}_3\text{PbI}_3$  thin film, *Thin Solid Films* 638 (2017) 277–281.
- [25] R. Jayathissa, C.A. Burns, A study of structural and dielectric properties of  $\text{Ba}^{2+}$  doped  $\text{CH}_3\text{NH}_3\text{PbI}_3$  crystals, *SN Appl Sci* 2 (2020) 349.
- [26] W. Li, Z. Man, J. Zeng, L. Zheng, G. Li, A. Kassiba, Relationship of Giant Dielectric Constant and Ion Migration in  $\text{CH}_3\text{NH}_3\text{PbI}_3$  Single Crystal Using Dielectric Spectroscopy, *Journal of Physical Chemistry C* 124 (2020) 13348–13355.
- [27] D. Sahoo, N.B. Manik, Study on the effect of temperature on electrical and photovoltaic parameters of lead-free tin-based Perovskite solar cell, *Indian Journal of Physics* 97 (2022) 447–455.
- [28] M. Sharma, S.K. Tripathi, Study of barrier inhomogeneities in I-V-T and C-V-T characteristics of  $\text{Al}/\text{Al}_2\text{O}_3/\text{PVA:n-ZnSe}$  metal-oxide-semiconductor diode, *J Appl Phys* 112 (2012) 024521.
- [29] S. Mahato, D. Biswas, L.G. Gerling, C. Voz, J. Puigdollers, Analysis of temperature dependent current-voltage and capacitance-voltage characteristics of an  $\text{Au}/\text{V}_2\text{O}_5/\text{n-Si}$  Schottky diode, *AIP Adv* 7 (2017) 085313.
- [30] A. Jain, P. Kumar, S.C. Jain, V. Kumar, R. Kaur, R.M. Mehra, Trap filled limit voltage (VTFL) and  $V^2$  law in space charge limited currents, *J Appl Phys* 102 (2007) 094505.
- [31] O.S. Cifci, A. Kocyigit, P. Sun, Perovskite/p-Si photodiode with ultra-thin metal cathode, *Superlattices Microstruct* 120 (2018) 492–500.
- [32] W. Luo, L. Yan, R. Liu, T. Zou, S. Zhang, C. Liu, Q. Dai, J. Chen, H. Zhou, High detectivity ITO/organolead halide perovskite Schottky photodiodes, *Semicond Sci Technol* 34 (2019) 074004.
- [33] P.A. Shaikh, D. Shi, J.R.D. Retamal, A.D. Sheikh, M.A. Haque, C.F. Kang, J.H. He, O.M. Bakr, T. Wu, Schottky junctions on perovskite single crystals: Light-modulated dielectric constant and self-biased photodetection, *J Mater Chem C Mater* 4 (2016) 8304–8312.
- [34] L. Chen, J. Deng, H. Gao, Q. Yang, G. Wang, L. Kong, M. Cui, Z. Zhang, Organometallic hybrid perovskites: structural, optical characteristic and application in Schottky diode, *Journal of Materials Science: Materials in Electronics* 27 (2016) 4275–4280.

# **Chapter 4: Effect of SWCNT on the Electrical Behaviour of a Lead-Free Methylammonium Tin Iodide ( $\text{CH}_3\text{NH}_3\text{SnI}_3$ ) Perovskite Schottky device**

## **4.1 Introduction**

## **4.2 Experimental Section**

### 4.2.1 Materials

### 4.2.2 Instruments Used

#### 4.2.2.1 Transmission Electron Microscope (TEM)

### 4.2.3 Sample Preparation

### 4.2.4 Development of Perovskite Schottky Device (PSD)

## **4.3 Characterization**

## **4.4 Results and discussions**

### 4.4.1 X-Ray Crystallography and Optical Characterization

### 4.4.2 X-ray Photoelectron Spectroscopy (XPS)

### 4.4.3 FESEM and TEM

### 4.4.4 Fourier Transform Infrared Spectroscopy (FTIR) and Thermal Gravimetric Analysis (TGA)

### 4.4.5 Optoelectronic Study

## **4.5 Conclusions**

## **4.6 References**

## 4.1 Introduction

In the previous work, we developed a nano-cubic perovskite-based ITO/  $\text{CH}_3\text{NH}_3\text{SnI}_3$ /Al Schottky device to estimate its electrical properties and found that its electrical performance is comparable to Pb-based perovskites [1]. We observed that the performance of  $\text{CH}_3\text{NH}_3\text{SnI}_3$  perovskite is quite impressive, except for its low conductivity, which may be due to several factors. Firstly, tin is an easily oxidizing element, and the resulting Sn perovskite thin films often have large hole concentrations, which is unfavourable for the effective production of optoelectronic devices [2,3]. We took extra care during synthesis and measurements, using a glove box and nitrogen-sealed container, respectively. However, some oxygen leakage might have occurred during the spin coating process, possibly contributing to the low conductivity of the device. Secondly, the most popular deposition technique, spin coating, does not always produce uniformly smooth Sn perovskite thin films with ease [4]. Consequently, defects and recombination centres form in the film, acting as charge trapping centres in the device. This could be another reason for the low conductivity observed in the device studied in the previous chapter.

To address the charge transport issues in the device, researchers have been using different nanomaterials such as CNTs,  $\text{TiO}_2$ , and ZnO as fillers and charge transporting mediums (HTL/ETL), as reviewed in detail in **Chapter 2**. Considering the merits of CNTs and the poor charge transport and oxidation sensitivity of  $\text{CH}_3\text{NH}_3\text{SnI}_3$  perovskite, we used SWCNTs as charge transporting medium to improve the charge transport of the perovskite film. The perovskite-SWCNT composite was synthesized and applied to develop a simple-structured Schottky device to analyse its charge transport mechanism. The simple sandwiched structure of the Schottky device is popular for understanding charge conduction. Devices were developed with and without CNTs to demonstrate the charge transportation capabilities of CNTs in the  $\text{CH}_3\text{NH}_3\text{SnI}_3$  perovskite film.

To explain the charge transport mechanism, current-voltage (I-V) characteristics were analysed. From this analysis, threshold voltage ( $V_{\text{th}}$ ), trap energy, barrier height ( $\phi_{\text{b}}$ ), the ideality factor ( $\eta$ ), and series resistance ( $R_{\text{s}}$ ) of the device were determined under light and dark conditions. The  $R_{\text{s}}$  was determined from the dark I-V forward-biased characteristics using the Cheung and Cheung method and the modified Cheung method. The I-V characteristics show that the device with SWCNT has 4.2 times higher conductivity in the dark and 4.9 times higher conductivity in light conditions at 1.5 V. Another important parameter,  $R_{\text{s}}$ , decreased

significantly in the presence of SWCNTs. The detailed charge transport analysis shows that the trap energy of the device decreased due to the incorporation of SWCNTs. The specific detectivity in visible light of this simple-structured Schottky device also improved. This study demonstrates that incorporating SWCNTs within hybrid perovskite is a viable and straightforward technique for developing optoelectronic applications with optimal performance.

## 4.2 Experimental Section

### 4.2.1 Materials

Tin (II) iodide ( $\text{SnI}_2$ , anhydrous, 99.99% purity), methylammonium iodide ( $\text{CH}_3\text{NH}_3\text{I}$ , 98% purity), and ITO-coated glass (surface resistivity 8-12  $\Omega/\text{sq.}$ ) were purchased from Sigma Aldrich. A few solvents like Dimethylformamide (DMF), Dimethyl sulfoxide (DMSO), and -COOH functionalized single wall carbon nanotube (SWCNT 90% OD: 1–2 nm) were purchased from SRL company, Extran MA 02 (Neutral) was purchased from Alfa-Aesar. **Figure 4.1(a)** shows the ball and stick structure of perovskite and **Figure 4.1(b)** shows the structure of COOH functionalized SWCNT. All of the compounds were utilized without being purified further. The experiment's deionized water was obtained from the departmental Milli (Q) water facility.

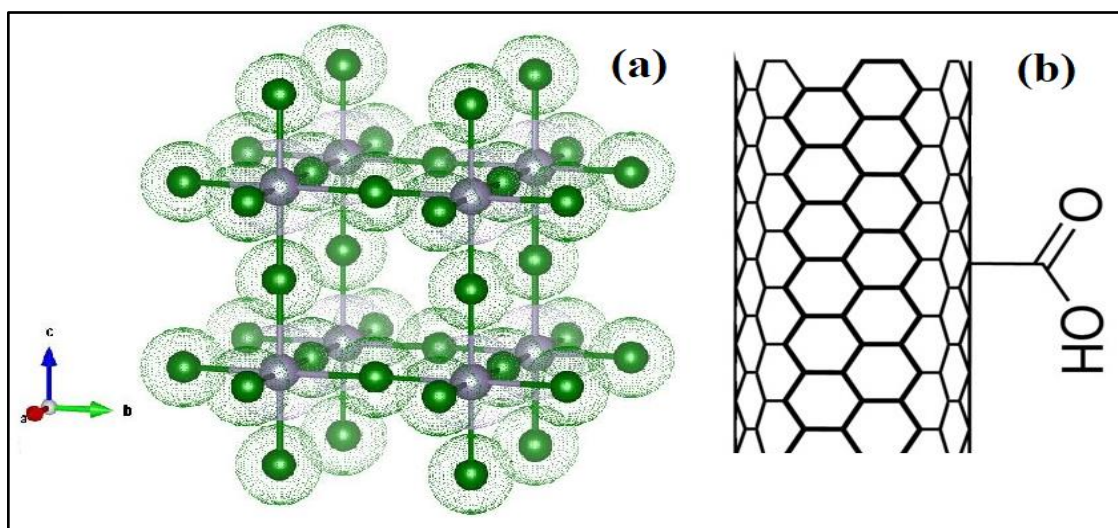


**Figure 4.1: Structure (a) Visualization of cubic  $\text{CH}_3\text{NH}_3\text{SnI}_3$  perovskite by VESTA (b) COOH functionalized SWCNT.**

### 4.2.2 Instruments Used

The instruments used in this work are mostly the same as those described in Chapter 4, with the exception of TEM. A detailed description of all the instruments can be found in Chapter 4. In the following section, a detailed description is provided only for TEM.

#### 4.2.2.1 Transmission Electron Microscope (TEM)

The TEM is a sophisticated instrument designed to analyse the internal structure of materials at the atomic or molecular level. We have used in our work, the TEM-2100 Plus model illustrated in the **Figure 4.2**. The core of the TEM's functionality begins with the electron gun, which generates a beam of electrons by heating a filament. This electron beam is then accelerated by an anode and shaped into a coherent stream. Condenser lenses focus this beam onto a very small spot on the specimen, where it interacts with the sample's atoms. The interaction of the electron beam with the specimen generates various signals, including transmitted, scattered, and secondary electrons.

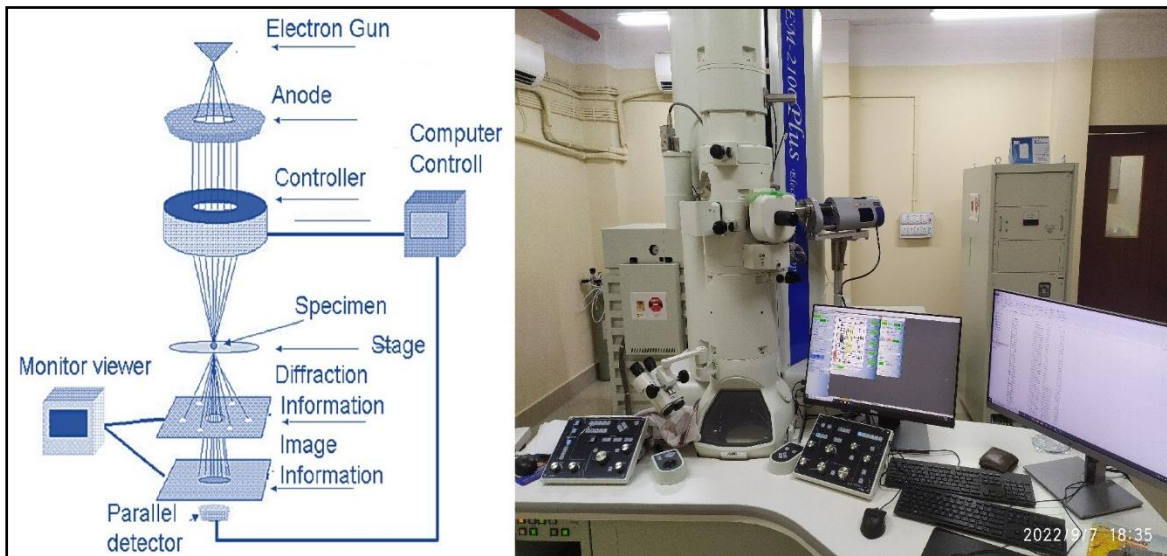


**Figure 4.2: (a) Schematic representation of components of TEM (b) Laboratory setup of TEM**

Following this, the objective lens collects the transmitted electrons, forming an initial image or diffraction pattern of the specimen. This image is then magnified by intermediate and projector lenses, producing a highly detailed magnified image. The magnified image is projected onto a fluorescent screen or captured by a detector, such as a CCD camera, for further analysis. Parallel detectors can also capture diffraction patterns, providing valuable information about

the crystalline structure of the sample. Finally, the monitor and computer interface display the magnified image, allowing for detailed examination and analysis of the material.

### 4.2.3 Sample Preparation

At first, two vials were taken and labeled as A and B. In each vial, 1 ml of DMF and DMSO mixture was taken in a 4:1 ratio. The vials were then placed on a magnetic stirrer hot plate and the temperature was set to 65 °C in an N<sub>2</sub> atmospheric glove box. In the next step, 10 mol% of SnF<sub>2</sub> and 10 mol% pyrazines were added to the solution mixtures as reducing additives and stirred for 30 min [5]. Then, 1 mg of COOH functionalized SWCNT was added to solution B and dispersed in an ultrasonic bath for 1 hour. In the next step, 1 mmol of SnI<sub>2</sub> (375 mg) was added to both A and B solutions. After the complete dissolution of SnI<sub>2</sub>, 1 mmol of CH<sub>3</sub>NH<sub>3</sub>I (159 mg) was added to both final solutions and stirred for 30 min at 70 °C. These perovskite precursor solutions were used to develop without and with SWCNT Schottky devices respectively.

### 4.2.4 Development of Perovskite Schottky Device (PSD)

Several ITO-coated glass substrates were cleaned in an ultrasonic bath for 10 minutes each with DI water, neutral solution (Extran MA 02), milli Q water, acetone, and lastly with isopropyl alcohol. Following cleaning, the substrates were dried by putting them on a hot plate pre-set at 80 °C for 15 mins. The electrode contact region of the ITOs was then masked with tape. After that, the synthesized perovskite precursor A was applied to ITO and spun for 30 seconds at 1600 rpm to form solely a CH<sub>3</sub>NH<sub>3</sub>SnI<sub>3</sub> perovskite thin layer. A comparable technique was employed to create a thin film composite of SWCNTs. Subsequently, the films were promptly placed on a preheated hot plate at 75 °C, resulting in a dark brown layer shift indicating the formation of perovskite. The next step involved using a shadow mask to deposit pure Al metal via plasma deposition at a pressure of  $1 \times 10^{-6}$  mbar. The effective device area measured on a standard scale was approximately  $4 \times 9$  mm<sup>2</sup>.

## 4.3 Characterization

The crystallinity of the synthesized perovskite samples was investigated using a Bruker D8 SWAX diffractometer with Cu-K<sub>α</sub> radiation of wavelength 1.5404 Å, operating at 35 mA and 35 kV. To obtain X-Ray diffraction peaks, the measurement was conducted within the two-theta range of 10-60°. The sample holder was rotated at a speed of 10 rpm during the scan to

capture all potential peak data. The optical characteristics of the films were studied using a SHIMADZU UV-Vis spectrophotometer (UV-1900). A Thermo Scientific K-Alpha X-ray Photoelectron Spectrometer with a monochromatic (1486.6 eV) Al- $K_{\alpha}$  source was used to evaluate the X-ray Photoelectron Spectroscopy (XPS) of the samples. To explore the morphological properties of the produced perovskite materials, two distinct thin films were formed on two glass slides, as previously described. The Quorum Q150R ES coating equipment was used to coat the sample with gold. The images are taken using a field emission scanning electron microscope (FESEM), and they were analysed using a Bruker energy dispersive spectroscopy (EDS) detector (Quantax, 200). To the image of the sample, a TEM-2100 plus electron microscope was utilized. The thermogravimetric analysis (TGA) was carried out with NETZSCH in the temperature range of 27 to 500 °C. To study bonds in the sample, PerkinElmer Spectrometer was used to measure FTIR spectroscopy in the range of 780-3500  $\text{cm}^{-1}$ . Keithley 2400 SMU was used to measure the I-V characteristics of the devices.

## 4.4 Results and Discussions

### 4.4.1 X-Ray Crystallography and Optical Characterization

The structure of the perovskite sample and its composite with SWCNT shows excellent crystallinity, shown in **Figure 4.3(a)** and conforms to the cubic space group Pm-3m symmetry. The computed and experimental PXRD results demonstrate that the high-quality  $\text{CH}_3\text{NH}_3\text{SnI}_3$ -perovskite and its composite have been synthesized.

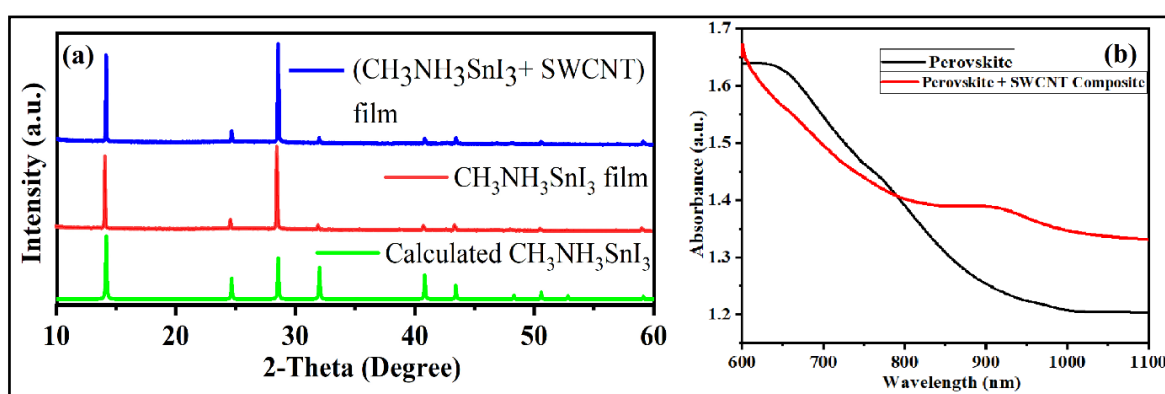


**Figure 4.3: (a) PXRD of experimentally observed  $\text{CH}_3\text{NH}_3\text{SnI}_3$  perovskite (Red), its composite with SWCNT (Blue), and referenced COD ID #7015448 sample (Green) in the two-theta range of  $10^\circ$ - $60^\circ$  (b) Solid state absorption spectra of  $\text{CH}_3\text{NH}_3\text{SnI}_3$  perovskite thin film in the range of 500-1100 nm**

All of the measured peaks matched the reference data COD ID #7015448. However, no additional signal was identified in the composite sample, possibly due to the low-intensity amorphous nature of carbon. This indicates that the addition of SWCNT did not affect the crystal structure of  $\text{CH}_3\text{NH}_3\text{SnI}_3$  perovskite. As a result, the device is projected to have a combined performance of optoelectronic capabilities of perovskite and SWCNT as an additive.

**Figure 4.3(b)** shows the optical properties of  $\text{CH}_3\text{NH}_3\text{SnI}_3$  films and their composite. The  $\text{CH}_3\text{NH}_3\text{SnI}_3$  is very sensitive in an open atmosphere hence, the thin films prepared for solid-state UV-Vis. spectroscopy were measured immediately. The absorption of  $\text{CH}_3\text{NH}_3\text{SnI}_3$  perovskite has increased from wavelength 939 nm, which corresponds to the optical bandgap of 1.32 eV, which is nearly the same as previously reported [6]. However, the synergistic action of both individuals has modified the exciton and improved light absorption, as there is a peak at 920 nm. The result shows that the composite sample has greater absorption in the visible region than only perovskite. This may lead to better optoelectronic performance in the presence of SWCNTs.

#### 4.4.2 X-ray Photoelectron Spectroscopy (XPS)

The XPS measurement was used to analyse the elemental composition and states of the elements present in the SWCNTs-perovskite composite sample. **Figure 4.4** depicts XPS measurements of the as-synthesized composite sample. The stoichiometric ratio of C, N, Sn, and I of  $\text{CH}_3\text{NH}_3\text{SnI}_3$  is 1:1:1:3 for the ideal case whereas from the analysis of **Figure 4.4**, the experimentally obtained ratio is 3.2:1.02:1.01:3.8 which is very close to the ideal value except for C. The higher value in element C is due to the presence of SWCNT. The main XPS peak positions of  $\text{I}3\text{d}_{5/2}$ , C1s, N1s, and  $\text{Sn}3\text{d}_{5/2}$  are 618.8, 284.4, 401.57, and 487 eV, respectively. The peak of Sn is mainly composed of one kind of tin, indicating that the +2-oxidation state of Sn is the only present [7]. The band of carbon C1s (1) lies at 284.4 eV representing SWCNT and the carbon component of methylammonium of perovskite composite. An additional deconvoluted carbon signal was arisen at 285.9 eV due to the surface defect at the perovskite grain or impurity from the deposition setup [7].

To determine the valence band maximum binding energy of the device, XPS measurements were taken in the valence band region of the material in the energy range of -3 to 5 eV, as shown in **Figure 4.5(a)**. It is standard procedure to linearly extend the strong emission onset to background intensity to calculate the magnitude of the valence band maximum from photoemission valence band spectra.

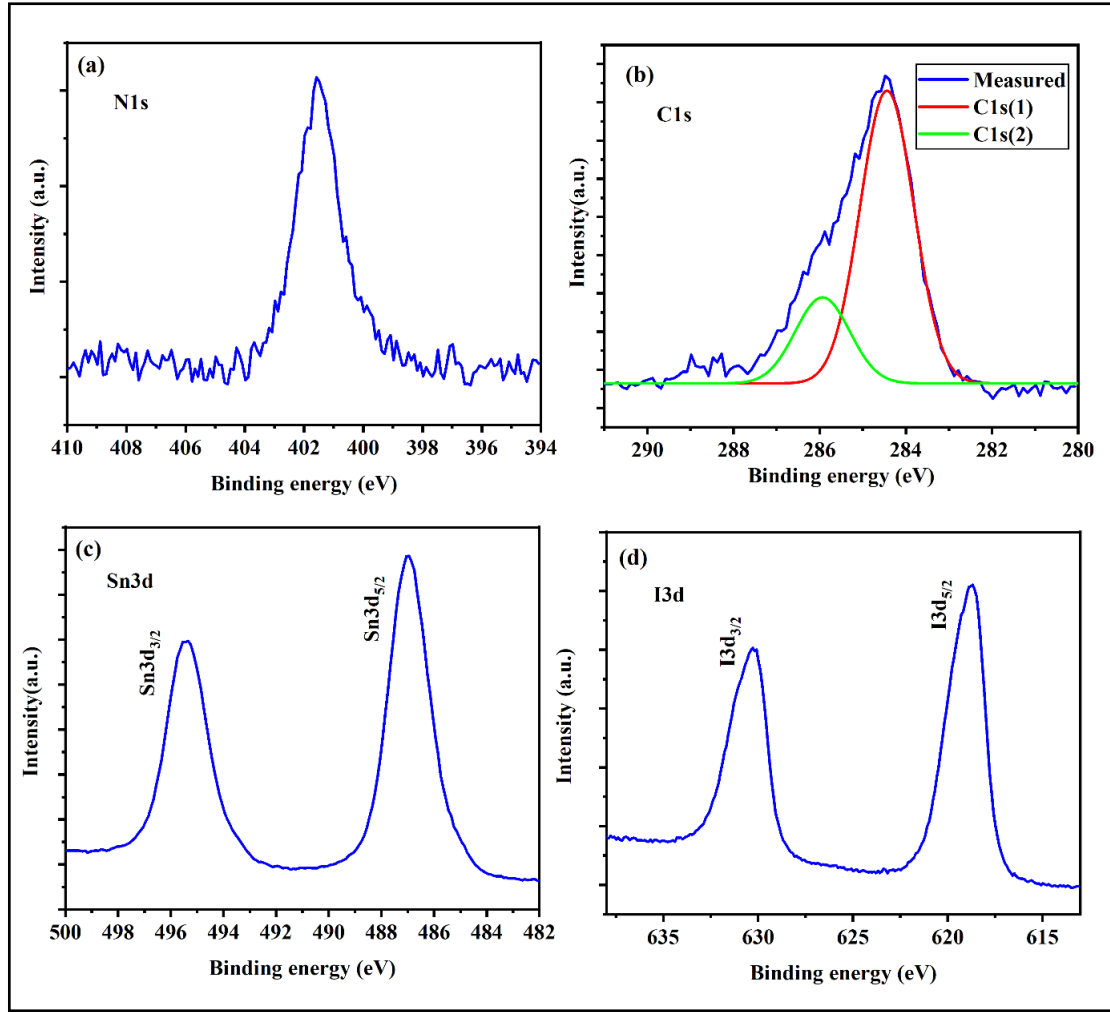


**Figure 4.4: Details XPS measurements of various elements present in the  $\text{CH}_3\text{NH}_3\text{SnI}_3$ -SWCNT composite sample**

The small amount of extra emission above this start might be attributed to the shallow gap states. The measurement showed that the sample is a p-type material with a valence band maximum (VBM)- $E_F$  of 0.43 eV. **Figure 4.5(b)** shows that Tauc's plot of absorbance spectra provides an optical bandgap of 1.32 eV. Using a work function of 4.75 eV [8] for  $\text{CH}_3\text{NH}_3\text{SnI}_3$  perovskite, a band diagram can be drawn, as shown in **Figure 4.5(c)**, which may be used for the initial selection of suitable hole and electron extraction layers based on the basic vacuum level alignment.

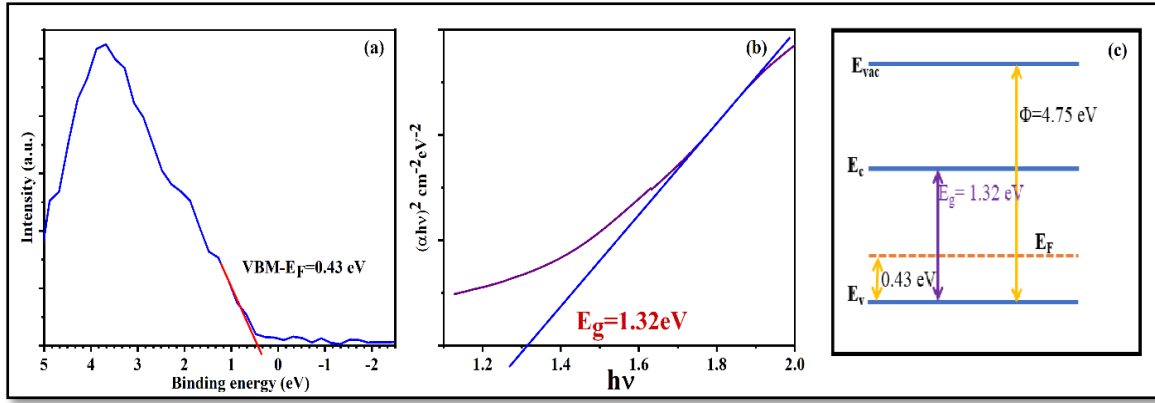


**Figure 4.5:** (a) XPS in the valence band region of composite perovskite (b) Tauc's plot to determine the optical bandgap of the perovskite (c) Concluded band diagram of the sample from (a) and (b), shows  $\text{CH}_3\text{NH}_3\text{SnI}_3$  is a p-type semiconductor

#### 4.4.3 FESEM and TEM

The structural characteristic of the perovskite and SWCNTs composite film has been analysed using FESEM. The film morphology of the as-prepared perovskite and its composite with SWCNTs have been demonstrated in **Figure 4.6(a) and (b)**, respectively. The SEM image of the pure perovskite film **Figure 4.6(a)** shows excellent particle distribution over the area. **Figure 4.6(b)**, on the other hand, clearly shows that some SWCNTs are visible on the surface of the perovskite grain, while the remainder is tightly embedded within the matrix. The TEM image **Figure 4.6(c)** provides a comparable confirmation. The TEM image displays the composite of perovskite and SWCNT, as well as how an SWCNT functions as a channel line to carry carries from one composite grain area to another. This implies that SWCNTs facilitate the collection of photogenerated carriers and their extraction to the surface, where the electrode is attached.

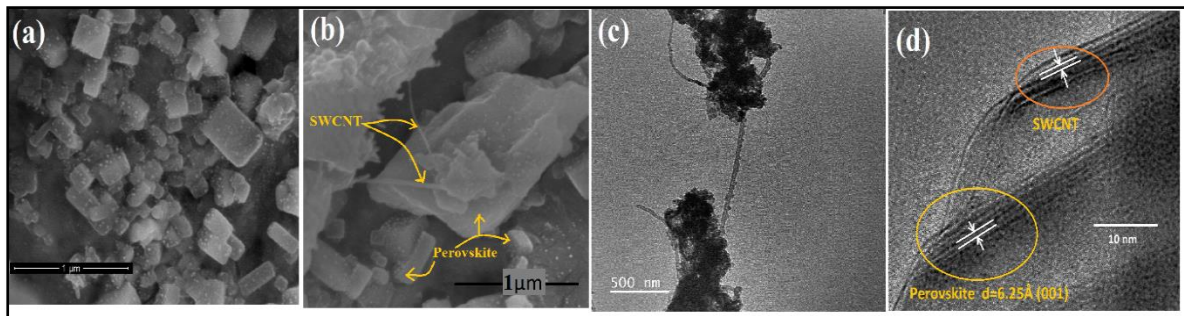


**Figure 4.6:** (a) FESEM images of  $\text{CH}_3\text{NH}_3\text{SnI}_3$  (b) and (c) represent FESEM and TEM image of SWCNT-perovskite composite shows SWCNT acts as a channel to carrier (d) TEM micrograph of a perovskite: SWCNTs composite with perovskite and SWCNTs nearby, producing intimate interfaces

In addition to SEM, HRTEM was utilized to study the crystal structure and interface properties of the perovskite and SWCNTs composite samples. The TEM image, shown in **Figure 4.6(d)** of the composite sample further demonstrates that crystalline perovskite is in close contact with SWCNTs, allowing efficient photoexcited charge carrier transport between the perovskite matrix and SWCNTs. The majority of areas show perovskite's (001) crystal planes, which suggests that the perovskite layers are flat on the ITO electrode. Additionally, in some regions, SWCNTs planes may also be seen.

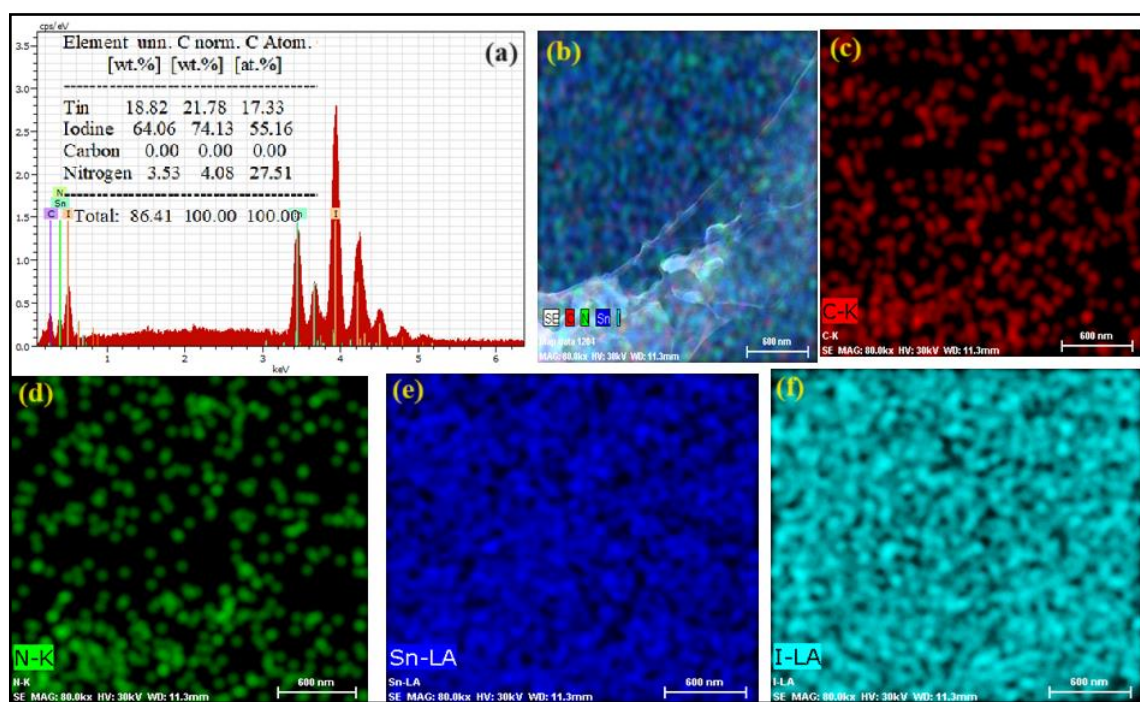


**Figure 4.7: (a) EDX spectra of the composite sample (inset shows the EDX compositional values of perovskite-SWCNT composite) (b)-(f) demonstrates its corresponding elemental (C, N, Sn, I) mapping**

Again, to ensure the elemental composition of the material, the EDS of the sample has been taken with an extra attachment from Bruker's Quantax 200 associated with the FESEM instrument. **Figure 4.7(a)** shows the EDS spectrum where the x-axis and y-axis represent dispersive energy in keV and count per sec (cps)/eV respectively. The elemental ratios and corresponding elemental mapping of the sample have been shown in inset of **Figure 4.7(a)** and **Figure 4.7(b)-(f)**. All these measurements show that the elements N, Sn, and I within the  $\text{CH}_3\text{NH}_3\text{SnI}_3$  composite exist in almost stoichiometry atomic proportion (1.58:1:3.18). The stoichiometry atomic proportionality for hydrogen and carbon was not acquired due to the

restriction of the measuring instrument. Moreover, the elemental composition is inferring that the organic-inorganic  $\text{CH}_3\text{NH}_3\text{SnI}_3$  perovskite was appropriately produced.

#### 4.4.4 Fourier Transform Infrared Spectroscopy (FTIR) and Thermal Gravimetric Analysis (TGA)

The relative transmittance spectre's have been depicted in **Figure 4.8(a)** of  $\text{CH}_3\text{NH}_3\text{SnI}_3$  and its composite with SWCNTs in the range of  $780$  to  $3500\text{ cm}^{-1}$  to investigate bonds in the samples. It can be seen from the figure that the vibrational peaks of both samples are similar except for a small band at  $1737\text{ cm}^{-1}$  which arises due to  $\text{C}=\text{O}$  of carbonyl stretching of the  $-\text{COOH}$  group of SWCNT. The peak at  $3101.62\text{ cm}^{-1}$  signifies hydroxyl group ( $\text{O}-\text{H}$ ) arises due to contaminated moisture in samples during measurements. The remaining vibrational peaks were identified in both samples due to the amine group ( $\text{CH}_3\text{NH}_3$ ). The band at  $2889.26\text{ cm}^{-1}$  is formed by symmetric stretching of the amine's  $\text{N}-\text{H}$  bond [9]. The in-plane bending vibration of  $\text{N}-\text{H}$  is shown by the peak at  $1568.69\text{ cm}^{-1}$ . The deformation and in-plane bending vibrations of  $\text{C}-\text{H}$  are represented by the bands at  $1420.01\text{ cm}^{-1}$  and  $1462.08\text{ cm}^{-1}$ . The weak bands at  $1246.11\text{ cm}^{-1}$ ,  $1179.52\text{ cm}^{-1}$ , and  $965.01\text{ cm}^{-1}$  are mostly caused by the weak  $\text{NH}_2$  rocking vibration, as well as amine stretching caused by the strong force between the  $\text{C}-\text{N}$  bonds and  $\text{C}-\text{N}$  bending [10,11]. The  $\text{N}-\text{H}$  wagging vibration generated by the change in  $\text{H}$ -bonding causes the peak at  $906\text{ cm}^{-1}$ . Once more, the FTIR measurements show that the chemical structure of perovskite has not changed. As a result, the sample's strong optoelectronic potential was not affected. SWCNT additives are used to improve the charge transport process in  $\text{CH}_3\text{NH}_3\text{SnI}_3$ -based devices.

The thermal stability of  $\text{CH}_3\text{NH}_3\text{SnI}_3$  perovskite and its SWCNT composite was tested under  $\text{N}_2$  flow from  $26^\circ\text{C}$  to  $500^\circ\text{C}$ . The thermograms shown in **Figure 4.8(b)** demonstrate diverse areas of weight loss, with a significant weight loss recorded from  $143.15^\circ\text{C}$  to  $312.18^\circ\text{C}$ . There is a weight loss of around 7% below  $143.15^\circ\text{C}$ , which can be related to the evaporation of the moisture absorbed by the materials. At this phase, no thermal degradation of the material was observed. In the following stage, a weight loss of 85 % was observed in  $\text{CH}_3\text{NH}_3\text{SnI}_3$  perovskite between  $143.15$  and  $232.75^\circ\text{C}$  and a weight loss of 57 % in  $\text{CH}_3\text{NH}_3\text{SnI}_3$ -SWCNT composite between  $143.15$  and  $192.23^\circ\text{C}$ . It can be interpreted to mean that the perovskite began to break owing to decomposition at about  $143.15^\circ\text{C}$ . The perovskite is broken down into  $\text{CH}_3\text{NH}_3\text{I}$  and  $\text{SnI}_2$ . Because the sublimation temperatures of  $\text{CH}_3\text{NH}_3\text{I}$  and  $\text{I}$  are around  $150^\circ\text{C}$  and  $184^\circ\text{C}$ , respectively, the obtained  $\text{CH}_3\text{NH}_3\text{I}$  sublimates quickly.

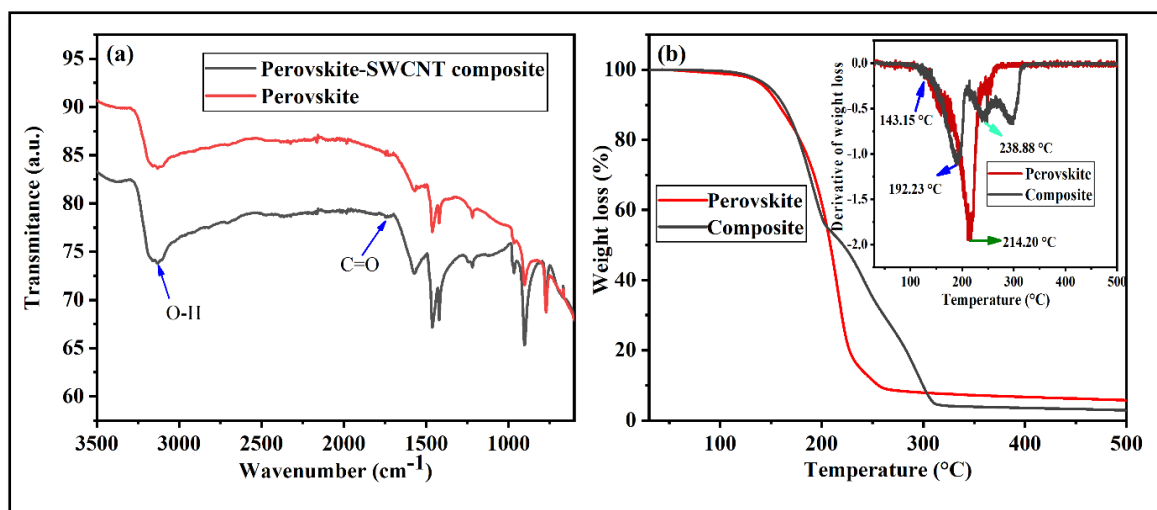


**Figure 4.8:** (a) IR spectra in the range of 500-3500 cm<sup>-1</sup> (b) TGA in the range of 27-500 °C of CH<sub>3</sub>NH<sub>3</sub>SnI<sub>3</sub> perovskite and its composite with SWCNT. The inset of the figure (b) represents the corresponding first derivative of TGA showing the major change in the curve

In contrast to the composite sample, as the SWCNT is thermally and mechanically stable so composite sample slowed down its mass loss. Though in the next step, SWCNT- perovskite composite steadily decayed its mass and produces residue in only 8% of the sample. When SnI<sub>2</sub> and SWCNT were sublimated at high temperatures, an 8 % final residue was produced. SnO<sub>2</sub> might be the ultimate remnant [12,13]. The corresponding first derivative of the whole decomposition for samples is shown in **Figure 4.8(b)** as an inset. The major temperature change occurs at 143.15 and 214.20 °C in the case of perovskite only and 143.15, 192.23, and 238.88 °C for SWCNT-perovskite composite. The former is due to water volatilization and the breakdown of the minor amounts of leftover CH<sub>3</sub>NH<sub>3</sub>I from the synthesizing process on the surface, whereas the latter is due to the perovskite sample and SWCNT disintegration. Thermal gravimetric analysis assisted in determining the range of thermal stability of the materials. In the next work, a temperature-dependent I-V investigation of the device was carried out till 90 °C, taking into account the thermal stability of the sample.

#### 4.4.5 Optoelectronic Study

The I-V characteristics were recorded as shown in **Figure 4.9(c)** and **(d)** at 300 K with and without light (Intensity 100 mW.cm<sup>-2</sup>) by applying bias within  $\pm 1.5$  V across two particular thin film-based ITO/CH<sub>3</sub>NH<sub>3</sub>SnI<sub>3</sub>/Al and ITO/composite CH<sub>3</sub>NH<sub>3</sub>SnI<sub>3</sub>/Al devices. The I-V characteristics exhibit a highly nonlinear rectifying nature in both dark and light circumstances,

indicating the Schottky behaviour of the device. To form a Schottky junction, the work function of the electrode has to be higher than that of the semiconductor. **Figure 4.9(a)** depicts the energy level diagram of the various layers, whereas **Figure 4.9(b)** demonstrates the band diagram of the device. According to the energy level diagram, Al has a lower work function ( $\phi_b = 4.2$  eV) than semiconducting perovskite ( $\phi_b = 4.75$  eV), although ITO has a higher work function than perovskite.

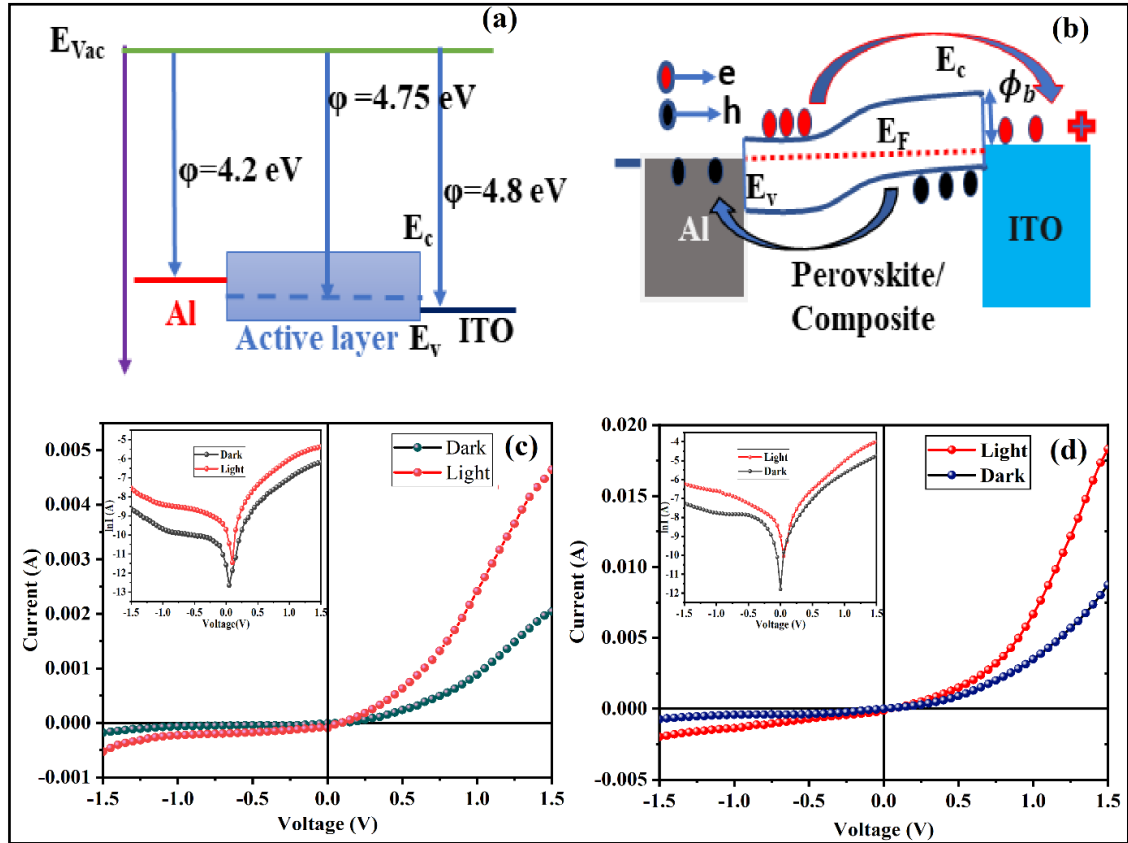


**Figure 4.9:** (a) Energy level diagram of the different layers (b) Device band alignment in a forward biased situation. Dark and light I-V characteristics of the device (c) ITO/CH<sub>3</sub>NH<sub>3</sub>SnI<sub>3</sub>/Al and (d) ITO/CH<sub>3</sub>NH<sub>3</sub>SnI<sub>3</sub>-SWCNT/Al measured at room temperature. The corresponding  $\ln I$  vs.  $V$  plot has been presented in the inset of both graphs

As a result of the development of the Schottky junction at the ITO/perovskite interface, the device exhibits Schottky behaviour, and the Al/perovskite interface behaves as an ohmic contact. **Figure 4.9(b)** depicts the presence of a barrier height ( $\phi_b = 0.682$  eV) at the junction formed by the diffusion of ITO and perovskite carriers to create built-in potential.

When a bias voltage was applied, the built-in potential drops according to the strength of the bias, and electrons transfer to the ITO electrode from the perovskite. However, when a reverse

bias is applied, the carriers are unable to pass to perovskite from ITO due to the existence of a high barrier height. As a result, a high rectification ratio is obtained from the device. The rectification ratios ( $I_{on}/I_{off}$ ) calculated at 1.5 V from the plots are 11.49 in the dark and 8.82 in the light for the perovskite-based device, and 11.92 in the dark and 10.17 in the light for the SWCNT-based device. The values of electrical conductivities are enlisted in **Table 4.1** of both devices, which shows that in presence of SWCNTs electrical conductivity has improved by 4.21 and 4.94 times in dark and light conditions, respectively. In the presence of photo illumination, conductivities improved by 2.13 and 2.50 times on devices without and with SWCNTs, respectively.

This improvement in conductivity in the presence of SWCNTs alludes to the smooth transmission of charge across the sample. The increase in conductivities in the presence of light shows the photosensitivity of the device. This increase in current under light encouraged us to analyse the photo-sensing characteristics of the devices.

In this regard, the photosensitivity ( $P_s$ ), responsivity ( $R$ ), the detectivity ( $D^*$ ), and photoconductive sensitivity ( $S$ ) have been estimated. The photosensitivity ( $P_s$ ) is expressed as the ratio of the produced photocurrent  $I_{pc}$  (where  $I_{pc} = I_{light} - I_{dark}$ ) to the current in the dark ( $I_{dark}$ ). This can be written as,

$$P_s = \frac{I_{pc}}{I_D} \quad (4.1)$$

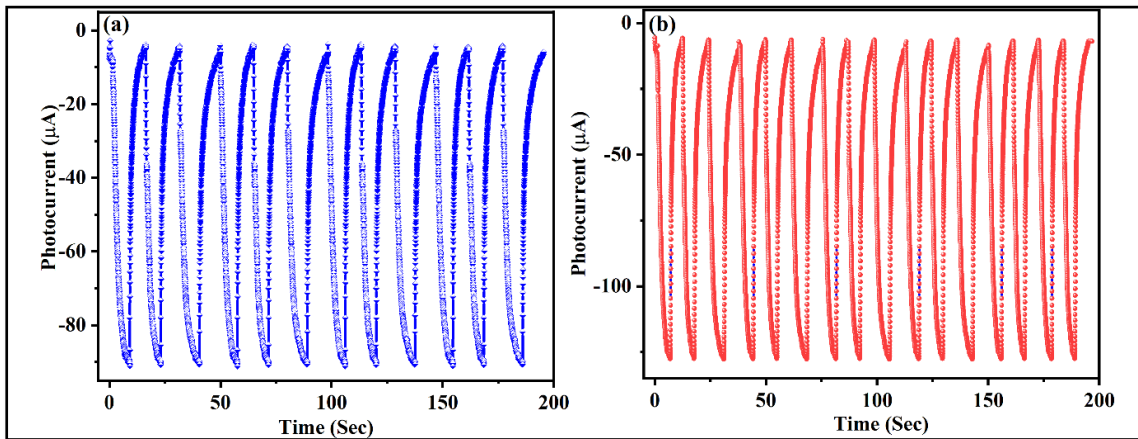


**Figure 4.10: Photocurrent growth in (a) perovskite device only (b) SWCNT and perovskite composite device. The figures show the first switching in presence of SWCNT in the perovskite active layer**

To get exact information on the potential applicability of the Schottky diode as a photodetector, the photoresponsivity ( $R$ ) and specific detectivity ( $D^*$ ) have been evaluated. The

photoresponsivity (R) is the ratio of produced photocurrent density to the incident optical power which can be expressed as the following equation,

$$R = \frac{I_{pc}}{P_i A_{ef}} \quad (4.2)$$

Where  $P_i$  is the incident optical power which is  $1000 \text{ W m}^{-2}$  for this study and  $A_{ef} (=3.6 \times 10^{-5} \text{ m}^2)$  is the effective area of the diode. Specific detectivity ( $D^*$ ) gives information about the suitability of the diode as a photodetector which has been given by the relation,

$$D^* = \frac{R}{\sqrt{2qI_D}} \quad (4.3)$$

Where  $q$  is the charge. Another important parameter, the photoconductive sensitivity (S), has been estimated using the following equation:

$$S = \frac{L I_{pc}}{V \cdot P_i \cdot A_{ef}} \quad (4.4)$$

It gives a conception of the improvement in conductivity due to the incidence of light with a certain supplied input power at a definite voltage. All these photo-sensing parameters have been listed in **Table 4.1**. The results reveal that the perovskite's S and  $D^*$  have been improved due to an increase in photosensitivity. This is due to the incorporation of SWCNT in the perovskite, which results in reduced recombination of the carriers in the active layer, indicating more collection at the electrode.

**Table 4.1: Photosensing parameters of the  $\text{CH}_3\text{NH}_3\text{SnI}_3$  perovskite Schottky devices**

Device structure	Condi tions	Electrical conductivi ty(S/m)	Rectific ation ratio	Photo sensi vity ( $P_s$ )	Respon sivity (R) ( $\text{AW}^{-1}$ )	Specific detectivit y ( $D^*$ ) (Jones)	Photocon ductivity sensitivity (S) ( $\text{m } \Omega^{-1} \text{ W}^{-1}$ )
ITO/ $\text{CH}_3\text{NH}_3\text{SnI}_3$ /Al	Dark	$3.8 \times 10^{-5}$	11.49	1.10	0.07	$2.73 \times 10^9$	$4.66 \times 10^{-8}$
	Light	$8.1 \times 10^{-5}$	8.82				
ITO/ $\text{CH}_3\text{NH}_3\text{SnI}_3$ +SWCNTs/Al	Dark	$1.6 \times 10^{-4}$	11.92	1.54	0.27	$5.10 \times 10^9$	$1.80 \times 10^{-7}$
	Light	$4.0 \times 10^{-4}$	10.17				

**Figure 4.10** depicts the photocurrent switching in both devices, demonstrating that zero bias devices have good photosensing and switching behaviour, but devices incorporating SWCNT execute first switching and create more photocurrent due to the strong photosensitivity of the SWCNT-CH<sub>3</sub>NH<sub>3</sub>SnI<sub>3</sub> perovskite composite. Therefore, the strong photosensitivity and specific detectivity in visible light of the composite make it an excellent candidate for photodiode applications.

The I-V analysis of Schottky device electrical characteristics is an efficient method for determining fundamental performance parameters. To study the I-V relationship, it has been considered that the charge conduction at the metal oxide-semiconductor junction is due to the thermionic emission (TE) effect. To explore the charge transport phenomena following standard **Equations 4.5** have been considered [14].

$$I = I_0 \left[ \exp \left( \frac{qV}{\eta kT} \right) - 1 \right] \quad (4.5)$$

Where V,  $\eta$ , q, k, and T are the applied bias voltage, the ideality factor, the electronic charge, the Boltzmann constant, and the operating temperature in kelvin respectively. The reverse saturation current,  $I_0$  extracted from the straight-line intercept of  $\ln(I)$  at  $V = 0$  and can be expressed by Richardson-Schottky TE theory as

$$I_0 = A_{ef} A^* T^2 \exp \left( -\frac{q\phi_b}{kT} \right) \quad (4.6)$$

Where  $\phi_b$  is the barrier height (BH) at the junction,  $A_{ef}$  is the effective area of the Schottky diode which is  $3.6 \times 10^{-5} \text{ m}^2$ ,  $A^*$  represents the effective Richardson constant. In most of the literature the value of  $A^*$  is considered as  $1.20 \times 10^6 \text{ AK}^{-2} \text{ m}^{-2}$  which is agreed for most of the semiconductor materials but literature shows that it varies from device to device. Again, the precise value of this parameter is essential since it is utilized to estimate the different device performance factors such as barrier height and series resistance.

Therefore, it is best practice to estimate the Richardson constant for a specific device before calculating the electrical parameters of any device. Hence in this work, for CH<sub>3</sub>NH<sub>3</sub>SnI<sub>3</sub> perovskite-based device, the value of  $A^*$  has been estimated using the Richardson plot depicted in **Figure 4.11**. The value of  $A^*$  is estimated as  $2.54 \times 10^{-4} \text{ A cm}^{-2} \text{ K}^{-2}$  from the intercept of this plot and this value has been used to calculate different parameters in this work. However, the slope of this graph also provides the value of voltage-dependent barrier height sometimes

known as the activation energy of the device. The voltage-dependent barrier height is found to be 0.28 eV.

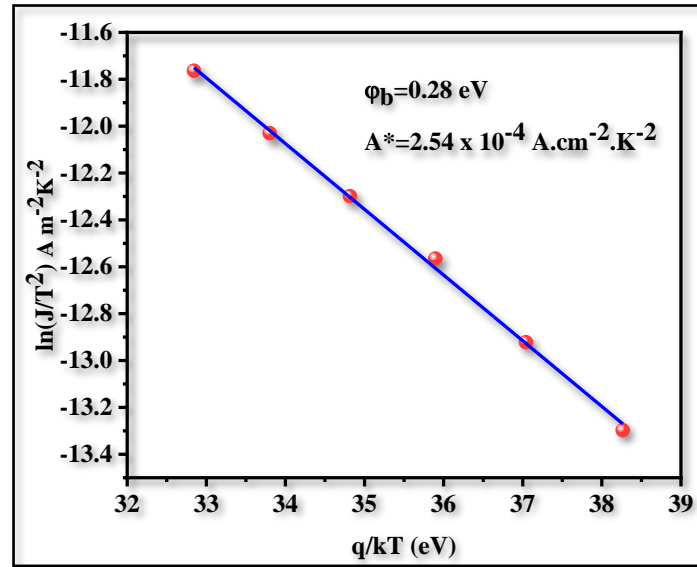


**Figure 4.11: Temperature dependent Richardson plot to estimate Richardson constant and voltage dependent barrier height**

Now, the temperature-dependent apparent BH at zero bias is provided by **Equation 4.7**.

$$\phi_b = \frac{kT}{q} \ln \left( \frac{AA^*T^2}{I_0} \right) \quad (4.7)$$

Another important parameter of a diode is ideality factor ( $\eta$ ) which describes the deviation of experimental I-V from ideal TE theory and can be obtained from **Equation 4.5** given by,

$$\eta = \frac{q}{kT} \left[ \frac{dV}{d(\ln I)} \right] = \frac{q}{kT} \times \frac{1}{\text{Slope of } \ln I \text{ vs. } V \text{ plot}} \quad (4.8)$$

The values of the  $\eta$  and  $\phi_{b0}$  of the Schottky devices obtained from the slope and intercept respectively of  $\ln I$  vs.  $V$  plots listed in **Table 4.2**. Generally, the ideal value of  $\eta$  of the Schottky devices is 1 but practically it is greater than 1 due to the existence of barrier inhomogeneity at the metal perovskite junction [15].

The Cheung and Cheung model was used to derive Schottky parameters such as series resistance ( $R_s$ ),  $\phi_{b0}$  and  $\eta$  using forward bias I-V characteristics. According to this method, the I-V behaviour of Schottky diodes may be expressed as follows,

$$\frac{dV}{d(\ln I)} = IR_s + \frac{\eta kT}{q} \quad (4.9)$$

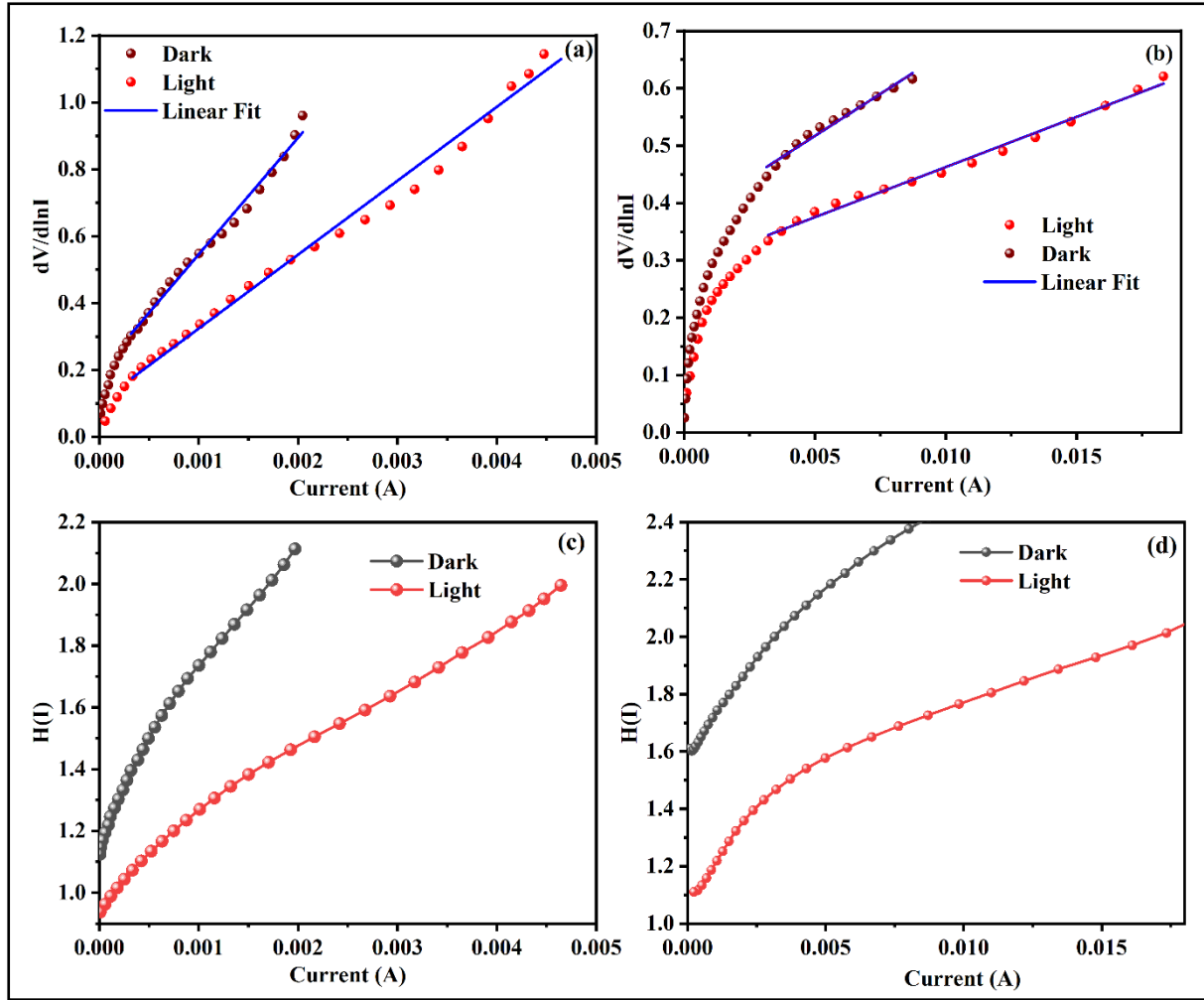


**Figure 4.12:** (a) and (b) depict  $dV/d\ln I$  vs.  $I$  and  $H(I)$  vs.  $I$  plot of ITO/ CH<sub>3</sub>NH<sub>3</sub>SnI<sub>3</sub>/Al device whereas (c), (d) represent the same plots of ITO/CH<sub>3</sub>NH<sub>3</sub>SnI<sub>3</sub>+ SWCNT/Al device in presence of light and dark conditions, respectively to estimate  $\phi_b$ ,  $\eta$ , and  $R_s$  of the devices

The  $dV/d\ln(I)$  vs.  $I$  plot for all devices under both conditions in the dark and under illumination have been demonstrated in **Figure 4.12(a)** and **(b)**. The values of  $R_s$  and  $\eta$  have been obtained from the slope and the y-axis intercept of the linear region of this plot. Using the previously estimated value of  $\eta$ , we have calculated  $\phi_{b0}$  and  $R_s$  using another Cheung and Cheung equation, which is specified as [16],

$$H(I) = V - \frac{\eta kT}{q} \ln \left( \frac{I}{AA^*T^2} \right) \quad (4.10)$$

$$= \eta \phi_{b0} + R_s I \quad (4.11)$$

The y-axis intercept of the linear region of the  $H(I)$  vs.  $I$  graph in **Figure 4.12(c)** and **(d)** indicates the values of  $\phi_{b0}$ , while the slopes reflect  $R_s$  for all devices. The value  $R_s$  obtained

from **Equation 4.11** using the  $H(I)$  vs.  $I$  plot also provides a second estimation of the series resistance. **Table 4.2** shows obtained values of  $\eta$ ,  $\phi_{b0}$ , and  $R_s$ .

**Table 4.2: The values of Schottky device parameters like ideality factor ( $\eta$ ), barrier height ( $\phi_b$ ), and series resistance ( $R_s$ ) estimated using different methods**

Cell	Condition	Experimental I-V analysis		dV/dlnI vs. I		H(I) vs. I	
		$\eta$	$\phi_b$ (eV)	$R_s$ ( $\Omega$ )	$\eta$	$\phi_b$ (eV)	$R_s$ ( $\Omega$ )
Perovskite	Dark	2.94	0.39	348.25	3.01	0.42	385
	Light	2.61	0.37	220.56	3.80	0.36	196
Perovskite+ SWCNT Composite	Dark	5.10	0.32	34.80	4.35	0.35	72
	Light	3.49	0.31	19.20	4.00	0.33	34

The values of the ideality factor under the dark condition diverged from the ideal behaviour due to barrier height inhomogeneities, a high chance of hole and electron recombination in the forbidden region, and the existence of interface states and series resistance [17,18]. However, when both devices were illuminated, the ideality factor value decreased. After soaking light, the  $R_s$  of all compounds drop, which may be due to the excess electron-hole pair generation in the sample. The presence of SWCNT reduces the value of  $\eta$ , indicating that SWCNT works as a filler in the traps present in the sample. As a result, interfacial trap states are minimized, indicating improved junction formation between the sample and electrode. The decrease in  $R_s$  indicates that SWCNT functions as a transporter for the carrier in the sample, reducing recombination and prompting the device for faster performance.

Additionally, some parameters like built-in potential ( $V_{bi}$ ), acceptor concentration ( $N_A$ ), and barrier height ( $\phi_b$ ) have been estimated using C-V measurements of the devices in the range of  $\pm 1.4$  V. The Mott-Schottky plot of C-V measurement is shown in **Figure 4.13**.

The depletion capacitance of the devices can be expressed as [19],

$$\frac{1}{C^2} = \frac{2(V_{bi}+V)}{q\epsilon_s A^2 N_A} \quad (4.12)$$

Where,  $V_{bi}$ ,  $V$ ,  $\epsilon_s$ ,  $A$ , and  $N_A$  are built-in-potential, applied bias, dielectric constant ( $\epsilon_s = \epsilon_0$ ), area of the device, and acceptor concentration of the device, respectively. The intercept of the  $1/C^2$  vs.  $V$  plot to the x-axis gives the value of  $V_{bi}$  which is 0.29 eV for the perovskite device only and 0.10 eV for the Perovskite and SWCNT composite-based device, respectively. Therefore, the barrier height ( $\phi_b$ ) of the device can be written as  $\phi_b = V_{bi} + E_F$ , (image force lowering and  $kT/q$  effect ignored)  $E_F$  is the difference between the fermi level and valence band maximum after the formation of the band. The value of  $E_F$  is 0.43 can be approximated from the band diagram obtained from the XPS measurement.

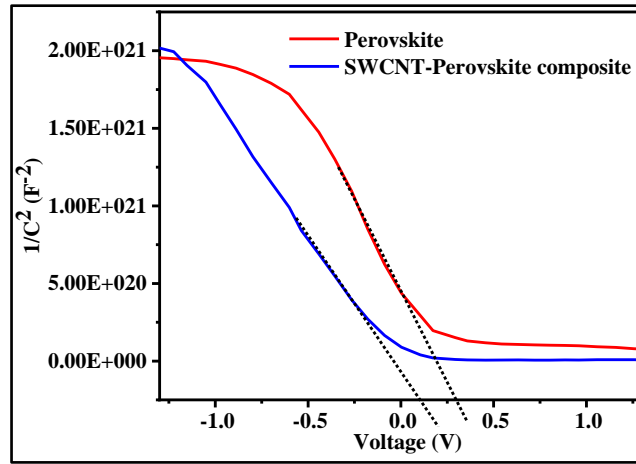


**Figure 4.13:  $1/C^2$  vs. voltage measurements of devices to estimate acceptor density and barrier height**

The barrier height was estimated as 0.72 eV for the perovskite-based device and 0.53 eV for the composite-based device. The negative slope behaviour of the Mott-Schottky plot again confirms the p-type nature of the sample. From the slopes of **Figure 4.13**, the values of  $N_A$  have been evaluated as  $5.53 \times 10^{18} \text{ cm}^{-3}$  and  $3.66 \times 10^{18} \text{ cm}^{-3}$  for perovskite and composite-based devices, respectively. It is found that the barrier height estimated from capacitance measurements of the ITO/sample contact as a function of voltage surpasses the I-V measured barrier height. Although the existence of excess capacitance at ITO/sample contacts due to an interfacial dielectric layer or trap states in the semiconductor could explain this discrepancy, the presence of barrier height inhomogeneity and image force lowering effect provides another explanation [17,20]. However, the acceptor density of the device with SWCNT was reduced by almost half of the value of the device without SWCNT, indicating that the carrier density is improved owing to the incorporation of SWCNT, which may lead to enhanced device conductivity.

To get better insight into the conduction mechanism of the devices, I-V characteristics were analysed considering the influence of traps in these systems. We previously [21,22] reported that trap charges play a major role in the current conduction mechanism of Schottky devices. Sn-based perovskite films are generally formed using the low-temperature solution-processable method, so the resulting film is highly possible to be polycrystalline and full of grain boundaries (GB). Also, in Sn-based perovskite, there is a high possibility of the formation of oxidation vacancies due to the transformation of  $\text{Sn}^{2+}$  to  $\text{Sn}^{4+}$ . As a result of the presence of surface defects, structural disorders, and oxidation vacancies, there is a high density of trap states at interfaces between perovskite grains in the form of GBs and in the bulk sample in the form of vacancy states, which severely damages the optoelectronic properties of the films [23–26]. It is generally believed that defects at GBs and trap states play a significant impact in defining the optoelectronic performance of the device. These traps state add extra energy levels to the energy. In presence of the trap states, the majority of the carriers injected from the electrodes are trapped and are usually crowded around the electrodes. When this mechanism dominates, it is referred to as trap charge limited conduction (TCLC). When the space charges become free carriers, the process is known as trap-free SCL conduction [27,28]. The trap energy level distribution can be characterized in one of three ways: (i) as discrete levels (ii) as an exponential distribution, or (iii) as a Gaussian distribution [29,30]. The semi-logarithmic plot of I-V measurements is often used to understand which kind of trap is present in the sample. The analysis of the trap-assisted electrical properties of various devices offers an efficient method for determining fundamental performance parameters. The  $\ln I$  vs.  $\ln V$  graph demonstrates that the current conduction process changes after a particular voltage. This transition voltage is known as the threshold voltage ( $V_{th}$ ). Before  $V_{th}$ ,  $I \propto V$ , which refers to ohmic transport, and beyond  $V_{th}$ ,  $I \propto V^m$ , where ( $m \geq 2$ ) is the slope of  $\ln I$  vs.  $\ln V$ .

The value of  $m=2$  has two approaches, which are SCLC given by Mott-Gurney [31] and discrete trap level distributed SCLC given by low current. The value of  $m$  greater than 2 indicates the existence of an exponential trap in the film. **Figure 4.14(a)** and **(b)** show the regional linear fittings of  $\ln I$  vs.  $\ln V$  plots of ITO/ $\text{CH}_3\text{NH}_3\text{SnI}_3$ /Al and ITO/ $\text{CH}_3\text{NH}_3\text{SnI}_3$ +SWCNT/Al device structures, respectively. The slopes of Region I of both graphs show the ohmic behaviour of the device with negligible electron-hole recombination as the value of  $m$  is nearly 1 in **Table 4.3**. In Region II,  $m$  is greater than 2, indicating the presence of exponential trap distribution in the films. The exponential trap states distribution is given by, [30]

$$g(E) = \frac{N_t}{k_B T_t} \exp\left(-\frac{E}{k_B T_t}\right) \quad (4.13)$$

Where  $k_B$  is Boltzmann constant,  $N_t$  is the total trap concentration, and  $T_t$  is the characteristic temperature of the exponential trap distribution correlated to  $E$ .

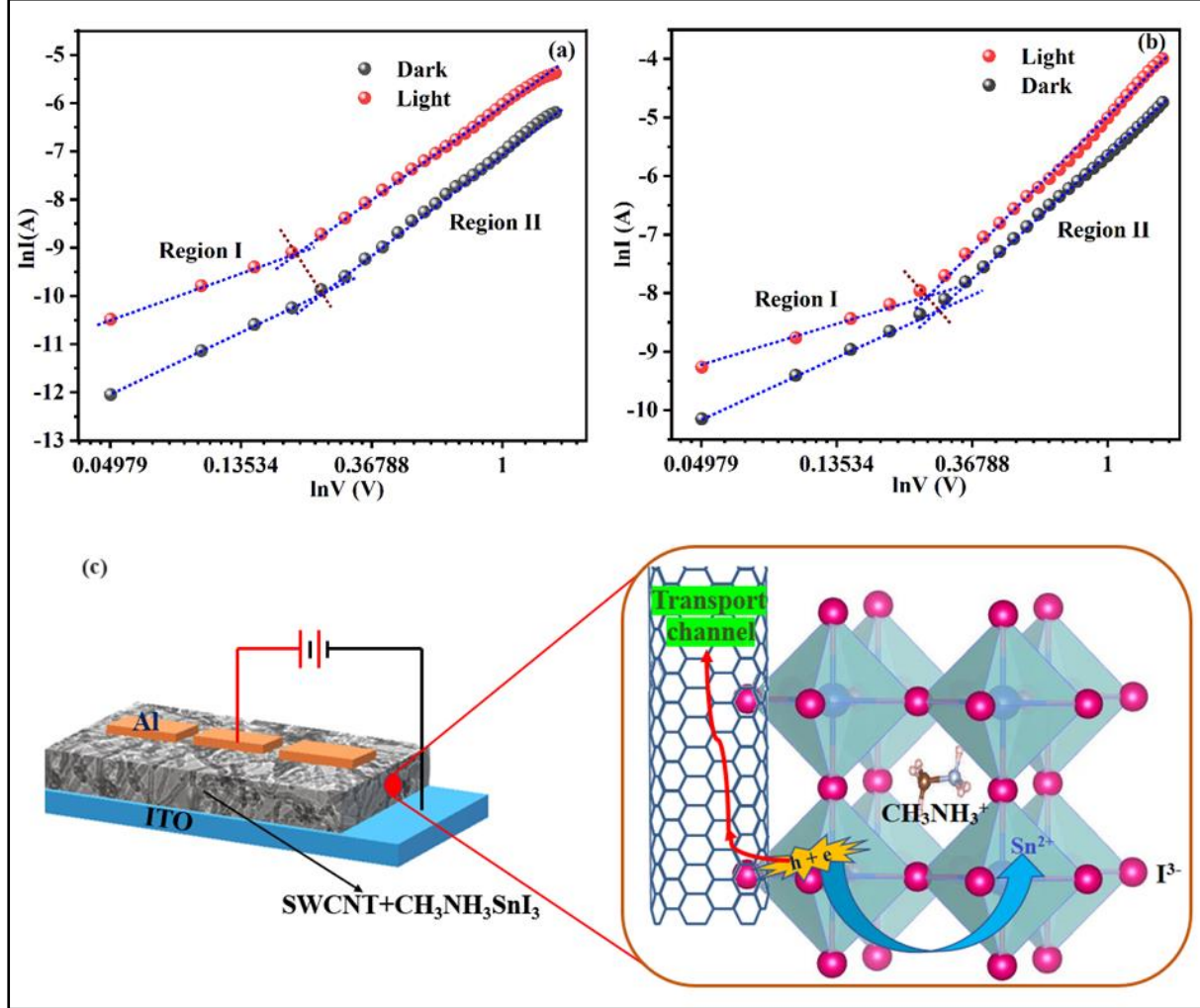


**Figure 4.14:**  $\ln I$  vs.  $\ln V$  curves of both (a) perovskite and (b) perovskite and SWCNT composite devices under dark and illumination conditions (c) shows Al/CH<sub>3</sub>NH<sub>3</sub>SnI<sub>3</sub>+SWCNT/ITO device configuration to explain the charge transport mechanism. The right-side image shows the transport mechanism of the middle layer (active) of the device made up of perovskite and SWCNT composite. Whenever an electron-hole pair generates within perovskite, the electron gets recombined with Sn<sup>2+</sup> and the hole gets transported through SWCNT as it works as a channel

Solving the Poisson equation with the help of this trap density of state according to **Equation 4.13**, the SCLC predicted by the Mark–Helfrich (MH) in the form of I-V characteristic is given by **Equation 4.14** [32].

$$I = A_{ef} N_{eff} \mu q^{1-m} \left( \frac{m\epsilon}{N_t(m+1)} \right)^m \left( \frac{2m+1}{m+1} \right)^{m+1} \frac{V^{m+1}}{L^{2m+1}} \quad (4.14)$$

Where  $A_{ef}$  is the effective area of the device,  $N_{eff}$  is the effective density of states at the valence band edge,  $\mu$  is the mobility of the majority carrier,  $L$  is the thickness of the layer,  $\epsilon$  is equal to  $\epsilon_0 \epsilon_r$  with  $\epsilon_0$  being the permittivity of vacuum and  $\epsilon_r$  the dielectric constant,  $V$  is the applied voltage. The value of  $m = T_t/T$ ,  $T$  is the absolute temperature.

Then trap energy is calculated by using  $E_T = k_B T_t = m k_B T$  and listed in **Table 4.3**. The threshold voltages are representing the onset voltage of the devices because, at this particular voltage, injected carrier dominates over the existing thermally generated charge carrier so effective transport starts. **Table 4.3** shows that in the presence of SWCNT, the trap energy is reduced from 103.22 to 79.70 meV in the dark and from 90.16 meV to 77.09 meV in light conditions. The reduction in trap energy in presence of light may be due to the photoinduced charge carrier generation. Light energy helps the carrier to emit from trap states. Also, carriers get a lower resistive pathway via SWCNT to release from the trap state and transport from one grain to another.

**Figure 4.14(c)** shows the combined effect of light and SWCNT to reduce trap energy. Due to the presence of light, perovskite produces excess e-h pair in the device and SWCNT helps the carriers to transport from that particular grain to another grain and/or to the electrode before their recombination. Hence, with the incorporation of SWCNT in  $\text{CH}_3\text{NH}_3\text{SnI}_3$  perovskite material, the optoelectronic performance of the device is improved.

**Table 4.3: Charge transport parameters of both devices in dark and light conditions.**

Cell	Condition	Region I	Region II		
		Value of slope ( $m_1$ )	Threshold voltage $V_{th}$ (V)	Value of slope ( $m_2$ )	Trap energy, $E_T$ (meV)
Perovskite	Dark	1.02	0.253	3.95	103.22
	Light	0.83	0.207	3.45	90.16
Perovskite+ SWCNT Composite	Dark	1.03	0.288	3.05	79.70
	Light	0.99	0.264	2.95	77.09

## 4.5 Conclusions

This work presents a novel method to improve the optoelectronic performance of the device by incorporating SWCNTs within the lead-free  $\text{CH}_3\text{NH}_3\text{SnI}_3$  perovskite. To demonstrate this,  $\text{CH}_3\text{NH}_3\text{SnI}_3$  perovskite and its composite with SWCNTs were synthesized and characterized using various techniques, including XRD, XPS, UV-Vis's spectroscopy, FESEM, TEM, TGA, FTIR, EDS spectroscopy, and elemental mapping. The results of this extensive range of measurements indicate that the incorporation of SWCNTs did not affect the structure of the perovskite, but instead improved the absorption coefficient and thermal stability of the composite material. These improvements in the composite may be due to the high surface-to-volume ratio and thermal and mechanical stability of the SWCNTs. Therefore, the samples were used to develop Schottky devices to compare their performance as optoelectronic devices. The estimation of photosensitivity performance shows that the photocurrent is increased due to the incorporation of SWCNTs in the perovskite. Electrical analysis shows that the series resistance of the device based on the SWCNT composite is reduced by five times in both dark and light conditions, which improves the device's conductivity. This improvement may be due to the SWCNTs acting as channels for the carriers to transport from one grain to another and to the electrode. Detailed charge transport analysis reveals that the trap energy of the device is decreased due to the incorporation of SWCNTs. This indicates that SWCNTs act as fillers in the trap states present in the perovskite, which also improves the performance of the device. Therefore, incorporating SWCNTs in optoelectronic  $\text{CH}_3\text{NH}_3\text{SnI}_3$  perovskite materials has resulted in a significant enhancement of charge transport within the devices, making it a valuable strategy for the development of high-performance optoelectronic devices. The findings of this study will provide valuable guidance to future researchers who seek to advance the development of perovskite-based devices.

## 4.6 References

- [1] D. Sahoo, A.K. Karan, Z. Mallick, N.B. Manik, Synthesis and complex impedance analysis of nano cubic  $\text{CH}_3\text{NH}_3\text{SnI}_3$  perovskite for the development of optoelectronic lead-free Schottky diode, *Materials Science in Semiconductor Processing* 155 (2023) 107253.
- [2] A. Mahata, D. Meggiolaro, L. Gregori, F. De Angelis, Suppression of Tin Oxidation by 3D/2D Perovskite Interfacing, *Journal of Physical Chemistry C* 125 (2021) 10901–10908.
- [3] R. Lin, K. Xiao, Z. Qin, Q. Han, C. Zhang, M. Wei, M.I. Saidaminov, Y. Gao, J. Xu, M. Xiao, A. Li, J. Zhu, E.H. Sargent, H. Tan, Monolithic all-perovskite tandem solar cells with 24.8% efficiency exploiting comproportionation to suppress Sn(ii) oxidation in precursor ink, *Nat Energy* 4 (2019) 864–873.

- [4] M.C. Jung, S.R. Raga, Y. Qi, Properties and solar cell applications of Pb-free perovskite films formed by vapor deposition, *RSC Adv* 6 (2016) 2819–2825.
- [5] S.J. Lee, S.S. Shin, Y.C. Kim, D. Kim, T.K. Ahn, J.H. Noh, J. Seo, S. Il Seok, Fabrication of Efficient Formamidinium Tin Iodide Perovskite Solar Cells through  $\text{SnF}_2$ -Pyrazine Complex, *J Am Chem Soc* 138 (2016) 3974–3977.
- [6] R. Prasanna, T. Leijtens, S.P. Dunfield, J.A. Raiford, E.J. Wolf, S.A. Swifter, J. Werner, Design of low bandgap tin–lead halide perovskite solar cells to achieve thermal, atmospheric and operational stability, *Nat Energy* 4 (2019) 939–947.
- [7] C. Mortan, T. Hellmann, O. Clemens, T. Mayer, W. Jaegermann, Preparation of Methylammonium Tin Iodide Perovskite Thin Films via Flash Evaporation, *Physica Status Solidi (A) Applications and Materials Science* 216 (2019) 1900209.
- [8] T. Hellmann, M. Wussler, C. Das, R. Dachauer, I. El-Helaly, C. Mortan, T. Mayer, W. Jaegermann, The difference in electronic structure of MAPI and MASI perovskites and its effect on the interface alignment to the HTMs spiro-MeOTAD and CuI, *J Mater Chem C Mater* 7 (2019) 5324–5332.
- [9] Y.Q. Huang, J. Su, Q.F. Li, D. Wang, L.H. Xu, Y. Bai, Structure, optical and electrical properties of  $\text{CH}_3\text{NH}_3\text{SnI}_3$  single crystal, *Physica B Condens Matter* 563 (2019) 107–112.
- [10] T. Glaser, C. Müller, M. Sendner, C. Krekeler, O.E. Semonin, T.D. Hull, O. Yaffe, J.S. Owen, W. Kowalsky, A. Pucci, R. Lovrinčić, Infrared Spectroscopic Study of Vibrational Modes in Methylammonium Lead Halide Perovskites, *Journal of Physical Chemistry Letters* 6 (2015) 2913–2918.
- [11] J. Idígoras, A. Todinova, J.R. Sánchez-Valencia, A. Barranco, A. Borrás, J.A. Anta, The interaction between hybrid organic-inorganic halide perovskite and selective contacts in perovskite solar cells: An infrared spectroscopy study, *Physical Chemistry Chemical Physics* 18 (2016) 13583–13590.
- [12] E.J. Juarez-Perez, Z. Hawash, S.R. Raga, L.K. Ono, Y. Qi, Thermal degradation of  $\text{CH}_3\text{NH}_3\text{PbI}_3$  perovskite into  $\text{NH}_3$  and  $\text{CH}_3\text{I}$  gases observed by coupled thermogravimetry-mass spectrometry analysis, *Energy Environ Sci* 9 (2016) 3406–3410.
- [13] Y. Yu, D. Zhao, C.R. Grice, W. Meng, C. Wang, W. Liao, A.J. Cimaroli, H. Zhang, K. Zhu, Y. Yan, Thermally evaporated methylammonium tin triiodide thin films for lead-free perovskite solar cell fabrication, *RSC Adv* 6 (2016) 90248–90254.
- [14] D. Sahoo, N.B. Manik, Study on the effect of temperature on electrical and photovoltaic parameters of lead-free tin-based Perovskite solar cell, *Indian Journal of Physics* 97 (2022) 447–455.
- [15] J.P. Sullivan, R.T. Tung, M.R. Pinto, W.R. Graham, Electron transport of inhomogeneous Schottky barriers: A numerical study, *J Appl Phys* 70 (1991) 7403–7424.
- [16] S.K. Cheung, N.W. Cheung, Extraction of Schottky diode parameters from forward current-voltage characteristics, *Appl Phys Lett* 49 (1986) 85–87.
- [17] S. Mahato, D. Biswas, L.G. Gerling, C. Voz, J. Puigdollers, Analysis of temperature dependent current-voltage and capacitance-voltage characteristics of an  $\text{Au/V}_2\text{O}_5/\text{n-Si}$  Schottky diode, *AIP Adv* 7 (2017) 085313.

- [18] M. Sharma, S.K. Tripathi, Study of barrier inhomogeneities in I-V-T and C-V-T characteristics of Al/Al<sub>2</sub>O<sub>3</sub>/PVA:n-ZnSe metal-oxide-semiconductor diode, *J Appl Phys* 112 (2012) 024521.
- [19] N.K. Sinha, D.S. Ghosh, A. Khare, Role of built-in potential over ETL/perovskite interface on the performance of HTL-free perovskite solar cells, *Opt Mater (Amst)* 129 (2022) 112517.
- [20] W. Luo, L. Yan, R. Liu, T. Zou, S. Zhang, C. Liu, Q. Dai, J. Chen, H. Zhou, High detectivity ITO/organolead halide perovskite Schottky photodiodes, *Semicond Sci Technol* 34 (2019) 074004.
- [21] D. Sahoo, N.B. Manik, Estimation of trap energy of fuchsin dye sensitized Organic Photovoltaic Device based on Titanium Dioxide (TiO<sub>2</sub>), *International Journal of Innovative Research in Physics* 1 (2020) 17-23.
- [22] S. Sen, N.B. Manik, Correlation between barrier potential and charge trapping under the influence of Titanium Di oxide nanomaterials in organic devices, *Results in Materials* 8 (2020) 100145.
- [23] D. Meggiolaro, D. Ricciarelli, A.A. Alasmari, F.A.S. Alasmari, F. De Angelis, Tin versus Lead Redox Chemistry Modulates Charge Trapping and Self-Doping in Tin/Lead Iodide Perovskites, *Journal of Physical Chemistry Letters* 11 (2020) 3546–3556.
- [24] X. Fu, K.J. Weber, T.P. White, Characterization of trap states in perovskite films by simultaneous fitting of steady-state and transient photoluminescence measurements, *J Appl Phys* 124 (2018) 073102.
- [25] S. Ghatak, A. Ghosh, Observation of trap-assisted space charge limited conductivity in short channel MoS<sub>2</sub> transistor, *Appl Phys Lett* 103 (2013) 122103.
- [26] T.S. Sherkar, C. Momblona, L. Gil-Escrig, J. Ávila, M. Sessolo, H.J. Bolink, L.J.A. Koster, Recombination in Perovskite Solar Cells: Significance of Grain Boundaries, Interface Traps, and Defect Ions, *ACS Energy Lett* 2 (2017) 1214–1222.
- [27] R.H. Bube, Trap Density Determination by Space-Charge-Limited Currents, *J Appl Phys* 33 (1962) 1733–1737.
- [28] M.A. Lampert, Theory of Space-Charge-Limited Currents in an Insulator with Traps, *Phys. Rev.* 103 (1956) 1648.
- [29] A. Baumann, S. Väh, P. Rieder, M.C. Heiber, K. Tvingstedt, V. Dyakonov, Identification of trap states in perovskite solar cells, *Journal of Physical Chemistry Letters* 6 (2015) 2350–2354.
- [30] H.T. Nicolai, M.M. Mandoc, P.W.M. Blom, Electron traps in semiconducting polymers: Exponential versus Gaussian trap distribution, *Phys Rev B Condens Matter Mater Phys* 83 (2011) 195204.
- [31] I.G. Austin, N.F. Mott, Polarons in Crystalline and Non-crystalline Materials, *Adv Phys* 18 (1969) 41–102.
- [32] P. Mark, W. Helfrich, Space-charge-limited currents in organic crystals, *J Appl Phys* 33 (1962) 205–215.

# **Chapter 5: Effect of MWCNT on the Electrical Behaviour of a Lead-Free Methylammonium Tin Iodide ( $\text{CH}_3\text{NH}_3\text{SnI}_3$ ) Perovskite Schottky device**

## **5.1 Introduction**

## **5.2 Experimental Section**

### **5.2.1 Materials**

### **5.2.2 Instruments Used**

### **5.2.3 Synthesis of Perovskite and Nanocomposite**

## **5.3 Material Characterization**

## **5.4 Van der Pauw Measurement Setup**

## **5.5 I-V Characterization**

## **5.6 Results and Discussions**

## **5.7 Conclusions**

## **5.8 References**

## 5.1 Introduction

In the previous chapter, it was observed that CNTs play a crucial role in enhancing the charge transport of electronic devices, leading to a significant improvement in overall device performance [1]. The current study is similar to the previous one, with the exception that MWCNTs were used instead of SWCNTs in the  $\text{CH}_3\text{NH}_3\text{SnI}_3$  perovskite. Additionally, the van der Pauw method was employed to measure the I-V properties, providing clearer and more reliable results. To our knowledge, no other study has investigated the impact of MWCNTs in lead-free  $\text{CH}_3\text{NH}_3\text{SnI}_3$  perovskites.

This study explores the impact of MWCNTs on the electrical properties and conductivity of the thin film. Conductivity was measured using two methods: the I-V measurement method and the van der Pauw method, which determines the resistivity of a sample using four small contacts on the sample. These measurements allow for the analysis of charge transport mechanisms and the evaluation of the performance of sandwich-structured devices incorporating MWCNTs in perovskite thin films. The results show that MWCNTs have significant potential for improving the conductivity of lead-free perovskite materials and advancing their practical implementation in photovoltaic devices.

## 5.2 Experimental Section

### 5.2.1 Materials

From Sigma Aldrich, we procured methylammonium iodide ( $\text{CH}_3\text{NH}_3\text{I}$ , 98 % purity), tin (II) iodide ( $\text{SnI}_2$ , anhydrous, 99.99 % purity), and indium tin oxide (ITO) coated glass (surface resistivity 8–12  $\Omega/\text{sq.}$ ). Some solvents were bought from Alfa-Aesar and SRL companies, including dimethylformamide (DMF), multi-walled carbon nanotube (MWCNT type 15, 95% purity, OD: 30-35 nm, length: 10-30  $\mu\text{m}$ ), and Extran MA 02 (neutral). Perovskite's ball and stick structure is depicted in **Figure 5.1(b)**, and the structure of MWCNT is shown in **Figure 5.1(a)**. The compounds were all used without further purification. The departmental Milli (Q) water facility provided deionized water for the experiment.

### 5.2.2 Instruments Used

The instruments used in this work are mostly the same as those described in Chapter 4 and Chapter 5. A detailed description of all the instruments can be found in Chapter 4 and Chapter 5.

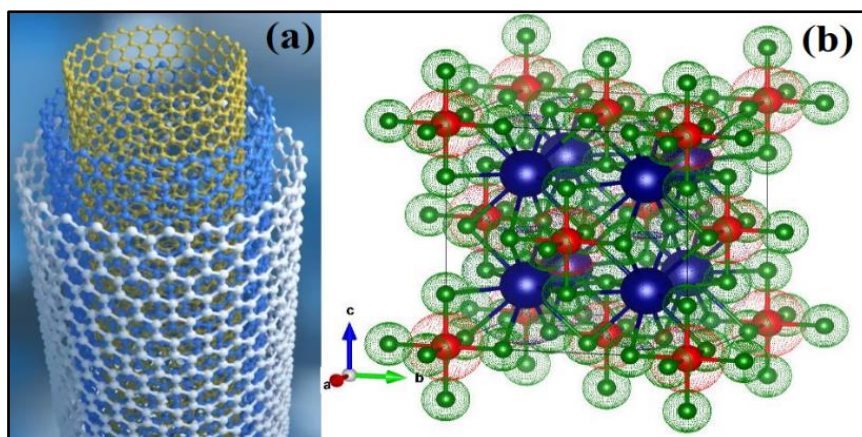


**Figure 5.1: Structure of (a) MWCNT and (b) visualization of cubic  $\text{CH}_3\text{NH}_3\text{SnI}_3$  perovskite by VESTA**

### 5.2.3 Synthesis of Perovskite and Nanocomposite

Two vials were initially taken and marked with the letters A and B. A 4:1 mixture of DMF and DMSO was added to one millilitre of each vial. In an  $\text{N}_2$  atmospheric glove box, the containers were placed on a hot plate-enabled magnetic stirrer and the temperature was then raised to  $65^\circ\text{C}$ . The solution mixtures were given 10 moles percent  $\text{SnF}_2$  and 10 moles percent pyrazines as reducing additives, and they were stirred for 35 minutes. Then, one milligram of MWCNT was added to solution B and mixed for an hour in an ultrasonic bath. The next step involved adding 375 mg of 1 mmol of  $\text{SnI}_2$  to both the A and B solutions. 1 mmol of  $\text{CH}_3\text{NH}_3\text{I}$  (159 mg) was added to both prepared solutions after  $\text{SnI}_2$  had completely dissolved, and they were stirred for 35 minutes at  $70^\circ\text{C}$ . To develop Schottky devices with and without MWCNT, these final perovskite precursor solutions were used. The films were developed with a spin coating unit at 1500 rpm for 1 min then dried immediately at  $75^\circ\text{C}$  and kept in a  $\text{N}_2$  atmospheric chamber for further characterization and measurements.

### 5.3 Material Characterization

A Bruker D8 SWAX diffractometer running at 35 mA and 35 kV was used to examine the crystallinity of the as-synthesized samples. Two different thin films were developed on two glass slides, as explained previously, to investigate the morphological characteristics of the prepared perovskite samples. The sample was gold coated using the Quorum Q150R ES coating apparatus. Field emission scanning electron microscopy (FESEM) was used to capture the images, and an energy dispersive spectroscopy (EDS) detector from Bruker was used to

analyse them (Quantax, 200). To measure the devices', I-V characteristics, a Keithley 2400 SMU was used.

## 5.4 Van der Pauw Measurement Setup

The Van der Pauw method is a useful technique for measuring the conductivity of a wide range of materials, including semiconductors, metals, and insulators. It is particularly useful for measuring the resistivity of thin films and other small samples. Ronald Chwang et al. investigated the impact of finite-sized contacts with certain shapes on a square sample's resistivity and Hall coefficient measurements using Van der Pauw's method [2-4].

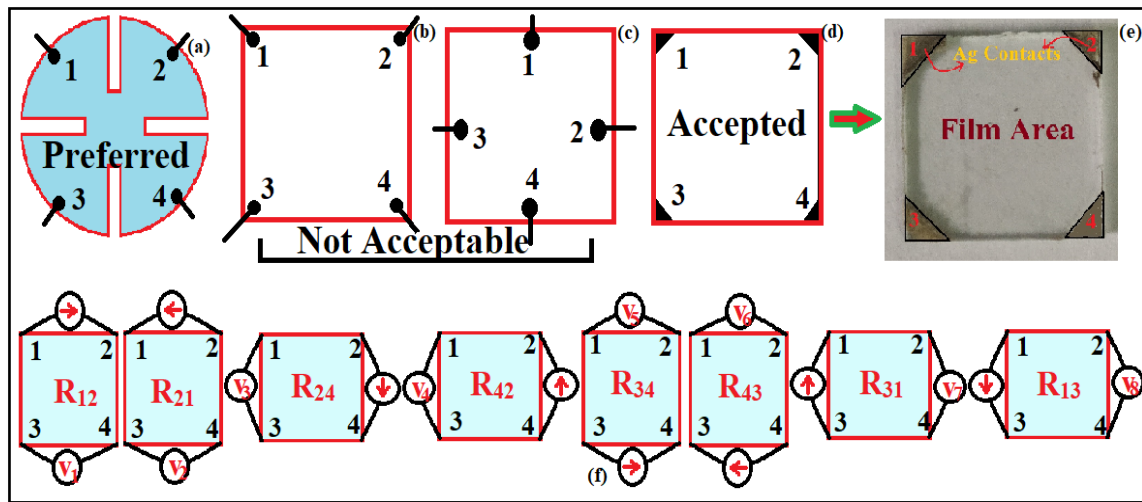


**Figure 5.2:** (a) Preferred (b) and (c) not acceptable (d) acceptable geometrical structures of the film used for Van der Pauw resistivity measurement (e) laboratory film formation set up on a glass plate (f) resistivity measurement of the thin films

**Figure 5.2(a-d)** illustrates the recommended shape of the sample, as well as the acceptable and unacceptable shapes. For optimal results, it is recommended that the contacts be small and positioned along the circumference of the sample. Additionally, the sample should maintain a consistent thickness throughout. As illustrated in **Figure 5.2(f)**, a total of eight voltage measurements are necessary.  $I_{21}$  represents the positive DC injected into contact 2 and extracted from contact 1 (in amperes, A). The indexing is similar, for  $I_{12}$ ,  $I_{24}$ ,  $I_{42}$ ,  $I_{43}$ ,  $I_{34}$ ,  $I_{13}$ , and  $I_{31}$ .  $V_{12}$  represents the DC voltage measured between contacts 1 and 2 ( $V_1 - V_2$ ).

The same applies to  $V_{21}$ ,  $V_{34}$ ,  $V_{43}$ ,  $V_{13}$ ,  $V_{31}$ ,  $V_{42}$ , and  $V_{24}$  (in volts, V). To perform the measurement, apply the current  $I_{21}$  and record the voltage  $V_{34}$ . Reverse the polarity of the

current ( $I_{12}$ ) and measure the voltage  $V_{43}$ . Repeat this procedure for the remaining six values. The eight voltage measurements yield eight resistance values, all of which should be positive:

$$R_{21} = \frac{V_{34}}{I_{21}}, R_{12} = \frac{V_{43}}{I_{12}}, R_{42} = \frac{V_{13}}{I_{42}}, R_{24} = \frac{V_{31}}{I_{24}}, R_{43} = \frac{V_{12}}{I_{43}}, R_{34} = \frac{V_{21}}{I_{34}}, R_{13} = \frac{V_{42}}{I_{13}}, R_{31} = \frac{V_{24}}{I_{31}}$$

According to the reciprocity theorem, if  $R_{12} + R_{21} \approx R_{34} + R_{43}$  and  $R_{24} + R_{42} \approx R_{31} + R_{13}$  then, two resistance values,  $R_A$  and  $R_B$ , are calculated as follows[26,28]:

$$R_A = \frac{(R_{12} + R_{21} + R_{34} + R_{43})}{4} \text{ and } R_B = \frac{(R_{23} + R_{32} + R_{41} + R_{14})}{4}$$

Therefore, the average resistivity can be approximated as  $\rho_{av} = \frac{\pi d(R_A + R_B)}{2 \ln 2}$  in ohm meters, and the conductivity is  $\frac{1}{\rho_{av}}$  in S/m.

**Table 5.1: Measurements of resistances using Van der Pauw method. These values were used to calculate conductivity of the perovskite and its MWCNTs nanocomposite films**

Film Type	$R_{12}$	$R_{21}$	$R_{24}$	$R_{42}$	$R_{34}$	$R_{43}$	$R_{31}$	$R_{13}$
<b>CH<sub>3</sub>NH<sub>3</sub>SnI<sub>3</sub></b>	17.60	17.40	17.23	17.01	17.20	17.80	17.62	17.9
	MΩ	MΩ	MΩ	MΩ	MΩ	MΩ	MΩ	MΩ
<b>CH<sub>3</sub>NH<sub>3</sub>SnI<sub>3</sub> + MWCNT</b>	187.81	188.23	188.9	187.96	189.76	189.90	188.68	188.01
	kΩ	kΩ	kΩ	kΩ	kΩ	kΩ	kΩ	kΩ

## 5.5 I-V Characterizations

To measure the conductivity of a material, another common method is I-V (current-voltage) characterization. The basic principle behind this method is to apply a voltage across the material and measure the resulting current flowing through it, then use Ohm's Law to calculate the conductivity.

To measure I-V, a device was developed, as shown in **Figure 5.3**. A thin film was developed on a cleaned ITO-coated glass substrate using a spin coater at the same speed that was used to develop film for Van der Pauw measurements, i.e., 1500 rpm for 60 seconds. Then the film was dried at 75°C for 15 mins. In the next step, a thin gold plate was placed on the film to develop a sandwich structure device. To measure I-V characteristics, a Keithley 2400 SMU was used.

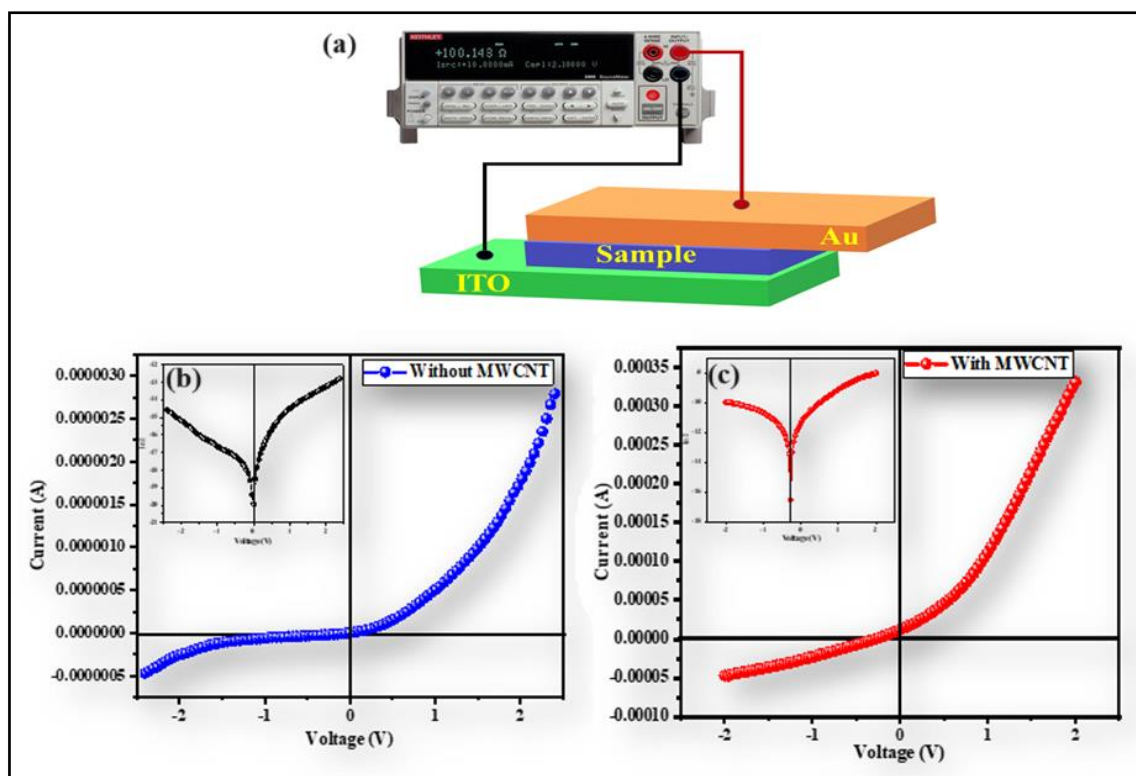


**Figure 5.3:** (a) I-V measurement setup of the sandwich structured device (b) I-V characteristics of the device Al/CH<sub>3</sub>NH<sub>3</sub>SnI<sub>3</sub>/ITO (blue) and Al/CH<sub>3</sub>NH<sub>3</sub>SnI<sub>3</sub>+MWCNT nanocomposite/ITO (red)

## 5.6 Results and Discussions

The XRD of a pure CH<sub>3</sub>NH<sub>3</sub>SnI<sub>3</sub> sample and its nanocomposite with MWCNT are shown in **Figure 5.4(a)**. The range of analysis was 10-60°. The perovskite sample (green) and its composite (blue) with MWCNT exhibited exceptional crystallinity and complied with the cubic space group  $Pm\bar{3}m$  symmetry. The measured peaks were successfully matched and indexed using the reference data COD ID #7015448 and reference [4,5]. The most prominent peaks were found at two-theta angles of 14.17°, 24.67°, 28.56°, 32.02°, 40.84°, and 43.44°, indicating the crystallographic planes 001, 111, 002, 012, 022, and 033, respectively.

The PXRD results of both pure and nanocomposite samples confirmed the synthesis of high-quality CH<sub>3</sub>NH<sub>3</sub>SnI<sub>3</sub>-perovskite and its composite. However, no extra signal was detected in the composite sample, which could be due to the low-intensity, amorphous nature of carbon. This suggests that the addition of MWCNTs did not affect the crystal structure of the CH<sub>3</sub>NH<sub>3</sub>SnI<sub>3</sub> perovskite. Consequently, the device is expected to exhibit the combined optoelectronic capabilities of perovskite and MWCNTs as an additive.

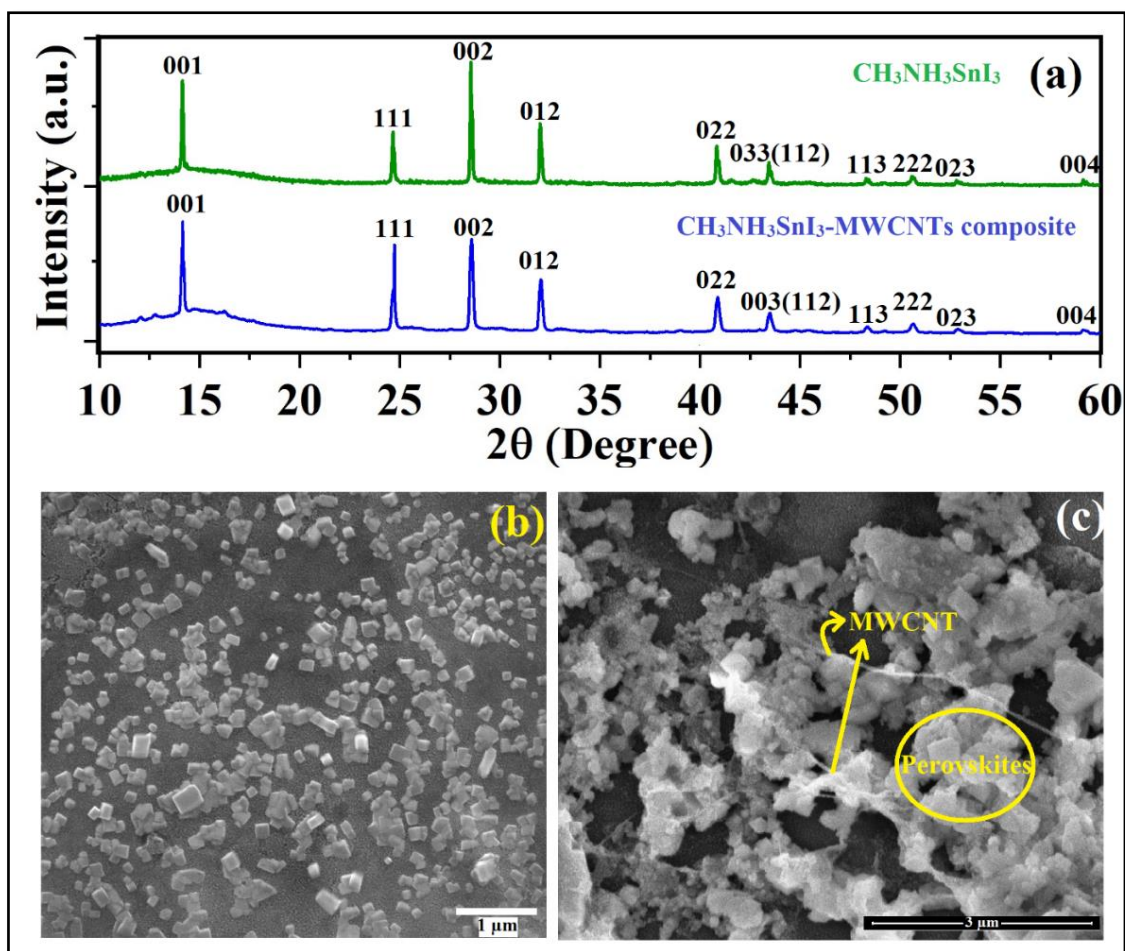


**Figure 5.4:** (a) Powder XRD of the as-synthesized sample and its MWCNT composite; (b) FESEM image of  $\text{CH}_3\text{NH}_3\text{SnI}_3$  perovskite film; (c) FESEM image of  $\text{CH}_3\text{NH}_3\text{SnI}_3$  perovskite and MWCNT nanocomposite film.

The FESEM images of the materials are presented in **Figures 5.4(b)** and (c). These images reveal noticeable differences in the morphology of the pure perovskite film and its nanocomposite (perovskite-MWCNT) film. The SEM images also confirm that the MWCNTs are evenly distributed and aligned horizontally within the perovskite matrix. The EDX spectra of the nanocomposite are illustrated in **Figures 5.5(a)** and the stoichiometric ratio of elements are also shown in the inset of the same figure. The analysis of EDX spectra shows that the stoichiometric ratio of the elements Sn and I in the nanocomposite samples is 1:2.7, which is close to the theoretical value of 1:3. This again confirms that the synthesized materials are pure. Due to the limitations of the instrument, the elemental ratio of nitrogen and carbon is not taken into account here. The corresponding mapping of the elements C, Sn, and I have been shown in **Figure 5.5(b)-(e)**.

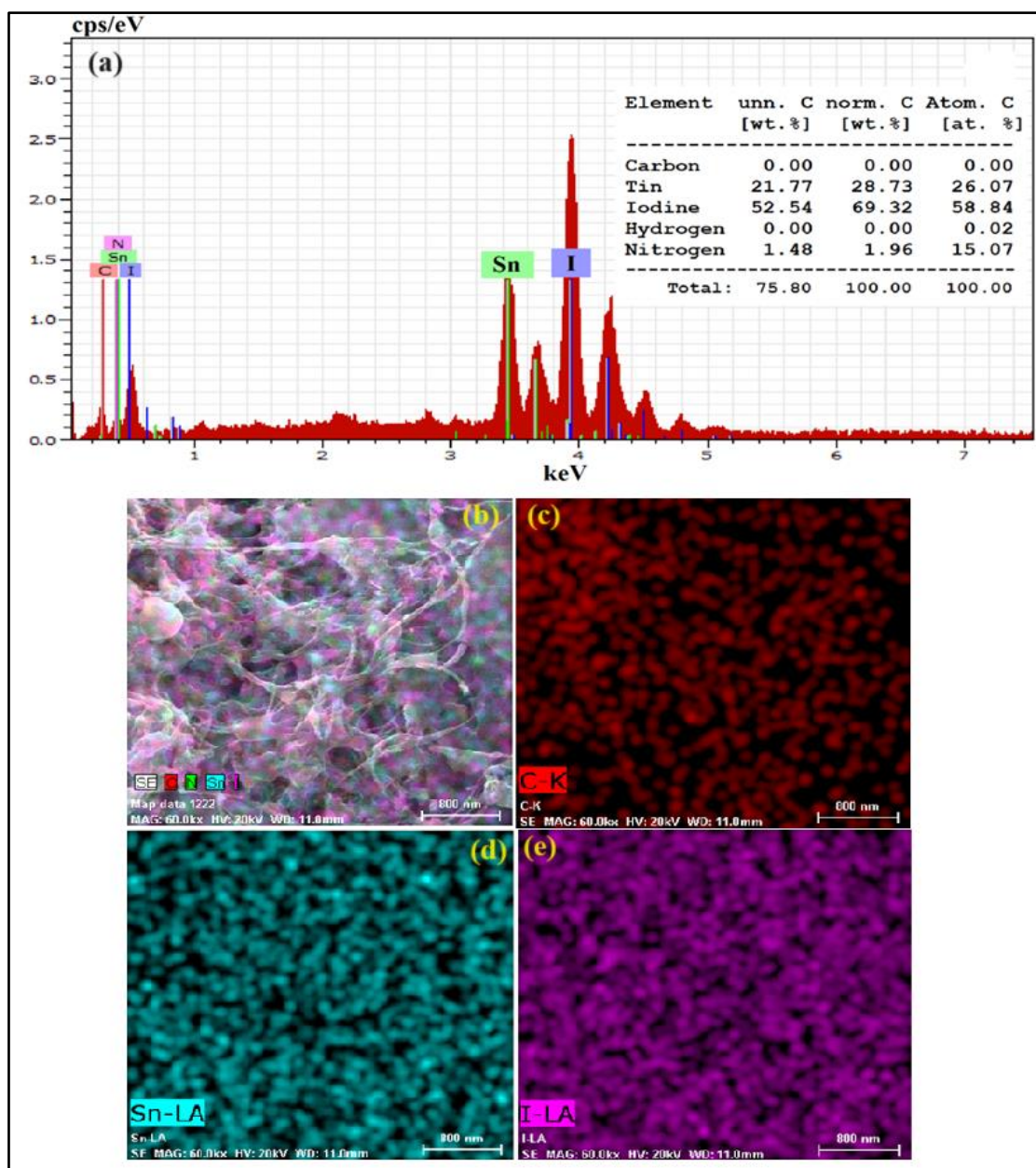


**Figure 5.5:** (a) EDX spectroscopy of CH<sub>3</sub>NH<sub>3</sub>SnI<sub>3</sub>-MWCNT nanocomposite. (b) to (e) elemental mapping of C, Sn, and I of CH<sub>3</sub>NH<sub>3</sub>SnI<sub>3</sub>-MWCNT nanocomposite. The mapping of N is omitted in this case because it is forbidden by the instrument

The electronic properties of two devices, ITO/CH<sub>3</sub>NH<sub>3</sub>SnI<sub>3</sub>/Al and ITO/ CH<sub>3</sub>NH<sub>3</sub>SnI<sub>3</sub>-MWCNTs composite/Al, were investigated by I-V analysis at room temperature (27°C). The schematic structure of the device is shown in **Figure 5.3(a)** and the individual I-V characteristics can be seen in **Figure 5.3(b)** and (c) exhibit good quality rectifying behaviour. The properties of the junctions in perovskite semiconductors depend on the interfacial properties of the two electrodes used for diode fabrication and the difference in their respective

work functions. To fabricate diodes that can be used as rectifiers, it is necessary to choose electrodes that make ohmic and non-ohmic contact with the semiconducting layer [6,7]

A series of tests were conducted to measure the electrical conductivities of the films. The initial test employed the Vander Pauw method to determine the sheet resistances of the films, and the corresponding results can be found in **Table 4.1**. During the measurement, it was observed that the resistance of the sample decreased drastically by approximately a hundred times in MWCNT and perovskite composite-based films. Assuming a film thickness of 15  $\mu\text{m}$ , the conductivity values were estimated using the equation mentioned above as  $8.4 \times 10^{-4} \text{ S/m}$  and  $7.80 \times 10^{-2} \text{ S/m}$  for pure  $\text{CH}_3\text{NH}_3\text{SnI}_3$  perovskite and MWCNT nanotube composite-based films, respectively. This result indicates that the incorporation of MWCNT in perovskite improved the conductivity of the film by approximately 92 times. Then, the films were used to develop ITO/sample/Al-based sandwiched structure devices to check how the conductivities improved in the device form.

As per the Schottky barrier theory, a rectifying barrier is formed at the interface when the work function of the metal is lower than that of the p-type semiconductor. The literature suggests that Al has a work function similar to that of perovskite, while ITO forms a rectifying contact with the perovskite [8]. This study follows the same principle. The current-voltage (I-V) characteristics of the devices ITO/perovskite/Al and ITO/perovskite+MWCNTs/Al were analysed based on the standard thermionic emission theory, which is expressed as the I-V relationship [9]:

$$I = I_0 \left[ \exp\left(\frac{eE}{mkT}\right) - 1 \right] \quad (4.1)$$

The equation provides the relationship between current (I) and voltage (V) in the diode, where  $\eta$  represents the ideality factor and  $I_0$  denotes the saturation current in the absence of external bias. In the equation,  $e$  represents the electronic charge,  $E$  is the applied voltage,  $T$  signifies the temperature in Kelvin, and  $k$  represents the Boltzmann constant. By analysing this equation, the Schottky barrier height ( $\phi_b$ ) and the ideality factor ( $\eta$ ) of the devices can be determined.

$$\phi_b = \frac{kT}{q} \ln\left(\frac{A A^* T^2}{I_0}\right) \quad (4.2)$$

$$\eta = \frac{q}{kT} \left[ \frac{dV}{d(\ln I)} \right] \quad (4.3)$$

The effective Richardson constant  $A^*$  has a value of  $2.54 \text{ Acm}^{-2}\text{K}^{-2}$ , which was determined by calculating the effective mass of the charge carrier in a perovskite thin film and  $\phi_b$  [33]. Using

these equations, we were able to calculate the  $I_0$ ,  $\eta$ , and  $\phi_b$  for the devices, which are presented in **Table 5.2**. The value of  $\eta$  for the ITO/perovskite-MWCNT nanocomposite/Al device is significantly better than that of the ITO/perovskite/Al device, possibly due to the presence of MWCNT in the perovskite matrix, which enhances charge transport through the interface. Although, the  $\eta$  for both devices is greater than one. For the ITO/perovskite/Al device, the value of  $\eta$  obtained is nearly two times higher than the earlier reported value for the same perovskite, which can be attributed to an increase in the film thickness [8].

**Table 5.2: Comparative electrical parameters of the devices**

Device	Reverse saturation current ( $I_0$ ) in A	Rectification ratio at 1.5 V	Ideality factor ( $\eta$ )	Barrier height ( $\phi_b$ ) eV	Conductivity ( $\sigma$ ) S/m
ITO/perovskite/Al	$1.52 \times 10^{-7}$	12.05	4.01	0.51	$1.21 \times 10^{-5}$
ITO/perovskite-MWCNT nanocomposite/Al	$4.5 \times 10^{-5}$	15.61	2.56	0.43	$1.02 \times 10^{-4}$

Ideality factors between 1 and 2 are typically associated with the Shockley charge carrier generation-recombination and drift-diffusion process [10], while values greater than 2 are due to trap-assisted tunnelling, carrier leakage, and barrier inhomogeneity [11–13]. The ideal diode equation assumes that all recombination occurs band-to-band in the bulk areas of the device and not at the junction. This assumption produces an ideal diode equation with an ideality factor of one. Furthermore, recombination can occur in other ways and in other areas of the perovskite device, such as via traps and at the junction area of the device [11,14–16].

As the bulk region of the device's thickness increases, so does the number of recombination sites. This additional recombination led to the value of  $\eta$  greater than one, deviating from the ideal diode. The forward region of the device displays exponential growth in current, while the reverse region does not conform to this pattern. The asymmetric and non-linear I-V curves in the forward region suggest that these devices demonstrate rectification behaviour. Prior

research has suggested possible conduction mechanisms for non-linear I-V characteristics [17-19].

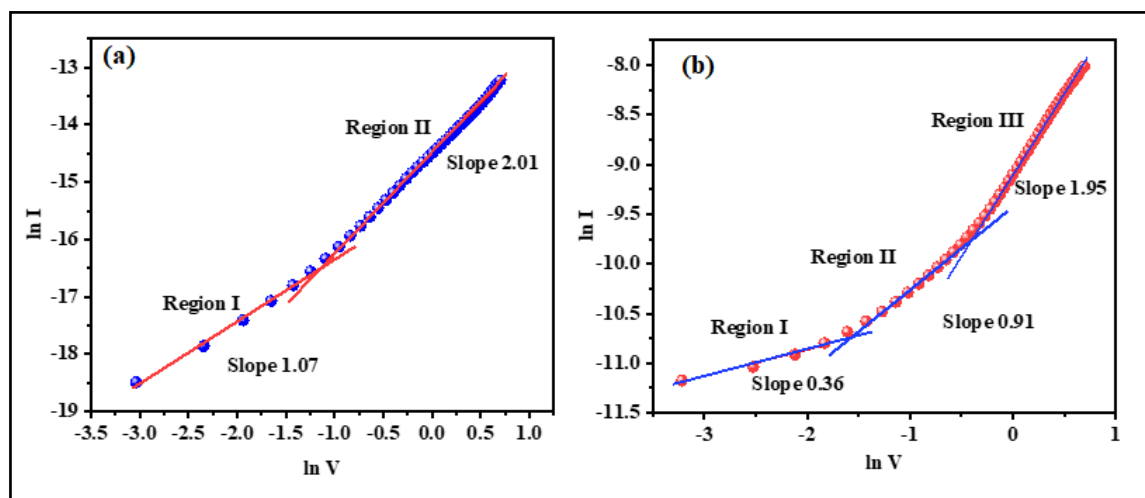


**Figure 5.6:  $\ln I$  vs  $\ln V$  plot of the I-V behaviours of the devices (a) ITO/perovskite/Al and (b) ITO/perovskite-MWCNTs composite/Al show distinct linear regions**

For the perovskite/metal junction, these mechanisms may include space-charge limited conduction (SCLC), Poole-Frenkel emission, or thermionic emission [20-22]. If the plot of  $\log I$  vs.  $\log V$  is linear, a system will follow the SCLC mechanism. The log-log plot of I-V characteristics of the devices ITO/  $\text{CH}_3\text{NH}_3\text{SnI}_3$ /Al has two distinct linear regions, with the slopes of regions I and II being 1.07 and 2.01, respectively. The device ITO/ $\text{CH}_3\text{NH}_3\text{SnI}_3$ -MWCNT nanocomposite/Al has three different linear regions: I, II, and III, with slopes of 0.36, 0.91, and 1.95, respectively. The first region of the MWCNT composite sample has a slope of less than one, which implies that in the lower voltage region, charge carriers flow through a tunnelling mechanism [23].

The first region and the second region of **Figure 5.6(a)** and **(b)** are nearly one, indicating that in this voltage region, devices exhibit ohmic behaviour. In the second region and the third region of **Figure 5.6(a)** and **(b)**, charge conduction is mainly governed by the SCLC transport mechanism, as the slope is nearly value 2, which is the hallmark of SCLC [24].

In **Figure 5.7(b)**, it is observed that the current of the  $\text{CH}_3\text{NH}_3\text{SnI}_3$ -MWCNTs nanocomposite is significantly higher than that of the pure  $\text{CH}_3\text{NH}_3\text{SnI}_3$ . This raises the question of why the composite exhibits such a high current compared to the pure material when both were deposited for the same duration of time and thickness. To understand the reasons, we can turn to **Figure 5.7(a)**, which depicts the potential pathways for charge carriers within the composite.

Essentially, three types of conduction pathways are observed in the composite. Firstly, charge carriers can move by hopping between adjacent perovskite bonds within the material itself, occurring within the perovskite crystals. Secondly, charge carriers can also hop between the multi-walled carbon nanotubes (MWCNTs) and the surrounding perovskite grains. This type of conduction involves the interaction between the carbon nanotubes and the individual grains of the polycrystalline material. Lastly, there is another conduction pathway where charge carriers move through the MWCNTs, effectively bridging the perovskite grains. This mechanism enables conduction between different MWCNTs via the perovskite bonds present in the material. The improved conductivity observed in the composite is unlikely to be solely attributed to the perovskite material, as its conductivity is typically lower than that of the MWCNTs. Instead, the composite system exhibits a percolating behaviour, where the interconnected MWCNTs create efficient pathways for charge transport, leading to the observed enhancement in conductivity. Briefly, introducing a small quantity of MWCNTs as a conductive filler in the polycrystalline material offers a more convenient percolation route between two electrodes, enabling the flow of charges. This enhances conduction by minimizing the distance required for variable range hopping between the electrodes, consequently reducing path resistance [25]. The increase in current is a direct result of this lowered resistance. Experimental data in Table I demonstrates a decrease in the ideality factor, affirming a reduction in recombination through traps and defects, as evidenced by the I-V curve.

FESEM analysis of the perovskite-MWCNT nanocomposites supports the homogeneous distribution of MWCNTs and the development of a compact film. The interaction between perovskite and the filler most likely results in an improved path and fewer traps for the carriers. The increase in the  $I_0$  and lower  $\phi_b$  in the perovskite-MWCNTs composite can be explained by the uniform distribution of MWCNTs in the perovskite matrix, which reduces the work function of the nanocomposite, resulting in a decrease in the  $\phi_b$  with a rise in the current compared to pure perovskite.

The incorporation of MWCNTs in the perovskite matrix enhances the uniformity of the nanocomposite film surface, which further lowers the  $\phi_b$  of the device. In addition, MWCNTs act as a dopant in the perovskite matrix, increasing its conductivity. The depletion width and barrier height of Schottky diodes are well known to be doping concentration dependent. As a result, MWCNTs in the perovskite matrix reduce the depletion width and barrier height of the diode, increasing the reverse saturation current in the Al/Perovskite-MWCNTs composite/ITO device compared to the Al/Perovskite/ITO device.

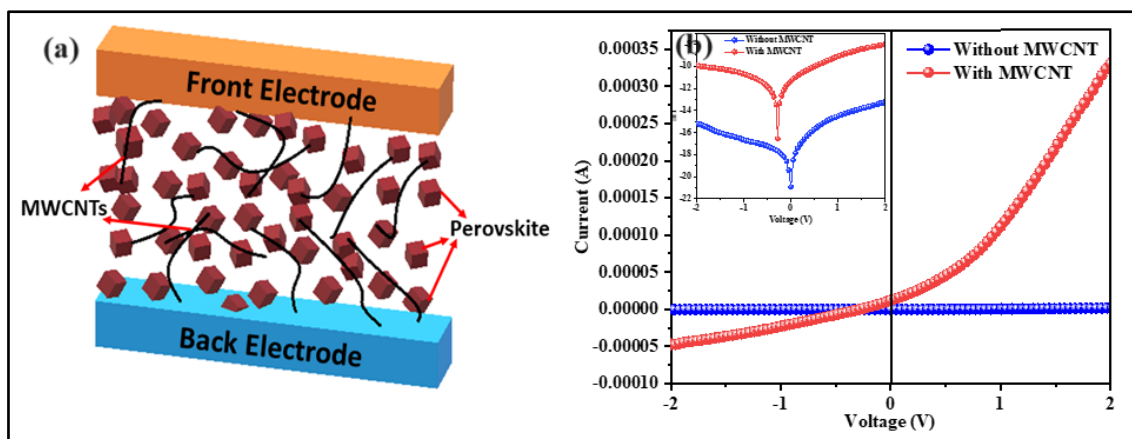


**Figure 5.7: (a) Comparative I-V characteristics of the devices ITO /perovskite/ Al (blue) and ITO /perovskite+MWCNT/ Al (red) (b) schematic diagram of a cross-sectional view of the device to understand the charge transport mechanism in a combined manner. It shows that some of the perovskite crystals are interconnected via MWCNTs and some of the perovskite crystals are connected to electrodes**

Our electrical measurement techniques, including Van der Pauw and I-V characterization, have revealed the potential of MWCNTs- $\text{CH}_3\text{NH}_3\text{SnI}_3$  composites for use in electronic device applications. Further investigations can be conducted using other perovskite and transporter materials. The incorporation of conducting nano transporters in the perovskite matrix has resulted in a reduction of the barrier height and an increase in conductivity. However, there are some discrepancies in the conductivity values, possibly due to the different methods and approximations used in the techniques. Nonetheless, both techniques yield the same results, indicating that the conductivity of the perovskite drastically increases with the incorporation of MWCNTs without altering the perovskite's crystalline properties.

## 5.7 Conclusions

In summary, the primary focus of this study is to synthesize an environmentally sustainable nanocomposite comprising  $\text{CH}_3\text{NH}_3\text{SnI}_3$  perovskite and MWCNTs to achieve an improved charge-transporting device. The study aims to harness the unique properties of the nanocomposite to enhance the charge transfer and transport within the device. Various characterization techniques, including XRD, FESEM, EDX, and elemental mapping, are employed to thoroughly analyse the materials. Subsequently, films and Schottky devices are fabricated using the materials for electrical measurements, aiming to explore the potential of MWCNTs in the perovskite. The analysis of Van der Pauw and I-V characteristics demonstrates a notable enhancement in the conductivity of the  $\text{CH}_3\text{NH}_3\text{SnI}_3$  perovskite

material. Moreover, the incorporation of MWCNTs in the perovskite leads to a decrease in the barrier height and ideality factor of the Schottky device, accompanied by an increase in the reverse saturation current. This improvement in device performance can be attributed to the uniformly distributed MWCNTs, which facilitate the transport of charge carriers, effectively reducing charge trapping and carrier recombination. Consequently, this research provides valuable insights for future investigations aimed at enhancing the optoelectronic performance of the device through the incorporation of other nano-transporter materials into perovskite structures.

## 5.8 References

- [1] D. Sahoo, A. Kanti Karan, N. Baran Manik, Influence of SWCNT on the Electrical Behaviour of an Environmentally Friendly  $\text{CH}_3\text{NH}_3\text{SnI}_3$  Perovskite-Based Optoelectronic Schottky Device, *ACS Applied Electronic Materials* 5 (2023) 2203–2214.
- [2] M. Mbilo, A.O. John, F.K. Mugwang, A, Correlation between the morphology and the opto-electronic and electrical properties of organometallic halide perovskite ( $\text{CH}_3\text{NH}_3\text{MH}_3$ ) thin films, *Mater Res Express* 6 (2019) 076431.
- [3] Y. Singh, Electrical resistivity measurements: A, *Int J Mod Phys Conf Ser* 22 (2013) 745–756.
- [4] N. Bajpai, M. Saleem, S. Tiwari, M. Soni, A. Mishra, Bismuth doped  $\text{La}_2\text{CoMnO}_6$ : A study of Williamson-Hall analysis and four-probe resistivity measurement, in: *AIP Conf Proc*, American Institute of Physics Inc., 2220 (2020) 040029.
- [5] D. Sahoo, A.K. Karan, Z. Mallick, N.B. Manik, Synthesis and complex impedance analysis of nano cubic  $\text{CH}_3\text{NH}_3\text{SnI}_3$  perovskite for the development of optoelectronic lead-free Schottky diode, *Mater Sci Semicond Process* 155 (2023) 095507.
- [6] Y. Dang, Y. Zhou, X. Liu, D. Ju, S. Xia, H. Xia, X. Tao, Formation of Hybrid Perovskite Tin Iodide Single Crystals by Top-Seeded Solution Growth, *Angewandte Chemie - International Edition* 55 (2016) 3447–3450.
- [7] A. Upadhyaya, C.M. Singh Negi, A. Yadav, S.K. Gupta, A. Singh Verma, Analysis of Perovskite Based Schottky Photodiode, 2100, 020134 (2019).
- [8] W. Luo, L. Yan, R. Liu, T. Zou, S. Zhang, C. Liu, Q. Dai, J. Chen, H. Zhou, High detectivity ITO/organolead halide perovskite Schottky photodiodes, *Semicond Sci Technol* 34 (2019) 074004.
- [9] D. Sahoo, A. Kanti Karan, N. Baran Manik, Influence of SWCNT on the Electrical Behaviour of an Environmentally Friendly  $\text{CH}_3\text{NH}_3\text{SnI}_3$  Perovskite-Based Optoelectronic Schottky Device, *ACS Appl Electron Mater* 5 (2023) 2203–2214.
- [10] S.M. Sze, D.C. Mattis, *Physics of Semiconductor Devices*, 1970.
- [11] C.-T. Sah, R.N. Noyce, W. Shockley, Carrier Generation and Recombination in P-N Junctions and P-N Junction Characteristics 45 (1957) 1228 – 1243.

- [12] J.P. Sullivan, R.T. Tung, M.R. Pinto, W.R. Graham, Electron transport of inhomogeneous Schottky barriers: A numerical study, *J Appl Phys* 70 (1991) 7403–7424.
- [13] J.H. Werner, H.H. Güttler, Barrier inhomogeneities at Schottky contacts, *J Appl Phys* 69 (1991) 1522–1533.
- [14] S. Mahato, D. Biswas, L.G. Gerling, C. Voz, J. Puigdollers, Analysis of temperature dependent current-voltage and capacitance-voltage characteristics of an Au/V<sub>2</sub>O<sub>5</sub>/ n -Si Schottky diode, *AIP Adv* 7 (2017) 085313.
- [15] G. Greco, P. Prystawko, M. Leszczyski, R. Lo Nigro, V. Raineri, F. Roccaforte, Electro-structural evolution and Schottky barrier height in annealed Au/Ni contacts onto p-GaN, *J Appl Phys* 110 (2011) 123703.
- [16] D.R. Lambada, S. Yang, Y. Wang, P. Ji, S. Shafique, F. Wang, Investigation of Illumination Effects on the Electrical Properties of Au/GO/p-InP Heterojunction with a Graphene Oxide Interlayer, *Nanomanufacturing and Metrology* 3 (2020) 269–281.
- [17] J.P. Sullivan, R.T. Tung, M.R. Pinto, W.R. Graham, Electron transport of inhomogeneous Schottky barriers: A numerical study, *J Appl Phys* 70 (1991) 7403–7424.
- [18] S. Sen, N.B. Manik, Effect of Different Sized Multi Walled Carbon Nanotubes on the Barrier Potential and Trap Concentration of Malachite Green Dye Based Organic Device, *Advances in Materials Science* 20 (2020) 16–26.
- [19] S. Chakraborty, N.B. Manik, Improvement of electrical and photovoltaic properties of methyl red dye based photoelectrochemical cells in presence of single walled carbon nanotubes, *Frontiers of Optoelectronics* 8 (2015) 289–297.
- [20] A. Rose, *Space-Charge-Limited Currents in Solids*, 1955.
- [21] P.N. Murgatroyd, H.H. Wills, Theory of space-charge-limited current enhanced by Frenkel effect, 1969.
- [22] O.C. Olawole, D.K. De, Theoretical studies of thermionic conversion of solar energy with graphene as emitter and collector, *J Photonics Energy* 8 (2018) 1.
- [23] X. Song, B. Han, X. Yu, W. Hu, The analysis of charge transport mechanism in molecular junctions based on current-voltage characteristics, *Chem Phys* 528 (2020) 110514.
- [24] M.A. Lampert, Theory of Space-Charge-Limited Currents in an Insulator with Traps, 103 (1956) 6.
- [25] O. Almora, A. González-Lezcano, A. Guerrero, C.J. Brabec, G. Garcia-Belmonte, Ion-mediated hopping electrode polarization model for impedance spectra of CH<sub>3</sub>NH<sub>3</sub>PbI<sub>3</sub>, *J Appl Phys* 128 (2020) 075104.

# **Chapter 6: Study on Charge Conduction Mechanisms of Lead-Free Cesium Tin Chloride Perovskite Microrods**

## **6.1 Introduction**

## **6.2 Experimental Section**

### 6.2.1 Materials

### 6.2.2 Perovskite Microstructure Synthesis

### 6.2.3 Measurement Methodology

### 6.2.4 Instruments Used

### 6.2.5 Characterizations

## **6.3 Results and Discussions**

## **6.4 Conclusions**

## **6.5 References**

## 6.1 Introduction

In the last three chapters, we discussed the effect of CNTs on the optoelectronic performance of lead-free organic-inorganic  $\text{CH}_3\text{NH}_3\text{SnI}_3$  perovskite. We observed that CNTs significantly improve the electrical and optical properties of  $\text{CH}_3\text{NH}_3\text{SnI}_3$ -based Schottky devices. Besides this efficient lead-free perovskite, many different purely inorganic lead-free perovskites are also available, which are quite efficient in terms of optoelectronic performance. Lead-free inorganic perovskites such as  $\text{CsSnCl}_3$ ,  $\text{CsSnBr}_3$ , and  $\text{CsSnI}_3$  are receiving significant attention as potential alternatives to lead-based perovskites in various applications [1–3].

Researchers are studying these perovskites to enhance their optoelectronic performance through morphological modifications and by understanding their electronic charge injection, transport, and collection dynamics [4–6]. In this context, synthesizing novel morphologies and understanding their charge transport mechanisms is crucial for developing high-performance devices.

In this work, we used a solution processing technique to synthesize  $\text{CsSnCl}_3$  perovskite with a novel microrod-like morphology (width: 136–356  $\mu\text{m}$ ). The sample was characterized by various methods such as XRD, field emission scanning electron microscopy (FESEM), energy-dispersive X-ray spectroscopy (EDS), and elemental mapping. The electrical potential of the microrods was determined by measuring their I-V characteristics. The charge injection from the electrode into the material was explained using Richardson-Schottky thermionic emission theory. The barrier height ( $\phi_b$ ) and ideality factor ( $\eta$ ) of the device were estimated.

The charge transport investigation shows that the sample exhibits a different conduction process after a transition voltage. This change can be attributed to the presence of traps in the sample, which arise due to structural defects or perturbed molecules in the lattice. These traps cause a charge of polarization energy in the perturbed zones, affecting the forbidden region and the Fermi energy level of the material [7,8]. The charge transport was modeled and fitted into different zones, including ohmic, trap-assisted space charge limited current (SCLC) conduction, and trap-free SCLC. Several useful electrical properties of the  $\text{CsSnCl}_3$  perovskite, such as transit time, threshold voltage, and trap density, were estimated. The results showed that the microrods have excellent conductivity and low trap concentration, making them suitable for use in optoelectronic devices.

## 6.2 Experimental Section

### 6.2.1 Materials

Sn powder (anhydrous, 99 % purity), CsCl (98% purity), pyrazine, and tin fluoride ( $\text{SnF}_2$ ) were purchased from Sigma Aldrich, and a few solvents like hydrochloric acid (HCl) and ethanol were purchased from Merck (India). All of the compounds were utilized without being purified further. The experiment's deionized water was obtained from the departmental Milli (Q) water facility.

### 6.2.2 Perovskite Microstructure Synthesis

1 mmol of Sn powder was dissolved in 3 M of 3 ml HCl in a beaker and put on a magnetic stirrer in an  $\text{N}_2$  atmospheric glove box. Then, 1mmol of CsCl was added to the solution and stirred for 3 hours at  $65^\circ\text{C}$ .

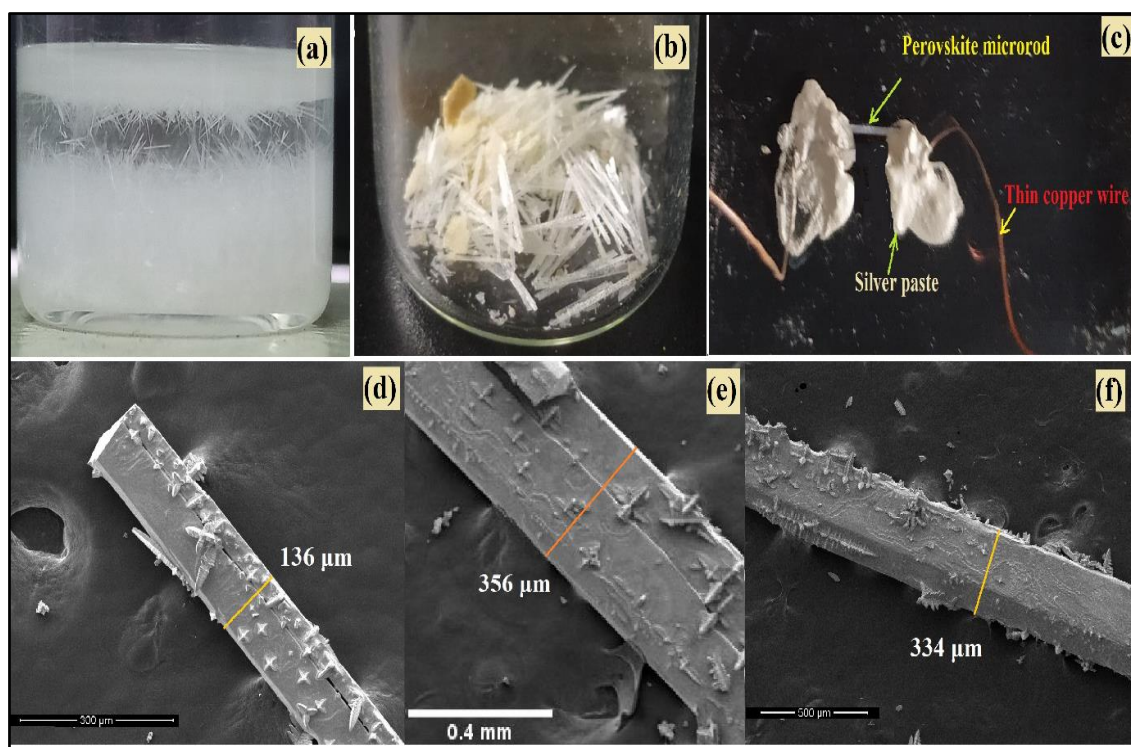


**Figure 6.1:**  $\text{CsSnCl}_3$  perovskite microrod (a) during synthesis (b) after solvent evaporation (c) laboratory electrical measurement setup (d-f) FESEM images of  $\text{CsSnCl}_3$  perovskite microrods of thickness 136, 356, and 334  $\mu\text{m}$

Next, the solution was kept aside to cool down and let the solution to developed perovskite microrods. **Figure 6.1(a)** and **(b)** shows the as-synthesized and after-wash perovskite microrods.

### 6.2.3 Measurement Methodology

The FESEM images of microrods with different thicknesses-356  $\mu\text{m}$  (rod 1), 334  $\mu\text{m}$  (rod 2), and 136  $\mu\text{m}$  (rod 3)-are shown in **Figure 6.1(d-f)**. To measure the I-V characteristics of the microstructures, two drops of silver paste were placed on a cleaned glass slide and left to dry. During the drying process, two very thin copper wires were connected to the silver paste for electrical connections. When the paste was nearly dry, one of the microrods was carefully placed over the two drops of silver paste, as shown in **Figure 6.1(c)**.

### 6.2.4 Instruments Used

The instruments used in this work are mostly the same as those described in Chapter 4. A detailed description of all the instruments can be found in Chapter 4.

### 6.2.5 Characterizations

The crystallinity investigation of these as-synthesized microrods was carried out using a Bruker D8 SWAX diffractometer with Cu-K $\alpha$  radiation of wavelength 1.5404 Å, operating at 35 kV and 35 mA at room temperature. The X-Ray diffraction measurement was carried out in the two-theta range of 20-60°. The rods were imaged using a field emission scanning electron microscope (FESEM), and the stoichiometric ratios of the elements were analysed using an energy dispersive spectroscopy (EDS) detector from Bruker (Quantax, 200). Each rod's current-voltage (I-V) characteristics were recorded using Keithley 2400 SMU to understand its electrical charge transport potential.

## 6.3 Results and Discussions

The calculated, and experimental PXRD measurements of the as-synthesized sample shown in **Figure 6.2(a)** demonstrate that all of the peaks were well matched with COD ID #1527954 having  $P 12_1/n 1$  space group symmetry. This result confirms that the high-quality CsSnCl<sub>3</sub>-perovskite was synthesized. The elemental composition of the material was measured using energy-dispersive X-ray spectroscopy as shown in **Figure 6.2(b)**, which demonstrates that the elements Cs, Sn, and Cl of CsSnCl<sub>3</sub> perovskite occur in a stoichiometric proportion of 0.87:1.04:3.08, which is very close to the ideal proportion of 1:1:3. Which again confirms that the all-inorganic CsSnCl<sub>3</sub> perovskite was effectively produced. **Figure 6.2(c-f)** depicts the corresponding mapping of elements Cs, Sn, and Cl of perovskite microrod.

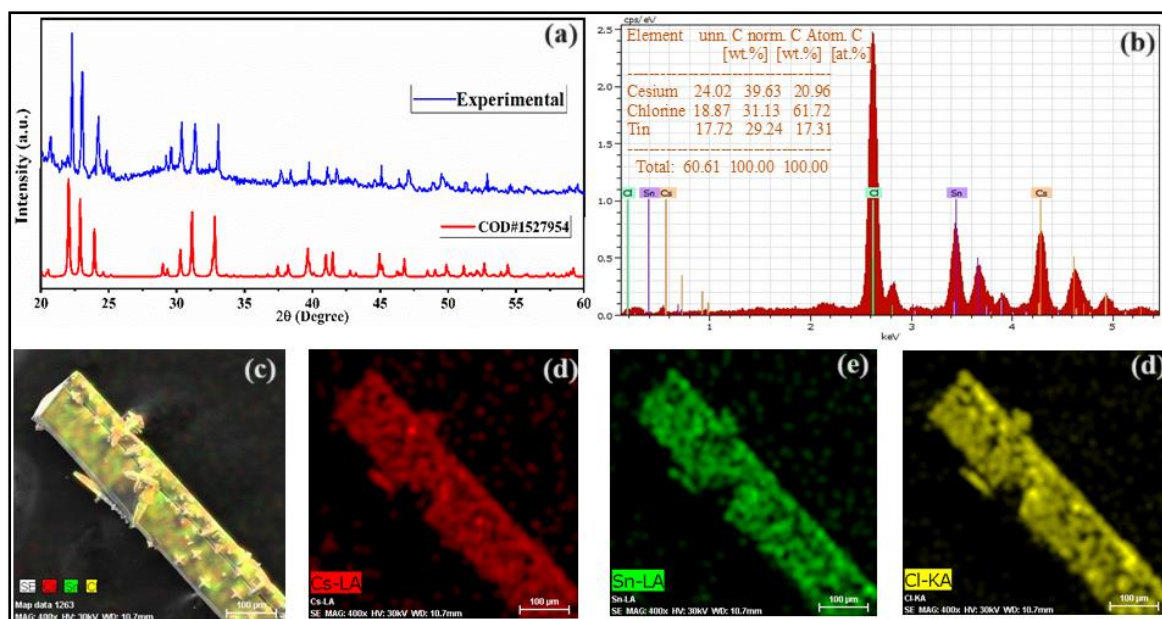


**Figure 6.2:** (a) Experimentally and calculated PXRD of CsSnCl<sub>3</sub> perovskite sample (b) EDS graph to show the elemental composition of the perovskite, inset of this figure represents atomic ration present in the sample and (c) to (d) demonstrates the FESEM image, Cs, Sn, and Cl elements mapping, respectively.

To analyse the electrical behaviour of the CsSnCl<sub>3</sub> perovskite microrods I-V characteristics were measured for three microrods of different thicknesses. The I-V characteristics were collected using a Keithley 2400 source meter applying a bias voltage in the range of  $\pm 2$  V across the perovskite rods as mentioned in the previous section. The I-V properties displayed in **Figure 6.3(a)** show a nonlinear rectifying nature, which indicates the Schottky behaviour of the device. As a result, the device produces a good rectification ratio. The rectification ratios ( $I_{on}/I_{off}$ ) of rods **1**, **2**, and **3** calculated at 2 V from the graphs are 3, 2.5, and 5.5. The values of electrical conductivities of all three rods are listed in **Table 6.1**, which shows that the thicker rod (356  $\mu\text{m}$ ) has greater conductivity. However, the average conductivity of the sample is  $2.05 \times 10^{-4}$  S/m, which indicates that lead-free CsSnCl<sub>3</sub> microrods have excellent potential in electrical applications like switching devices.

The analysis of electrical I-V characteristics of such metal (ITO)-semiconductor (perovskite) (M/S) contact is an efficient method for determining the fundamental charge injection parameters of the device. To study the I-V relationship, it has been considered that the charge conduction that occurs at the metal-semiconductor junction is due to the thermionic emission (TE) effect. To explore the charge transport phenomena following standard **Equations 6.1** has been considered [9].

$$I = I_0 \left[ \exp\left(\frac{qV}{\eta kT}\right) - 1 \right] \quad (6.1)$$

Where  $V$ ,  $\eta$ ,  $q$ ,  $k$ , and  $T$  are the applied bias voltage, the ideality factor, the electronic charge, the Boltzmann constant, and the operating temperature in kelvin respectively. The reverse saturation current,  $I_0$  extracted from the straight-line intercept of  $\ln(I)$  at  $V = 0$  and can be expressed by Richardson-Schottky TE theory [10] as

$$I_0 = A_{ef} A^* T^2 \exp\left(-\frac{q\phi_b}{kT}\right) \quad (6.2)$$

Where  $\phi_b$  is the barrier height (BH) at the junction,  $A_f$  is the effective area of Schottky diode which is  $8.01 \times 10^{-9}$ ,  $4.89 \times 10^{-8}$  and  $5.49 \times 10^{-8} \text{ m}^2$  for microrod **3**, **2** and **1**, respectively.  $A^*$  represents the effective Richardson constant. In most of the literature the value of  $A^*$  is considered as  $1.20 \times 10^6 \text{ AK}^{-2} \text{ m}^{-2}$  [11,12]. Now, the temperature-dependent apparent BH at zero bias can be obtained from **Equation 6.2** given by

$$\phi_b = \frac{kT}{q} \ln\left(\frac{A A^* T^2}{I_0}\right) \quad (6.3)$$

Another important parameter of a diode is  $\eta$ , which describes the deviation of experimental I-V from ideal TE theory and can be obtained from **Equation 6.1** given by

$$\eta = \frac{q}{kT} \left[ \frac{dV}{d(\ln I)} \right] = \frac{q}{kT} \times \frac{1}{\text{Slope of } \ln I \text{ vs. } V \text{ plot}} \quad (6.4)$$

The values of the ideality factor and barrier height of the Schottky devices can be obtained from the slope and intercept of  $\ln I$  vs.  $V$  plots, which are listed in **Table 6.1**. Generally, the ideal value of the ideality factor of the Schottky devices is 1 but practically as can be seen from **Table 6.1**, it is greater than 1. It is maybe due to the presence of barrier inhomogeneity, defects, and traps at the metal perovskite junction[13–15].

**Table 6.1: The values of electrical parameters of the samples**

Sample	Rectification ratio	Conductivity S/m	Barrier height ( $\phi_b$ ) in eV	Ideality factor ( $\eta$ )
1 (356 $\mu\text{m}$ )	3	$3.08 \times 10^{-4}$	0.84	2.09
2 (334 $\mu\text{m}$ )	2.5	$1.76 \times 10^{-4}$	0.83	2.10
3 (136 $\mu\text{m}$ )	5.5	$1.32 \times 10^{-4}$	0.78	2.86

A low-temperature solution-processable method was used to synthesize perovskite, resulting in a polycrystalline sample with grain boundaries and oxidation vacancies that contribute to trapping states affecting the sample's optoelectronic properties [16,17]. The  $\ln I$ - $\ln V$  plots shown in **Figure 6.3(b-d)** are used to identify the trap type in the sample and reveal electrical parameters such as threshold voltages, transit time, and trap concentration.

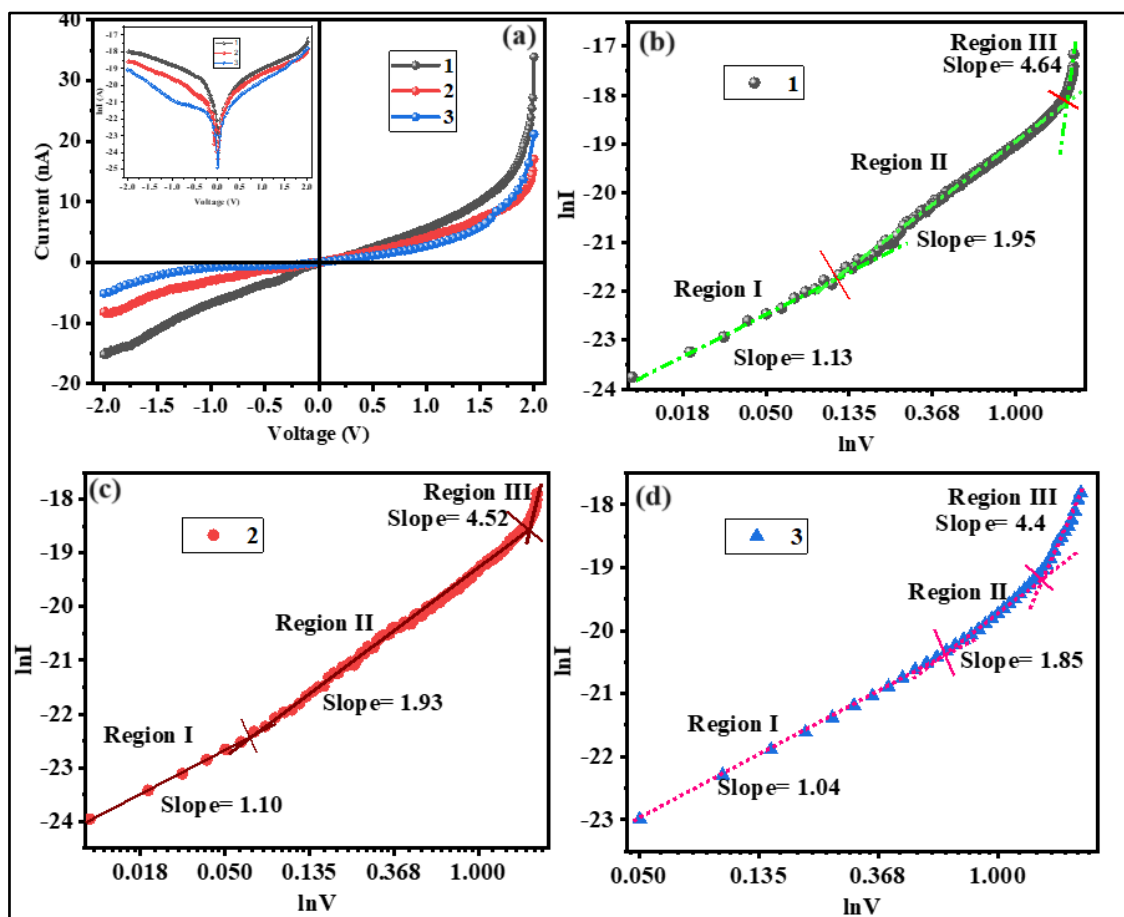


**Figure 6.3: (a) The I-V characteristics of cesium tin tri-chloride perovskite microrods (b)-(d)  $\ln I$  vs  $\ln V$  plots of corresponding I-V characteristics showing different zones of the charge transport mechanism**

The figures illustrate that the current conduction process transforms after a certain applied voltage, referred to as the threshold voltage ( $V_{th}$ ). The region before  $V_{th1}$  (Region I),  $I \propto V$  (i.e., slope,  $m$  is nearly 1), refers to the ohmic transport of the device with negligible electron-hole recombination. This region is governed by the thermally generated charge carriers dominating over the very low number of injected carriers. The slope of the curve changes after the first  $V_{th}$  because injected carriers predominate over inherent carriers in the device. Therefore, this  $V_{th}$  can also be referred to as  $V_{on}$  voltage representing the ‘onset’ of the device. Further increase of applied voltage increases the charge injection and beyond  $V_{th2}$ , the value of the slope is almost

2, which is the hallmark of SCLC (Region II). In the trap-free case, this SCLC is governed by the Mott Gurney law ( $I \propto V^2$ ) [18].

However, in the presence of a discrete trap level due to the extrinsic point defects in the band gap, the SCLC model still follows the same slope ( $\approx 2$ ) as the trap-free MG law, but the magnitude of the current is considerably reduced as a result of transport carrier trapping. In this scenario, for a shallow trap having an energy level  $E_t$  below the conduction band, the current density is given by the equation,  $J_{discrete} = \frac{9}{8} \frac{\theta \epsilon \mu V^2}{s^3}$  instead of MG law according to the SCLC model [19]. Where  $\theta = \frac{N_c}{g_n N_t} \exp\left(\frac{E_t - E_c}{kT}\right)$ , the ratio of free carrier density to the total carrier (free and trapped) density.  $N_t$  is the total trap density,  $g_n$  and  $N_c$  are the degeneracy of the energy state and the density of the states in the conduction band. In this Region II, injected carriers gradually fill the traps present in the forbidden gap hence current changes rapidly. Under the consideration of a discrete trap in the system, the  $V_{on}$  is given by the equation,  $V_{on} = \frac{8}{9} \frac{en_0 s^2}{\epsilon \theta}$  [20]. The carrier transit time,  $\tau_c$  is equal to dielectric relaxation time  $\tau_d$  at  $V_{on}$ . However, once all the traps get filled, the current conduction mechanism again changed as shown in Region III. The voltage at which all the traps get filled is known as trap-filled voltage ( $V_{TF}$ ). In this region, the current increased sharply to reach SCLC current limit provided by Child's law ( $I \propto V^2$ ). This sharp increase in current indicates that the material has a discrete trap.

**Table 6.2: Trap density, threshold voltages, and carrier transit time of perovskite microrods.**

Microrod	First threshold voltage or on voltage $V_{th1}/V_{on}$	Second threshold Voltage or trap-filled voltage $V_{th2}/V_{TF}$	Transit time S	Trap density ( $m^{-3}$ )
1	0.11	1.85	$3.76 \times 10^{-8}$	$9.82 \times 10^{14}$
2	0.07	1.83	$3.86 \times 10^{-8}$	$8.79 \times 10^{14}$
3	0.61	1.46	$4.08 \times 10^{-8}$	$7.69 \times 10^{14}$

The trap-filled voltage  $V_{TF}$  is given by the equation,  $V_{TF} = \frac{e N_t s^2}{2\epsilon}$ . This equation was used to estimate trap density. The value of  $\tau_c$  can be estimated from the relation,  $\tau_c \cong \tau_d = \frac{\epsilon_0 \epsilon_r V}{s J}$  [20] assuming the value of  $\epsilon_r$  as 4.80 [21]. By utilizing the gradient,  $J/V$ , from the ohmic region of the  $\ln I - \ln V$  plot, the value of  $\tau_c$  was calculated to be in the range of  $(3.76 \text{ to } 4.08) \times 10^{-8}$  seconds.

All these values including trap density and threshold voltages are presented in **Table 6.2**. The results demonstrate that the microrods have a low trap density, efficient charge transportation, and a very low "onset" voltage, making them suitable for use in electronic devices.

## 6.4 Conclusions

In this work, lead-free all inorganic  $\text{CsSnCl}_3$  perovskite microrods have been synthesized using a solution processing technique. The rod samples were characterized by XRD, FESEM, EDX, and elemental mapping. The results reveal that a highly crystalline with a proper stoichiometry of elements have been synthesized. To determine the electrical potential of each microrod, the I-V characterization of three microrods having different cross-sectional areas has been measured and analysed to estimate different electrical parameters such as ideality factor and barrier height. The results show that the device has good non-linear characteristics like a semiconductor diode. The detailed charge transport analysis of the sample using I-V characteristics provides some charge conducting parameters like threshold voltage or device on-state voltage, carrier transit time, and trap density in the sample. It is found that the device has very low trap density and fast charge conduction properties which may allow the  $\text{CsSnCl}_3$  microrods to use in different electrical applications in the future.

## 6.5 References

- [1] B. Li, R. Long, Y. Xia, Q. Mi, All-Inorganic Perovskite  $\text{CsSnBr}_3$  as a Thermally Stable, Free-Carrier Semiconductor, *Angewandte Chemie* 130 (2018) 13338–13342.
- [2] K.P. Marshall, M. Walker, R.I. Walton, R.A. Hatton, Enhanced stability and efficiency in hole-transport-layer-free  $\text{CsSnI}_3$  perovskite photovoltaics, *Nat Energy* 1 (2016) 16178.
- [3] M.S. Ali, S. Das, Y.F. Abed, M.A. Basith, Lead-free  $\text{CsSnCl}_3$  perovskite nanocrystals: Rapid synthesis, experimental characterization and DFT simulations, *Physical Chemistry Chemical Physics* 23 (2021) 22184–22198.
- [4] T. Zhang, H. Li, H. Ban, Q. Sun, Y. Shen, M. Wang, Efficient  $\text{CsSnI}_3$ -based inorganic perovskite solar cells based on a mesoscopic metal oxide framework via incorporating a donor element, *J Mater Chem A Mater* 8 (2020) 4118–4124.
- [5] M. Kayumov, M.M. Kayumov, S.S. Giyosov, Structural stability of polymorphic  $\text{CsSnI}_3$  Structural stability of  $\text{CsSnI}_3$  polymorphous, 56 (2017) 84-91.
- [6] C. Hartmann, S. Gupta, T. Bendikov, X. Kozina, T. Kunze, R. Félix, G. Hodes, R.G. Wilks, D. Cahen, M. Bär, Impact of  $\text{SnF}_2$  Addition on the Chemical and Electronic Surface Structure of  $\text{CsSnBr}_3$ , *ACS Appl Mater Interfaces* 12 (2020) 12353–12361.

- [7] S. Ghatak, A. Ghosh, Observation of trap-assisted space charge limited conductivity in short channel MoS<sub>2</sub> transistor, *Appl Phys Lett* 103 (2013) 122103.
- [8] T.S. Sherkar, C. Momblona, L. Gil-Escrig, J. Ávila, M. Sessolo, H.J. Bolink, L.J.A. Koster, Recombination in Perovskite Solar Cells: Significance of Grain Boundaries, Interface Traps, and Defect Ions, *ACS Energy Lett* 2 (2017) 1214–1222.
- [9] O.C. Olawole, D.K. De, Theoretical studies of thermionic conversion of solar energy with graphene as emitter and collector, *J Photonics Energy* 8 (2018) 1.
- [10] A.K. Karan, D. Sahoo, S. Sen, S. Rakshit, N.B. Manik, Effect of titanium-dioxide nanoparticle on Richardson constant and barrier height of tartrazine dye based Schottky device, *Discover Materials* 3 (2023) 5.
- [11] K. Sarpatwari, O.O. Awadelkarim, M.W. Allen, S.M. Durbin, S.E. Mohny, Extracting the Richardson constant: IrOx /n-ZnO Schottky diodes, *Appl Phys Lett* 94 (2009) 242110.
- [12] C.R. Crowbll, The Richardson constant for thermionic emission in Schottky barrier diodes, *Solid-State Electronics* 8 (1965) 395-399.
- [13] D. Han, C. Dai, S. Chen, Calculation studies on point defects in perovskite solar cells, *Journal of Semiconductors* 38 (2017) 011006.
- [14] J.H. Werner, H.H. Güttler, Barrier inhomogeneities at Schottky contacts, *J Appl Phys* 69 (1991) 1522–1533.
- [15] Ş. Aydoğan, M. Sağlam, A. Türüt, On the barrier inhomogeneities of polyaniline/p-Si/Al structure at low temperature, *Appl Surf Sci* 250 (2005) 43–49.
- [16] S. Sen, N.B. Manik, Correlation between barrier potential and charge trapping under the influence of Titanium Di oxide nanomaterials in organic devices, *Results in Materials* 8 (2020) 100145.
- [17] M. Sharma, S.K. Tripathi, Study of barrier inhomogeneities in I-V-T and C-V-T characteristics of Al/Al<sub>2</sub>O<sub>3</sub>/PVA:n-ZnSe metal-oxide-semiconductor diode, *J Appl Phys* 112 (2012) 024521.
- [18] J.A. Röhr, D. Moia, S.A. Haque, T. Kirchartz, J. Nelson, Exploring the Validity and Limitations of the Mott-Gurney Law for Charge-Carrier Mobility Determination of Semiconducting Thin-Films, *J Phys Condens Matter*. 30 (2018) 105901.
- [19] Z. Chiguvare, J. Parisi, Current conduction in poly(3-hexylthiophene) and in poly(3-hexylthiophene) doped [6,6]-phenyl c61-butyric acid methylester composite thin film devices, *Zeitschrift Fur Naturforschung - Section A Journal of Physical Sciences* 67 (2012) 589–600.
- [20] P. Zhang, Y.S. Ang, A.L. Garner, Á. Valfells, J.W. Luginsland, L.K. Ang, Space-charge limited current in nanodiodes: Ballistic, collisional, and dynamical effects, *J Appl Phys* 129 (2021) 100902.
- [21] P. Singh, P.K. Rout, H. Pandey, A. Dogra, Temperature-dependent space-charge-limited conduction in BaTiO<sub>3</sub> heterojunctions, *Journal of Material Science* (2018) 4806–4813.

# **Chapter 7: Study on Charge Transport Mechanisms in $\text{Cs}_2\text{SnCl}_6$ Double Perovskite Schottky Device in Presence of MWCNTs**

## **7.1 Introductions**

## **7.2 Experimental Section**

### 7.2.1 Materials

### 7.2.2 Instruments Used

### 7.2.3 Synthesis of $\text{Cs}_2\text{SnCl}_6$ Perovskite and Its MWCNT Composite

### 7.2.4 Fabrication of UV Detector

### 7.2.5 Smartphone Interfacing with Device

## **7.3 Device Measurement and Characterization**

## **7.4 Results and Discussions**

### 7.4.1 Optoelectronic Study

### 7.4.2 Smartphone Interfaced UV Detector

## **7.5 Conclusions**

## **7.6 References**

## 7.1 Introductions

In the work of our previous chapters, we synthesized  $\text{CH}_3\text{NH}_3\text{SnI}_3$ , CNT- $\text{CH}_3\text{NH}_3\text{SnI}_3$  composites, and  $\text{CsSnCl}_3$  perovskites, systematically characterizing them using various methods before developing Schottky devices and analysing their charge transport mechanisms. During synthesis, we took extensive precautions by conducting the process in a nitrogen-atmosphere glove box to prevent Sn oxidation. Additionally, we designed an encapsulated characterization container to prevent sample degradation during measurements.

However, in this work, we have shifted our focus to synthesizing materials in an open atmosphere. Using the same synthesis recipe for  $\text{CsSnCl}_3$ , we successfully synthesized  $\text{Cs}_2\text{SnCl}_6$  double perovskite in an open atmosphere.  $\text{Cs}_2\text{SnCl}_6$  is inherently stable because it is an already oxidized version of  $\text{CsSnCl}_3$  perovskite, or we can say it is a defect version of  $\text{CsSnCl}_3$  [1,2]. We found that  $\text{Cs}_2\text{SnCl}_6$  perovskite has a large indirect band gap with maximum absorption in the UV region [3]. We developed a Schottky device using this material, but its performance was not very impressive due to its low charge transport capability.

Here, we propose the incorporation of MWCNTs into this double perovskite material,  $\text{Cs}_2\text{SnCl}_6$ , to improve charge transport properties and ultimately enhance the optoelectronic performance of UV detectors [3].  $\text{Cs}_2\text{SnCl}_6$  is a double perovskite material that has shown air stability and promising electronic properties, making it a suitable candidate for use in UV detectors. This chapter discusses the simple synthesis of the  $\text{Cs}_2\text{SnCl}_6$  double perovskite and the incorporation of MWCNTs into the  $\text{Cs}_2\text{SnCl}_6$  matrix in detail. Both materials have been characterized by a range of techniques, including UV-Vis, FESEM, XRD, and XPS.

We evaluated the electrical and optical properties of the  $\text{Cs}_2\text{SnCl}_6$ -MWCNT composite to assess its potential as an active layer in UV detectors. The electrical conductivity of the composite material was measured using I-V measurement techniques. We then discussed the results in terms of the charge transport potential of  $\text{Cs}_2\text{SnCl}_6$ -MWCNT composites as active layers in UV detectors. Our findings demonstrate the exciting potential of the composite material in enhancing the charge transport properties and optoelectronic performance of UV detectors. This enables the development of a smartphone-interfaced UV photodetector module, taking advantage of modern smartphones' capabilities for real-time UV radiation monitoring through Wi-Fi or Bluetooth.

Our focus was on showcasing the effectiveness of the MWCNT nanocomposite, and we successfully collected digital data wirelessly, demonstrating the nanocomposite's ability to

function as a digital signal producer in the form of binary signals or even as a pulse train generator. These results pave the way for further exploration in developing nanocomposite-based lead-free perovskite devices for optoelectronic applications. The study provides a comprehensive evaluation of the properties of  $\text{Cs}_2\text{SnCl}_6$ -MWCNT composites and offers valuable insights into the combined charge transport mechanism to optimize their performance for UV detector applications.

## 7.2 Experimental Section

### 7.2.1 Materials

Alfa Aesar provided  $\text{SnCl}_2 \cdot 2\text{H}_2\text{O}$  powder (98% purity), and CsCl (98% purity), while Merck (India) supplied Dimethyl formamide (DMF), Isopropyl alcohol (IPA) and acetone etc solvents. MWCNT Type 15 (98%, OD: 30-35 nm and L: 10-30  $\mu\text{m}$ , -OH functionalized) was procured from SRL company. All chemicals were used as received without any additional purification. The deionized water utilized in the experiment was obtained from the departmental Milli (Q) water facility.

### 7.2.2 Instruments Used

The instruments used in this work are mostly the same as those described in Chapter 4. A detailed description of all the instruments can be found in Chapter 4.

### 7.2.3 Synthesis of $\text{Cs}_2\text{SnCl}_6$ Perovskite and Its MWCNT Composite

Using simple solution processing techniques, the double perovskite  $\text{Cs}_2\text{SnCl}_6$  and its nanocomposite with MWCNT were synthesized. Initially, 3 ml DMF were taken in two separate vials with a magnetic stir bar. These vials were placed on a magnetic stirrer hot plate with a temperature of 75 °C. 2 mmol of  $\text{SnCl}_2 \cdot 2\text{H}_2\text{O}$  powder was added to both vials and stirred for 45 minutes till the solution became transparent. Then, 4 mmol of CsCl was added to both vials and stirred for another 8 hours. After 9 to 10 hours, the clear solution started to white precipitate, and after sometime stirring was stopped. The solution was then filtered into fresh and clean vials to remove large particles and unreactants. To prepare the  $\text{Cs}_2\text{SnCl}_6$ -MWCNT composite, 5wt% MWCNT of perovskite raw samples were added to one of the vials and sonicated for 3 hours, followed by stirring for 2 hours. The resulting two solutions were used to develop devices.

### 7.2.4 Fabrication of UV Detector

The process involved in preparing the ITO-coated glass substrates for the development of perovskite thin layer is described as follows. Initially, multiple ITO-coated glass substrates were subjected to a series of cleaning steps. This included cleaning in an ultrasonic bath for 15 minutes with DI water, Extran MA 02 (Neutral) solution, Milli Q water, acetone, and IPA. Subsequently, the cleaned substrates were dried by placing them on a hot plate set at 75 °C for 15 minutes. Next, the electrode contact region of the ITOs was masked with tape to prevent unwanted deposition of the samples. Then, perovskite precursor was applied to the ITO and spun for 60 seconds at 1600 rpm to develop a thin layer of perovskite only. Similarly, a thin film composite of MWCNT was also developed using a similar process. The films were then immediately placed on a preheated hot plate at 75 °C. After a few seconds, a white and another one greyish layer shift was observed, indicating the successful development of the perovskite thin layer. Finally, pure Al metal electrodes were placed on the films to form sandwiched structure device with an effective area of approximately  $4 \times 9 \text{ mm}^2$  when measured on a standard scale.

### 7.2.5 Smartphone Interfacing with Device

The developed photodetector device exhibited sufficient current generation capability. This enabled the utilization of the  $\text{Cs}_2\text{SnCl}_6$  perovskite-nanocomposite UV detector as a remotely accessible photodetector module. To achieve this, we designed a smartphone interfaced photodetector, and its basic configuration is illustrated in **Figure 7.1** as a block diagram.

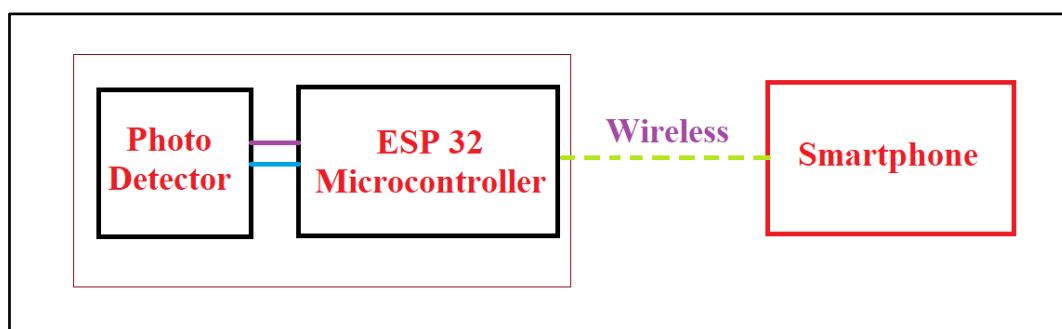


**Figure 7.1: Block diagram of smartphone-based photo detector using ESP 32 MCU**

To integrate the photodetector with a smartphone, we employed an Arduino based ESP32 microcontroller unit (MCU). The photodetector's negative terminal was connected to a general-purpose input/output (GPIO) pin  $V_P$  and another one was connected to GND pin on the MCU.

Subsequently, we developed a suitable program that facilitated the communication between the MCU and the smartphone via Bluetooth. This allowed us to remotely collect data from the photodetector. On the smartphone side, we used a serial Bluetooth connector and data recorder to capture both analog and digital information remotely.

### 7.3 Device Measurement and Characterization

The synthesized perovskite samples were characterized for crystal structure properties using a Bruker D8 SWAX diffractometer with  $\text{Cu-K}_\alpha$  as the radiation source ( $\lambda = 1.541 \text{ \AA}$ ), operating at 35 mA and 35 kV. The measurement was conducted in the two-theta range of  $10\text{--}60^\circ$  to obtain X-Ray diffraction peaks, and the sample holder was rotated by 10 rpm during the scan to gather all possible peak information. The optical characteristics of the films were studied using a SHIMADZU UV-1900, while a Thermo Scientific  $\text{K}_\alpha$ -X-ray Photoelectron Spectrometer with a monochromatic (1486.6 eV)  $\text{Al-K}_\alpha$  source was used to evaluate the XPS of the samples. To explore the morphological properties of the perovskite materials, two distinct thin films were formed on two glass slides as previously described. The sample was coated with gold using the Quorum Q150R ES coating equipment, and images were taken using a FESEM. These samples were then analysed using a Bruker EDS detector (Quantax, 200). The TGA was conducted with NETZSCH within a temperature range of 32 to  $600^\circ\text{C}$ . The I-V and I-t characteristics of the devices were measured using Keithley 2400 source metre unit. The spectral responses of the fabricated devices were measured using a Xe-lamp solar simulator assembled with a monochromator as the light source.

### 7.4 Results and Discussions

The  $\text{Cs}_2\text{SnCl}_6$  is a defect variant of the perovskite, which adopts a vacancy-ordered double perovskite structure (space group  $\text{Fm}\bar{3}\text{m}$ ) with isolated  $[\text{SnCl}_6]$  octahedra [4]. As shown in **Figure 7.2(b)**, 12-Cl atoms surrounding the Cs atom form a  $[\text{CsCl}_{12}]$  cuboctahedron, and the Sn atom is octahedrally coordinated with six halogens to form  $[\text{SnCl}_6]$  octahedra. The measured X-ray diffraction (XRD) patterns of the synthesized  $\text{Cs}_2\text{SnCl}_6$  materials are illustrated in **Figure 7.2(a)**, which are consistent with the standard  $\text{Cs}_2\text{SnCl}_6$  phase (ICSD #07-0197).

The XRD patterns show a high degree of crystallinity in the both sample with CNT and without CNT. In the composite, the XRD peaks are lies on a small hump which may be arisen due to the amorphous nature of CNT. However, in both cases strong peaks due to perovskites indicates its high crystallinity.

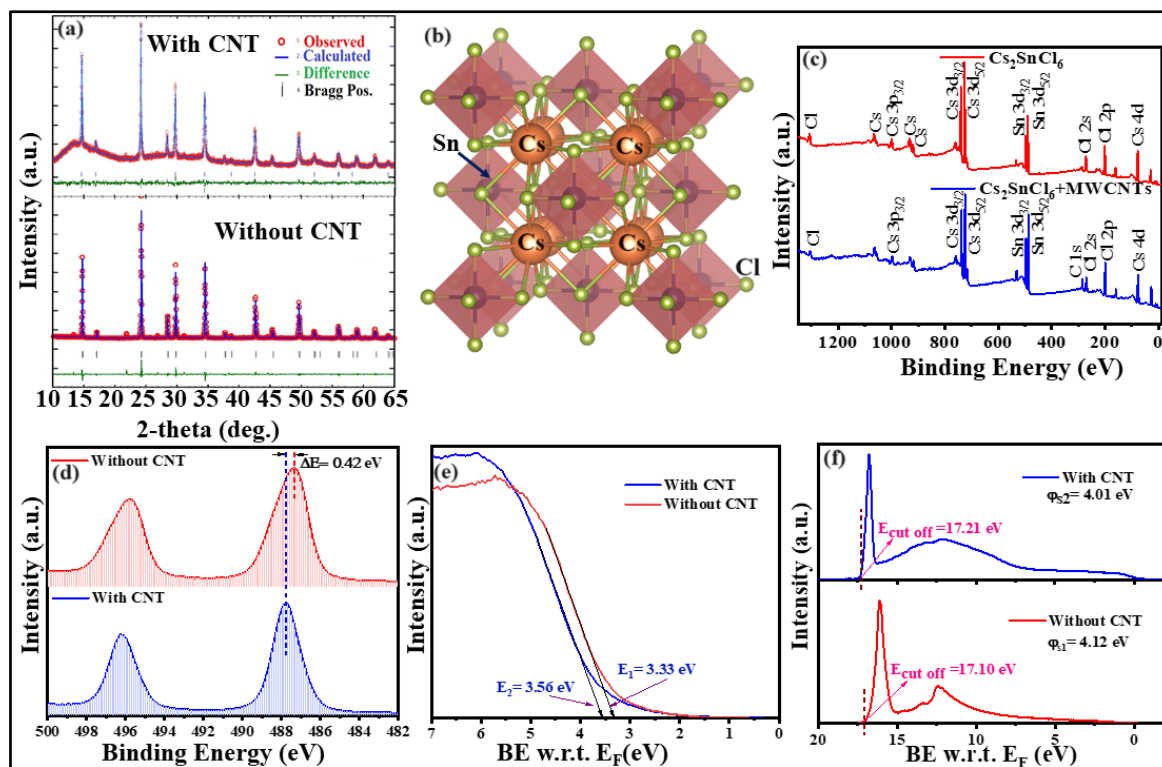


**Figure 7.2:** (a) X-Ray crystallography measurements of perovskite and nanocomposite perovskite (b) lattice structure of  $\text{Cs}_2\text{SnCl}_6$  double perovskite (c) XPS survey curves (d) characteristics XPS peak spectra of the Sn element of samples (e) Fermi energy spectra (f) UPS spectra for work function measurements

XPS was performed to analyse further the chemical composition and oxidation state of  $\text{Cs}_2\text{SnCl}_6$  perovskite. Binding energy (BE) of elements was calibrated against C 1s (284.6 eV). XPS survey shows Cs, Sn and Cl peaks as shown in **Figure 7.2(c)** and confirms  $\text{Cs}_2\text{SnCl}_6$  formation [5]. The signal peaks in the both with and (without) CNT spectra located at 725.08 (724.13) eV and 739.08 (738.07) eV corresponded to the Cs  $3d_{3/2}$  and  $3d_{5/2}$  orbitals, respectively. The two strong peaks at 487.77 eV and 496.25 eV can be attributed to state Sn  $3d_{3/2}$  and  $3d_{5/2}$ , respectively. These results are consistent with the values of  $\text{Sn}^{4+}$  reported in the different literature [6,7]. The BE difference between these two peaks is 8.48 eV, which is also very close to that reported in the literature (8.5 eV) [8,9]. No distinct  $\text{Sn}^{2+}$  peak (for which the corresponding binding energy is approximately 485.8 eV) is observed. Therefore, it is clear that Sn is present in the compound in the form of oxidation state i.e. in the state of  $\text{Sn}^{4+}$ . From **Figure 7.2(d)** compared two samples XPS peaks of these Sn  $3d_{3/2}$  and  $3d_{5/2}$  states and shows that in presence of CNTs the peaks were shifted by an amount of  $\Delta E = 0.42$  eV towards high binding energy. This shift of BE in the composite toward higher energies compared to the pristine perovskite demonstrates the improved interface interaction between perovskite and

CNTs. A large amount of charge transfer at the interface enhances the separation and migration of photogenerated carriers.

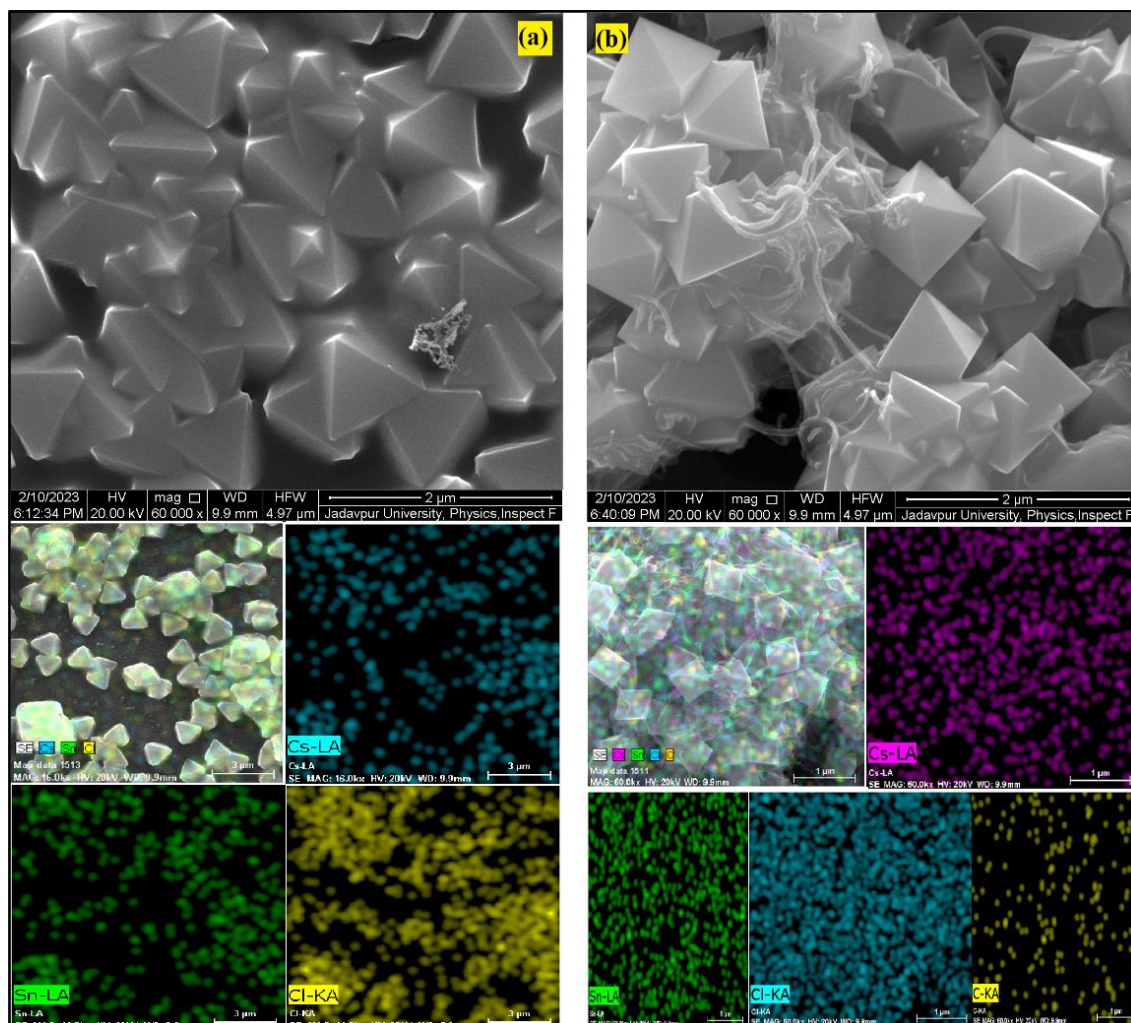


**Figure 7.3:** (a) and (b) demonstrate FESEM images for morphology of  $\text{Cs}_2\text{SnCl}_6$  and CNT- perovskite composite, while below their SEM images show elemental mappings of  $\text{Cs}_2\text{SnCl}_6$  and CNT-perovskite composite.

**Figure 7.3** SEM images offer visual examination of material structure and shape. **Figure 7.3(a)** clearly indicates that perovskites are three-dimensional in shape. However, films are not as uniform. Non-uniformity of films or gaps, as well as defects in the films, are referred to as trap states for charge carriers. Because of the presence of these defect states, charge transfer is interrupted. In **Figure 7.3(b)**, SEM scans demonstrate that the nanotubes surround the perovskite structure in three dimensions from all directions. As it is well known that carbon nanotubes exhibit excellent electrical conductivity this incorporation them into perovskite structures can enhance the charge transport properties of the material, also can provide

mechanical strength to the film which can improve the performance of perovskite-based devices such as solar cells or sensors. This incorporation of CNTs may help mitigate these defects, leading to more efficient and reliable charge transporting active layer.

Elemental signals of C, Cs, Sn, and Cl can be detected in EDX spectroscopy and elemental mapping images given below their SEM images. From the atomic weight ratio analysis shown in **Figure 7.4 (a)** and **(b)** for both the samples, it can be concluded that Cs, Sn and Cl lies in the compound in approximately 2:1:6 ratio and for CNT-composite sample there is a small signal in low binding energy region of composite sample shown inset of **Figure 7.4(b)**, which indicate that the CNTs are homogeneously dispersed in the perovskite sample.

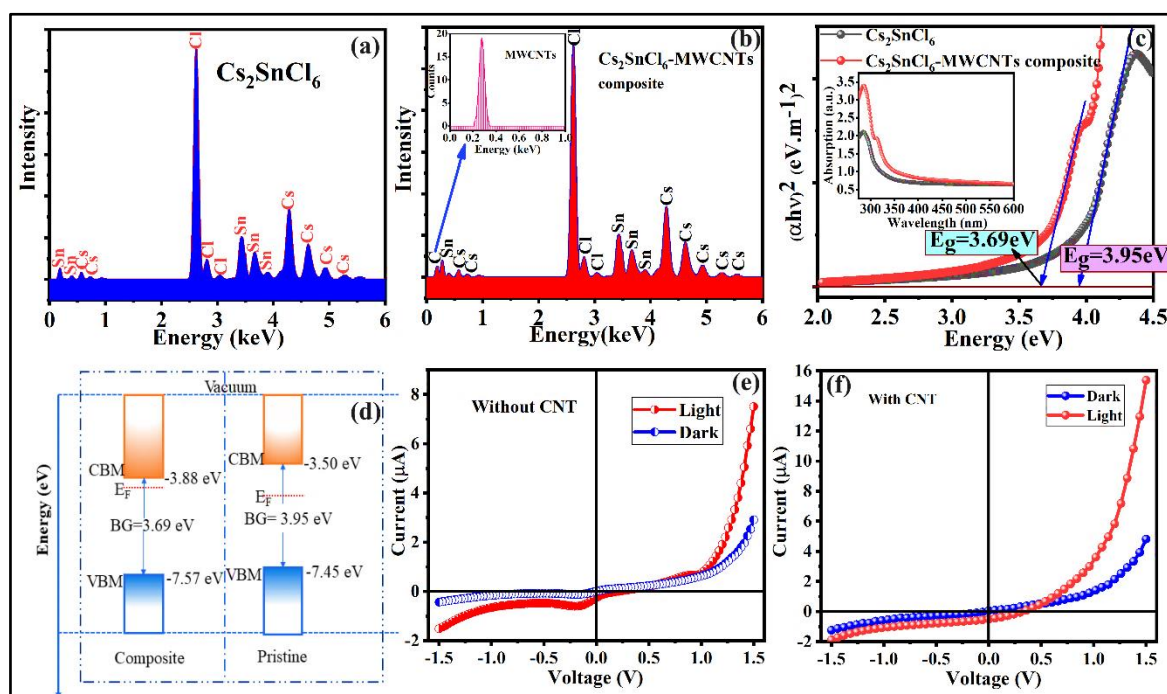


**Figure 7.4:** (a) and (b) EDX spectra of  $\text{Cs}_2\text{SnCl}_6$  and nanocomposite- $\text{Cs}_2\text{SnCl}_6$  perovskite, respectively (c) absorption spectre and Tauc plots to determine the optical bandgaps of the samples (d) energy band diagrams of both the samples drawn using information obtained from UPS (work function) and Tauc plots (bandgap). Dark and UV light I-V characteristics of the device (e) ITO/  $\text{Cs}_2\text{SnCl}_6$ /Al and (f) ITO/  $\text{Cs}_2\text{SnCl}_6$ -MWCNT/Al measured at room temperature

Now to draw the band diagram of the device, the differences between the Fermi level ( $E_f$ ) and valance band maximum ( $E_{\text{VBM}}$ ) were evaluated from the UPS spectra as shown in **Figure 7.2(e)**. This was done by extrapolating the leading edge of the UPS spectra to the baseline and gives values of ( $E_f - E_{\text{VBM}} \Rightarrow$ ) 3.56 and 3.33 eV for composite and pristine perovskite, respectively [10–12]. The work functions (WF) of the samples were measured with the help of

formula:  $\phi_{WF} = W - (h\nu)_{He I}$ , where  $W$  is the width of the UPS spectrum taken from the Fermi level to the secondary-electron cut-off (SECO) shown in **Figure 7.2(f)** and  $h\nu$  is the incident photon energy i.e. 21.22 eV He I radiation [13].

In a calibrated spectrometer, the  $E_F$  position for the  $KE_{max}$  electron can be established, in which the electron binding energy (BE) becomes zero. Therefore, the spectrometer WF is not necessary to be considered afterwards [11,13]. What has to be measured is the position of  $KE_{min}$  or SECO position. The SECO of UPS spectres shown above mention figure. Therefore, the work functions of the composite and pristine perovskites were found to be -4.01 and -4.12 eV vs. vacuum, respectively. So, VBMs of the samples were found to be -4.01-3.56= -7.57 eV and -4.12-3.33= -7.45 eV vs. vacuum, respectively from composite and pristine perovskite.

Another crucial parameter required to draw band diagram is bandgap of the samples. These values are calculated from the solid-state UV–vis absorption spectrum, which is shown in the inset of **Figure 7.4(c)**. Using these absorption data of the samples the Tauc's plot have been drawn to estimate the bandgap values of the semiconducting double perovskites. The Tauc's relation can be written as [14]:  $(\alpha h\nu)^\gamma = A(h\nu - E_g)$ , where the exponent “ $\gamma$ ” is the electron transition process-dependent constant (i.e. 2 for direct BG sample and  $\frac{1}{2}$  for indirect BG sample) and  $\alpha$ ,  $E_g$ , and  $h\nu$  stand for absorption coefficient, bandgap of bulk, and photon energy, respectively. “ $A$ ” is a proportionality constant that is considered as 1 for the ideal case. By extrapolating the linear region of the Tauc plot  $(\alpha h\nu)^2$  vs.  $h\nu$  to  $\alpha = 0$  absorption, the value of optical band gap ( $E_g$ ) of the composite and pristine perovskite films were found to be 3.69 and 3.95 eV, respectively. Therefore, using these bandgap values and position of VBM the CBM also can be obtained as -7.57+3.69= -3.88 eV and -7.45+3.95= -3.50 eV for composite and pristine perovskites, respectively. Finally, the complete energy level structure of samples is depicted in **Figure 7.4(d)**.

### 7.4.1 Optoelectronic Study

The current-voltage (I-V) characteristics were recorded as shown in **Figure 7.5(c)** and **(d)** in the temperature range of 308-393K by applying bias within  $\pm 2$  V across two particular thin film-based ITO/Cs<sub>2</sub>SnCl<sub>6</sub>/Al and ITO/nanocomposite-Cs<sub>2</sub>SnCl<sub>6</sub>/Al devices. Whereas, in **Figure 7.4(e)** and **(f)** the IV characteristics are shown at room temperature only in both dark and light conditions for both the devices. The I-V characteristics exhibit a highly nonlinear rectifying nature in dark circumstances, indicating the Schottky behaviour of the device. In

addition, to form a Schottky junction, the work function of the electrode has to be higher than that of the semiconductor [15,16]. **Figure 7.5(a)** depicts the energy level diagram of the various layers, whereas **Figure 7.5(b)** demonstrates band diagram of the device. According to the energy level diagram, Al has a lower work function ( $\phi_{\text{Al}} = 4.2$  eV) than semiconducting perovskite ( $\phi_{s1} = 4.01$  eV and  $\phi_{s2} = 4.12$  eV), although ITO has a higher work function ( $\phi_{\text{ITO}} = 4.8$  eV) than perovskite. As a result of the development of the Schottky junction at the ITO/perovskite interface, the device exhibits Schottky behaviour, and the Al/perovskite interface behaves as an ohmic contact. **Figure 7.5(b)** depicts the presence of a barrier height ( $\phi_{bi} = 0.68$  eV: pristine and 0.79 eV: composite) at the junction formed by the diffusion of ITO and perovskite carriers to create built-in potential.

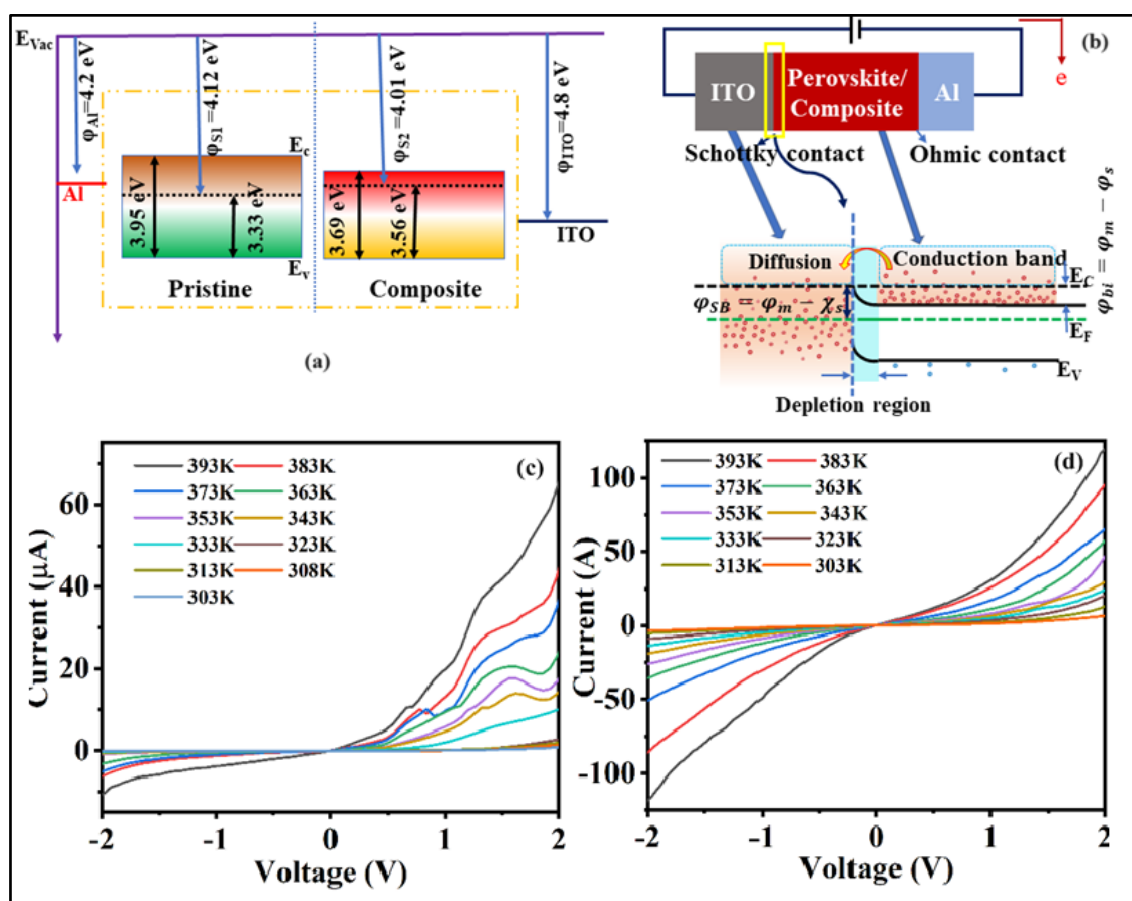


**Figure 7.5:** (a) Energy level diagram of the different layers (b) device band alignment in forward biased situation. I-V characteristics recorded in the temperature range of 308-393K by applying bias within  $\pm 2$  V across two thin film-based (c) ITO/ $\text{Cs}_2\text{SnCl}_6$ /Al and (d) ITO/nanocomposite- $\text{Cs}_2\text{SnCl}_6$ /Al devices

When a bias voltage was applied, the built-in potential drops according to strength of bias, and electrons transfer to the ITO electrode from the perovskite. However, when a reverse bias is applied, the carriers are unable to pass to perovskite from ITO due to the existence of a high

barrier height. As a result, a high rectification ratio is obtained from the device. The rectification ratios ( $I_{on}/I_{off}$ ) calculated at 1.5 V are 7.72 in the dark and 5.35 in the light for the perovskite-based device, and 4.85 in the dark and 10.30 in the light for the CNT-based device. The values of electrical conductivities are listed in **Table 7.1** of both devices, which shows that in presence of CNTs electrical conductivity has improved by 1.66 and 2.05 times in dark and light conditions, respectively. In the presence of photo illumination, conductivities improved by 2.55 and 3.28 times on devices without and with CNTs, respectively.

The I-V analysis of Schottky device electrical characteristics is an efficient method for determining fundamental electrical performance parameters. To study the I-V relationship, it has been considered that the charge conduction at the metal oxide/semiconductor junction is due to the thermionic emission (TE) effect. To explore the charge transport phenomena following standard **Equations 7.1** has been considered [17,18].

$$I = I_0 \left[ \exp\left(\frac{qV}{\eta kT}\right) - 1 \right] \quad (7.1)$$

Where V,  $\eta$ , q, k, and T are the applied bias voltage, the ideality factor, the electronic charge, the Boltzmann constant, and the operating temperature in kelvin respectively. The reverse saturation current,  $I_0$  extracted from the straight-line intercept of  $\ln(I)$  at  $V = 0$  and can be expressed by TE theory as

$$I_0 = A_{ef} A^* T^2 \exp\left(-\frac{q\phi_b}{kT}\right) \quad (7.2)$$

Where  $\phi_b$  is the barrier height (BH) at the junction,  $A_{ef}$  is the effective area of the Schottky diode which is  $4 \times 10^{-6} \text{ m}^2$ ,  $A^*$  represents the effective Richardson constant. In most of the literature the value of  $A^*$  is considered as  $1.20 \times 10^6 \text{ A K}^{-2} \text{ m}^{-2}$  which is agreed for most of the semiconducting materials. But literatures also shows that it may vary from device to device. Again, the precise value of this parameter is essential since it is utilized to estimate the different device performance factors such as barrier height and series resistance. Therefore, it is best practice to estimate the Richardson constant for a specific device before calculating the electrical parameters of any device. Hence in this work, for Cs<sub>2</sub>SnCl<sub>6</sub> perovskite-based device, the value of  $A^*$  has been estimated.

For that, the temperature dependent dark I-V characteristics for both devices has been recorded. However, beside the estimation of Richardson constant, the temperature dependent I-V characteristics also enabled us to understand the behaviour of different electrical parameters

like ideality factor and barrier height with the variation of temperature. The Richardson plots for the  $\text{Cs}_2\text{SnCl}_6$  perovskite-based device has been shown in **Figure 7.6(a)** and **(b)**. The value of  $A^*$  is estimated as  $2.22 \text{ A} \cdot \text{K}^{-2} \cdot \text{m}^{-2}$  and  $7.17 \times 10^{-4} \text{ A} \cdot \text{K}^{-2} \cdot \text{m}^{-2}$  from the intercept of Richardson plots for perovskite and CNT nanocomposite perovskite, respectively, and which therefore used to calculate others electrical parameters.

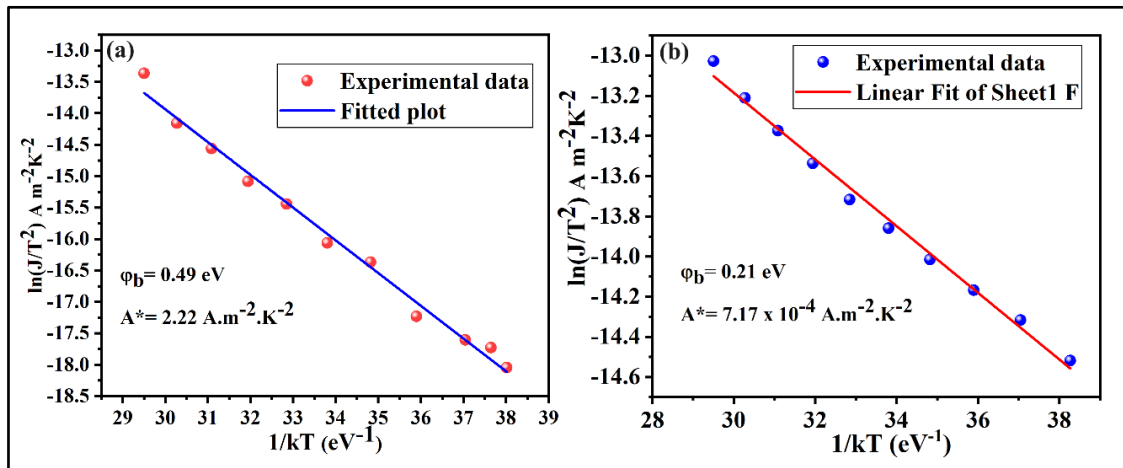


**Figure 7.6:** Shows Richardson plot to estimate the Richardson constant value for (a)  $\text{Cs}_2\text{SnCl}_6$  perovskite (b)  $\text{Cs}_2\text{SnCl}_6$ -MWCNT composite

However, slopes of these graph also provide the values of voltage-dependent barrier height sometimes known as activation energy of the device. The voltage-dependent barrier heights are found to be 0.47 eV and 0.21 eV for perovskite and CNT nanocomposite perovskite, respectively. The values of the ideality factor,  $\eta$  and barrier heights  $\phi_b$  of the Schottky devices obtained from the slopes and intercepts of  $\ln I$  vs.  $V$  plots for both devices and in both light and dark condition has been listed in **Table 7.2**. Generally, the ideal value of  $\eta$  of the Schottky devices is 1 but experimentally we got it greater than 1 this is maybe due to the existence of barrier inhomogeneity at the metal perovskite junction [19].

The Cheung and Cheung model [20] was used to derive Schottky parameters such as series resistance ( $R_s$ ),  $\phi_{b0}$  and  $\eta$  using forward bias I-V characteristics. According to this method, I-V behaviour of Schottky diodes may be expressed as follows,

$$\frac{dV}{d(\ln I)} = IR_s + \frac{\eta kT}{q} \quad (7.3)$$

The  $dV/d(\ln I)$  vs.  $I$  plot for all devices under both conditions in the dark and under illumination have been demonstrated in **Figure 7.7 (a) and (b)**. The values of  $R_s$  and  $\eta$  have been obtained from the slope and the y-axis intercept of the linear region of this plot.

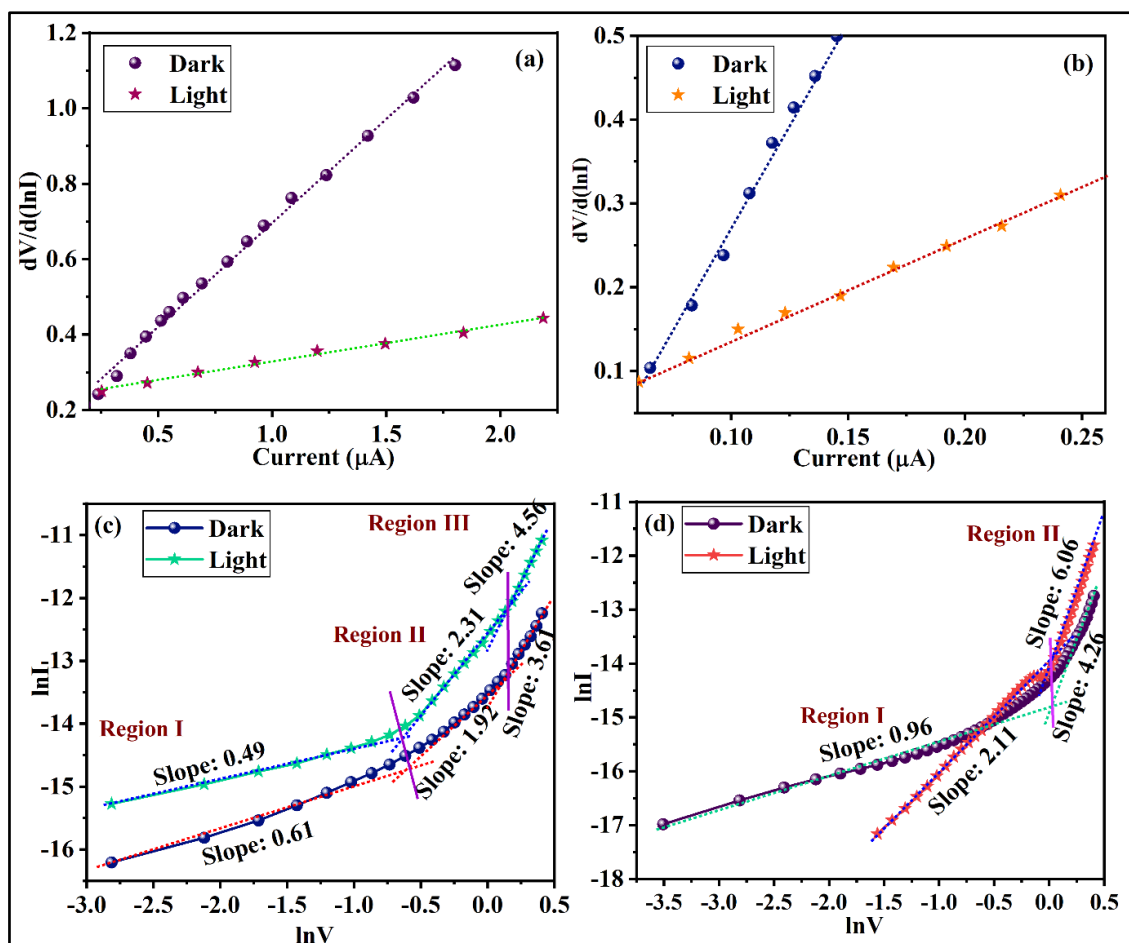


**Figure 7.7:** (a) and (b) depict  $dV/d(\ln I)$  vs.  $I$  plot for the determination of series resistances whereas (c) and (d) represents  $\ln I$  vs  $\ln V$  plots to explain charge transport mechanism of the devices based on perovskite and CNT based perovskites, respectively

The values of  $\eta$  under the dark condition diverged from the ideal behaviour due to barrier height inhomogeneities, a high chance of hole and electron recombination in the forbidden region, and the existence of interface states and series resistance [21]. However, when both devices were illuminated, the  $\eta$  value decreased. After soaking light, the series resistance ( $R_s$ ) of all compounds drops, which may be due to the excess electron-hole pair generation in the sample. The presence of MWCNT reduces the value of  $\eta$ , indicating that MWCNT works as a filler in the traps present in the sample. As a result, interfacial trap states are minimized, indicating improved junction formation between the sample and electrode. The decrease in  $R_s$  indicates

that MWCNT functions as a transporter for the carrier in the sample, reducing recombination and prompting the device for faster performance.

**Table 7.1: The values of Schottky device parameters like ideality factor ( $\eta$ ), barrier height ( $\phi_b$ ) and series resistance ( $R_s$ ) estimated using different methods**

Cell	Condition	Electrical conductivity (S/m)	Rectification ratio	Experimental I-V analysis		dV/dlnI vs. I	
				$\eta$	$\phi_b$ (eV)	$R_s$ ( $\Omega$ )	$\eta$
Perovskite	Dark	$3.8 \times 10^{-5}$	11.49	3.86	0.53	$4.83 \times 10^6$	3.01
	Light	$8.1 \times 10^{-5}$	8.82	2.57	0.51	$1.26 \times 10^6$	2.70
Perovskite + CNT Composite	Dark	$1.6 \times 10^{-4}$	11.92	1.93	0.60	551412	2.01
	Light	$4.0 \times 10^{-4}$	10.17	1.48	0.57	97659	1.49

To get better insight into the conduction mechanism of the devices, I-V characteristics were analysed considering the influence of traps in these systems. We previously [22,23] reported that trapped charges play a major role in the current conduction mechanism of Schottky devices. Sn-based perovskite films are generally formed using the low-temperature solution-processable method, so the resulting film is highly possible to be polycrystalline and full of grain boundaries (GB). Also, in Sn-based perovskite, there is a high possibility of the formation of oxidation vacancies due to the transformation of  $\text{Sn}^{2+}$  to  $\text{Sn}^{4+}$ . As a result of the presence of surface defects, structural disorders, and oxidation vacancies, there is a high density of trap states at interfaces between perovskite grains in the form of GBs and in the bulk sample in the form of vacancy states, which severely damages the optoelectronic properties of the films [24–27]. It is generally believed that defects at GBs and trap states play a significant impact in defining optoelectronic performance of the device. These traps state add extra energy levels to the energy. In presence of the trap states, the majority of the carriers injected from the electrodes are trapped and are usually crowded around the electrodes. When this mechanism dominates, it is referred to as trap charge limited conduction (TCLC). When the space charges become free carriers, the process is known as trap-free SCL conduction [28,29]. The trap

energy level distribution can be characterized in one of three ways: (i) as discrete levels (ii) as an exponential distribution, or (iii) as a Gaussian distribution [30,31].

The logarithmic plot of I-V measurements is often used to understand which kind of trap is present in the sample. The analysis of the trap-assisted electrical properties of various devices offers an efficient method for determining fundamental performance parameters. The  $\ln I$  vs.  $\ln V$  graph in **Figure 7.7(c)** and **(d)** demonstrates that the current conduction process changes after a particular voltage. This transition voltage is known as the threshold voltage ( $V_{th}$ ).

**Table 7.2: Charge transport parameters of both devices in dark and light conditions.**

Cell	Condi tion	Region I	Region II	Region III	
		Value of slope ( $m_1$ )	Value of slope ( $m_2$ )	Value of slope ( $m_3$ )	Trap energy, $E_t$ (meV)
Perovskite	Dark	0.61	1.92	3.61	103.22
	Light	0.49	2.31	4.56	90.16
Perovskite + MWCNT Composite	Dark	-	0.96	4.26	79.70
	Light	-	2.11	6.06	77.09

Before  $V_{th}$ ,  $I \propto V$ , which refers to ohmic transport, and beyond  $V_{th}$ ,  $I \propto V^m$ , where ( $m \geq 2$ ) is the slope of  $\ln I$  vs.  $\ln V$ . The value of  $m=2$  has two approaches, which are SCLC given by Mott-Gurney [32] and discrete trap level distributed SCLC given by low current. The value of slope ( $m$ ) greater than 2 indicates the existence of an exponential trap in the film [33]. **Figure 7.7(c)** and **(d)** show the regional linear fittings of  $\ln I$  vs.  $\ln V$  plots of ITO/ $\text{Cs}_2\text{SnCl}_6$ /Al and ITO/ $\text{Cs}_2\text{SnCl}_6$ +MWCNT/Al device structures, respectively. The slopes of Region I of both graphs show the ohmic behaviour of the device with negligible electron-hole recombination as the value of  $m$  is nearly 1 in **Table 7.2**. In Region II,  $m$  is greater than 2, indicating the presence of exponential trap distribution in the films. The exponential trap states distribution is given by, [33]

$$g(E) = \frac{N_t}{k_B T_t} \exp\left(\frac{E}{k_B T_t}\right) \quad (7.4)$$

Where  $k_B$  is Boltzmann constant,  $N_t$  is the total trap concentration, and  $T_t$  is the characteristic temperature of the exponential trap distribution correlated to  $E$ . Solving the Poisson equation with the help of this trap density of state according to **Equation 7.4**, the SCLC predicted by the Mark–Helfrich (MH) in the form of I-V characteristic is given by **Equation 7.5** [34].

$$I = A_{ef} N_{eff} \mu q^{1-m} \left( \frac{m\varepsilon}{N_t(m+1)} \right)^m \left( \frac{2m+1}{m+1} \right)^{m+1} \frac{V^{m+1}}{L^{2m+1}} \quad (7.5)$$

Where  $A_{ef}$  is the effective area of the device,  $N_{eff}$  is the effective density of states at the valence band edge,  $\mu$  is the mobility of the majority carrier,  $L$  is the thickness of the layer,  $\varepsilon$  is equal to  $\varepsilon_0 \varepsilon_r$  with  $\varepsilon_0$  being the permittivity of vacuum and  $\varepsilon_r$  the dielectric constant,  $V$  is the applied voltage. The value of  $m = T_t/T$ ,  $T$  is the absolute temperature. Then trap energy is calculated by using  $E_t = k_B T_t = m k_B T$  and listed in **Table 7.2**. The threshold voltages are representing the onset voltage of the devices because, at this particular voltage, injected carrier dominates over the existing thermally generated charge carrier so effective transport starts. **Table 7.2** shows that in the presence of MWCNT, the trapped energy is reduced from 103.22 to 79.70 meV in the dark and from 90.16 meV to 77.09 meV in light the condition. In all circumstances, trap energy is lower in light than in dark, possibly due to the generation of photoinduced charge carriers. Light provides more energy to charge carriers, allowing them to overcome barriers.

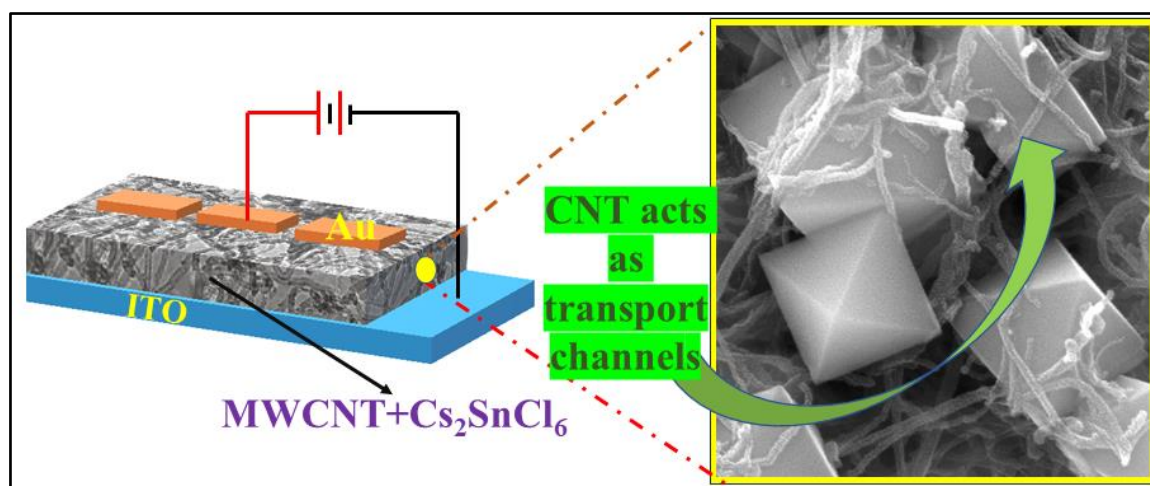


**Figure 7.8:** Shows Al/ $\text{Cs}_2\text{SnCl}_6$ +MWCNT/ITO device configuration to explain the charge transport mechanism. The right-side image shows the transport mechanism of the middle layer (active) of the device made up of perovskite and MWCNT composite.

Whenever an electron-hole pair generates within perovskite, the electron gets recombined with  $\text{Sn}^{2+}$  and the hole gets transported through MWCNT as it works as a channel

Again, carriers get a lower resistive pathway via MWCNT to release from the trap state and transport easily from one grain to another. Therefore, due presence of MWCNTs a drastic change is observed in case of trap energy. We have tried to demonstrate these phenomena in a schematic diagram in **Figure 7.8**, which shows the combined effect of light and MWCNT to reduce trap energy. Due to the presence of light, perovskite produces excess e-h pair in the device and MWCNT helps the carriers to transport from that particular grain to another grain and/or to the electrode before their recombination. Hence, incorporation of MWCNT in perovskite material, the optoelectronic performance of the device is improved. This improvement in conductivity in the presence of CNTs alludes to the smooth transmission of charge across the sample. The increase in conductivities in the presence of light shows photosensitivity of the device. The photoresponsivity, external quantum efficiency (EQE), and detectivity are the important parameters employed to check the performance of a photodetector.

The photosensitivity ( $P_s$ ) is expressed as the ratio of the produced photocurrent  $I_{pc}$  (where  $I_{pc} = I_{light} - I_{dark}$ ) to the current in the dark ( $I_D$ ). This can be written as,

$$P_s = \frac{I_{pc}}{I_D} \quad (7.6)$$

The photoresponsivity ( $R$ ) measure of efficiency of a photodetector in response to an incident photon, and it is defined as the amount of photogenerated current per unit power incident on the effective device area, which can be expressed as the following **Equation 7.7**,

$$R = \frac{I_{pc}}{P_i A} \quad (7.7)$$

Where  $P_i$  is the incident optical power density which is  $1000 \text{ W.m}^{-2}$  for this study and  $A_{ef} (= 4 \times 10^{-6} \text{ m}^2)$  is the effective area of the diode. Specific detectivity ( $D^*$ ) gives the information about the suitability of the diode as a photodetector which has been given by the relation,

$$D^* = \frac{R\sqrt{A}}{\sqrt{2eI_D}} \quad (7.8)$$

Where  $e$  is the electronic charge. The IV characteristics under illumination on different wavelengths in reversed biased measured for the both devices as shown in **Figure 7.9(a)** and **(b)**. From the spectral photoresponses shown in **Figure 7.9(c)**, we observe that devices have increasing photoresponsive behaviour over the wavelength region and maximum in UV region. The photoresponsivity of  $\sim 2.57 \text{ mA/W}$  is observed in the presence of MWCNTs in device whereas photoresponsivity of  $\sim 1.15 \text{ mA/W}$  found in the perovskite-based device only under

ultraviolet illumination of 360 nm wavelength. This shows that the nanocomposite-based photodetector is highly sensitive in UV regions. Next, we estimated the values of another important parameters of the devices using **Equations 7.6** and **7.8** photosensitivity and detectivity and listed in **Table 7.3**.

**Table 7.3: Photosensing parameters of the  $\text{Cs}_2\text{SnCl}_6$  perovskite Schottky junction device**

Device structure	Photosensitivity ( $P_s$ )	Responsivity (R) (mA/W)	Specific detectivity ( $D^*$ ) (Jones)
ITO/ $\text{Cs}_2\text{SnCl}_6$ /Al	1.57	1.15	$1.18 \times 10^9$
ITO/ $\text{Cs}_2\text{SnCl}_6$ +MWCNTs/Al	2.78	2.57	$2.38 \times 10^9$

It is important to note that the performance of the device is significantly impacted by the addition of MWCNTs to perovskite. The device's excellent photoresponsivity and detectivity are a result of its wide surface to volume ratio and smooth charge transfer, both of which promote effective light absorption.

Next, temporal response was recorded for photodetectors using a light of 360 nm wavelength at 1.5 V by manually switching the light. The light was switched on and off periodically. Photocurrent was initially found to increase sharply when the light was on, followed by a slow rise later, and when the light was turned off, the photocurrent was found to have a sharp fall followed by a relatively slower decay as shown in **Figure 7.9(d)**. The rise and fall in photocurrent in response to the light illumination on the photodetector has been expressed mathematically by the equations,  $I(t) = I_0[1 - \exp(-t/\tau_r)]$  and  $I(t) = I_0[\exp(-t/\tau_d)]$ , where  $I_0$  is the current at the steady state;  $\tau_r$  and  $\tau_d$  are the time constants; and  $t$  is the time [35]. The rise time is defined as the time taken by the photocurrent to enhance from 10 to 90% of its maximum value; in contrast, the decay time is defined as the time taken by the photocurrent to fall from 90 to 10% of its maximum value.

In our case, the MWCNTs based photodetector shows a fast rise and decay time of 0.29 and 0.89 s (**Figure 7.9(f)**), respectively, whereas in case of perovskite device only, rise and decay times are 0.59 and 1.82 s (**Figure 7.9(e)**), respectively. The fast response of the device in presence of MWCNTs is most probably due to overcoming effects CNTs over defects,

nonuniformity of the films. In the following section we have developed a smartphone interfaced UV detector using MWCNTs- perovskite nanocomposite sample due to its high responsivity and fast switching capabilities.

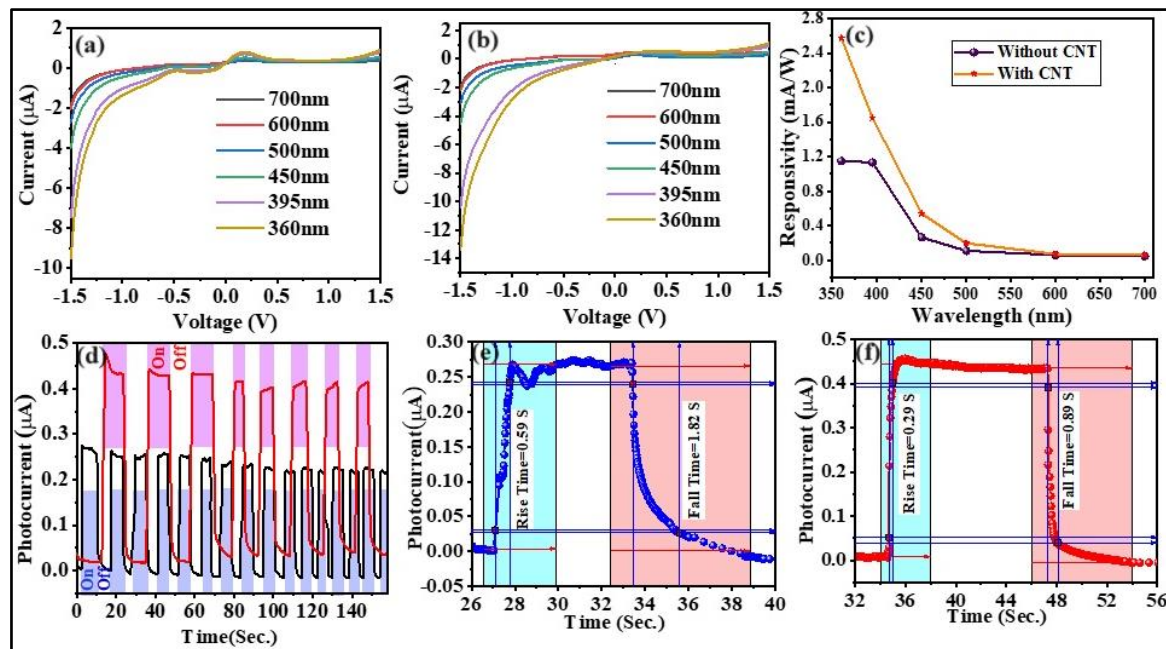


**Figure 7.9:** (a) and (b) show the I-V characteristics of UV photodetectors without and with MWCNTs, respectively. (c) illustrates the spectral responses of both devices. (d) depicts the temporal response under 360 nm illumination at a bias of 1.5 V for the perovskite device (black) and the MWCNT-perovskite composite device (red). (e) and (f) display the photocurrent rise and decay for both devices

### 7.4.2 Smartphone Interfaced UV Detector

The smartphone interfaced UV detector offers a state-of-the-art solution to keep us well-informed about UV radiation levels, empowering us to take proactive measures to protect our skin during outdoor activities. Its role extends beyond promoting sun safety; it also raises awareness about the critical importance of sun protection for overall well-being. As the demand for wirelessly controlled modules grows, we developed a cost-effective solution utilizing the  $\text{Cs}_2\text{SnCl}_6$ -MWCNTs nanocomposite material. The complete module, depicted in **Figure 7.10**, comprises the ESP32 MCU, the UV detector device, and a smartphone.

The UV detector's functioning involves passing light through a monochromator, producing UV light that gets reflected at a 90-degree angle onto the UV detector. The MCU sends corresponding Analog voltage changes across the device, which are then transmitted to the smartphone for display. By modifying the MCU's programming, the module can transform

Analog signals into a digital pulse train which is illustrated in **Figure 7.10** in the form of ‘0’ and ‘1’.

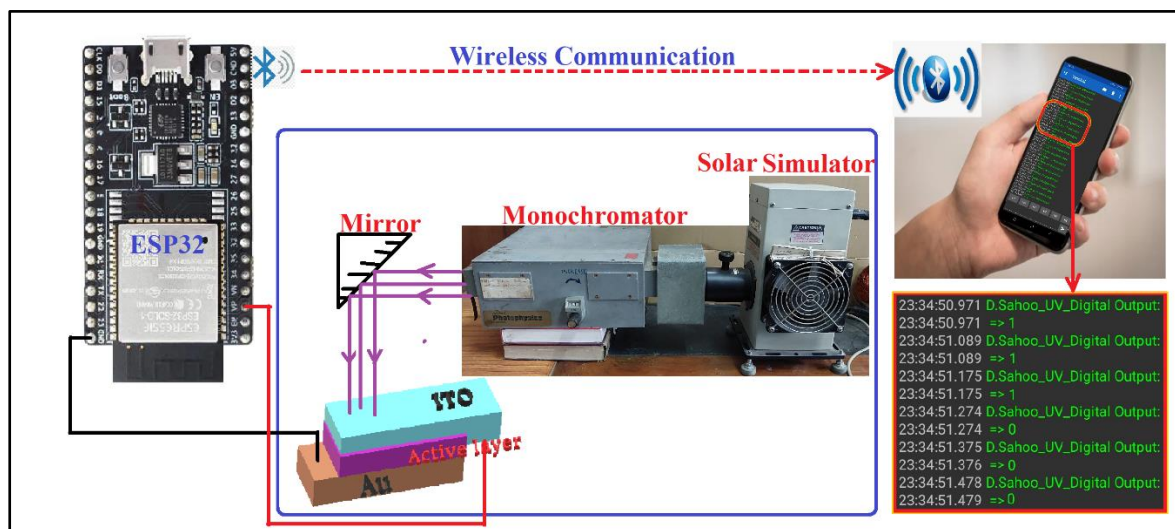


**Figure 7.10: UV photodetector module with full setup wirelessly connected to smartphone showing digitized ‘0’ and ‘1’ output under UV light and absence of UV light, respectively**

This work shows that a simple technique can be used to develop a wireless smart phone interfaced module for multipurpose use like UV alert, pulse train signal generation etc. by enhancing the performance of the device incorporating MWCNTs. Here we have presented data in the form of digital pulse train but with a slight modification to the instructions, the data can be transformed into UV index format for commercialisation.

## 7.5 Conclusions

Finally, our findings highlight the great potential of lead-free perovskite materials, particularly  $\text{Cs}_2\text{SnCl}_6$ , for use in UV detectors. Although pure  $\text{Cs}_2\text{SnCl}_6$  perovskite has limited performance due to its low charge transport capabilities, incorporating MWCNTs to the material significantly improved its optoelectronic properties. The perovskite-MWCNT composite had much greater conductivity, improved rectification ratio and barrier height, and a lower series resistance. Additionally, lower trap energy levels suggested fewer trap concentrations in the composite material. The composite device's increased photosensitivity, responsivity, and specific detectivity demonstrate the usefulness of MWCNT integration in improving photodetector performance. The composite device's photosensitivity and responsivity in dark circumstances substantially increased when compared to the pure perovskite device. These

enhancements make the Cs<sub>2</sub>SnCl<sub>6</sub>-MWCNT composite a promising candidate for high-performance, environmentally friendly optoelectronic applications.

## 7.6 References

- [1] Q. Chang, D. Wu, Y. Huang, C. Liang, L. Liu, H. Liu, Y. Liu, J. Qiu, X. Tang, G. Han, Ultrahigh Response Humidity Sensor Based on Lead-Free Cs<sub>2</sub>SnCl<sub>6</sub> Perovskite Films, *IEEE Electron Device Letters* 43 (2022) 805–808.
- [2] T. Tan, X. Wang, X. Zhou, H. Ma, R. Fang, Q. Geng, F. Dong, Highly active Cs<sub>2</sub>SnCl<sub>6</sub>/C<sub>3</sub>N<sub>4</sub> heterojunction photocatalysts operating via interfacial charge transfer mechanism, *J Hazard Mater* 439 (2022) 129694.
- [3] Y. Yao, S.W. Zhang, Z. Liu, C.Y. Wang, P. Liu, L. Ma, G. Wei, F. Kang, Air stable and highly efficient Bi<sup>3+</sup>-doped Cs<sub>2</sub>SnCl<sub>6</sub> for blue light-emitting diodes, *RSC Adv* 11 (2021) 26415–26420.
- [4] Y. Zhong, Y.E. Huang, T. Deng, Y.T. Lin, X.Y. Huang, Z.H. Deng, K.Z. Du, Multi-Dopant Engineering in Perovskite Cs<sub>2</sub>SnCl<sub>6</sub>: White Light Emitter and Spatially Luminescent Heterostructure, *Inorg Chem* 60 (2021) 17357–17363.
- [5] M. Pi, D. Wu, J. Wang, K. Chen, J. He, J. Yang, D. Zhang, S. Chen, X. Tang, Real-time and ultrasensitive humidity sensor based on lead-free Cs<sub>2</sub>SnCl<sub>6</sub> perovskites, *Sens Actuators B Chem* 354 (2022) 131084.
- [6] J. Shao, X.-T. Wang, H. Xu, X.-D. Zhao, J.-M. Niu, Z.-D. Zhang, Y.-L. Huang, J.-Z. Duan, Photoelectrochemical Performance of SnS<sub>2</sub> Sensitized TiO<sub>2</sub> Nanotube for Protection of 304 Stainless Steel, *J Electrochem Soc* 168 (2021) 016511.
- [7] T. Zhang, H. Li, H. Ban, Q. Sun, Y. Shen, M. Wang, Efficient CsSnI<sub>3</sub>-based inorganic perovskite solar cells based on a mesoscopic metal oxide framework via incorporating a donor element, *J Mater Chem A Mater* 8 (2020) 4118–4124.
- [8] K.P. Marshall, M. Walker, R.I. Walton, R.A. Hatton, Enhanced stability and efficiency in hole-transport-layer-free CsSnI<sub>3</sub> perovskite photovoltaics, *Nat Energy* 1 (2016) 16178.
- [9] M. Kayumov, M.M. Kayumov, S.S. Gilyosov, Structural stability of polymorphic CsSnI<sub>3</sub> Structural stability of CsSnI<sub>3</sub> polymorphous, 56 (2017) 84-91.
- [10] S. Pansri, R. Supruangnet, H. Nakajima, S. Rattanasuporn, S. Noothongkaew, Band offset determination of p-NiO/n-TiO<sub>2</sub> heterojunctions for applications in high-performance UV photodetectors, *J Mater Sci* 55 (2020) 4332–4344.
- [11] T. Schultz, T. Lenz, N. Kotadiya, G. Heimel, G. Glasser, R. Berger, P.W.M. Blom, P. Amsalem, D.M. de Leeuw, N. Koch, Reliable Work Function Determination of Multicomponent Surfaces and Interfaces: The Role of Electrostatic Potentials in Ultraviolet Photoelectron Spectroscopy, *Adv Mater Interfaces* 4 (2017) 1700324.
- [12] D. Sahoo, A. Kanti Karan, N. Baran Manik, Influence of SWCNT on the Electrical Behaviour of an Environmentally Friendly CH<sub>3</sub>NH<sub>3</sub>SnI<sub>3</sub> Perovskite-Based Optoelectronic Schottky Device, *ACS Appl Electron Mater* 5 (2023) 2203–2214.
- [13] J.W. Kim, A. Kim, Absolute work function measurement by using photoelectron spectroscopy, *Current Applied Physics* 31 (2021) 52–59.

- [14] Tauc, J. Optical Properties and Electronic Structure of Amorphous Ge and Si. *Materials Research Bulletin* 3 (1968) 37-46.
- [15] J.H. Werner, H.H. Güttler, Barrier inhomogeneities at Schottky contacts, *J Appl Phys* 69 (1991) 1522–1533.
- [16] A. Upadhyaya, C.M. Singh Negi, A. Yadav, S.K. Gupta, A. Singh Verma, Analysis of Perovskite Based Schottky Photodiode, *AIP Conference Proceedings*, 2100 (2019) 020134.
- [17] D. Sahoo, N.B. Manik, Study on the effect of temperature on electrical and photovoltaic parameters of lead-free tin-based Perovskite solar cell, *Indian Journal of Physics* 97 (2023) 447–455.
- [18] L. Chen, J. Deng, H. Gao, Q. Yang, G. Wang, L. Kong, M. Cui, Z. Zhang, Organometallic hybrid perovskites: structural, optical characteristic and application in Schottky diode, *Journal of Materials Science: Materials in Electronics* 27 (2016) 4275–4280.
- [19] J.P. Sullivan, R.T. Tung, M.R. Pinto, W.R. Graham, Electron transport of inhomogeneous Schottky barriers: A numerical study, *J Appl Phys* 70 (1991) 7403–7424.
- [20] S.K. Cheung, N.W. Cheung, Extraction of Schottky diode parameters from forward current-voltage characteristics, *Appl Phys Lett* 49 (1986) 85–87.
- [21] M. Sharma, S.K. Tripathi, Study of barrier inhomogeneities in I-V-T and C-V-T characteristics of Al/ $\text{Al}_2\text{O}_3$ /PVA:n-ZnSe metal-oxide-semiconductor diode, *J Appl Phys* 112 (2012) 024521.
- [22] D. Sahoo, N.B. Manik, Estimation of trap energy of fuchsin dye sensitized Organic Photovoltaic Device based on Titanium Dioxide ( $\text{TiO}_2$ ), *International Journal of Innovative Research in Physics* 1 (2020) 17-23.
- [23] S. Sen, N.B. Manik, Correlation between barrier potential and charge trapping under the influence of Titanium Di oxide nanomaterials in organic devices, *Results in Materials* 8 (2020) 024521.
- [24] D. Meggiolaro, D. Ricciarelli, A.A. Alasmari, F.A.S. Alasmari, F. De Angelis, Tin versus Lead Redox Chemistry Modulates Charge Trapping and Self-Doping in Tin/Lead Iodide Perovskites, *Journal of Physical Chemistry Letters* 11 (2020) 3546–3556.
- [25] X. Fu, K.J. Weber, T.P. White, Characterization of trap states in perovskite films by simultaneous fitting of steady-state and transient photoluminescence measurements, *J Appl Phys* 124 (2018) 073102.
- [26] S. Ghatak, A. Ghosh, Observation of trap-assisted space charge limited conductivity in short channel  $\text{MoS}_2$  transistor, *Appl Phys Lett* 103 (2013) 122103.
- [27] T.S. Sherkar, C. Momblona, L. Gil-Escrig, J. Ávila, M. Sessolo, H.J. Bolink, L.J.A. Koster, Recombination in Perovskite Solar Cells: Significance of Grain Boundaries, Interface Traps, and Defect Ions, *ACS Energy Lett* 2 (2017) 1214–1222.
- [28] R.H. Bube, Trap Density Determination by Space-Charge-Limited Currents, *J Appl Phys* 33 (1962) 1733–1737.
- [29] M.A. Lampert, Theory of Space-Charge-Limited Currents in an Insulator with Traps, *Phys. Rev.* 103 (1956) 1648.

- [30] A. Baumann, S. V  th, P. Rieder, M.C. Heiber, K. Tvingstedt, V. Dyakonov, Identification of trap states in perovskite solar cells, *Journal of Physical Chemistry Letters* 6 (2015) 2350–2354.
- [31] J.A. Carr, The identification and characterization of electronic defect bands in organic photovoltaic devices. *Energy Environ. Sci.* 6 (2013) 3414–3438.
- [32] J.A. R  hr, D. Moia, S.A. Haque, T. Kirchartz, J. Nelson, Exploring the Validity and Limitations of the Mott-Gurney Law for Charge-Carrier Mobility Determination of Semiconducting Thin-Films, *J Phys Condens Matter.* 30 (2018) 105901.
- [33] D. Joung, A. Chunder, L. Zhai, S.I. Khondaker, Space charge limited conduction with exponential trap distribution in reduced graphene oxide sheets, *Appl. Phys. Lett.* 97 (2010) 093105.
- [34] P. Mark, W. Helfrich, Space-charge-limited currents in organic crystals, *J Appl Phys* 33 (1962) 205–215.
- [35] S. Yang, Y. Li, X. Wang, N. Huo, J.B. Xia, S.S. Li, J. Li, High performance few-layer GaS photodetector and its unique photo-response in different gas environments, *Nanoscale* 6 (2014) 2582–2587.

# **Chapter 8: Conclusions and Future Scope**

## **8.1 Summary**

## **8.2 Findings of the Work**

## **8.3 Overall Conclusion**

## **8.4 Future Scopes of the Work**

## 8.1 Summary

This thesis focuses on the development and charge transport analysis of lead-free perovskite materials for optoelectronic devices in presence and absence of CNTs. We explore the importance and current status of lead-free perovskite technology, which is still in its early stages. Significant research and development efforts are needed to advance and commercialize lead-free perovskite-based devices.

In this study, we synthesized several lead-free perovskites, such as  $\text{CH}_3\text{NH}_3\text{SnI}_3$ ,  $\text{CsSnCl}_3$  perovskites and  $\text{Cs}_2\text{SnCl}_6$  double perovskite, using a solution processing method. We characterized the physical and optical properties of these materials using various techniques. Then, we fabricated multiple lead-free perovskite devices incorporating these materials and investigated their charge transport mechanisms. Our analyse emphasizes the role of traps at the M/S interface in controlling charge injection within these devices. We found that the presence of traps significantly influences electrical parameters such as barrier height, ideality factor, and trap energy at the M/S interface.

Furthermore, we discuss interfacial barriers, ideality factors, trap energies, and threshold voltages considering the effect of charge trapping. Various charge transport models were examined to elucidate device characteristics. By analysing I-V characteristics, we calculated these parameters and correlated them with trap energies at the M/S interface.

In the next part of our study, we studied the impact of SWCNT and MWCNT on the optoelectronic properties of lead-free  $\text{CH}_3\text{NH}_3\text{SnI}_3$  perovskite and explored how MWCNT effects optoelectronic parameters in  $\text{Cs}_2\text{SnCl}_6$  double perovskite.

We have designed our present work into the following chapters

In **Chapter 1**, a brief introduction to perovskite structures and classifications has been provided. The current state of lead-free perovskite technology, the importance of studying double perovskites, and perovskites based on CNTs in the current context have been discussed in the motivation section of this chapter. Following this, we have outlined the objectives of this thesis.

In **Chapter 2**, we extensively reviewed the development and necessity of lead-free perovskite devices as alternatives to efficient lead-based perovskite devices. We also examined the current status and limitations of lead-free perovskites in detail. Additionally, we discussed various transport models, including injection-limited models like thermionic emission and direct

tunnelling, as well as bulk-limited charge transport models like ohmic transport and space-charge-limited transport, which are relevant to our current study. Furthermore, within the scope of our primary objective, which is the study of lead-free perovskites in the presence of CNTs, we conducted a detailed analysis of the current status of CNT-based perovskite optoelectronic devices.

Moving forward, **Chapter 3** detailed the synthesis and characterization of lead-free  $\text{CH}_3\text{NH}_3\text{SnI}_3$  nanocubic perovskite, employing a modified solution processing technique under controlled atmospheric conditions. Device performance was comprehensively analysed through impedance, dielectric, and conductivity studies, alongside the fabrication of a Schottky device to investigate charge conduction behaviours.

**Chapters 4 and 5** focused on investigating the impact of CNTs on  $\text{CH}_3\text{NH}_3\text{SnI}_3$  perovskite, synthesizing and characterizing nanocomposites before developing thin-film perovskite devices to evaluate charge transport capabilities. The incorporation of CNTs significantly improved device performance, demonstrating the potential of these composites for enhancing optoelectronic properties.

In **Chapter 6**, we explored the synthesis and characterization of lead-free  $\text{CsSnCl}_3$  perovskite microrods, investigating their electrical properties through detailed I-V characteristic analysis. Charge injection mechanisms and conduction behaviours were elucidated, highlighting the importance of understanding material-specific properties for optimizing device performance.

Lastly, **Chapter 7** focused on studying  $\text{Cs}_2\text{SnCl}_6$  double perovskite and MWCNT composites, synthesizing and characterizing materials for the development of a Schottky UV detector. The analysis of I-V characteristics revealed promising enhancements in charge transport properties and optoelectronic performance, paving the way for smartphone-integrated UV photodetectors.

In conclusion, this thesis presents a comprehensive exploration of lead-free perovskite materials in presence of CNTs and their potential for advancing optoelectronic technologies. The findings underscore the importance of ongoing research efforts to refine film surfaces, enhance charge transport mechanisms, and optimize material-device interfaces, ultimately driving the development of practical and efficient lead-free perovskite-based optoelectronic devices for real-world applications.

## 8.2 Findings of the Work

### Results from lead-free nano cubic $\text{CH}_3\text{NH}_3\text{SnI}_3$ perovskite-based devices

Our main work is described in five experimental chapters. The findings are described in each chapter with sufficient data. In this section, we will mention some salient features of our findings.

In our work we have performed experiment with  $\text{CH}_3\text{NH}_3\text{SnI}_3$  perovskite. Recalling **Table 3.4** we can say that the analysis of Schottky device parameters under dark and light conditions reveals several notable differences in performance metrics, indicating significant effects of illumination on the device behaviour. Under dark conditions, the conductivity is  $1.04 \times 10^{-6} \text{ S/m}$  which increases to  $1.95 \times 10^{-6} \text{ S/m}$  under light. This indicates that illumination enhances the electrical conductivity of the device. The ideality factor decreases slightly from 2.36 in the dark to 2.29 in the light, suggesting excess generated charges filled the traps at the junction, which improved diode quality under illumination. The series resistance, derived from both  $dV/d\ln I$  vs.  $I$  and  $H(I)$ - $I$  plots, shows a significant reduction under light conditions (from  $4.91 \times 10^5 \Omega$  to  $2.24 \times 10^5 \Omega$  and from  $4.39 \times 10^5 \Omega$  to  $2.71 \times 10^5 \Omega$  respectively). This reduction indicates better charge transport under illumination. The barrier height shows a slight decrease from 0.682 eV (dark) to 0.671 eV (light) in the  $dV/d\ln I$  vs.  $I$  plot and from 0.652 eV to 0.635 eV in the  $H(I)$ - $I$  plot, suggesting that light slightly lowers the energy barrier for charge carriers to move faster. Again, from the charge conduction analysis of IV characteristics shows that the effective mobility increases from  $1.07 \times 10^{-11} \text{ m}^2\text{V}^{-1}\text{s}^{-1}$  in the dark to  $1.61 \times 10^{-11} \text{ m}^2\text{V}^{-1}\text{s}^{-1}$  under light, indicating enhanced carrier mobility with illumination. The transit time decreases from  $5.98 \times 10^{-8} \text{ s}$  (dark) to  $4.99 \times 10^{-8} \text{ s}$  (light), reflecting faster charge carrier transit, confirming the improved charge transport properties with illumination. The diffusion length increases from 1.81 nm (dark) to 2.03 nm (light), suggesting that carriers can travel longer distances before recombining under illumination.

Overall, the findings demonstrate that illumination significantly enhances the electrical and transport properties of the Schottky device, improving conductivity, reducing series resistance, and increasing both mobility and diffusion coefficients. These improvements suggest that light exposure optimizes the device's performance by facilitating better charge transport and reduced recombination losses.

We reviewed a few literatures to compare the performance of our lead-free device with conventional Pb-based Schottky devices in terms of the above-mentioned parameters. Based

on the discussion, we have concluded that the parameter values found in this work, such as barrier height and ideality factor, are equivalent to the reported values of lead-based devices. However, we found that the  $\text{CH}_3\text{NH}_3\text{SnI}_3$  perovskite-based device has limited conductivity due to high series resistance. The reason could be related to Sn oxidation, film defects, charge carrier trapping, and so on. However, the toxicity of Pb is the most important concern in this investigation. This comparison analysis demonstrates that the  $\text{CH}_3\text{NH}_3\text{SnI}_3$  perovskite could be a feasible alternative for replacing and developing Schottky devices with improved conductivity.

### Findings of lead-free $\text{CH}_3\text{NH}_3\text{SnI}_3$ perovskite-based devices in presence of SWCNTs

In the preceding chapter we have studied the performance of  $\text{CH}_3\text{NH}_3\text{SnI}_3$  perovskite is quite interesting except low conductivity due to oxidation of Sn, defects present in film, charge carrier trapping, and so on. To address these issues in this work we have incorporated SWCNTs in  $\text{CH}_3\text{NH}_3\text{SnI}_3$  perovskite and studied the effect of it on device performance. However, in this work samples were prepared freshly in different solution processing method and devices were also developed directly from the precursor solutions. The analysis of Schottky device parameters for  $\text{CH}_3\text{NH}_3\text{SnI}_3$  perovskite-based devices, with and without SWCNTs, under dark and light conditions reveals significant performance improvements due to illumination. Recalling **Table 4.1-4.3** we can say that the electrical conductivity of the perovskite device increases from  $3.8 \times 10^{-5}$  S/m in the dark to  $8.1 \times 10^{-5}$  S/m under light, and for the perovskite-SWCNT composite, it increases from  $1.6 \times 10^{-4}$  S/m to  $4.0 \times 10^{-4}$  S/m, indicating enhanced electrical conductivity with light exposure. The rectification ratio slightly decreases under light, from 11.49 to 8.82 for the pure perovskite device, and from 11.92 to 10.17 for the composite device, while photosensitivity, responsivity, specific detectivity, and photoconductivity sensitivity all improve significantly with the addition of SWCNTs, demonstrating better photoresponse and device performance.

In terms of Schottky device parameters, the ideality factor ( $\eta$ ) decreases from 2.94 in the dark to 2.61 under light for the perovskite device, and from 5.10 to 3.49 for the composite device, indicating improved diode quality. The barrier height ( $\phi_b$ ) shows a slight reduction under light, from 0.39 eV to 0.37 eV for the perovskite device and from 0.32 eV to 0.31 eV for the composite device, suggesting lower energy barriers for charge carriers. Under light circumstances, series resistance ( $R_s$ ) reduces dramatically, from 348.25  $\Omega$  to 220.56  $\Omega$  for the perovskite device and 34.80  $\Omega$  to 19.20  $\Omega$  for the SWCNTs composite device, showing

enhanced charge transport. It should be highlighted that the series resistance of the only perovskite-based device is substantially lower than that obtained in prior work, which could be attributed to superior film formation and less oxidation of Sn.

However, these findings indicate that illumination significantly enhances the electrical transport properties of the  $\text{CH}_3\text{NH}_3\text{SnI}_3$  perovskite Schottky devices, particularly with the addition of SWCNTs. The improvements in conductivity, reduced series resistance, and enhanced photoresponse confirm that SWCNTs optimizes device performance, making lead-free  $\text{CH}_3\text{NH}_3\text{SnI}_3$  perovskite with SWCNTs a promising alternative for high-performance, environmentally friendly optoelectronic applications.

### **Findings of lead-free $\text{CH}_3\text{NH}_3\text{SnI}_3$ perovskite-based devices in presence of MWCNTs**

The current study is similar to the previous one, with the exception that MWCNTs were used instead of SWCNTs in the  $\text{CH}_3\text{NH}_3\text{SnI}_3$  perovskite, and the Vander Paw Method was used to measure the IV properties, resulting in more clear and reliable ideas. According to **Table 5.2**, both results show that adding MWCNTs into lead-free  $\text{CH}_3\text{NH}_3\text{SnI}_3$  perovskite devices significantly improves their electrical properties. Devices using a perovskite-MWCNT nanocomposite show a notable increase in conductivity ( $1.02 \times 10^{-4}$  S/m compared to  $1.21 \times 10^{-5}$  S/m in pure perovskite) and rectification ratio (15.61 versus 12.05). Additionally, the ideality factor is reduced from 4.01 to 2.56, indicating improved charge transport properties. However, the barrier height decreases slightly from 0.51 eV to 0.43 eV.

### **Study of lead-free $\text{CsSnCl}_3$ perovskite microrods**

In this study, a distinct perovskite sample was synthesized in the shape of microrods, its IV properties were measured, and the charge transport of the microrods was investigated. The production of  $\text{CsSnCl}_3$  perovskite microrods of various lengths suggests a relationship between microrod length and device performance. As per the **Table 6.1** the thicker microrods (356  $\mu\text{m}$ ) have better conductivity ( $3.08 \times 10^{-4}$  S/m) and lower barrier height (0.84 eV), whereas thinner microrods (136  $\mu\text{m}$ ) have lower conductivity ( $1.32 \times 10^{-4}$  S/m) and barrier height (0.78 eV). The rectification ratio and ideality factor also vary with microrod length, showing the possibility of modifying device attributes using microrod dimensions.

### Findings of lead-free $\text{Cs}_2\text{SnCl}_6$ perovskite in presence of MWCNTs

In our previous work, we synthesized  $\text{CH}_3\text{NH}_3\text{SnI}_3$ , CNT-  $\text{CH}_3\text{NH}_3\text{SnI}_3$  composites, and  $\text{CsSnCl}_3$  perovskites. During synthesis, we took extensive precautions, conducting the process in a nitrogen-atmosphere glove box to prevent Sn oxidation. Additionally, we designed an encapsulating characterization container to prevent sample degradation during measurements. However, we have since shifted our focus to synthesizing materials in an open atmosphere. Using the same synthesis recipe for  $\text{CsSnCl}_3$ , we successfully synthesized  $\text{Cs}_2\text{SnCl}_6$  double perovskite in an open atmosphere.  $\text{Cs}_2\text{SnCl}_6$  is inherently stable because it is an already oxidized version of  $\text{CsSnCl}_3$  perovskite, or we can say it is a defect version of  $\text{CsSnCl}_3$ . We found that  $\text{Cs}_2\text{SnCl}_6$  perovskite has a large indirect band gap with maximum absorption in the UV region. We developed a Schottky device using this material, but its performance was not very impressive due to its low charge transport capability. To enhance its electrical performance, we integrated MWCNTs into the  $\text{Cs}_2\text{SnCl}_6$  perovskite, which led to significant improvements in the optoelectronic performances. According to **Table 7.1** The perovskite-MWCNT composite shows significantly higher conductivity ( $1.6 \times 10^{-4}$  S/m in dark and  $4.0 \times 10^{-4}$  S/m in light) compared to pure  $\text{Cs}_2\text{SnCl}_6$  perovskite ( $3.8 \times 10^{-5}$  S/m in dark and  $8.1 \times 10^{-5}$  S/m in light). The rectification ratio and barrier height also improve, along with a substantial decrease in series resistance, which is particularly beneficial for photovoltaic applications. Additionally, the composite material exhibits lower trap energy levels, indicating reduced defect densities

The photosensitivity, responsivity, and specific detectivity of ITO/ $\text{Cs}_2\text{SnCl}_6$ /Al and ITO/ $\text{Cs}_2\text{SnCl}_6$  +MWCNTs/Al devices show marked improvements with the addition of MWCNTs. The photosensitivity and responsivity in the dark conditions of the composite device are nearly double those of the pure perovskite device, with values of 2.78 and 2.57 mA/W compared to 1.57 and 1.15 mA/W, respectively (**Table 7.3**). The specific detectivity also increases significantly, highlighting the potential of MWCNT incorporation for enhancing photodetector performance.

In conclusion, our findings on lead-free  $\text{CH}_3\text{NH}_3\text{SnI}_3$  perovskite-based devices show that the addition of SWCNTs and MWCNTs improves electrical and transport properties by lowering series resistance, energy barriers, and photoresponse. We also synthesized  $\text{CsSnCl}_3$  microrods, and our charge conduction study revealed that microrod length effects device performance and exhibits SCLC transport in the bulk. Furthermore, the synthesis of stable  $\text{Cs}_2\text{SnCl}_6$  double

perovskite in an open atmosphere, particularly when combined with MWCNTs, yields substantial improvements in electrical conductivity and optoelectronic performance. These findings highlight the potential of lead-free perovskites, particularly those with carbon nanotube incorporation, for high-performance and environmentally friendly optoelectronic applications.

### 8.3 Overall Conclusions

The summary of this thesis emphasizes the importance and potential of lead-free perovskite materials in developing optoelectronic device, particularly with the introduction of CNTs. Our research journey began with a thorough examination of lead-free perovskite synthesis methods, with an emphasis on materials such as  $\text{CH}_3\text{NH}_3\text{SnI}_3$ ,  $\text{CsSnCl}_3$ , and  $\text{Cs}_2\text{SnCl}_6$  double perovskite. We investigated their physical and optical features before developing devices to analyse charge transport mechanisms.

The emphasis was on understanding and overcoming problems such as trap-mediated charge injection at the M/S interface, which revealed insights into electrical characteristics important for device optimization. Our research expanded to investigate the effect of CNTs on perovskite optoelectronic properties, demonstrating increases in charge transport and device performance.

The chapters addressed crucial issues in a systematic manner, ranging from producing lead-free perovskite nanocubes and microrods and analysing their conduction behaviour to creating Schottky UV detectors using  $\text{Cs}_2\text{SnCl}_6$  and MWCNT composites. CNT integration not only improved charge transport qualities, but it also paved the way for smartphone-integrated UV photodetection modules that utilize wireless communication for real-time monitoring.

Moving ahead, the future holds potential for developing perovskite film surfaces to eliminate imperfections and improve charge transport in devices. Further research will require enhancing interfacial interactions between perovskites and carbon materials, as well as understanding the fundamental mechanisms that influence device performance.

### 8.4 Future Scopes of the Work

While metal-halide lead-based perovskites demonstrate excellent performance in various optoelectronic applications, their practical use is hindered by health concerns associated with lead. Therefore, it is crucial to explore various lead-free perovskite-based options from

different perspectives. This includes addressing challenges such as oxidation issues in tin-based perovskites and tailoring the bandgap of stable double perovskites to enhance light absorption in the visible range.

Future prospects for lead-free tin-based perovskite materials may involve refining the film surface to reduce intrinsic defects and improving charge transport in devices. Carbon-based perovskite composite devices represent a promising approach; therefore, further research efforts should focus on enhancing the efficiency of these devices to facilitate their commercialization. Additionally, future research should aim to improve interfacial contact and surface morphology with the perovskite surface, while elucidating the working mechanisms between perovskites and carbon materials at the interface.

Furthermore, to address hysteresis effects in perovskite optoelectronic devices, more investigations on carbon-based devices are necessary to fully understand the underlying mechanisms and develop strategies to mitigate these undesirable effects. This comprehensive approach will drive advancements in the field and accelerate the development of practical, high-performance lead-free perovskite-based devices.

-----0-----

## List of Publications

### Journal Papers

- [1] **D. Sahoo**, A.K. Karan, Z. Mallick, N.B. Manik, Synthesis and complex impedance analysis of nano cubic  $\text{CH}_3\text{NH}_3\text{SnI}_3$  perovskite for the development of optoelectronic lead-free Schottky diode, **Materials Science in Semiconductor Processing** 155 (2023) 107253.
- [2] **D. Sahoo**, A. Kanti Karan, N. Baran Manik, Influence of SWCNT on the Electrical Behaviour of an Environmentally Friendly  $\text{CH}_3\text{NH}_3\text{SnI}_3$  Perovskite-Based Optoelectronic Schottky Device, **ACS Applied Electronic Materials** 5 (2023) 2203–2214.
- [3] **D. Sahoo**, P. Sengupta, A.K. Karan, N.B. Manik, Improvement in conductivity of lead-free  $\text{CH}_3\text{NH}_3\text{SnI}_3$  perovskite thin film using multi-walled carbon nanotubes as a transporter, **Surfaces and Interfaces** 41 (2023) 103222.
- [4] **D. Sahoo**, N.B. Manik, Study on the effect of temperature on electrical and photovoltaic parameters of lead-free tin-based Perovskite solar cell, **Indian Journal of Physics** 97 (2023) 447–455.
- [5] **D. Sahoo**, A.K. Karan, N.B. Manik, Electrical charge transport properties of caesium tin chloride perovskite microrods: An analysis of microstructure conductivity and charge trapping, **Materials Letters** 339 (2023) 134119.
- [6] A.K. Karan, **D. Sahoo**, S. Sen, N.B. Manik, Electrical conduction mechanism of carmoisine dye-based natural organic device, **Indian Journal of Physics** 98 (2024) 577–583.
- [7] A.K. Karan, **D. Sahoo**, S. Sen, S. Rakshit, N.B. Manik, Effect of titanium-dioxide nanoparticle on Richardson constant and barrier height of tartrazine dye based Schottky device, **Discover Materials** 3 (2023) 5.
- [8] A.K. Karan, **D. Sahoo**, N.B. Manik, Investigating the effects of  $\text{TiO}_2$  nanoparticles on the barrier inhomogeneity of brilliant-blue fruit dye-base solar cell, **Current Applied Physics** 59 (2024) 95–104.
- [9] A.K. Karan, **D. Sahoo**, S. Sen, S. Rakshit, N.B. Manik, Modification of barrier height inhomogeneity in the presence of titanium dioxide nanoparticles on Carmoisine dye-based Schottky device, **Surfaces and Interfaces** 46 (2024) 103952.
- [10] A.K. Karan, **D. Sahoo**, N.B. Manik, Enhanced electrical conductivity and charge conduction mechanisms in Nano-cubical Sunset Yellow dye incorporated with titanium dioxide nanoparticles, **Physica B: Condensed Matter** 674 (2024) 415570.
- [11] M. Shit, **D. Sahoo**, B. Dutta, S. El Fallah, A. Kundu, N.B. Manik, C. Sinha, Exploration of Variable Temperature Magnetism and Electrical Properties of a Pyridyl-isonicotinoyl Hydrazone Bridged Three-Dimensional Mn-Metal-Organic Framework with a Thiophene Dicarboxylate Link, **Crystal Growth & Design** 22 (2022) 7143–7152.
- [12] S. Bhunia, **D. Sahoo**, B. Dutta, S. Maity, N.B. Manik, C. Sinha, Correlation in Structural Architecture toward Fabrication of Schottky Device with a Series of Pyrazine Appended Coordination Polymers, **Inorganic Chemistry** 62 (2023) 20948–20960.
- [13] S. Bhunia, **D. Sahoo**, S. Maity, B. Dutta, S. Bera, N.B. Manik, C. Sinha, Aminoisophthalate Bridged Cd (II)-2D Coordination Polymer: Structure Description, Selective

Detection of Pd<sup>2+</sup> in Aqueous Medium, and Fabrication of Schottky Diode, **Inorganic Chemistry** 62 (2023) 11976–11989.

[14] M. Shit, A.K. Karan, **D. Sahoo**, N.B. Manik, B. Dutta, C. Sinha, Strategy for the improvement of electrical conductivity of a 3D Zn(ii)-coordination polymer doubly bridged by mesaconato and pyridyl-isonicotinoyl hydrazide based Schottky diode device, **New Journal of Chemistry** 47 (2023) 5922–5929.

[15] S. Bhunia, S. Halder, K. Naskar, B. Dutta, **D. Sahoo**, K. Jana, C. Sinha, Spectrophotometric Determination of Trace Amount of Total FeII/FeIII and Live Cell Imaging of a Carboxylato Zn (II) Coordination Polymer, **Inorganic Chemistry** 61 (2022) 19790–19799.

### Article Communicated

[1] Enhanced Charge Transport in Smartphone Interfaced UV Photodetector by Incorporation of MWCNT in Cs<sub>2</sub>SnCl<sub>6</sub> Double Perovskite, **D. Sahoo**, A.K. Karan, N.B. Manik.

### Conference Proceedings

[1] **D. Sahoo**, A. Kanti Karan, N. Baran Manik, Study on the effect of temperature on electrical parameters of lead free methylammonium tin halide-based Perovskite Schottky Devices, International Journal of Innovative Research in Physics 4 (2022) 6-16.

[2] **D. Sahoo**, N.B. Manik, Estimation of trap energy of fuchsin dye sensitized Organic Photovoltaic Device based on Titanium Dioxide (TiO<sub>2</sub>), International Journal of Innovative Research in Physics 1 (2020) 17-23.

[3] A. K. Karan, **D. Sahoo**, S. Sen, N.B. Manik, Evaluation of Richardson Constant of Fruit dyes using Carmoisine and Tartrazine, International Journal of Innovative Research in Physics 3 (2022) 25-31.

[4] A.K. Karan, **D. Sahoo**, S. Sen, S. Rakshit, S. Bhunia, N.B. Manik, Estimation of activation energy of Tartrazine dye based natural organic device, AIP Conf Proc, American Institute of Physics 3067 (2024) 020023.

### List of International or National Conferences Attended

1. Charge Trapping Effect on Series Resistance (R<sub>s</sub>) of Crystal Violet (CV) Dye Based Organic Device in Presence of Single-Walled Carbon Nanotubes (SWCNT), Pallab Kumar Das, Kushal Chakraborty, **Dipankar Sahoo**, Nabin Baran Manik, **National Seminar on Physics at Surfaces and Interfaces of Soft Materials (PSISM – 2019)**, Condensed Matter Physics Research Centre, Department of Physics, Jadavpur University, 26- 27<sup>th</sup> September, 2019.

2. Estimation of trap energy of fuchsin dye sensitized Organic Photovoltaic Device based on Titanium Dioxide (TiO<sub>2</sub>), **Dipankar Sahoo**, Nabin Baran Manik, **International**

**Conference on Condensed Matter Physics (IEMPHYS -19)**, Institute of Engineering and Management, 14-16<sup>th</sup> November, 2019.

3. Effect of Titanium Dioxide (TiO<sub>2</sub>) nanoparticles on malachite green (MG) Dye based Organic Diode, Subhra Rakshit, **Dipankar Sahoo**, Arnab Kanti Karan, N. B. Manik, Jadavpur University, **NDPS 2020**.
4. Environment friendly lead-free perovskite solar cell using N, N'-diphenyl-N, N'-bis (1-naphthyl)-1,1'-biphenyl-4,4'-diamine as hole transport layer, **Dipankar Sahoo**, Nabin Baran Manik, Akal University, **ICRTGC 2021**, 28- 30<sup>th</sup> September 2021.
5. Study on the effect of temperature on electrical parameters of lead free methylammonium tin halide-based Perovskite Schottky Devices, **Dipankar Sahoo**, Arnab Kanti Karan and Nabin Baran Manik, **International Conference on Advanced Physics (IEMPHYS-22)**, Department of Basic Science & Humanities, Institute of Engineering & Management, Kolkata-91, 22-24<sup>th</sup> September 2022.
6. Evaluation of Richardson Constant of Fruit dyes using Carmoisine and Tartrazine Arnab Kanti Karan, **Dipankar Sahoo**, Sudipta Sen, N. B. Manik, **International Conference on Advanced Physics (IEMPHYS-22)**, Department of Basic Science & Humanities, Institute of Engineering & Management, Kolkata-91, 22-24<sup>th</sup> September 2022.
7. Estimation of Activation Energy of Tartrazine Dye based Organic Natural Device, **International Conference on Current Trends in Materials Science and Engineering (CTMSE-2022)**, Arnab Kanti Karan, **Dipankar Sahoo**, Sudipta Sen, Subhra Rakshit, Swapan Bhunia, N. B. Manik, 28- 30<sup>th</sup> July 2022.
8. Effect of Multiwalled Carbon Nanotubes on Trap Energy and Electrical parameters of Environment-Friendly CH<sub>3</sub>NH<sub>3</sub>SnI<sub>3</sub> Perovskite Schottky Device, **Dipankar Sahoo**, Arnab Kanti Karan, Sudipta Sen, and Nabin Baran Manik **International Conference on Nanotechnology (ICNT-22)**, Oral Presentation, Haldia, 23-24<sup>th</sup> December 2022.
9. Estimation of barrier height in presence of titanium dioxide nanoparticle on fruit dye based Schottky device using Tartrazine dye, Arnab Kanti Karan, **Dipankar Sahoo**, Sudipta Sen, Subhra Rakshit, Nabin Baran Manik, **30<sup>th</sup> National Conference on Condensed Matter Physics, (CMDAYS-2022)**, NIT Nagaland, December 14-16<sup>th</sup> 2022.
10. Impact of single walled carbon nanotubes (SWCNTS) on injection barrier of thionine dye based organic device, Sudipta Sen, Arnab Kanti Karan, **Dipankar Sahoo**, Nabin Baran Manik, **International Conference on Nanotechnology (ICNT-22)**, Poster Presentation, 23-24<sup>th</sup> December 2022.
11. Effect of Titanium-Dioxide nanoparticle on Richardson Constant of Sunset Yellow dye-based Cell, Arnab Kanti Karan, **Dipankar Sahoo**, Sudipta Sen, N. B. Manik, **International Conference on Nanotechnology (ICNT-22)**, Poster Presentation, Haldia, 23-24<sup>th</sup> December 2022.
12. Improvement in conductivity of the lead-free CH<sub>3</sub>NH<sub>3</sub>SnI<sub>3</sub> perovskite thin film using multi-walled carbon nanotubes (MWCNT) as a transporter. **Dipankar Sahoo**, Arnab Kanti Karan, Sudipta Sen, and Nabin Baran Manik. **7<sup>th</sup> International Conference on Nanoscience and Nanotechnology (ICONN-2023)**, Department of Physics and Nanotechnology SRM Institute of Science and Technology, Kattankulathur, India. Oral Presentation March 27-29, 2023.

**List of National/ International Seminars/Webinars Attend**

1. One day seminar on “Recent Trend in Frontier Research in Physics (RTFRP 2018)” Department of Physics, Jadavpur”, Department of Physics, Jadavpur University, 6<sup>th</sup> March 2018.
2. One day national Webinar on “Recent Research and Opportunities in the Field of Renewable Energy sources”, Ramsaday College, 30<sup>th</sup> September 2020.
3. International Seminar on “Recent Advances on Chemistry and Material Science (RACMS-22)”, 30-31<sup>st</sup> July and 2-3<sup>rd</sup> August 2022.
4. One Day National Webinar on “Recent Trends in Communication” In Celebration of Azadi Ki Amrit Mahotsav, Department of Electronics, Vidyasagar University, 24<sup>th</sup> January 2022.

**List of Workshop/Skill Development Program Attended**

1. Six Days Faculty Development Program (FDP) on “Recent Advancement in Science and Technology”, Department of Basic Science, Alliance University, March 06-10 2023.
2. One-week Hands-On Training Workshop on “Fabrication and Characterization of Advanced Photovoltaic Devices” Department of Physics, Indian Institute of Engineering Science & Technology (IIST), Shibpur, in collaboration with Indian Institute of Technology (IIT-ISM), Dhanbad and DST-IIST Solar PV Hub, Funded by Department of Science & Technology (DST), Govt. of India, December 12-18, 2022.
3. Six Days Virtual Workshop on "Research Opportunities in Semiconductor Materials and Devices (ROSMD-2022)" Department of Electronics and Communication Engineering, SRM Institute of Science and Technology, Kattankulathur Campus in association with the Indian Institute of Information Technology, Design, and Manufacturing, Kancheepuram, October 19-24, 2022.

*Dipankar Sahoo*  
19.06.2024